# Examining orthohantavirus host cell interactions

Katherine Anna Davies

Submitted in accordance with the requirements for the degree of
Doctor of Philosophy

The University of Leeds
The Astbury Centre for Structural Molecular Biology
School of Molecular and Cellular Biology

July 2019

The candidate confirms that the work submitted is his/her own, except where work which has formed part of jointly-authored publications has been included. The contribution of the candidate and the other authors to this work has been explicitly indicated below. The candidate confirms that appropriate credit has been given within the thesis where reference has been made to the work of others.

**Chapters 3 and 4** are based on work contributed to a jointly authored manuscript:

Davies K., Afrough B, Mankouri J, Hewson R, Edwards TA and Barr JN (accepted June 2019) *Tula orthohantavirus nucleocapsid protein is cleaved in infected cells and may sequester activated caspase-3 during persistent infection to supress apoptosis.*

*Chapter 3:* Katherine Anna Davies designed and executed all cloning, expression, purification, viral titration and molecular biology.

Mass spectrometry analysis was performed as a service by the University of Leeds Mass Spectrometry facility (James Ault)

*Chapter 4:* Katherine Anna Davies designed and executed all immunofluorescent and western blot analysis.

## Acknowledgements

*I'd like to thank my supervisors, John, Ed, Darren and Roger for their support and advice throughout the entirety of my PhD. Particularly to John for his guidance and encouragement when I felt especially lost. I'd also like to thank Jamel for his advice on confocal microscopy.*

*A massive thank you to everyone in Virology at Leeds, especially 8.61 and all the other virus TC users for all of the conversations that helped me direct my project. I especially have to thank my lab partner Amelia. Thank you so much for your support, help, company, conversation and coffee drinking. Thanks to Joe for being my cinema buddy and helping me with all the RNA and IncuCyte assays. A big thank you to Ben for all the electron microscopy (and for the cell cabbages!).*

*And thank you most of all to everyone who helped keep me sane. My parents who had to deal with an extremely stressed daughter and for setting me straight when I thought it was all too much. My wonderful housemates; Sophie, Sîan and Anna (Da Ladiez) who dealt with me at my worst and made my life so much better. The LUU taekwondo group, especially Simon, Jess and Macha, who helped improve my self-confidence and kept me fighting. And the Wine Wednesday gals, for letting me vent about all my science woes!*

*And finally to all the people who stopped to chat to me over the years, providing invaluable comments of support and advice. Thank you!*

## Abstract

Orthohantaviruses are negative sense single stranded RNA viruses that are capable of causing severe respiratory and haemorrhagic disease in humans. Currently, many aspects of the orthohantavirus lifecycle are poorly understood predominantly due to difficulties in detecting and quantifying orthohantavirus components. Here, I developed new and efficient techniques to quantify orthohantavirus proteins, RNA and infectious viral particles. These techniques were used to provide a detailed understanding of the orthohantavirus lifecycle kinetics. Additionally, I examined the interactions of the orthohantavirus nucleocapsid protein (NP) with the host cell. The NP has functions in viral transcription, translation and immune evasion as well as encapsidation of viral RNAs. As orthohantaviruses have been found to form persistent infections *in vitro* the molecular mechanisms behind this were of particular interest I examined the interaction of the Tula orthohantavirus (TULV) NP with host-cell components using co-localisation assays at early, peak and persistent infections. Furthermore, to explore the sites of viral replication within the host cell, RNA labelling techniques were utilised in combination with immunofluorescent analysis. RNA fluorescent *in situ* hybridisation probes designed against the sense and anti-sense S segment RNA were used to assess the localisation of viral RNA *in vitro* in conjunction with TULV NP and previously identified interacting host cell proteins.

Here, I identified distinct localisation of TULV NP in Vero E6 cells at 36 hpi, 7 dpi and 30 dpi notably the formation of large filamentous structures in the perinuclear region of infected cells in addition to establishing multinucleate cells during persistent infection. These filamentous structures appear to be maintained through the vimentin intermediate network. Additional TULV NP was found to show high levels of co-localisation with the Golgi and the stress granule marker, TIA-1. These markers also showed high-levels of co-localisation with sense and anti-sense TULV S segment RNA which may indicate these sites to be areas of viral replication and accumulation.

# Table of Contents

# List of Tables

# List of Figures

## Abbreviations

| | | | |
|---|---|---|---|
| **5-EU** | 5-ethynyl uridine | **JNK** | c-Jun N-terminal kinases |
| **6-FAM** | 6-Carboxyfluorescein | **KHF** | Korean haemorrhagic fever |
| **$A_{280nm}$** | Absorbance 280 nm | **L** | Large |
| **ACBD3** | Acyl-CoA Binding Domain Containing 3 | **L** | Lysosome |
| **ActD** | Actinomycin D | **Lab6** | Lanthanum hexaboride |
| **AKI** | Acute kidney injury | **LAMP1** | Lysosomal-associated membrane protein 1 |
| **APS** | Ammonium per sulphate | **LB** | Luria-Bertani |
| **ARDS** | Adult respiratory distress syndrome | **LB** | Lamellar body |
| **BAP** | Biotinylation acceptor protein | **LSCM** | Laser scanning confocal microscopy |
| **BB** | Blocking buffer | **M** | Medium |
| **BHQ** | Black hole quencher | **M** | Mitochondria |
| **BSA** | Bovine serum albumin | **MDA5** | Melanoma Differentiation-Associated protein 5 |
| **casp-3** | Procaspase 3 | **MOI** | Multiplicity of infection |
| **casp-3C** | Cleaved caspase 3 | **mRNA** | messenger RNA |
| **cDNA** | complementary DNA | **NE** | Nephropathia epidemica |
| **CHD3** | Chromodomain helicase DNA-binding protein 3 | **NFκβ** | Nuclear factor kappa beta |
| **co-IP** | co-immunoprecipitation | **NOC** | Nocodazole |
| **ConA** | Concanavalin A | **NP** | Nucleocapsid protein |
| **CPE** | Cytopathic effect | **NP-40** | Nonyl phenoxypolyethoxylethanol-40 |
| **cRNA** | copy RNA | **$NP_{core}$** | Nucleocapsid protein core region |
| **Ct** | Cycle threshold | **NSs** | Non-structural protein |

| | | | |
|---|---|---|---|
| **CTL** | Cytotoxic T lymphocyte | **Nu** | Nucleus |
| **Cy5** | Cyanine-5 | **NW** | New world |
| **CytD** | Cytochalasin D | **OA** | Okadaic acid |
| **DAF** | Decay accelerating factor | **$OD_{600nm}$** | Optical density 600 nm |
| **DAPI** | 4',6-Diamidino-2-Phenylindole | **ORF** | Open reading frame |
| **Daxx** | Dead domain associated protein-6 | **OW** | Old world |
| **DCP1a** | Decapping MRNA 1A | **P bodies** | Processing bodies |
| **DDSA** | Dodecenylsuccinic anhydride | **PAGE** | Polyacrylamide gel electrophoresis |
| **DEPC** | Diethylpyrocarbonate | **PARP** | Poly (ADP-ribosome) polymerase |
| **DEPC** | Diethylpyrocarbonate | **PARP-C** | Cleave poly (ADP-ribosome) polymerase |
| **DIC** | Differential interference contrast | **PCR** | Polymerase chain reaction |
| **DMEM** | Dulbecco's modified Eagle's medium | **PEG** | Poly(ethylene glycol) |
| **DMP30** | 2,4,6-Tris(dimethylaminomethyl)phenol | **PHE** | Public Health England |
| **DMSO** | Dimethyl sulfoxide | **PKR** | Protein kinase R |
| **dpi** | days post infection | **PRNT** | Plaque reduction neutralisation test |
| **dsRNA** | double stranded RNA | **PVDF** | Polyvinylidene difluoride |
| ***E. coli*** | *Escherichia coli* | **Rab11** | Ras-related protein 11 |
| **EDTA** | Ethylene-diamine-tetraacetic acid | **Rab5** | Ras-related protein 5 |
| **EEA-1** | Early endosome antigen 1 | **Rab7** | Ras-related protein 7 |
| **EHNA** | Erythro-9-(2-hydroxy-3-nonyl)adenine | **RdRp** | RNA dependent RNA polymerase |
| **EL** | Endolysosome | **RER** | Rough endoplasmic reticulum |
| **EM** | Electron microscopy | **RIG-1** | Retinoic acid-inducible gene 1 |

| | | | |
|---|---|---|---|
| **ER** | Endoplasmic reticulum | **RIPA** | Radioimmunoprecipitation assay buffer |
| **ERGIC** | ER-Golgi intermediate compartment | **RNP** | Ribonucleoprotein |
| **FBS** | Foetal bovine serum | **RPM** | Revolutions per minute |
| **FISH** | Fluorescent *in-situ* hybridisation | **RT-PCR** | Reverse transcriptase-polymerase chain reaction |
| **FITC** | Fluorescein isothiocyanate | **S** | Small |
| **FRNT** | Focus reduction neutralisation assay | **SDS** | Sodium dodecyl sulphate |
| **G3BP** | Ras-GAP SH3 binding protein | **SFM** | serum free media |
| **GAPDH** | Glyceraldehyde 3-phosphate dehydrogenase | **ssDNA** | single stranded DNA |
| **GPC** | Glycoprotein precursor | **SUMO-1** | Small ubiquitin-related modifier-1 |
| **GuHCl** | Guanidinium hydrochloride | **TBK1** | TANK Binding Kinase 1 |
| **HBC** | High binding capacity | **TCID50** | Tissue culture infective dose |
| **HBC** | High binding capacity | **TEM** | Transmission electron microscopy |
| **HCPS** | Hantavirus cardiopulmonary syndrome | **TEMED** | Tetramethylethylenediamine |
| **HFRS** | Haemorrhagic fever with renal syndrome | **TGF** | Tumour growth factor |
| **HIPK2** | Homeodomain-interacting protein kinase 2 | **TNF** | Tumour necrosis factor |
| **HLA** | Human leukocyte antigen | **TRAF** | TNF receptor associated factors |
| **hpi** | hours post infection | **TRITC** | Tetramethylrhodamine |
| **IB** | Inclusion body | **TTRAP** | TRAF and TNF receptor-associated protein |
| **IF** | Immunofluorescence | **Ulp1** | Ubl-specific protease 1 |
| **IFN** | Interferon | **UTR** | Untranslated region |

| | | | |
|---|---|---|---|
| **IL** | Interleukin | **VEGF** | Vascular endotheial growth factor |
| **IP** | Immunoprecipitation | **VEGFR2** | Vascular endothelial growth factor receptor 2 |
| **IPTG** | Isopropyl β-D-1-thiogalactopyranoside | **vRNA** | viral RNA |
| **IRF3** | Interferon regulatory transcription factor 3 | **WFDM** | Widefield fluorescent deconvolution microscopy |
| **IU** | immunofluorescent units | **β-ME** | β-mercaptoethanol |

**Virus Abbreviations**

| **Hantaviridae** | | **Other** | |
|---|---|---|---|
| **ANDV** | Andes virus | **ASFV** | African swine fever virus |
| **BCCV** | Black creek canal virus | **BUNV** | Bunyamwera |
| **DOBV** | Dobrava-Belgrade virus | **CHIKV** | Chikungunya virus |
| **HTNV** | Hantaan virus | **DENV** | Dengue virus |
| **NYV** | New York virus | **FMDV** | Foot-and-mouth disease virus |
| **PHV** | Prospect Hill virus | **HIV** | Human immunodeficiency virus |
| **PUUV** | Puumala virus | **hRSV** | human respiratory syncytial virus |
| **SANGV** | Sangassou virus | **JUNV** | Junin virus |
| **SEOV** | Seoul virus | **MVM** | Parvovirus minute virus of mice |
| **SNV** | Sin Nombre virus | **RVFV** | Rift valley fever virus |
| **TULV** | Tula virus | **UUKV** | Uukuniemi virus |
| | | **WNV** | West Nile virus |

# Chapter 1 : Introduction

## 1.1 General Introduction

### 1.1.1 Bunyavirales

#### 1.1.1.1 Bunyavirales order

Orthohantaviruses are negative sense single-stranded RNA viruses which belong to the *Negarnaviricota* phylum, which contains nearly all the negative sense RNA viruses that have been classified to date. The phylum is divided into the subphyla *Haploviricotina* (haplo 'simple', generally non-segmented) and *Polyploviricotina* (polyplo 'complex', generally segmented). The *Bunyavirales* order is located within the *Ellioviricetes* class of the *Polyploviricota* sub-phylum. At the time of writing, the *Bunyavirales* order contains twelve viral families; *Arenaviridae*, *Crulivirdae*, *Fimoviridae*, *Hantaviridae*, *Leishbuviridae*, *Mypoviridae*, *Nairoviridae*, *Peribunyaviridae*, *Phasmaviridae*, *Phenuiviridae, Tospoviridae* and *Wupedeviridae*. These families comprise negative sense RNA viruses with between 2 and 3 genome segments and contain a variety of pathogens of mammals, bird, fish, reptiles and plants in addition to apathogenic virus species (Maes et al., 2019). Table 1 describes different viral species within the *Negarnaviricota* phylum. A phylogenetic representation of selected members of the Negarnaviricota can be seen in Figure 1.

#### 1.1.1.2 The *Hantaviridae* family

As of March 2019, the *Hantaviridae* family contains four genera; *Loanvirus*, *Mobatvirus*, *Orthohantavirus* and *Thottimvirus* that together comprise a total of 41 recognised species (Maes et al., 2019). Table 2 describes various characteristics of each of these species, including geographic distribution, host species and pathogenicity in humans. The phylogenetic relationship of hantaviruses based on the nucleotide sequence of the small (S) genome segment reveals clustering into four groups, representing each of the four genera (Figure 2). Within the *Orthohantavirus* genera, species are further clustered due to geographic location and virus pathogenicity in humans (Table

2). There is strong evidence for co-evolution of the orthohantaviruses with their host species over the past 90-100 million year and additionally for host-switching events due to close geographic proximity of different potential hosts. These two mechanisms have shaped orthohantavirus evolution and the relationship between viral host and pathogenicity (Plyusnin and Sironen, 2014).

Recently several sub-families, genera and species have been added to the family. These include the *Actantavirinae* and *Agantavirinae* sub-families which comprise fish-borne hantaviruses and the *Repantavirinae* sub-family, which contains a Gecko-borne hantavirus. These recent additions bring the total number of orthohantavirus species to 46 (Abudurexiti et al., 2019). Hereafter members of the *Hantaviridae* family or *Orthohantavirus* genus will be referred to by the generic titles of “hantaviruses” or “orthohantaviruses”, respectively.

### 1.1.2 History

#### 1.1.2.1 Identification

Orthohantaviruses have likely been associated with human disease throughout history, with anecdotal descriptions of orthohantavirus-like disease described in Chinese medical records as far back as AD680 and it has been suggested that the epidemic of sweating sickness in medieval England may have been caused by a person-to-person transmitted orthohantavirus (Taviner et al., 1998). More recently, documentations of disease consistent with hantaviral infections appear in Russian hospital records in the early 1900s, along with descriptions of field nephritis outbreaks during World Wars I and II (Casals et al., 1970; Johnson, 2000), as well as during the Korean conflict (1950-1953), when soldiers were diagnosed with a disease referred to at the time as Korean haemorrhagic fever (KHF) (Johnson, 2000). In 1978, Hantaan virus (HTNV) was identified as the etiological agent of KHF, isolated from Korean striped field mouse (*Apodemus agrarius coreae*) (Lee et al., 1978; Lee et al., 1982). Isolated HTNV virions were described to contain a tripartite genome of negative sense RNA which placed them within the *Bunyaviridae* family (present: *Bunyavirales* order) but lack of serological cross reactivity with existing bunyavirus members placed HTNV within its own, separate genus (present: *Hantaviridae* family, containing four genera)

(Schmaljohn et al., 1983; Schmaljohn and Dalrymple, 1983). HTNV remains the prototypical hantavirus member, and type species of the orthohantavirus genus.

The description of KHF is entirely consistent with the hantavirus-mediated disease now known as haemorrhagic fever with renal syndrome (HFRS). Other human disease outcomes caused by hantavirus infections include nephropathia epidemica (NE), which is considered to be a milder form of HFRS, and hantavirus cardiopulmonary syndrome (HCPS).

Since 1978, many more orthohantavirus species have been isolated. In 1980, the causative agent of NE was found to be Puumala virus (PUUV) isolated from *Myodes glareolus* (bank vole, formerly *Clethrionomys glareolus*) (Brummer-Korvenkontio et al., 1980). The causative agent of an acute respiratory disease HCPS in the USA was isolated from the deer mouse, *Peromyscus maniculatus*, and named Sin Nombre virus (SNV) (Feldmann et al., 1993; Hallin et al., 1996). Together, HFRS, NE and HCPS are the three recognised clinical syndromes caused by hantavirus infection, see section 1.1.3 for more details. It should be noted that orthohantavirus species are frequently identified and it is likely that this family will continue to expand, with further reclassification likely.

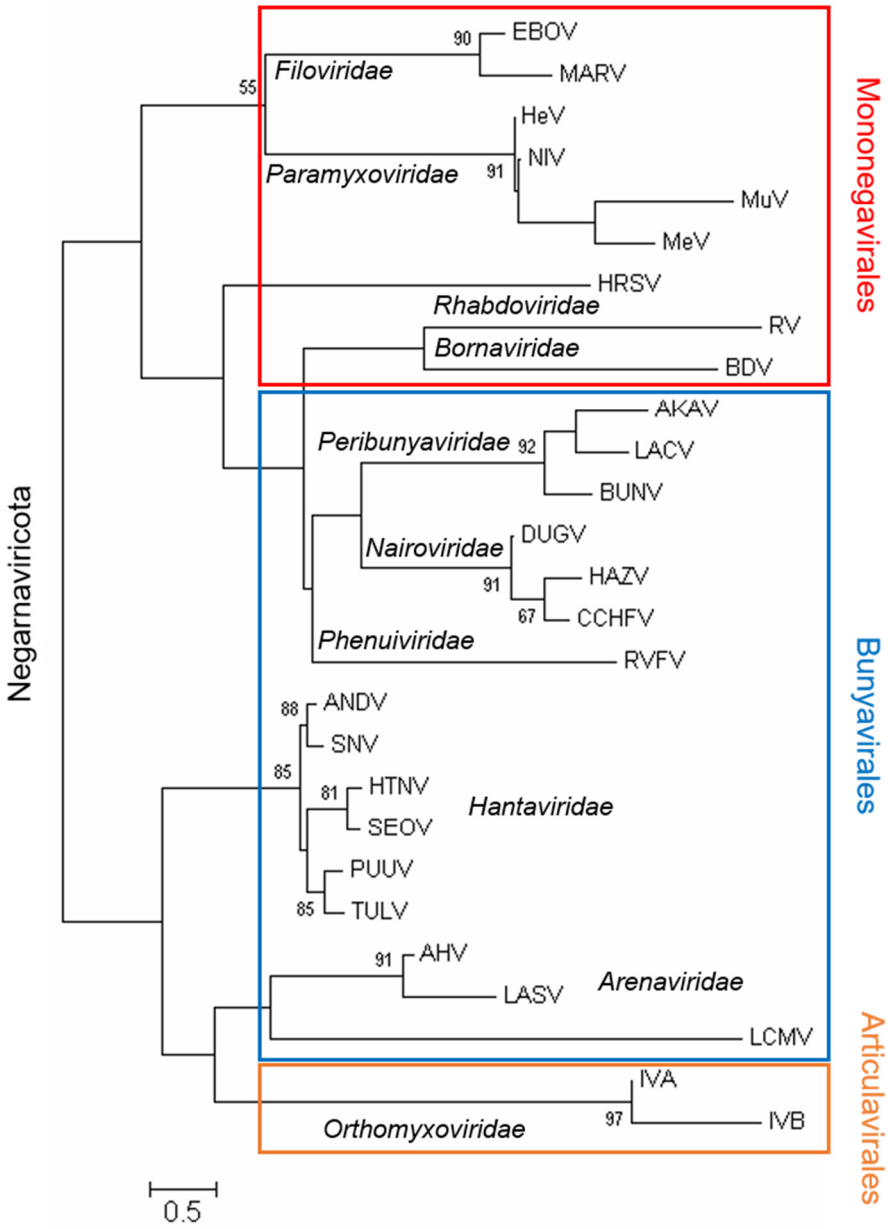


**Figure 1 Molecular phylogenetic analysis of selected members of the Negarnaviricota phylum by maximum likelihood method.**

The evolutionary history was inferred by using the maximum likelihood method (Whelan and Goldman, 2001). The tree with the highest log likelihood (-10322.31) is shown. The percentage of trees in which the associated taxa clustered together is shown next to the branches. Initial tree(s) for the heuristic search were obtained automatically by applying Neighbor-Join and BioNJ algorithms to a matrix of pairwise distances estimated using a JTT model, and then selecting the topology with superior log-likelihood value. The tree is drawn to scale, with branch lengths measured in the number of substitutions per site. The analysis involved 27 amino acid sequences from *Negarnaviricota* phylum. All positions containing gaps and missing data were eliminated. There was a total of 176 positions in the final dataset. Evolutionary analyses were conducted in MEGA7 (Kumar et al., 2016).

| Phylum | Subphylum | Class | Order | Family | Genus | Species | Abb. | NCBI | References |
|---|---|---|---|---|---|---|---|---|---|
| Negarnaviricota | Polyploviricotina | Ellioviricetes | Bunyavirales | *Arenaviridae* | *Mammarenavirus* | Lassa virus | LASV | K03362 | (Clegg and Oram, 1985) |
| | | | | | | Lymphocytic choriomeningitis virus | LCMV | GQ862982 | (Palacios et al., n.d.) |
| | | | | | | Junin virus | AHV | D10072 | (Ghiringhelli et al., 1989) |
| | | | | *Hantaviridae* | *Orthohantavirus* | Andes virus | ANDV | NC003466 | (Gu et al., 2013) |
| | | | | | | Puumala virus | PUUV | KJ994776 | (Ali et al., 2015) |
| | | | | | | Hantaan virus | HTNV | KT935057 | (Song and Kim, n.d.) |
| | | | | | | Seoul virus | SEOV | KP645198 | (Wang et al., 2015) |
| | | | | | | Sin Nombre virus | SNV | L37904 | (Chizhikov et al., 1995) |
| | | | | | | Tula virus | TULV | NC005227 | (Plyusnin et al., 1995) |
| | | | | *Nairoviridae* | *Orthonairovirus* | Dugbe virus | DUGV | NC_004157 | (Bridgen et al., 2002) |
| | | | | | | Hazara virus | HAZV | NC_038711 | (Lewandowski et al., n.d.) |
| | | | | | | Crimean Congo haemorrhagic fever virus | CCHFV | AJ010649 | (Chinikar et al., 2016) |
| | | | | *Phenuiviridae* | *Phlebovirus* | Rift valley fever virus | RVFV | MG273460 | (Ikegami et al., 2017) |
| | | | | *Peribunyaviridae* | *Orthobunyavirus* | Bunyamwera virus | BUNV | NC_001927 | (Elliott, 1989) |
| | | | | | | Akabane virus | AKAV | LC217487 | (Yanase et al., 2018) |
| | | | | | | La Crosse virus | LACV | KP271116 | (Lambert, n.d.) |
| | | Insthoviricetes | Articulavirales | *Orthomyxoviridae* | *Alphainfluenzavirus* | Influenza A H1N1 virus | IVA | M63767 | (Gorman et al., 1991) |
| | | | | | *Betainfluenzavirus* | Influenza B virus | IVB | M20174 | (DeBorde et al., 1988) |
| | Haploviricotina | Monjiviricetes | Mononegavirales | *Bornaviridae* | *Orthobornavirus* | Borna disease virus | BDV | EU095836 | (Puorger et al., 2010) |
| | | | | *Filoviridae* | *Ebolavirus* | Zaire virus | EBOV | L11365 | (Sanchez et al., 1989) |
| | | | | | *Marburgvirus* | Marburg virus | MARV | GQ433353 | (Lofts et al., 2011) |
| | | | | *Paramyxoviridae* | *Henipavirus* | Hendra virus | HeV | NC_001906 | (Wang et al., 2000) |
| | | | | | | Nipah virus | NIV | AF376747 | (Chua et al., 2002) |
| | | | | | *Morbillivirus* | Measles virus | MeV | AJ250073 | (Truong et al., 2001) |
| | | | | | *Rubulavirus* | Mumps virus | MuV | AJ937822 | (Mallya et al., n.d.) |
| | | | | *Pheumoviridae* | *Orthopneumovirus* | Human respiratory syncytial virus | HRSV | DQ780568 | (Sun et al., n.d.) |
| | | | | *Rhabdoviridae* | *Lyssavirus* | Rabies virus | RV | L20672 | (Nadin-Davis et al., 1993) |

**Table 1 Negarnaviricota phylum virus species.**

List of notable viruses within the *Negarnaviricota* phylum.

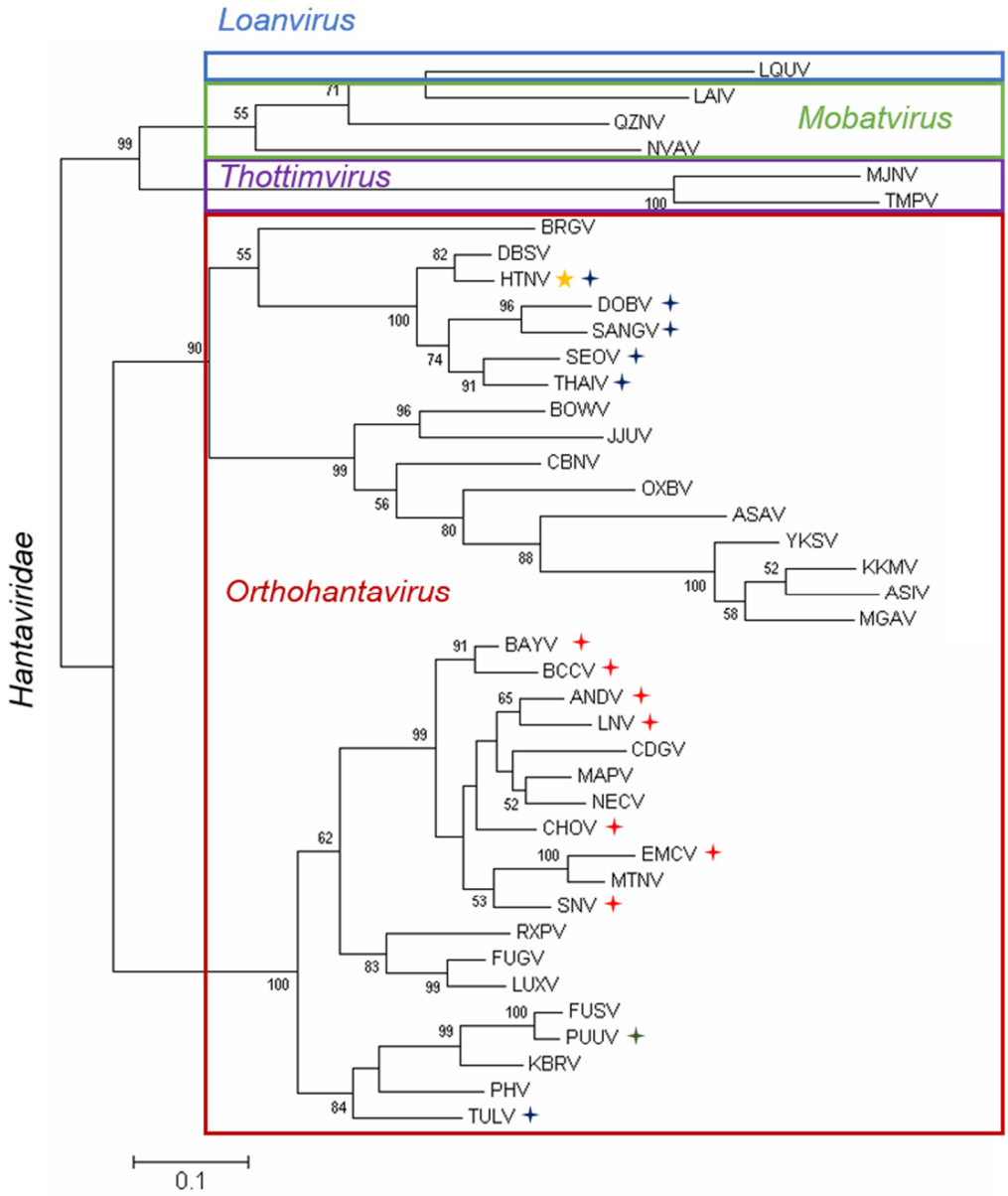


**Figure 2 Molecular phylogenetic analysis of selected members of the *Hantaviridae* family by the maximum likelihood method.**

The evolutionary history was inferred by using the maximum likelihood method (Whelan and Goldman, 2001). Tree with the highest log likelihood (-14249.66) is shown. Percentage of trees in which the associated taxa clustered together is shown next to the branches. Initial tree(s) for the heuristic search were obtained by applying Neighbor-Join and BioNJ algorithms to a matrix of pairwise distances estimated using a JTT model, and then selecting the topology with superior log-likelihood value. Tree is drawn to scale, with branch lengths measured in the number of substitutions per site. Analysis involved 41 amino acid sequences from Hantaviridae family with a total of 416 positions in the final dataset. All positions containing gaps and missing data were eliminated. Evolutionary analyses were conducted in MEGA7 (Kumar et al., 2016). Blue cross – HFRS, red cross – HCPS, green cross – NE, yellow star – prototype virus

| Hantavirus genus | Hantavirus sp. | Abb. | NCBI | Geographical Distribution | Host Family/Order | Host Species | Associated Disease | References |
|---|---|---|---|---|---|---|---|---|
| *Loanvirus* | *Longquan* | LQUV | JX465422 | Asia | Chiroptera | Horseshoe bats (*Rhinolophus sp.*) | Unknown | (Guo et al., 2013) |
| *Mobatvirus* | *Laibin* | LAIV | KM102247 | Asia | Chiroptera | Black-Bearded Tomb Bat (*Taphozous melanopogon*) | Unknown | (Xu et al., 2015) |
| | *Nova* | NVAV | KR072621 | Hungary and France | Chiroptera/Soricidae/Talpidae | European Mole (*Talpa europaea*), bats and shrews | Unknown | (Gu et al., 2015) |
| | *Quezon* | QZNV | KU950713 | Philippines | Chiroptera | Geoffroy's rousette bat (*Rousettus amplexicaudatus*) | Unknown | (Arai et al., 2016) |
| *Orthohantavirus* | *Amda* | MGAV | KF974360 | Japan | Muridae | Laxmann's Shrew (*Sorex caecutiens*) | Unknown | (Bennett et al., 2014) |
| | *Andes* | ANDV | NC003466 | Chile, Argentina | Cricetidae | Long-Tailed Colilargo (*Oligoryzomys longicaudatus*) | HCPS | (Meissner et al., 2002) |
| | *Asama* | ASAV | EU929072 | Japan | Talpidae | Japanese Shrew Mole (*Urotrichus talpoides*) | Unknown | (Arai et al., 2008) |
| | *Asikkala* | ASIV | KC880341 | Europe | Soricidae | Common Shrew (*Sorex araneus*) | Unknown | (Radosa et al., 2013) |
| | *Bayou* | BAYV | GQ200820 | North America | Cricetidae | Marsh Rice Rat (*Oryzomys palustris*) | HCPS | (Richter et al., n.d.) |
| | *Black Creek Canal* | BCCV | AB689163 | North America | Cricetidae | Cotton Rat (*Sigmodon hispidus*) | HCPS | (Koma et al., 2012) |
| | *Bowe* | BOWV | KC631782 | Africa | Soricidae | Doucet's Musk Shrew (*Crocidura douceti*) | Unknown | (Gu et al., 2013) |
| | *Bruges* | BRGV | KX551960 | Europe | Talpidae | European Mole (*Talpa europaea*) | Unknown | (Laenen et al., 2018) |
| | *Cano Degladito* | CDGV | DQ285566 | South America | Cricetidae | Alston's Cotton Rat (*Sigmodon alstoni*) | Unknown | (Milazzo et al., 2006) |
| | *Cao Bang* | CBNV | EF543524 | Asia | Soricidae | Common Shrew (*Sorex araneus*) | Unknown | (Song et al., 2007) |
| | *Choclo* | CHOV | DQ285046 | Central and South America | Cricetidae | Northern Pygmy Rice Rat (*Oligoryzomys fulvescens*) | HCPS | (Nelson et al., 2010) |
| | *Dabieshan* | DBSV | JF796022 | Asia | Muridae | Chinese White-Bellied Rat (*Niviventer confucianus*) | Unknown | (Wang et al., n.d.) |
| | *Dobrava-Belgrade* | DOBV | GU904031 | Europe | Muridae | Mice (*Apodemus sp.*) | HFRS | (Kirsanovs et al., 2010) |
| | *El Moro Canyon* | EMCV | NC038423 | North and Central America | Cricetidae | Western Harvest Mouse (*Reithrodontomys megalotis*), Mexican Woodrat (*Neotoma mexicana*) | HCPS | (Hjelle et al., 1994) |
| | *Fugong* | FUGV | KT899701 | Asia | Cricetidae | Small Oriental Vole (*Eothenomys eleusis*) | Unknown | (Ge et al., 2016) |
| | *Fusong* | FUSV | EF442087 | Asia | Cricetidae | Grey Red-Backed Vole (*Myodes rufocanus*) | Unknown | (Zhang et al., 2007) |
| | *Hantaan* | HTNV | KT935057 | Asia | Muridae | Striped Field Mouse (*Apodemus agrarius*) | HFRS | (Song and Kim, n.d.) |
| | *Jeju* | JJUV | HQ834695 | Asia | Soricidae | Asian Lesser White-Toothed Shrew (*Crocidura shantungensis*) | Unknown | (Arai et al., 2012) |

| | | | | | | | | |
|---|---|---|---|---|---|---|---|---|
| | Kenkeme | KKMV | KJ857341 | Asia | Soricidae | Flat-Skulled Shrew (*Sorex roboratus*) | Unknown | (Wang et al., 2014) |
| | Khabarovsk | KBRV | KJ857345 | Eurasia | Cricetidae | Maximowicz's Vole (*Microtus maximowiczii*) | Unknown | (Wang et al., 2014) |
| | Laguna Negra | LNV | AF005727 | South America | Cricetidae | Small Vesper Mouse (*Calomys laucha*) | HCPS | (Johnson et al., 1997) |
| | Luxi | LUXV | HM756286 | Asia | Cricetidae | Yunnan Red-Backed Vole (*Eothenomys miletus*) | Unknown | (Zhang et al., 2011) |
| | Maporal | MAPV | AB689164 | Central and South America | Cricetidae | Pygmy Rice Rat (*Oligoryzomys sp.*) | Unknown/Apathogenic | (Koma et al., 2012) |
| | Montano | MTNV | AB620100 | Central and South America | Cricetidae | Orizaba Deer Mouse (*Peromyscus beatae*) | Unknown | (Kariwa et al., n.d.) |
| | Necocli | NECV | KF481954 | South America | Cricetidae | Short-Tailed Zygodont (*Zygodontomys brevicauda cherriei*) | Unknown | (Montoya-Ruiz et al., 2015) |
| | Oxbow | OXBV | FJ539166 | North America | Talpidae | American Shrew Mole (*Neurotrichus gibbsii*) | Unknown | (Kang et al., 2009) |
| | Prospect Hill | PHV | M34011 | North America | Cricetidae | Meadow vole (*Microtus pennsylvanicus*) | Unknown/Apathogenic | (Parrington and Kang, 1990) |
| | Puumala | PUUV | KJ994776 | Northern Europe | Cricetidae | Bank vole (*Myodes glareolus*) | NE | (Ali et al., 2015) |
| | Rockport | RXPV | HM015223 | North America | Talpidae | Eastern mole (*Scalopus aquaticus*) | Unknown | (Kang et al., 2011) |
| | Sangassou | SANGV | JQ082300 | Africa | Muridae | Flat-nosed wood mouse (*Hylomyscus simus*) | HFRS (not confirmed) | (Klempa et al., 2012) |
| | Seoul | SEOV | KP645198 | Europe, Asia and Americas | Soricidae/Muridae | Asian house shrew (*Suncus murinus*), Rat (*Rattus sp.*) | HFRS | (Wang et al., 2015) |
| | Sin Nombre | SNV | L37904 | North America | Cricetidae | North American deermouse (*Peromyscus maniculatus*) | HCPS | (Chizhikov et al., 1995) |
| | Thailand | THAIV | KC490916 | Asia | Muridae | Greater bandicoot rat (*Bandicota indica*), Black rats (*Rattus rattus*) | HFRS | (Reynes et al., 2014) |
| | Tula | TULV | NC005227 | Europe | Cricetidae | European common vole (*Microtus arvalis*) | HFRS | (Plyusnin et al., 1995) |
| | Yakeshi | YKSV | JX465423 | Asia | Soricidae | Taiga shrew (*Sorex isodon*) | Unknown | (Guo et al., 2013) |
| Thottimvirus | Imjin | MJNV | KJ420559 | Asia | Soricidae | Ussuri White-Toothed Shrew (*Crocidura lasiura*) | Unknown | (Lin et al., 2014) |
| | Thottopalayam | TMPV | NC010704 | India and Asia | Soricidae | Asian house shrew (*Suncus murinus*) | Apathogenic | (Song et al., n.d.) |

**Table 2 Orthohantavirus genus and species.**

Geographical location, host family/order, host species and associated disease are shown. HFRS – Haemorrhagic fever with renal syndrome, NE – Nephropathia Epidemica, HCPS – orthohantavirus cardiopulmonary syndrome

### 1.1.3 Transmission, Disease and Pathogenesis

#### 1.1.3.1 Rodent to rodent transmission

Hantaviruses are maintained in rodent populations by indirect transmission through inhalation of infected excreta and horizontal transmission through aggressive behaviour, grooming and sexual contact (Camaioni et al., 2001; Botten et al., 2002; Kallio et al., 2006; Hardestam et al., 2008). There is also evidence that orthohantaviruses can be maintained in rodent populations through transmission from bites of trombiculid and gamasid mites. Orthohantaviruses may be maintained in the mite populations through vertical transovarial transmission (Yu and Tesh, 2014). Orthohantaviruses tend to cause asymptomatic, persistent infections in host species (Schountz et al., 2007; Easterbrook and Klein, 2008; Sanada et al., 2011; Perley et al., 2019). However, some orthohantavirus species have been shown to have a negative impact on host survival, such as PUUV which impairs the winter survival of bank voles (Kallio et al., 2007; Voutilainen et al., 2016).

#### 1.1.3.2 Rodent to human transmission

Hantaviruses are zoonotic pathogens of humans, transmitted to humans from infected rodents. Infections in humans primarily arise from indirect transmission of the virus through the inhalation of infected rodent excreta (faeces, urine or saliva) (Figure 3) (Hart and Bennett, 1999). Orthohantavirus infections can be linked to rodent invasion into homes, workspaces or close contact with infected rodents (Zeitz et al., 1995; Hjelle et al., 1996; Plyusnin et al., 1997; Ahlm et al., 1997; Van Loock et al., 1999). Rodent bites have also been implicated in the transmission of orthohantaviruses to humans (Schultze et al., 2002; Hirsch et al., 2003).

#### 1.1.3.3 Human to human transmission

Generally humans act as a dead-end host for orthohantaviruses and only ANDV has been documented to be transmitted person-to-person (Wells et al., 1997; Padula et al., 1998; Martinez et al., 2005). Other examples of human-to-human transmission of orthohantaviruses have occurred through organ transplantation and blood transfusion. Vertical transmission has also been documented (Lee, 1989; Sinisalo et al., 2010).

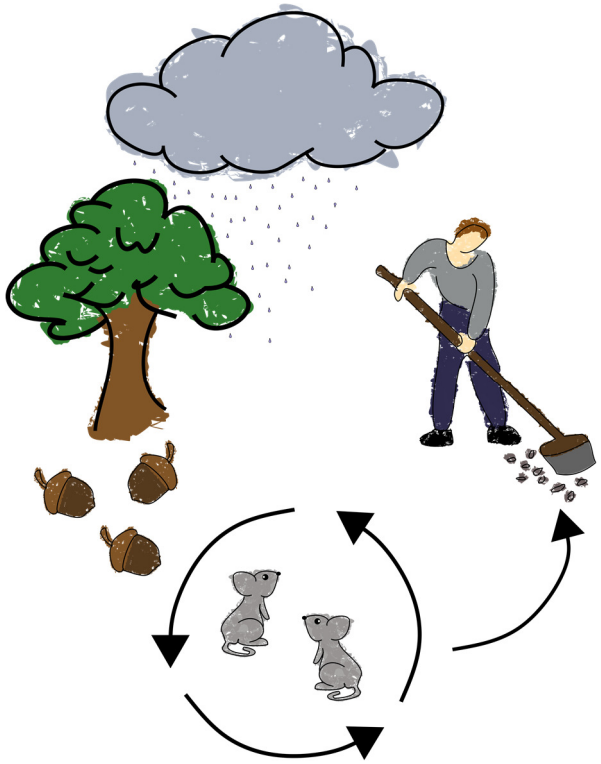

**Figure 3 Transmission cycle of orthohantaviruses.**

Orthohantaviruses are transmitted by rodent hosts where they form persistent, asymptomatic infections. Increased rainfall causes an abundance of food leading to larger rodent populations. Rodent invasion into human habitats increase risk of transmission due to aerosolization of rodent excreta such as when cleaning. Aerosolised infective particles are inhaled leading to human infection.

#### 1.1.3.4 Haemorrhagic fever with renal syndrome

There are estimated to be 150,000-200,000 hospitalisations due to HFRS per year with a case fatality rate of 1-10%. The majority of hospitalisations occur in China, Korea and Russia (Bi et al., 2008). In China, there were 1,625,002 cases of HFRS between 1950-2014 with a fatality rate of 2.89% (Jiang et al., 2016). In Europe, a milder form of HFRS is prevalent with mortality rates of 0.1-1%. This milder disease is named nephropathic epidemica (Mustonen et al., 2013). It is likely due to similarities in symptoms between HFRS/NE and other diseases such as leptospirosis and influenza (Clem et al., 2008) that orthohantavirus disease is underreported in the general population. In the UK 32.9 % pet fancy rat owners were seropositive for orthohantavirus antigens but very few hospitalisations have been reported (Duggan et al., 2014).

HFRS has an incubation period of 10 days to 6 weeks and is characterised by fever, hypotension leading to circulatory collapse, haemorrhage and acute

kidney injury (AKI). There are typically five phases to HFRS: febrile, hypotensive, oliguric, polyuric and convalescent. The cause of death is typically due to renal insufficiency, shock or haemorrhage (Jonsson et al., 2010; Jiang et al., 2016).

#### 1.1.3.5 Hantavirus cardiopulmonary syndrome

New World orthohantaviruses in the Americas are known to cause HCPS, a severe, respiratory disease which has mortality rates of up to 40% (Hjelle and Torres-Pérez, 2010). HCPS has an incubation period of 1-6 weeks and is characterised by fever, haemorrhage, hypotension, rapid onset respiratory failure and cardiogenic shock. There are five phases to HCPS: incubation, febrile prodrome, cardiopulmonary, diuretic and convalescent. Cause of death is usually due to pulmonary oedema and cardiogenic shock (Jonsson et al., 2010; Hjelle and Torres-Pérez, 2010).

#### 1.1.3.6 Pathogenesis

Both HFRS and HCPS diseases are characterised by a loss in vascular integrity and capillary leakage (Hjelle and Torres-Pérez, 2010). Orthohantaviruses are known to replicate in capillary endothelial cells but rarely show signs of cytopathic effect suggesting the pathogenesis must be due to an alternate mechanism (Pensiero et al., 1992; Temonen et al., 1993). Orthohantavirus infection of the vascular endothelium induces increased permeability of the capillary monolayer. This may be due to the use of β3 integrins for host cell entry. β3 integrins are reported to interact with vascular endothelial growth factor receptor 2 (VEGFR2) which interacts with VE-cadherin for maintenance of the endothelial barrier. Orthohantavirus infection induces upregulation of vascular endothelial growth factor (VEGF), a cytokine which is a potent promoter of vascular permeability. VEGF binds to VEGFR2 and induces degradation of VE-cadherin leading to disruption in the adherens junctions and, in doing so, increases vascular permeability.

Orthohantavirus infection leads to structural remodelling of kidney cells causing disruption of tight junctions and reduced vascular integrity. Vascular leakage may be the cause of pulmonary oedema in the lungs and acute nephritis in the kidneys (Geimonen et al., 2002; Shrivastava-Ranjan et al., 2010; Krautkramer et al., 2011; I. Gavrilovskaya et al., 2012). Pathogenic orthohantavirus interactions

with β3 integrins may also impact platelet function. Thrombocytopenia (low blood platelet count) is characteristic of most orthohantavirus infections. Orthohantaviruses may bind to β3 integrins on quiescent platelets and recruit these platelets to endothelial cell surface where they form a surface layer over infected cells. This recruitment of platelets may lead to the development of thrombocytopenia in patients (Gavrilovskaya et al., 2010; Vaheri, Henttonen, et al., 2013).

An increased level of cytotoxic T lymphocytes (CTLs) has been associated with orthohantavirus infection. Infected cell cultures treated with $CD8^+$ T cells displayed increased permeability suggesting CTLs may also be involved in increased endothelial cell permeability during orthohantavirus infection (Kanerva et al., 1998; Terajima and Ennis, 2011; Rasmuson et al., 2011). Orthohantaviruses have been shown to have developed escape mechanisms to avoid killing by CTLs. Infected endothelial cells obtained from patients show little to no damage by CTLs. Orthohantaviruses are able to block CTL mediated cell-death by interfering with the action of granzyme-B and caspase-3 through interactions with the nucleocapsid protein (NP) (Gupta et al., 2013; Solà-Riera et al., 2019). Remarkably, NK cells activated by orthohantavirus infected cells were shown to not kill infected cells but instead targeted uninfected cells for cell-death. This suggests orthohantavirus induce killing of uninfected endothelial cells by decreasing the activation threshold of NKs so that normal expression of human leukocyte antigen-1 (HLA-1) triggers cell death mechanisms. Orthohantavirus infected cells display a higher than normal expression of HLA-1 antigens and so are not targeted for cell death (Gupta et al., 2013; Braun et al., 2014). The death of uninfected cells would reduce the integrity of the vasculature epithelium and contribute to capillary leakage.

Infected individuals also display high levels of cytokines, especially tumour necrosis factor alpha (TNFα), interleukin-1 (IL-1), IL-2, IL-6 and IL-8. Disease severity can be correlated with high levels of IL-6 (pro-inflammatory) and TNFα but with low levels of tumour growth factor beta (TGFβ) (immunosuppressive) (Linderholm et al., 1996; Borges et al., 2008; Outinen et al., 2010; Sadeghi et al., 2011). The immune response to orthohantavirus infection contributes significantly to pathogenesis and disease severity in humans.

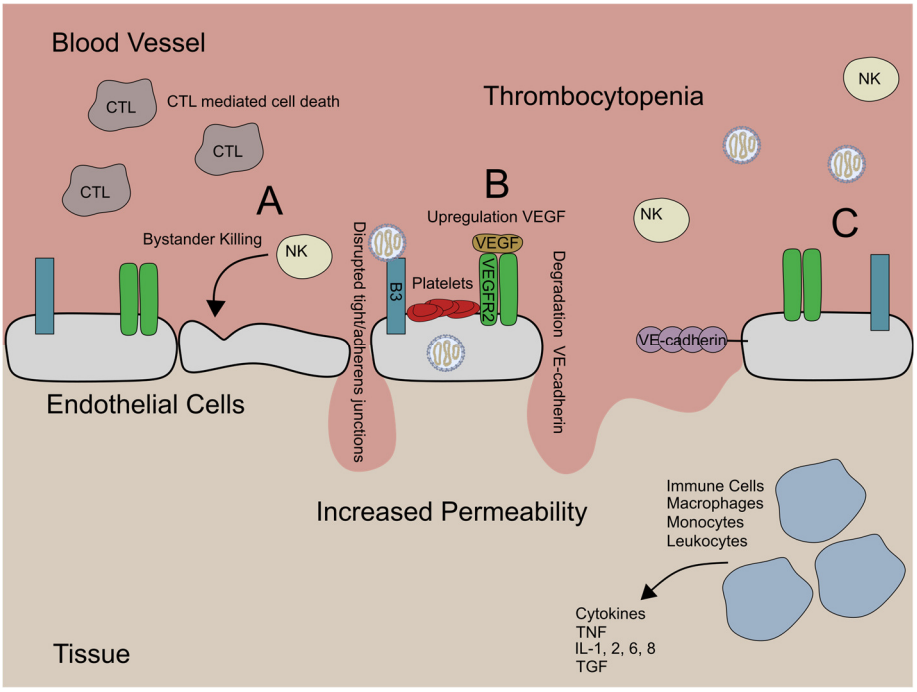


**Figure 4 Orthohantavirus pathogenesis.**

Orthohantavirus pathogenesis is characterised by thrombocytopenia and increased permeability of the vascular endothelium. A) Activation of natural killer cells by orthohantavirus infected cells may lead to killing of neighbouring uninfected cells. B) Virus binding to β3 integrins leads to disruption of tight and adherens junctions and viral induced upregulation of VEGF leads to degradation of VE-cadherin via binding to VEGFR2. Both these mechanisms lead to reduced vascular integrity. C) Additionally, release of cytokines from immune cells leads to a pro-inflammatory response which leads to immune-mediated pathogenesis.

#### 1.1.3.7 Global distribution and notable outbreaks

Orthohantaviruses have been discovered on every continent, with the exception of Antarctica. The type of human disease outcome associated with orthohantavirus infection correlates with global location (Figure 5); HCPS is associated with hantaviruses from the Americas, such as SNV and Andes virus (ANDV) whereas Asian and Europe hantaviruses such as SEOV and HTNV typically cause HFRS. In contrast, NE is the most common disease outcome of hantaviruses isolated from European countries, with PUUV, and to a lesser extent, Dobrava virus (DOBV) being responsible for the majority of human infections (Schmaljohn and Nichol, 2012).

No orthohantavirus-related disease has been reported in other countries. However in Africa, Sangassou virus (SANGV) was identified in the African wood mouse (*Hylomyscus simus*) (Klempa et al., 2006; Klempa et al., 2012) and rodents seropositive for orthohantavirus antigens have been identified in Australia (Bi et al., 2005) (Table 2, Figure 5). It is possible that either orthohantaviruses in these countries (Australia and Africa) are apathogenic in humans or that pathogenic orthohantaviruses have yet to be identified. This may be the more likely option due to many orthohantavirus infections causing subclinical presentations in humans, such is the example of PUUV where it is estimated that at least 80% of cases do not require medical attention (Vaheri, Henttonen, et al., 2013).

The impact of industrial globalisation on the distribution of orthohantavirus infections is apparent, especially in the example of SEOV, which uniquely among orthohantaviruses, has an almost global distribution due to the world-wide transport of its host, *Rattus norvegicus* (Lin et al., 2012; Jameson et al., 2013). The importation of infected laboratory or pet rats and the unintentional importation of wild rats on ships have introduced SEOV into local rat populations (Kerins et al., 2018). In the USA and UK, several SEOV outbreaks have been linked to pet fancy rat ownership and can be traced back to imported rats or infected rat-breeding colonies (McElhinney et al., 2016; Kerins et al., 2018).

Increased transmission of orthohantavirus to soldiers during wartime is likely due to increased exposure to rodents due to the poor living conditions and hygiene. During World War I, “trench nephritis” may have been caused by orthohantavirus infections and during World War II a leptospirosis-like disease afflicted soldiers

in Finnish Lapland (Clement, 1997). During the Korean War, more than 3000 united nation soldiers were affected by a condition known as field nephritis characterised by acute renal failure with a mortality rate of 7% (Johnson, 2000; Muranyi et al., 2005).

In the US, an acute illness characterised by adult respiratory distress syndrome (ARDS) was identified in the Four Corners region, the intersection of Utah, New Mexico, Arizona and Colorado. Throughout 1993, 24 patients were identified with a mortality rate of 50%, with over half belonging to Native American and Hispanic minority groups (Koster et al., 1993). This virus responsible for this outbreak was later identified and named SNV (originally Four Corners virus). Since 1993 several other hantaviruses have been identified to cause HCPS in America such as Black Creek Canal virus, Bayou virus and Chocolo virus.

Other important hantavirus outbreaks in the Americas were the 1996 Argentina ANDV outbreak and the 2011 Chile ANDV outbreak. Unusually, these outbreaks were characterised by person-to-person transmission of the virus. Generally, only infection in the index patient reported exposure to rodents, with the other patients having no rodent-interaction and with low occupational risk of rodent contact. Through epidemiological investigation, it was identified that transmission was likely through inhalation of infective saliva or aerosols due to close contact between individuals (Martinez et al., 2005). Often, attending physicians became symptomatic, followed by their spouses or other close contacts which is indicative of person-to-person transmission (Wells, Estani, et al., 1997). Phylogenetic analysis of viruses isolated from the 1996-1997 Argentina-Chile outbreak provided evidence for person-to-person transmission through nearly identical viral sequences despite geographic distance (>2200 km) (P. J. Padula et al., 1998). ANDV remains the only orthohantavirus to display of person-to-person transmission and has high case fatality rates of 15-36% which appears to depend on the experience of the attending physician (Wells, Estani, et al., 1997; Wells, Young, et al., 1997; P J Padula et al., 1998; Chaparro et al., 1998; Martinez et al., 2005; Alonso et al., 2019).

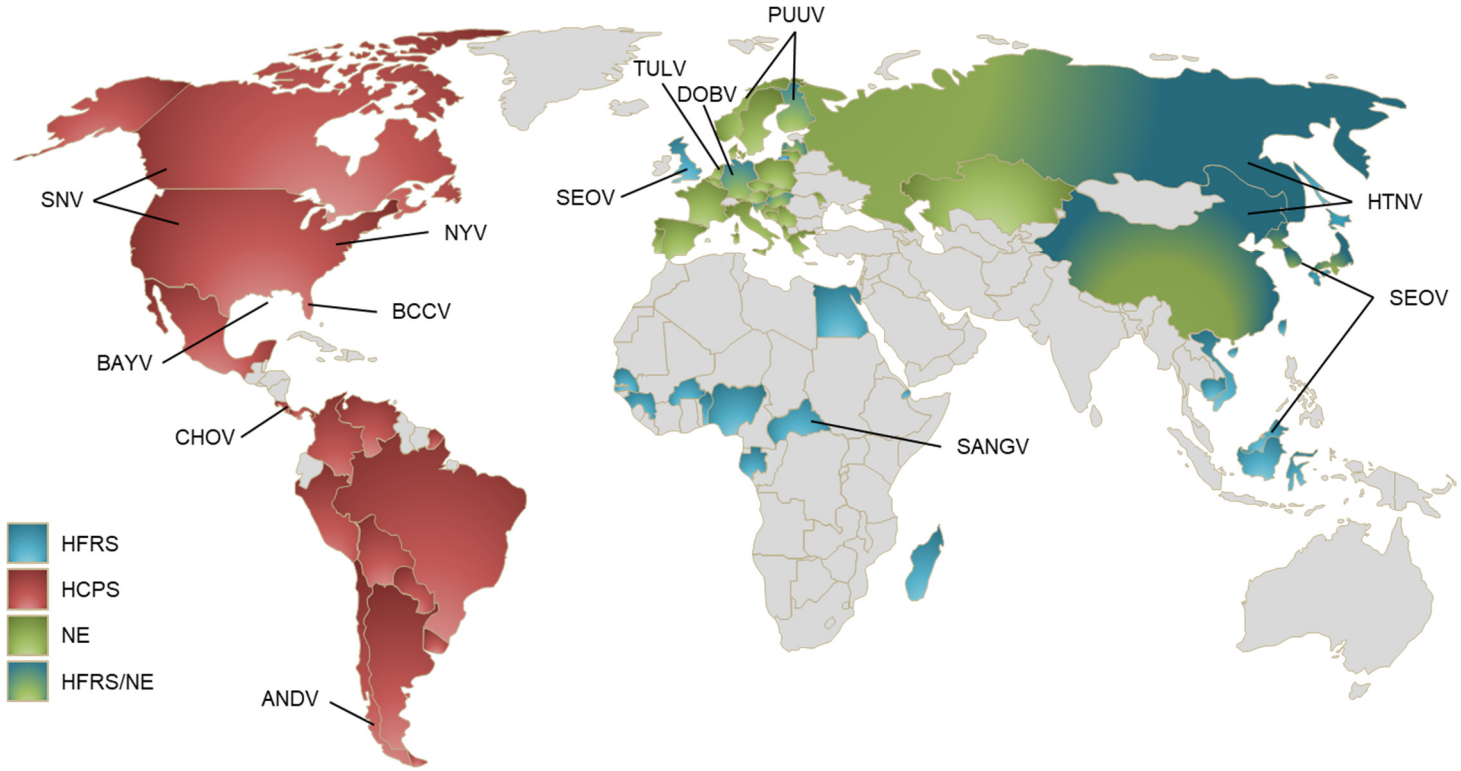


**Figure 5 Geographical distribution of pathogenic orthohantaviruses.**

Global location of incidence of pathogenic orthohantaviruses. Orthohantavirus cardiopulmonary syndrome (HCPS) shown in red, haemorrhagic fever with renal syndrome (HFRS) shown in blue and Nephropathia Epidemica (NE) shown in green. The map is annotated with examples of orthohantaviruses causing these diseases (Bi et al., 2008; Jonsson et al., 2010; Milholland et al., 2018).

#### 1.1.3.8 Environmental impact on orthohantavirus disease

As orthohantaviruses are primarily transmitted to humans by exposure to rodents and/or rodent excreta, the environmental determinants of rodent populations are important for tracking outbreaks in human populations. Climate is a significant factor for increased outbreaks in human populations. Climate conditions, such as El Niño, cause increased rainfalls leading to increased vegetation, more food availability and consequently larger rodent populations. This increases the likelihood of human-to-rodent contact and orthohantavirus transmission (Guterres and de Lemos, 2018).

Deforestation, agriculture and land-conversion all contribute to increased exposure to rodent populations. Individuals working in unsanitary conditions or with occupational risks (e.g. forestry, farming, sewage work, veterinarians) will have a greater chance of contact with rodents. In addition, reduced habitats or extreme weather scenarios, such as unseasonal snow, leads to increased rodent home invasion and a higher chance of exposure and transmission of orthohantaviruses to humans (Jonsson et al., 2010). It is likely in the current climate of deforestation and urbanisation that orthohantavirus outbreaks will become more common.

#### 1.1.3.9 Antivirals, vaccines and control

Currently, there are no effective recognised antiviral therapeutics or vaccines available in the UK or the USA. Treatment is generally limited to supportive palliative care including fluid replacement, supplemental oxygen and, if required, mechanical ventilation (WHO, 2015).

However, some antivirals have shown a degree of effect on orthohantaviral infection. Ribavirin, Favipiravir and 1-beta-d-ribofuranosyl-3-ethynyl-[1,2,4] triazole (ETAR) are antivirals which affect the function of the virus encoded RNA dependant RNA polymerase (RdRp) (Szabó, 2017). Ribavirin and ETAR are nucleoside analogues which have an inhibitory effect on inosine monophosphate dehydrogenase and limit the synthesis of GTP. Ribavirin in addition to showing effectiveness in *in vivo* models of HFRS has been associated with decreased morbidity and mortality in HFRS patients but has proved ineffective in HCPS cases (Huggins et al., 1991; Mertz et al., 2004; Chung et al., 2013). Other antiviral drugs have shown promise, ETAR has

been described to show antiviral effects against HTNV (Chung et al., 2008) and Favipiravir has been associated with decreased viral replication in cell culture (Buys et al., 2011). Other antiviral drugs which may prove efficacious in the treatment of orthohantaviral disease include; lactoferrin which may interfere with viral adsorption (Murphy et al., 2001) and immunotherapies utilising the protective effect of neutralising antibodies or polyclonal sera against orthohantaviruses (Xu et al., 2002).

In addition to antivirals, some inactivated orthohantavirus vaccines are currently in use in China, Korea and Russia. Hantavax™ is a formalin-inactivated HTNV vaccine produced by amplifying HTNV in mouse brains. In Russia, a bivalent PUUV/Dobrava-Belgrade (DOBV) formalin-inactivated vaccine has been developed (Krüger et al., 2011; Song et al., 2016). However, it is worth noting that most antivirals and vaccines still need to pass pre-clinical or clinical stages of testing.

## 1.2 Orthohantavirus life cycle

### 1.2.1 Genome Organisation

Hantaviruses are single-stranded negative-sense RNA viruses with a tripartite segmented genome. These segments are denoted as the small (S), medium (M) and large (L) segments based on their relative nucleotide lengths, and each has a common organisation with an ORF flanked by highly-conserved untranslated regions (UTRs). The S segment encodes the NP, the M segment encodes the glycoprotein precursor (GPC) and the L segment encodes the RNA dependent RNA polymerase (RdRp). The S segment, in some orthohantavirus species, encodes an additional non-structural (NSs) protein from an overlapping ORF via leaky scanning (Vera-Otarola et al., 2012; Muyangwa et al., 2015).

### 1.2.2 Virus structure

Mature hantavirus particles are pleomorphic in shape forming broadly spherical particles (60-160 nM diameter) in addition to tubular particles (~350 nM long and ~80 nM diameter) (Hart and Bennett, 1999; Huiskonen et al., 2010; Battisti et al., 2011). The viral RNA segments are wrapped into ribonucleoproteins (RNPs) by the NP. Orthohantavirus RNPs appear to form rigid helices with the virion and have been visualised by negative stain electron microscopy within virus particles and cells (Goldsmith et al., 1995; Huiskonen et al., 2010; Battisti et al., 2011; Arragain et al., 2019) (Figure 6). Each segment is packaged into a virus particle made up of a lipid bilayer studded with glycoprotein spikes that comprise heterodimer complexes of Gn and Gc proteins that are derived through processing of the GPC (Elliott, 1990; Huiskonen et al., 2010; Reguera et al., 2014; Li et al., 2016). Gn-Gc complexes form a lattice to encapsulate the viral bilayer envelope with Gn localising to outer surface (Rissanen et al., 2017). Figure 6 shows a schematic of a generic hantavirus particle alongside electron micrographs of purified TULV and SNV virions.

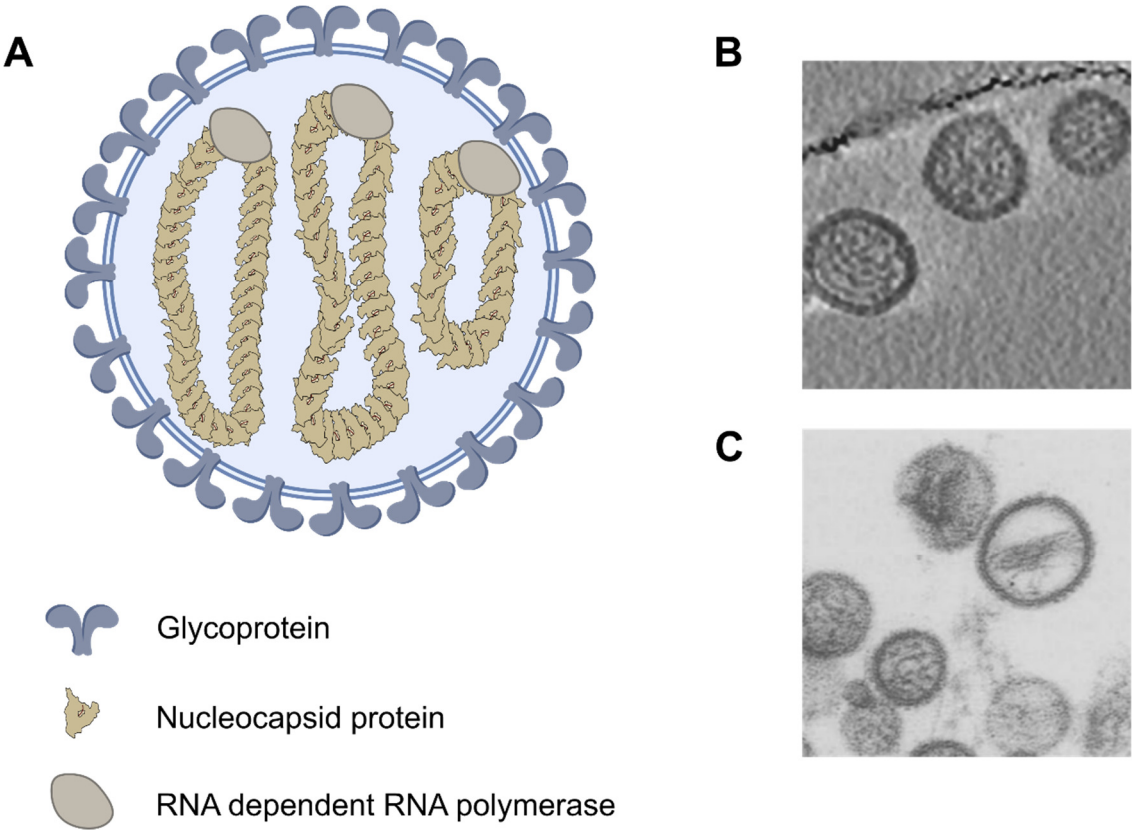


**Figure 6 Schematic of the orthohantavirus virus particle.**

A) Orthohantaviruses are comprised of a lipid bilayer studded with glycoprotein Gn and Gc tetramers. Contained within the virus particle is the tripartite genome making up the small, medium and large segment. The nucleocapsid protein encapsidates the viral genome and complexes with the RdRp to form the RNP. B-C) Representative images of orthohantavirus virions B) Cryo-electron tomogram section of TULV particles (Huiskonen et al., 2010) C). Thin-section transmission electron microscopy of SNV particles (Goldsmith et al., 1995)

### 1.2.3 Virus entry

Current evidence suggests multiple orthohantaviruses including HTNV, SNV, SEOV, PUUV and NYV (Gavrilovskaya et al., 1999; Mou et al., 2006) utilise the abundant cell-surface receptors αvβ3 and αIIbβ3 integrins on endothelial cells for cell attachment and internalization. Integrins are heterodimeric proteins made up of an α and β subunit. There are 8 different β subunits and 18 different α subunits which combine to form 24 different integrins (Hynes, 2002). The αvβ3 and αIIbβ3 are expressed on the vascular endothelium and platelets respectively and interaction with orthohantavirus may alter their normal function and induced the pathogenic effects seen in orthohantavirus infection (Gavrilovskaya et al., 1998).

The HTNV glycoprotein spikes bind integrin β3 via interactions at a conserved CNP (Cys-Asn-Pro) motif located in the N-terminal of glycoprotein Gc (Mou et al., 2006). The use of β3 integrins may be linked to the pathogenicity of orthohantavirus due to their function in maintaining vascular integrity and involvement in vasodilation and vasoconstriction (Gavrilovskaya et al., 1999). Alternatively, it has been suggested that pathogenic orthohantaviruses (HTNV and PUUV) additionally require the decay-accelerating factor (DAF) for viral entry in polarised epithelial cells. The DAF-receptor is located on the apical surface of epithelial and endothelial cells, whereas β3 integrins are located on the basolateral surface. DAF-binding may lead to the opening of tight junction suggesting that the polarisation of virus entry may be another, important, factor in the pathogenesis of orthohantaviruses (Krautkramer and Zeier, 2008; Klempa et al., 2012; Dalrymple and Mackow, 2014). The correlation between viral pathogenesis and entry receptor is supported by the observation that the non-pathogenic orthohantavirus PHV utilises β1 integrins and not β3 integrins for cell entry, whereas pathogenic orthohantaviruses utilise β3 integrins (Gavrilovskaya et al., 1998; Gavrilovskaya et al., 1999). As viral pathogenesis is a complex process it is likely this mechanism alone may not account completely for orthohantavirus pathogenesis. SANGV, purported to be a pathogenic orthohantavirus, has been suggested to utilise β1 integrins for cell attachment suggesting more complex interactions than just viral entry receptor interactions are responsible for pathogenesis (Klempa et al., 2012). After attachment to the cell, internalisation may be achieved by clathrin-mediated endocytosis (HTNV) (Jin et al., 2002). ANDV may be internalised through clathrin-mediated endocytosis but may also utilise micropinocytosis in a clathrin-independent mechanism (Chiang et al., 2016). Additionally, it has been reported that pro-cadherin 1 is a critical receptor for the entry of New world hantaviruses such as ANDV and SNV. Orthohantavirus glycoproteins are thought to recognise the extracellular cadherin repeat domain of pro-cadherin-1 leading to viral attachment and entry (Jangra et al., 2018).

### 1.2.4 Virus RNA transcription and replication

After orthohantaviruses are internalized within cells, virions are trafficked to early- and late-endosomes where they undergo pH-mediated uncoating to

release the viral genome segments into the cytoplasm (Cifuentes-Muñoz et al., 2014; Mancini et al., 2015). The low pH (~5.0-6.0) of endosomes triggers a conformational change in the glycoprotein structure which stimulates fusion of the viral and endosomal membranes (Jin et al., 2002; Vaheri, Strandin, et al., 2013).

The glycoprotein Gc contains conserved histidine residues which allow sensing of low pH environments which induce the Gn-Gc lattice to undergo a dramatic conformational change where Gn dissociates from Gc (Cifuentes-Muñoz et al., 2014; Rissanen et al., 2017). The Gc protein forms a stable homotrimer with an exposed fusion loop which inserts into the endosomal membrane (Figure 7). This extended conformation collapses which brings the viral and endosomal membranes into close proximity allowing membranes to fuse and form a viral fusion pore. Viral RNPs can then be released into the cytoplasm (Cifuentes-Muñoz et al., 2014; Mancini et al., 2015). The pH required for fusion of viral and target membranes varies between different orthohantavirus species with HTNV requiring pH 6.3 and ANDV requiring pH 5.6 (Arikawa et al., 1985; Cifuentes-Munoz et al., 2011).

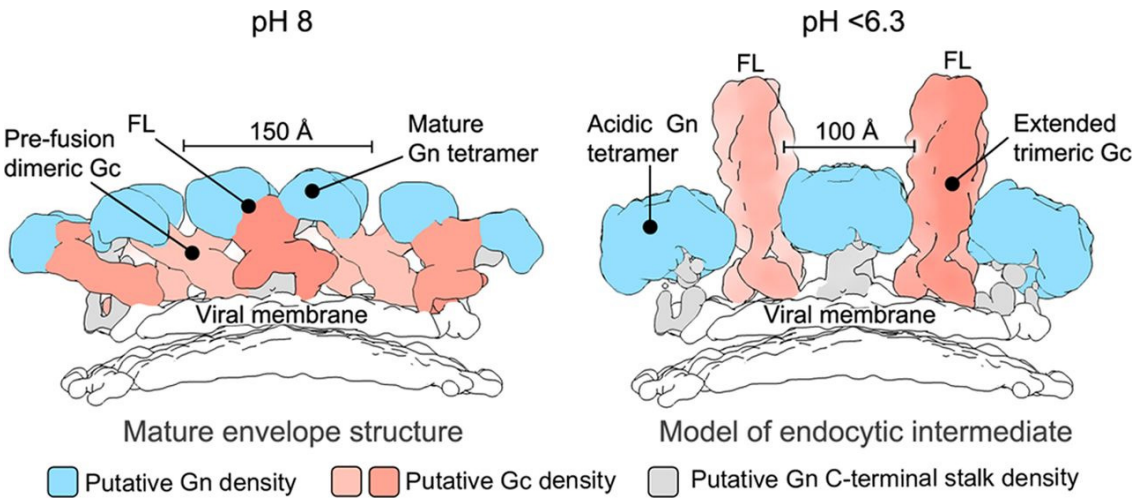


**Figure 7 Schematic of low-pH induced conformational change of orthohantavirus glycoproteins Gn and Gc.**

Left displays mature viral envelope structure with Gn as a mature tetramer and Gc in its pre-fusion dimeric form. Acidification (right) induces disassembly of the Gn-Gc heterodimeric complex and formation of extended Gc trimer. The fusion loop (FL) extends outward to contact target membrane. Schematic from Rissanen et al., 2017.

After release, viral genomes are transported to sites of replication which have yet to be identified (Jin et al., 2002; Vaheri, Strandin, et al., 2013). Orthohantavirus replication sites are likely to be similar to other members of the *Bunyavirales* order such as Bunyamwera virus (BUNV) where viral replication factories are located around the Golgi complex (Fontana et al., 2008). Transcription and replication of orthohantaviruses are thought to occur on membranes due to the membrane-association of NP and the RdRp and the co-localisation of these proteins in a similar spatial location to the Golgi complex (Ravkov and Compans, 2001; Kukkonen et al., 2004). The RdRp initially carries out the primary transcription of the viral segments into mRNA which can be used as a template for viral protein synthesis. Segmented negative-sense RNA viruses (e.g. influenza virus) utilise a process called “cap-snatching” in which host-cell mRNAs are cleaved at a site close to their 5’ ends by a RdRp-resident endonuclease, and the capped RNA oligonucleotide is then used as a primer for viral transcription (Bouloy et al., 1978). For orthohantaviruses, this process has been suggested to occur via a “prime and re-align’ mechanism (Garcin et al., 1995) in cytoplasmic processing bodies (P bodies). NP-associated capped-mRNAs are targeted to P bodies, where they are cleaved by endonucleases (cellular or potentially RdRp endonuclease activity) at G residues resulting in an NP-associated capped-host mRNA primer ($m^7$GpppN) that will be used for viral transcription (Mir et al., 2008; Cheng and Mir, 2012). Orthohantavirus, replication occurs without the requirement for capped-mRNA primers, with both transcription and replication occurring through the prime-and-realign mechanism. The G of either the $m^7$GpppN (transcription) or triphosphorylated G (pppG, replication) aligns to the C of the first AUC in the AUC repeat region located in the vRNA 3’-end. Successive bases are added followed by a “slip” and realigning with these terminal sequence repeats (Figure 8) (Vaheri, Strandin, et al., 2013).

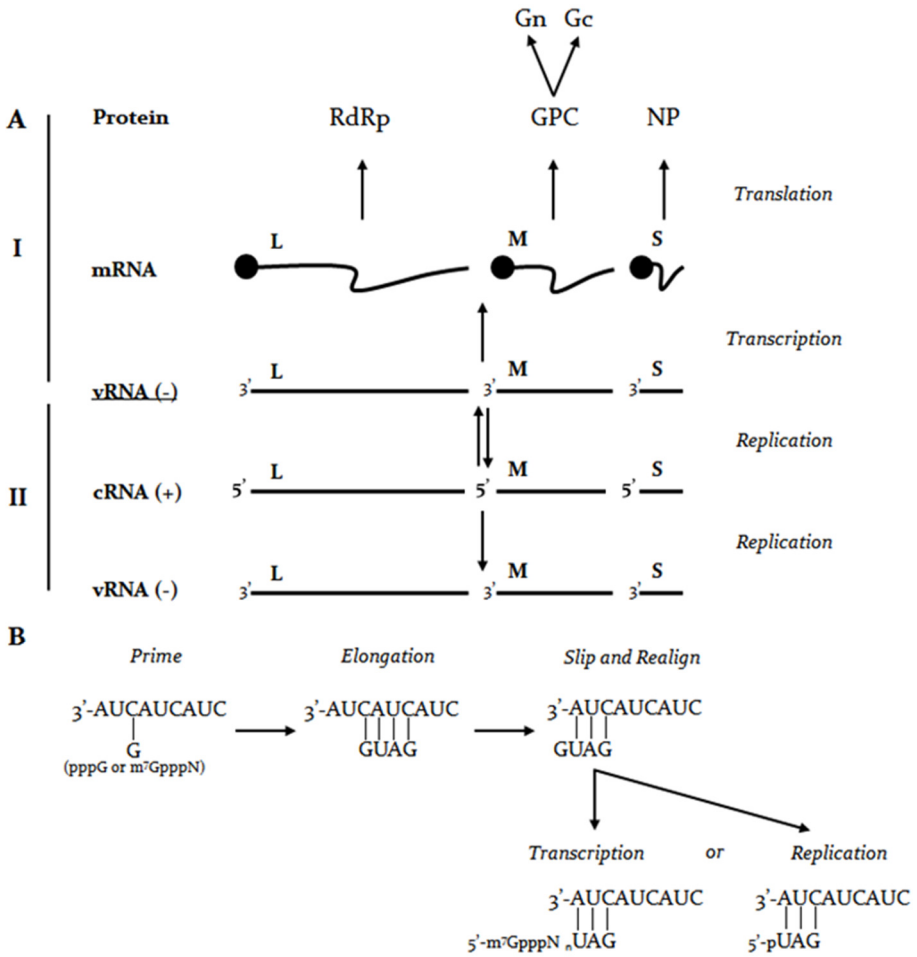


**Figure 8 Orthohantavirus replication, transcription and translation.**

A) Negative-sense viral RNA (vRNA) is transcribed into viral mRNA and subsequently translated into viral protein. vRNA is also replicated into positive sense copy RNA (cRNA), which is used as a template for synthesis of nascent negative sense RNA. This is bound by NP and packaged into the mature virion as RNPs. B) Transcription and replication vRNA through the prime-and-realign mechanism. Guanosine (G) from guanosine triphosphate (pppG) or capped-RNA primer ($m^7$GpppN) align with cytosine (in AUC) within 3'-vRNA pan-handle. Elongation occurs, nascent RNA "slips" and realigns with preceding AUC repeat. Figure adapted from Vaheri et al., 2013 and Muyangwa et al., (2015).

### 1.2.5 Virus assembly and egress

After replication, both vRNA and cRNA are encapsidated by NP. vRNA contains highly conserved 3'- and 5'- complementary sequences in the UTR which have the potential to form a structure known as the 'panhandle'. It has been proposed that binding of trimeric NP to the panhandle results in a conformational change which may be essential for further NP oligomerisation and RNA encapsidation (Mir and Panganiban, 2005; Severson et al., 2005; Mir et al., 2006).

The viral glycoprotein precursor (GPC) mRNA is targeted to the ER for translation via a signal motif, "YxxL", located in the 5'-end. A second signal motif, "WAASA", facilitates the cleavage of GPC into the glycoproteins Gn and Gc (Hepojoki et al., 2012). The glycoproteins are transported as a heterodimer to the Golgi complex, which is believed to be the site of assembly for old world (OW) hantaviruses. Assembled virions are trafficked to the plasma membrane via recycling endosomes, and mature orthohantavirus virions bud from the plasma membrane by exocytosis (Rowe et al., 2008; Vaheri, Strandin, et al., 2013) (Figure 9). In contrast, new world (NW) hantaviruses are thought to assemble and bud from the plasma membrane (Elliott, 1990; Ravkov et al., 1998; Spiropoulou et al., 2003; Deyde et al., 2005).

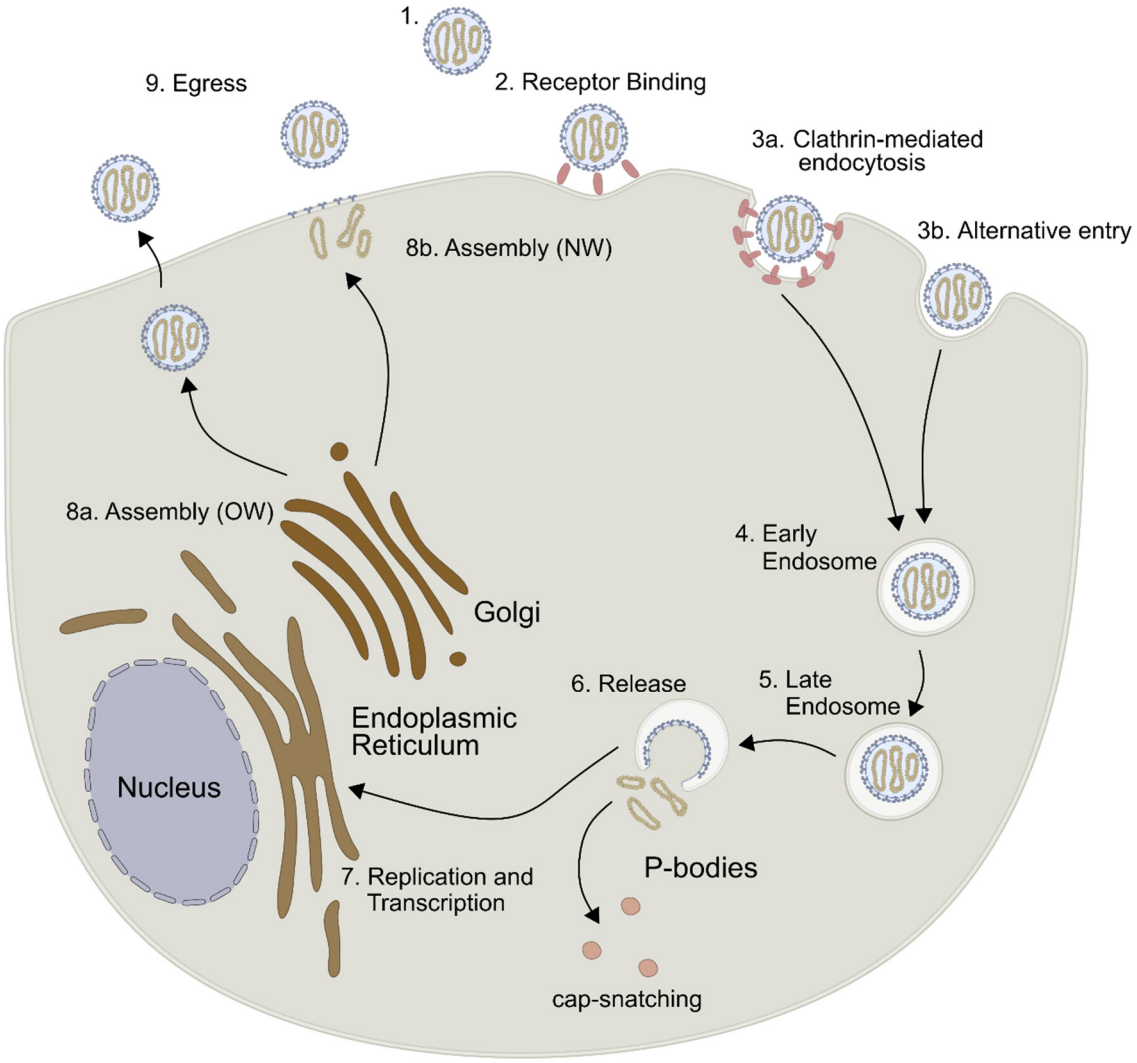


**Figure 9 Orthohantavirus cellular lifecycle.**

1. Orthohantavirus particle 2. Virus particle binds and attaches to the cell via interaction with host surface protein (e.g. β1/β3 integrin) 3a. Virion enters the cell by clathrin-dependent endocytosis 3b. Virion enters the cell by clathrin-independent mechanism (e.g. micropinocytosis, caveolin-mediated endocytosis) 4. Virus particles are trafficked in early endosome 5. Virus particle reaches late endosome 6. Low pH of late endosome induces a conformational change in viral glycoproteins causing the viral membrane to fuse with endosome releasing viral genomes and protein into the cytoplasm, some NP localises to P-bodies where “cap-snatching” occurs 7. Replication and transcription of viral genome products 8a. Assembly of old world (OW) orthohantaviruses occurs at the Golgi before transport of virions to plasma membrane 8b. New World (NW) Orthohantavirus replication products and proteins are transported to the plasma membrane where viral assembly occurs 9. Virus particles egress from the cell by budding from the plasma membrane.

## 1.3 Proteins

### 1.3.1 The nucleocapsid protein

#### 1.3.1.1 Structure

The orthohantavirus NPs are encoded by the S segment ORF and are 429-435 residues in length, with an average molecular weight of around 50 kDa. Several high resolution structures of the orthohantavirus NP have been solved by either X-ray crystallography analysis of truncated NP constructs (ANDV and SNV $NP_{core}$ (111-399 residues) and HTNV the $NP_{\Delta N}$ (113-429 residues)) (Guo et al., 2016; Olal et al., 2016) or cryo-electron microscopy of helical NP oligomers (Arragain et al., 2019).

The orthohantavirus NP is a compact protein mostly made up of α-helices. It is comprised of an N-terminal lobe domain and a C-terminal lobe domain, which together form the core region. The N-lobe is made up of a helical core of α-helices and a bulge structure (N-bulge) comprised of four anti-parallel β-sheets. The C-lobe is made up α-helices and a bulge structure (C-bulge) formed of an α-helix with an extended structure (Guo et al., 2016; Olal et al., 2016). The N-terminal is formed by an antiparallel coiled-coil stabilised by ionic bridges (Figure 10D) (Boudko et al., 2007). The N-terminal coiled-coil domain and the C-terminal domain are thought to be essential for NP oligomerisation (Alfadhli et al., 2001; Alfadhli et al., 2002).

A flexible hinge from the core connects to the C-terminal helical arm which extends from the C-lobe and can interact with neighbouring molecules for oligomerisation. The C-terminal arm binds to a hydrophobic pocket located within the C-lobe of an adjacent NP molecule (Kaukinen et al., 2003a; Yoshimatsu et al., 2003; Kaukinen et al., 2004; Olal et al., 2016). The N-terminal domain is thought to interact with a conserved hydrophobic surface of the N-lobe (Olal et al., 2016; Arragain et al., 2019) (Figure 11). NP oligomerisation with RNA results in the formation of a left-handed RNP helix formed of 3.6 NP subunits per turn (Figure 10). Electrostatic surface potential analysis of the crystal structure of NP revealed a positively charged cleft between the N-lobe and C-lobe. Residues thought to be involved in RNA binding line the RNA binding groove and may form hydrogen bonds with the

RNA bases or phosphate backbone (Olal et al., 2016; Guo et al., 2016) (Figure 10).

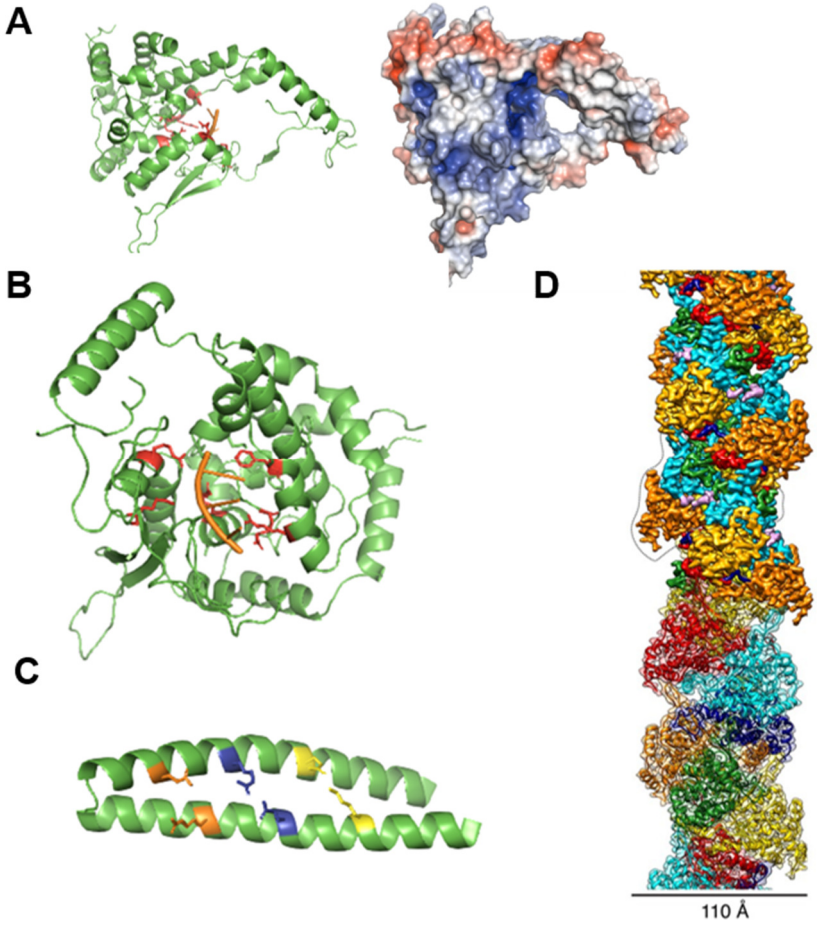


**Figure 10 Structure of the orthohantavirus nucleocapsid protein.**
A-B) HTNV nucleocapsid protein (PDB: 6I2N), residues 80-429 bound to RNA (orange), residues involved in RNA binding (red) and electrostatic surface representation displaying RNA binding cleft (Arragain et al., 2019), C) Sin Nombre virus N-terminal coiled-coil domain (PDB: 2IC6), residues pairs forming ionic bridges contributing to the structure of the coiled-coil are displayed in orange, blue and yellow (Boudko et al., 2007). Structures generated using PyMOL D) Helical organisation of HTNV RNP with each individual NP coloured, from Arragain et al., 2019.

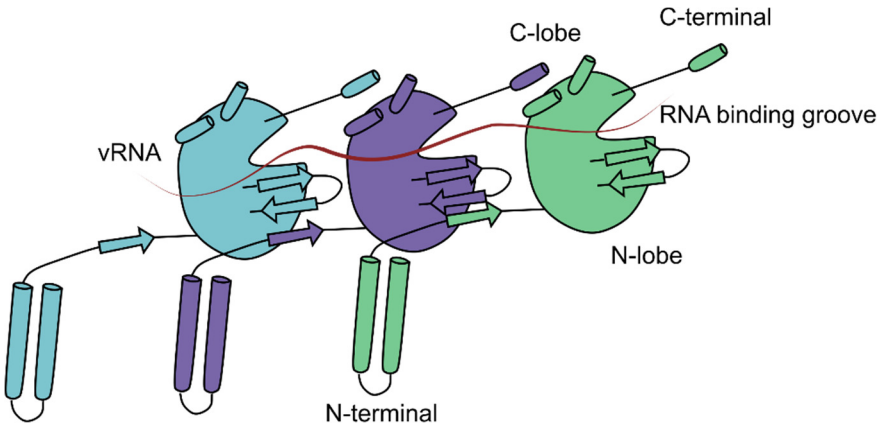


**Figure 11 Representation of NP-NP interaction and oligomerisation.**
NP oligomerisation occurs through interactions of the C-terminal and N-terminal of the NP interacting with the hydrophobic surfaces of neighbouring NP's C-lobe and N-lobe respectively. Viral RNA segments are packaged into NPs through interactions with the positively charged RNA binding groove. Figure adapted from Arragain et al., 2019.

#### 1.3.1.2 NP functions

An important function of the orthohantavirus NP is its role as an RNA binding protein, where NP encapsidates the viral genome to form the RNP. The roles of the NP-RNA association are likely in the protection of the RNA from degradation from host cell nucleases, structural ordering of the RNA strand, and avoiding detection of the RNA by immune surveillance mechanisms. Cytosolic RNA sensors, RIG-I and MDA5, recognise viral RNAs as induce intracellular signalling pathways culminating in the expression of pro-inflammatory cytokines and Type I interferons. These inflammatory molecules further induce activation of immune mechanisms for pathogen clearance (Tan et al., 2018). Orthohantaviruses RNA contain a 5'-monophosphate which is linked to the ability of orthohantaviruses to avoid RIG-I recognition and fail to induce IFN signalling and in doing so avoid host immune surveillance mechanisms (Habjan et al., 2008).

Selective encapsidation of viral RNA by the NP is potentially carried out due to the self-complimentary terminal structures with highly conserved sequences at the 3' termini (3'-AUCAUCAUCUGAGG-5') and 5' termini (5'-UAGUAGUAU(G/A)CUCC-3') of the viral segments 5'- and 3'- UTRs (Muyangwa et al., 2015).

Reportedly, NP contains independent sites for viral RNA and mRNA binding, and it has been proposed that NP bound to the capped mRNA primer,

generated by cap-snatching, undergoes a conformational change and further binds to vRNA at the highly conserved 3' end. This function assists the viral RdRp in viral genome transcription and replication (Mir et al., 2010). NP also directly interacts with the RdRp to recruit the polymerase to viral genomes for transcription initiation (Cheng et al., 2014). NP is able to bind to multiple sites on the cytoplasmic tails of the glycoproteins, Gn and Gc and this interaction may direct trafficking to the Golgi apparatus for incorporation of the RNP segments within assembled virions (Shimizu et al., 2013).

The orthohantavirus NP has been purported to possess other functions in addition to interactions with the Gn, Gc, RdRp and viral RNA. Orthohantavirus NP is thought to be involved in protein translation by replacing the eIF4F complex during translation initiation. In addition, NP may also interact with the S19 ribosomal protein, a component of the 43S pre-initiation complex, potentially recruiting the ribosome to capped viral mRNAs leading to the preferential translation of viral proteins (Mir and Panganiban, 2008; Haque and Mir, 2010).

NP has been reported to have conserved DNA-specific metal-dependent endonuclease activity. This is proposed to function in immune evasion either preventing sensing of cytoplasmic ssDNA which can induce immune responses or preventing binding of cellular nucleic acids or DNA/RNA hybrids which may inhibit orthohantavirus replication (Möncke-Buchner et al., 2016). In addition, interaction of orthohantavirus NP with actin microfilaments or microtubules to assist viral assembly and release have been reported (Ravkov et al., 1998; Ramanathan et al., 2007; Ramanathan and Jonsson, 2008).

Orthohantaviral NPs have also been implicated in other methods of immune evasion such as modulating apoptosis (Gupta et al., 2013). ANDV has been suggested to interfere with IFN signalling by inhibiting the dsRNA sensors RIG-1/MDA5 and by interfering with TBK1 phosphorylation (Cimica et al., 2014). NP may also be involved in anti-apoptotic mechanisms such as the ubiquitination of the tumour suppressor p53 to target it for degradation (Park et al., 2013). HTNV NP has been shown to bind to and inhibit the nuclear import activity of importin α. This prevents the nuclear shuttling of nuclear factor kappa beta (NFκβ) and prevents its function as a transcription factor for the regulation of pro-inflammatory factors (Taylor et al., 2009). ANDV has

been shown to prevent protein kinase R (PKR) dimerization avoiding host cell translation shutdown as this prevents the phosphorylation of eIF2α. The deficit in phosphorylated eIF2α aids efficient translation of viral proteins by preventing downregulation of protein synthesis by the host cell (Wang and Mir, 2015).

Orthohantavirus NP has been identified to interact with Daxx (dead domain associated protein-6), a Fas-death domain adaptor protein. Daxx is a pro-apoptotic protein that promotes Fas-mediated apoptosis through activation of the JNK pathway. NP interaction with Daxx may interfere with the pro-apoptotic function and promote survival of the infected cell (Li et al., 2002; Jang et al., 2002; Khaiboullina et al., 2013). Other proteins identified to interact with orthohantavirus NP are the small ubiquitin-related modifier-1 (SUMO-1) which has functions in sumoylation of proteins, and the SUMO-1 conjugating enzyme, Ubc9. SUMO-1 and Ubc9 have been shown to interact with Daxx and together they regulate NP localisation to the perinuclear region. Orthohantavirus NP also interacts with other SUMO-1 related proteins such as chromodomain helicase DNA-binding protein 3 (CHD3), human homeodomain-interacting protein kinase 2 (HIPK2) and TRAF and TNF receptor-associated protein (TTRAP) suggesting that sumoylation may be important for the orthohantavirus lifecycle specifically in host-cell survival mechanisms (Maeda et al., 2003; Kaukinen et al., 2003b; Lee et al., 2003).

Other anti-apoptotic functions of the orthohantavirus NP have been reported. ANDV, DOBV, HTNV, PUUV, SEOV and TULV have all been shown to mediate apoptotic induction by interaction with activated caspase-3. In addition to this, ANDV, DOBV and PUUV NPs inhibit the action of granzyme B during NK mediated cell killing. ANDV NP contains the conserved caspase-3 recognition site, DLID. Orthohantaviruses appear to inhibit apoptosis by interfering with the caspase cascade, where a series of cysteine-aspartate proteases are activated by sequential cleavage. Orthohantavirus NP interacts with cleaved, activated caspase 3 to prevent its downstream cleavage action and inhibit cell apoptosis (Gupta et al., 2013; Solà-Riera et al., 2019).

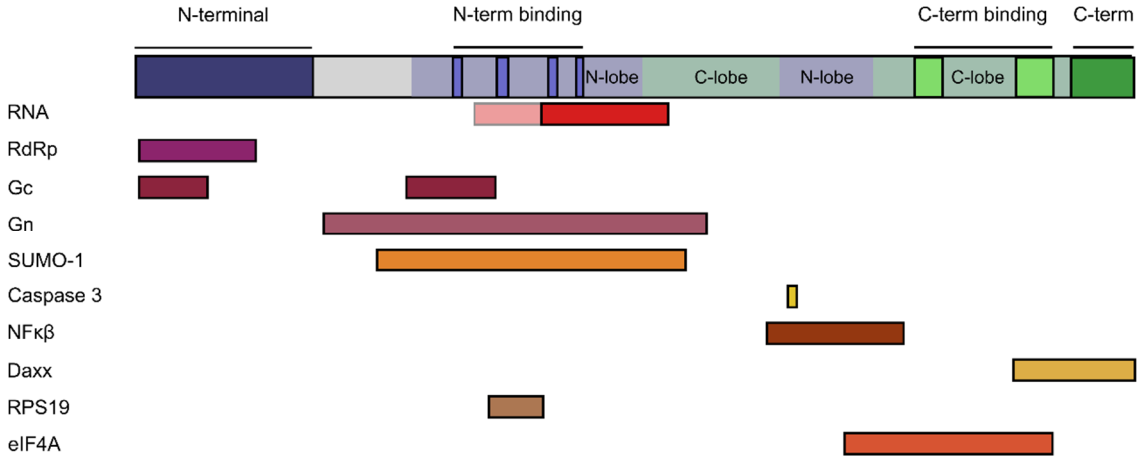


**Figure 12 Schematic of orthohantavirus NP interaction sites and functional domains.**

Predicted or confirmed interactions of NP with other proteins are depicted. NP-NP interactions are shown in blue (N-term) or green (C-term) (Arragain et al., 2019). Figure adapted from Reuter and Krüger, 2018

#### 1.3.1.3 The non-structural NSs protein

The S segment in some orthohantaviruses (PUUV, TULV, PHV, SNV, ANDV) also contains a second ORF which encodes the small, ~11 kDa, non-structural protein (NSs). The NSs ORF is in the +1 register relative to the NP ORF and is proposed to be accessed through leaky ribosomal scanning. NSs localises to the perinuclear region during orthohantavirus infection. The NSs may have immune regulatory functions, where it can inhibit IFNβ expression and the action of NFκβ and type I IFN which may promote viral replication (Jääskeläinen et al., 2007; Jääskeläinen et al., 2008; Virtanen et al., 2010; Vera-Otarola et al., 2012). The cellular protein ACBD3 is thought to interact with NSs. ACBD3 is involved in Golgi structure maintenance and may also be involved in the immune response to viral infection. The NSs likely has a major role in immune evasion and promotes virus replication within the host cell (Rönnberg et al., 2012).

### 1.3.2 The glycoprotein

#### 1.3.2.1 Structure and functions

The orthohantavirus M segment encodes the glycoprotein precursor (GPC) which is cleaved by host cell proteases at the highly conserved ‘WAASA’ motif

into the glycoproteins Gn (~ 70 kDa) and Gc (~ 50-55 kDa) (previously G1 and G2) (Schmaljohn and Dalrymple, 1983; Löber et al., 2001; Spiropoulou et al., 2003; Muyangwa et al., 2015). Gn and Gc interact to form a heterodimer which protrudes through the lipid bilayer of the viral envelope to form spikes on the mature virus particle. The glycoprotein spike ectodomain is formed from four globular domains connected to the viral membrane by a thin stalk, with a small endodomain that protrudes inside the virus particle (Huiskonen et al., 2010; Battisti et al., 2011) (Figure 10).

Viral glycoproteins contain multiple highly conserved N-linked glycosylation sites which are required for correct folding of the protein and for intracellular transport to the *cis*-Golgi. Trafficking to the Golgi network is also dependent on the interaction of Gn and Gc (Ruusala et al., 1992; Shi and Elliott, 2002; Shi and Elliott, 2004; Deyde et al., 2005), which are transported as a heterodimer complex. The cytoplasmic tail of Gn for pathogenic orthohantaviruses has been implicated in the inhibition of IFNβ production. Gn prevents IRF3 from instigating the IFNβ anti-viral response by binding to TRAF3 which prevents interaction with TBK-1 and formation of the TBK1-TRAF complex required for phosphorylation and activation of IRF3 (Alff et al., 2008; Matthys et al., 2014; Mackow et al., 2014).

Glycoprotein induced fusion of the viral membrane and endosomal membrane allows virus uncoating. Cell-surface glycoproteins can also mediate syncytia formation of an infected cell with both infected and uninfected neighbouring cells (Ogino et al., 2004; Barriga et al., 2016; Willensky et al., 2016). The glycoprotein Gn at neutral pH forms an outer layer which shields the fusion-loop of Gc preventing premature membrane fusion. At acidic pH, conformational changes in the Gn exposes Gc which forms a fusion homotrimer which can insert into the target membrane and induce a membrane fusion event (Li et al., 2016; Rissanen et al., 2017).

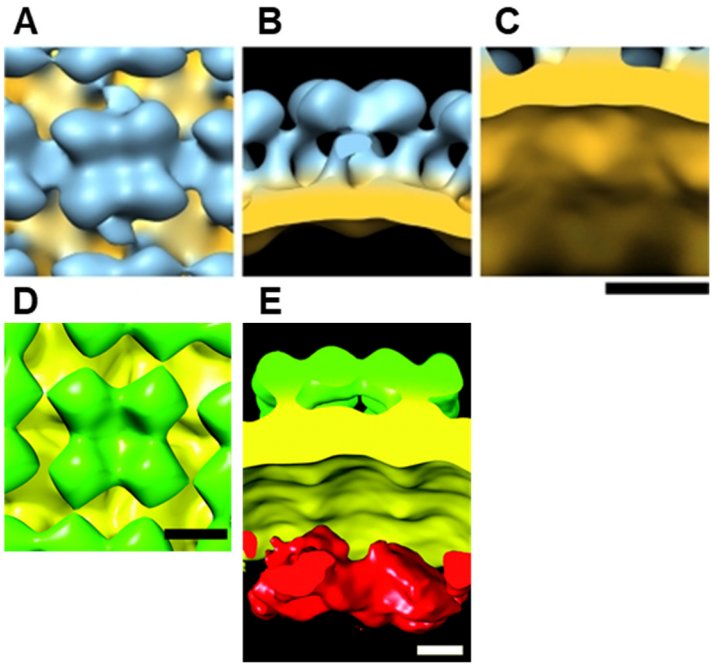


**Figure 13 Averaged structure of the orthohantavirus glycoprotein spike.** A-C) Glycoprotein spike from TULV shown from the top (A), side (B) and below, scale bar 10 nM (C) viewpoints (Huiskonen et al., 2010) D-E) Glycoprotein spike from HTNV shown from the top (D) and side (E) viewpoint, scale bar 5 nM (Battisti et al., 2011)

### 1.3.3 The RNA dependent RNA polymerase

#### 1.3.3.1 Structure and functions

The L segment of orthohantaviruses encodes the RNA dependent RNA polymerase (RdRp). The RdRp is a 200-250 kDa protein which primarily acts to transcribe and replicate the viral genome. For orthohantaviruses, the RdRp is a membrane-associated protein which localises to the perinuclear region of the cell and co-localises with the Golgi network (Kukkonen et al., 2004). Virions contain a functioning RdRp which is required for initial primary transcription of the viral genome (Schmaljohn and Dalrymple, 1983).

The orthohantavirus RdRp possesses conserved motifs of other bunyavirus RdRps and therefore it is likely that it shares similar structural features (Amroun et al., 2017). The only bunyaviral RdRp for which the high resolution structure has been solved to date, is for La Crosse virus. The bunyavirus RdRp contains a conserved N-terminal endonuclease domain which functions in the cap-snatching process to cleave 5'-capped RNAs from host cell mRNAs (Gerlach et al., 2015). The orthohantavirus RdRp has a highly conserved endonuclease which cleaves host cell 5'-capped mRNAs a few nucleotides

downstream of the cap. This capped-primer, used during transcription, allows the synthesis of 5'-capped viral mRNAs which can be further translated into the viral proteins (Rothenberger et al., 2016).

Additionally, The RdRp has been shown to degrade viral and cellular nucleic acids, leading to a reduction in both host and viral mRNAs (Heinemann et al., 2013; Rothenberger et al., 2016). This may help the virus evade host cell responses and select for viral protein translation by host cell ribosomes.

The RdRp binds to the vRNA genome segment with a separate binding site for the 3'- and 5'-vRNA panhandles (Figure 14) (Gerlach et al., 2015). The panhandle sequences were found to, in most cases, contain a mismatch at position 9 and a non-canonical U-G pair in position 10. These non-complementary regions with the panhandle may serve to function as the polymerase binding site, as in influenza virus replication, and may act as transcription initiation signals (Tiley et al., 1994; Chizhikov et al., 1995; Meyer and Schmaljohn, 2000; Nichol et al., 2002). Several orthohantaviruses (e.g. TULV, HTNV PUUV) have been found to contain CCACCC motifs at the 3'-end of the S viral RNA segment. These motifs are predicted to form stem-loop structures which may act as termination signals. The M segment mRNA was found to be polyadenylated, which may also act as a signal for transcription termination (Hutchinson et al., 1996).

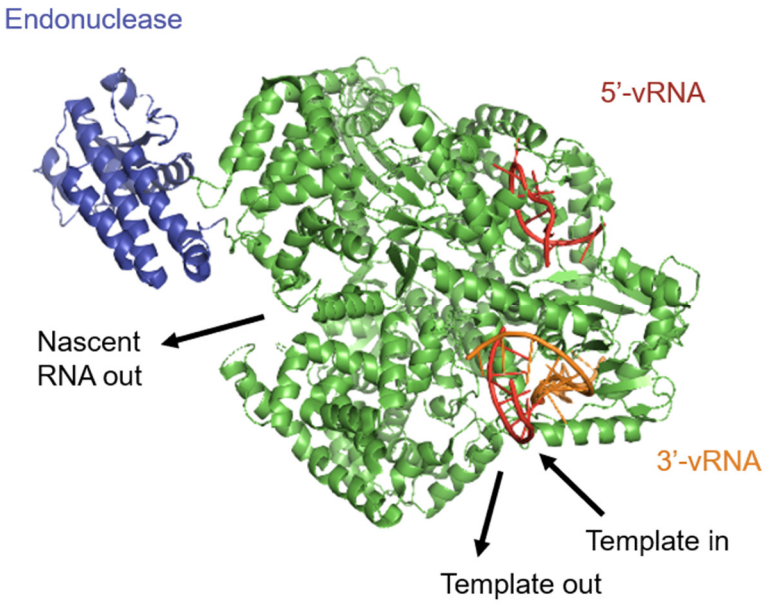


**Figure 14 Structure of the La Crosse RdRp.**

Structure of the La Crosse RdRp (PDB: 5AMQ) as a representative structure of the Bunyavirus RdRp. The endonuclease domain in indicated in blue and vRNA indicated in orange (3'-vRNA) and red (5'-vRNA). Arrows indicate where template vRNA enters and exits the polymerase as well as the exit of the newly synthesised RNA product. Figure adapted from Gerlach et al., 2015.

The RdRp has also been associated with the increased genetic diversity in orthohantaviruses through the copy-choice mechanism leading to recombination of viral segments (Sironen et al., 2001; Plyusnin et al., 2002). The copy choice mechanism occurs when two viruses of different lineages co-infect the same cell and replicate. During replication the RdRp switches from one viral template to the other, still attached to nascent RNA, resulting in a recombinant genome segment (Worobey and Holmes, 1999). This template switching has been shown to generally occur singly during replication in recombination 'hot spots' (Plyusnin et al., 2002). The RdRp is known to have a high error rate and these recombination events may help the virus overcome deleterious issues caused by a transcriptional error (Niemimaa et al., 2000).

## 1.4 Project Aims

Currently, many fundamental aspects of the orthohantavirus lifecycle are poorly understood and this is predominately due to difficulties in both the detection and quantification of hantavirus components. The generation of new and efficient techniques to quantify hantavirus proteins, RNAs and infectious particles will provide a more detailed understanding of the hantavirus life cycle and will aid in the development of therapeutics and antivirals that are currently lacking.

Here, three experimental aims were identified:

**1). Development of new approaches for the detection of hantavirus protein and RNA components.** Methodologies for detection and quantification of hantavirus components and infectivity are often laborious and inefficient. The first aim was to develop multiple complementary methods to allow quick and efficient quantification of orthohantavirus components that could produce a greater understanding of orthohantavirus replication kinetics. To this end, an antibody against the NP was generated to allow its detection by western blot or immunofluorescent analysis. This NP antiserum was subsequently used for an IF viral titration assay developed for infective particle quantification. In addition, a qRT-PCR was standardised for the quantification of viral genomes.

**2). Examining orthohantavirus-host cell interactions.** The orthohantavirus NP is purported to have multiple functions within the viral lifecycle. Along with its function to bind to and encapsidate viral RNAs, the NP also has roles in viral transcription and translation and evasion of the host immune system. The interactions of TULV NP with host cell components, including the cytoskeleton, organelles and transport vesicles were assessed using co-localisation analysis. As orthohantaviruses can form persistent infections *in vitro* without significant evidence of cytopathic effect, the induction of apoptotic factors and the interaction of NP with caspase-3 was examined to assess whether orthohantavirus NP has a role in viral persistence.

**3). Identification of orthohantavirus replication sites.** As of yet, the replication sites of orthohantavirus have not been identified. It has been suggested that like other Bunyaviruses, replication factories are associated with the Golgi network. However, this has not been experimentally proven. RNA labelling techniques were employed with the aim to identify viral replication sites by IF analysis. Nascent TULV RNA was labelled by incorporating a nucleoside analogue, 5EU, into the genome during replication and transcription. Subsequently, the localisation of RNA-FISH probes complementary to the sense and anti-sense S segment ORF was assessed by IF analysis in conjunction with TULV NP and previously identified interacting host-cell proteins.

# Chapter 2 : Materials and Methods

## 2.1 Materials

### 2.1.1 Vectors

Various recombinant cDNA plasmid constructs were generated for expression of the Seoul virus (SEOV) and Tula virus (TULV) nucleocapsid protein (NP) in both bacterial and mammalian cell systems. These proteins will be used for the generation of antisera against SEOV NP and to recombinantly express orthohantavirus NP in mammalian cell culture to examine interaction of the NP independent from other viral proteins.

The NP open reading frame (ORF) from SEOV sub-strain Humber virus, was optimised for bacterial protein expression and synthesised by Thermo Fisher Scientific as an insert within the pMK-RQ vector. For protein expression in bacterial cultures, this ORF and a subsequently truncated ORF produced by polymerase chain reaction (PCR), were sub-cloned into a pET28a(+) SUMO expression vector. These vectors will be used for the bacterial cell expression of the SEOV NP. SEOV NP core region (NP amino acids 111-399) was sub-cloned into a pET28a-SUMO expression vector in-frame with the coding sequence for biotin accepter peptide (BAP) tag. This vector will be used for the bacterial cell expression of a BAP-tagged SEOV NP.

For expression of TULV NP in mammalian cells, the TULV NP ORF was isolated by reverse-transcriptase PCR (RT-PCR) from TULV infected cell culture supernatant. TULV NP ORF was sub-cloned into the pcDNA3.1(+) mammalian cell expression vector, under the control of the chicken actin pol II promoter.

Relating to the production of SEOV NP specific affimers various affimer ORFs with alternative variable loop sequences were sub-cloned into a pET11a expression vector. This vector will be used for the bacterial cell expression of a 8 X His-N-terminal tagged affimer protein.

### 2.1.2 Bacterial Strains

Plasmid constructs were amplified using by transformation and subsequent growth of *Escherichia coli* (*E. coli*), DH5α strain, produced in-house by Sue Matthews *E. coli* expression strains used are listed in Table 3.

| Abb. | Host Strain | Genotype |
|---|---|---|
| Gold | BL21-Gold(DE3)pLysS | *E. coli* B F$^-$ *ompT hsd*S($r_B^-m_B^-$) *dcm*$^+$ Tet$^r$ *gal* λ(DE3) *endA* Hte [pLysS Cam$^r$] |
| Star | BL21-Star(DE3)pLysS | *E. coli* F$^-$ *ompT hsd*SB($r_B^-m_B^-$) *gal dcmrne*131 (DE3) [pLysS Cam$^r$] |
| Rosetta | BL21-Rosetta(DE3)pLysS | *E. coli* F$^-$ *ompT hsd*SB($r_B^-m_B^-$) *gal dcm* (DE3) [pLysSRARE Cam$^r$] |
| Rosetta 2 | BL21-Rosetta 2(DE3)pLysS | *E. coli* F$^-$ *ompT hsd*SB($r_B^-m_B^-$) *gal dcm* (DE3) [pLysSRARE2 Cam$^r$] |
| CD+ | BL21-CodonPlus(DE3)-RIPL | *E. coli* B F$^-$ *ompT hsd*S($r_B^-m_B^-$) *dcm*$^+$ Tet$^r$ *gal* λ(DE3) *endA* Hte [argU proL Cam$^r$] [argU ileY leuW Strep/Spec$^r$) |

**Table 3 Bacteria expression strains used for expression of recombinant protein**

### 2.1.3 Media

Media used for the growth of *E. coli* bacterial strains were Luria-Bertani (LB) broth (10 g/L sodium chloride, 10 g/L tryptone, 5 g/L yeast extract), LB-agar (10 g/L sodium chloride, 10 g/L tryptone, 5 g/L yeast extract, 15 g/L agar) and 2YT broth (5 g/L sodium chloride 16 g/L tryptone, 10 g/L yeast extract). Media used for the growth of cell lines included Dulbecco's modified essential medium (DMEM) supplemented with foetal bovine serum (FBS) (Life Technologies), 100 U/mL penicillin and 100 µg/mL streptomycin (Sigma).

### 2.1.4 Buffers

#### 2.1.4.1 Soluble protein purification buffers

Buffers used for the purification of soluble recombinant SEOV NP are described in Table 4.

#### 2.1.4.2 Insoluble protein purification buffers

Buffers used for the purification of insoluble recombinant SEOV NP are described in Table 5.

| | Lysis Buffer | Soluble Protein Purification Buffers | | | | | | | |
|---|---|---|---|---|---|---|---|---|---|
| | | **25 mM Wash** | **50 mM Wash** | **75 mM Wash** | **100 mM Wash** | **1 M Wash** | **High Salt** | **Elution** | **Dilution** |
| **Sodium chloride** | 500 mM | 500 mM | | | | | 1 M | 500 mM | |
| **Tris-HCl** | 20 mM (pH 8.0) | 20 mM (pH 7.4) | | | | | | | |
| **Glycerol** | 5 % | 5 % | | | | | | | |
| **β-mercaptoethanol** | 5 mM | 5 mM | | | | | | | |
| **Imidazole** | 25 mM | 25 mM | 50 mM | 75 mM | 100 mM | 1 M | 25 mM | 500 mM | 20 mM |
| **RNase** | 2 U/mL | | | | | | | | |
| **DNase** | 1 U/mL | | | | | | | | |
| **Chicken egg white lysozyme** | 1 mg/mL | | | | | | | | |
| **Triton X-100** | 1.0 % | | | | | | | | |
| **Protease inhibitor** | 1 tablet | | | | | | | | |

**Table 4 Composition of buffers used for soluble protein purification.**

| | Insoluble Protein Purification Buffers | | | | | | | | |
|---|---|---|---|---|---|---|---|---|---|
| | **IB Wash I** | **IB Wash II** | **IB Wash III** | **IB Solubilisation** | **IB Refolding I** | **IB Refolding II** | **IB Refolding III** | **IB Refolding IV** | **IB Refolding V** |
| **Sodium chloride** | 500 mM | 1 M | 500 mM | | | | | | 500 mM |
| **Tris-HCl** | 20 mM (pH 7.8) | | | | | | | | |
| **Glycerol** | 5 % | | | | | | | | |
| **β-mercaptoethanol** | 5 mM | | | | | | | | |
| **Imidazole** | | | | 25 mM | | 50 mM | 75 mM | 100 mM | 100 mM |
| **Triton X-100** | 2 % | 1 % | | | | | | | |
| **Guanidinium Hydrochloride** | | | | 6 M | 4.2 M | 3.0 M | 2.0 M | 1.0 M | |

**Table 5 Composition of buffers used for insoluble protein purification.**

### 2.1.5 Cell Lines

Vero E6 cells (ATCC® CRL-1586™) were used for the propagation of TULV and expression of recombinant protein. Vero E6 cells were kindly provided by Dr Roger Hewson (PHE, UK). Vero E6 cells are a clone of Vero 76 cells isolated from *Cercopithecus aethiops* (African green monkey) kidney cells. Vero E6 cells are known to exhibit contact inhibition and can be used for the growth of slow replicating viruses, such as orthohantaviruses.

### 2.1.6 Virus Strains

Tula virus (TULV) was kindly provided by Dr Roger Hewson (PHE, UK). Sequence analysis of the TULV S segment ORF of this isolate confirmed the strain identity as Moravia/5302v/95 with two synonymous and one non-synonymous differences in the coding sequence.

### 2.1.7 Fluorescent *in-situ* hybridisation (FISH) Probes

Fluorescent *in-situ* hybridisation DNA probes were designed against the sense and anti-sense TULV S segment ORF sequenced using the Stellaris® Probe Designer version 4.2. The Stellaris® Probe Designer provided 48 oligonucleotide probe sequences that were 20 nucleotides in length with a minimum spacing of 2 nucleotides. Target TULV S segment ORF sequence was obtained from sequencing viral RNA isolated from TULV infected cell culture medium (Genewiz). Probes were assessed using NCBI Nucleotide Blast against *C. aethiops* (taxid:9534) mRNA and against the M and L segment sense and anti-sense sequences (strain: Tula/Moravia/5302v/95). Any probes with more than 15 consecutive complimentary nucleotides were discarded. TULV S segment sense and anti-sense probes were labelled with Quasar670. Custom-designed TULV S segment probes and ShipReady GAPDH probes labelled with Quasar570 were synthesised by 2B Scientific (UK). Probe sequences can be seen in Table 6.

| Probe Name | Probe Sequence 5' – 3' |
|---|---|
| TULV S Segment Sense 1 | TGTTCATGGCGGGTGATTTC |
| TULV S Segment Sense 2 | TTGCCGGGCAATGACAATTT |
| TULV S Segment Sense 3 | CCGTCTTTTCTACATCTTTA |
| TULV S Segment Sense 4 | CTCCAATGCTGACACAGCTG |
| TULV S Segment Sense 5 | AACAGGCTTTTCACCCATTT |
| TULV S Segment Sense 6 | TGATCTCTCCTTGAGGTGAT |
| TULV S Segment Sense 7 | CTGTAATGTACTGGCCGATA |
| TULV S Segment Sense 8 | ATGCCTTCAAGATTATTGCA |
| TULV S Segment Sense 9 | CCTCTAGTTGACAGCATATA |
| TULV S Segment Sense 10 | CTTAAACCGGATTCTTGTCC |
| TULV S Segment Sense 11 | GATGTTTCGGGCGTCTAATG |
| TULV S Segment Sense 12 | GCTGTTGGCATAGACACATA |
| TULV S Segment Sense 13 | AATTCATCGGCTTTCATGGT |
| TULV S Segment Sense 14 | TGAGCAGGAAAGAGTCCACA |
| TULV S Segment Sense 15 | TCTTTTCAGGCCAATCTTTA |
| TULV S Segment Sense 16 | AATCTTCTTCCTTACTAGGA |
| TULV S Segment Sense 17 | GGTAAGCATCATTACTCACA |
| TULV S Segment Sense 18 | AATGCCTTTTCACGTCCTAA |
| TULV S Segment Sense 19 | TATCTCAGCAAGGTGTGACT |
| TULV S Segment Sense 20 | AGCTGCAAGGTCAATCAAGT |
| TULV S Segment Sense 21 | GTGCTTGTGGTGACTTTATA |
| TULV S Segment Sense 22 | AAAAATGCTCCCAACTCTGC |
| TULV S Segment Sense 23 | GTTTTGGATGCCATAATCGT |
| TULV S Segment Sense 24 | GAGTGCGTCTCAGATATGAC |
| TULV S Segment Sense 25 | GTTGACAATATCAGAACCCC |
| TULV S Segment Sense 26 | GACTTTGTGCAAGTGTTCTG |
| TULV S Segment Sense 27 | TAGATTTTTAGCGGTTCCTG |
| TULV S Segment Anti-Sense 1 | GATTTCAAACCAGGAACCGC |
| TULV S Segment Anti-Sense 2 | GAGCTCAGAACACTTGCACA |
| TULV S Segment Anti-Sense 3 | TCTGGGTGATGATATGGACC |
| TULV S Segment Anti-Sense 4 | CTGATATTGTCAACCACTTC |
| TULV S Segment Anti-Sense 5 | AGACGCACTCAATCTATGGG |
| TULV S Segment Anti-Sense 6 | GGGCACAGCAGAGGAAAAAT |
| TULV S Segment Anti-Sense 7 | CGATTATGGCATCCAAAACT |
| TULV S Segment Anti-Sense 8 | CAGAGTTGGGAGCATTTTTT |
| TULV S Segment Anti-Sense 9 | CAACACCACCAGACTCTATA |

| | |
|---|---|
| TULV S Segment Anti-Sense 10 | TGACTTGATTGACCTTGCAG |
| TULV S Segment Anti-Sense 11 | GATGCTTACCTTTTAGGACG |
| TULV S Segment Anti-Sense 12 | TTCGTTAAAGATTGGCCTGA |
| TULV S Segment Anti-Sense 13 | GGGTGTGATTGGATTTTCTT |
| TULV S Segment Anti-Sense 14 | GAAACATCATAAGTCCTGTC |
| TULV S Segment Anti-Sense 15 | GACTCTTTCCTGCTCAAATT |
| TULV S Segment Anti-Sense 16 | TCTACCATGAAAGCCGATGA |
| TULV S Segment Anti-Sense 17 | TGTATGTGTCTATGCCAACA |
| TULV S Segment Anti-Sense 18 | AATCAATGGCATTAGACGCC |
| TULV S Segment Anti-Sense 19 | TAAGGGGACAAGAATCCGGT |
| TULV S Segment Anti-Sense 20 | GGCTTTGCACTTGCAATAAT |
| TULV S Segment Anti-Sense 21 | AGTGGACAGACAGCAGATTG |
| TULV S Segment Anti-Sense 22 | CCTTCGATATGGAAATGTCC |
| TULV S Segment Anti-Sense 23 | ATCACCTCAAGGAGAGATCA |
| TULV S Segment Anti-Sense 24 | TGGGTGAAAAGCCTGTTGAC |
| TULV S Segment Anti-Sense 25 | TGGCAGACTTCAAGAGGCAG |
| TULV S Segment Anti-Sense 26 | GTGTCAGCATTGGAGGACAA |
| TULV S Segment Anti-Sense 27 | ACTACAGAGTAGACGGGCAG |
| TULV S Segment Anti-Sense 28 | TAGAAAAGACGGTGGAAGCC |
| TULV S Segment Anti-Sense 29 | CATTGCCCGGCAAAAACTTA |

**Table 6 RNA FISH Probes designed against TULV S Segment ORF sense and anti-sense sequences**

## 2.2 Methods

### 2.2.1 Cloning Strategies

#### 2.2.1.1 The Polymerase Chain Reaction (PCR)

PCR was used to modify and truncate various cDNA. SEOV NP ORF, SEOV $NP_{core}$ (111-399 amino acids), TULV NP ORF and anti-SEOV $NP_{core}$ affimer cDNAs were amplified using PCR. PCR was carried out in 50 µL reaction volumes containing; 50 ng template DNA, 200 µM dNTPs, 0.5 µM forward primer, 0.5 µM reverse primer, 1X Q5® Reaction Buffer (New England Biolabs) and 0.02 U/µL Q5® High Fidelity DNA Polymerase (New England Biolabs). PCR cycling was carried out in a thermocycler (Eppendorf) with cycling conditions; 98 °C for 2 minutes, followed by 40 cycles of 98 °C for 30 seconds, 58 °C for 30 seconds, 72 °C for 1 minute, followed by 72 °C for 10 minutes. Oligonucleotide primers are shown in Table 7 and were designed to incorporate terminal restriction endonuclease recognition sites for insertion into expression vectors. PCR products were purified using the QIAquick PCR Purification Kit (Qiagen).

| Primer Name | Primer Sequence 5' – 3' |
|---|---|
| SEOV NP Forward | GTTGGATCCATGGCAACCATGGAAG |
| SEOV NP Reverse | GTGCTCGAGTTACAGTTTCATCGGTTCTTG |
| SEOV $NP_{core}$ Forward | TGTTGGATCCGAACCGACAGGTCAGACCGCAGATTG |
| SEOV $NP_{core}$ Reverse | GGTGCTCGAGTTAACCCAGGTGAAAGTTATCCACGGC |
| SEOV $NP_{core}$ BAPtag Forward | TGTTGGATCCGAACCGACAGGTCAGACCGCAGATTG |
| SEOV $NP_{core}$ BAPtag Reverse | GGCCTCGAGAAGCTTACCCAGGTGAAAGTTATCCACGGC |
| BAPtag Forward | GGTAAGCTTGGATCCGCCGGAGGCTCTGGAGGCCTGAACGATATTTTCGAAGCTCAG |
| BAPtag Reverse | GGCCTCGAGTTATTCGTGCCATCCGATTTTCTGAGCTTCGAAAATATCG |
| TULV S Segment Forward | GTTGGATCCATGAGCCAACTCAAAG |
| TULV S Segment Reverse | GTGCTCGAGTTAGATTTTTAGCGG |
| Affimer Forward | TTCTGGCGTTTTCTGCGTCTGC |
| Affimer Reverse | TACCCTAGTGGTGATGATGGTGATGC |

**Table 7 Oligonucleotide primers used for amplification of DNA inserts.**

#### 2.2.1.2 Dpn1 Digest

In order to remove *dam* methylated template DNA from PCR products, 10 U DpnI (New England Biolabs) was added to each PCR reaction used for production of cDNA inserts for ligation and incubated for 1 hour at 37 °C.

#### 2.2.1.3 Restriction Digest

Restriction enzyme digests were carried out to facilitate sub-cloning into expression vectors or for diagnostic purposes. Restriction digests were carried out in 20 µL volumes containing 1 µg DNA, 1X CutSmart® buffer (New England Biolabs) and 10 U restriction enzyme. Digests were incubated at 37 °C for 1-2 hours and analysed by agarose gel electrophoresis. Products of digestion for sub-cloning were purified by gel extraction using the NEB Monarch® gel extraction kit (New England Biolabs) as per the manufacturer's instructions.

#### 2.2.1.4 Agarose gel electrophoresis

Separation of DNA fragments resulting from restriction digest were carried out using 1 % or 2 % agarose gels containing 1 X TAE (40 mM Tris-acetate, 1 mM ethylene-diamine-tetra acetic acid (EDTA)) with SYBR Safe DNA stain (Life Technologies) diluted 1:10,000. DNA samples were mixed with 1X DNA gel loading dye (New England Biolabs) before loading onto gel. Hyperladder I (Bioline) was used as a molecular maker. Electrophoresis was carried out at 100 V for 30-90 minutes in 1 X TAE buffer. Blue light transillumination was used for the visualisation of DNA.

#### 2.2.1.5 Ligation

Ligations were carried out in 20 µL reaction volumes containing 7:1 molar ratio of insert: vector DNA, 1 X T4 DNA ligase reaction buffer (50 mM Tris-HCl, 10 mM magnesium chloride, 10 mM dithiothreitol, 1 mM ATP, pH 7.5) and 2.5 % poly(ethylene glycol) (PEG) 6000 and 10 U T4 DNA ligase (New England Biolabs). Ligase reactions were either incubated on ice for 1 hour and then at room temperature for 1 hour or overnight at 4 °C before being transformed into DH5α cells.

#### 2.2.1.6 Bacterial transformations

Bacterial transformations were carried out by adding 50-100 ng plasmid DNA or 5-10 µL of ligation mixture to 50 µL competent *E. coli* cells that were thawed on ice. Transformation mixtures were incubated on ice for 20 minutes before being heat-shocked at 42 °C for 45 seconds and then cooled on ice for 5 minutes. To the transformed mixes, 400 µL LB broth was added and incubated at 37 °C with shaking for 1 hour. Either 50 µL or 200 µL transformation mixture was spread onto LB agar plates supplemented with appropriate antibiotic-selection (50 µg/mL kanamycin or 100 µg/mL ampicillin) and incubated at 37 °C overnight.

#### 2.2.1.7 Plasmid DNA amplification

Single colonies were picked from transformation plates and used to inoculate 10 mL (small-scale), 50 mL (large-scale high copy number) or 200 mL (large-scale low copy number) LB broth with appropriate antibiotic-selection and incubated at 37 °C with shaking overnight. Bacterial cells were pelleted by centrifugation at 4000 **g** at 4 °C for 20 minutes. Plasmid DNA was isolated using QIAprep Spin Miniprep Kit (Qiagen) or QIAGEN Plasmid Midi Kit (Qiagen) following the manufacturer's instructions. Purity and quantity of DNA through spectrophotometry using a NanoDrop 1000 (Thermo Scientific).

### 2.2.2 Recombinant Protein Expression and Purification

#### 2.2.2.1 Starter cultures

pET28a-SUMO-SEOV NP and pET28a-SUMO-SEOV $NP_{core}$ plasmids were transformed into *E. coli* Gold, Star, Rosetta, Rosetta-2 and CD+ expression strains. pET11a-affimer plasmids were transformed into *E. coli* Rosetta-2 expression strains. Single colonies were picked from transformation plates and used to inoculate 10-75 mL LB broth with appropriate antibiotic-selection and incubated at 37 °C with shaking overnight. 0.1 mL of starter culture or 10 mL of starter culture were used to inoculate 10 mL or 1000 mL 2YT broth for protein expression.

#### 2.2.2.2 IPTG Induction

Protein expression cultures were grown to $OD_{600nm}$ 0.6-0.8 shaking at 37 °C before being induced with 100-500 µM Isopropyl β-D-1-thiogalactopyranoside (IPTG) and incubated at 18 °C or 12 °C with shaking for 18-24 hours.

#### 2.2.2.3 Soluble protein isolation

Bacterial cells were pelleted by centrifugation at 4000 **g** for 20 minutes at 4 °C. Each 1 L bacterial pellet was resuspended in 25 mL bacterial cell lysis buffer (Table 4) and incubated for 30 minutes on ice. Cell lysates containing affimers were incubated at 50 °C for 20 minutes to heat denature non-specific proteins. Sonication was carried out on ice using 20 cycles of 20 seconds on and 40 seconds off at 6 micron amplitude. Cell lysates were clarified by centrifugation at 20,000 **g** for 1 hour at 4 °C. Supernatant contained soluble protein and the pellet contained insoluble protein. Soluble protein was filtered through 0.45 µm filter to remove large protein aggregates and remaining cell debris. Recombinant SEOV $NP_{core}$ was isolated from both soluble and insoluble protein using nickel affinity chromatography. Recombinant SEOV $NP_{core}$ with BAPtag were isolated from soluble protein using nickel affinity chromatography. Anti-SEOV $NP_{core}$ affimers were isolated from soluble protein using batch nickel affinity chromatography.

#### 2.2.2.4 Nickel affinity chromatography purification of soluble SOEV $NP_{core}$

Clarified bacterial supernatant containing soluble protein was applied to nickel Sepharose™ pre-packed 5mL HisTrap HP column (GE Healthcare) at 4 °C for 1 hour using a peristaltic pump. Resin was washed with 5 column volumes of 25 mM imdazole wash buffer followed by 5 column volumes of high salt wash buffer. Contaminating proteins were removed by washing with 5 column volumes of increasing concentration of 25-100 mM imidazole wash buffers. Recombinant protein was removed with 2-10 successive 5 mL washes with elution buffer. Any remaining bound protein was removed by washing with 5 column volumes of 1M imidazole wash buffer. Eluted protein was pooled and 6xHis-SUMO tag removed by overnight cleavage at 4 °C with 10 U Ubl-specific protease 1 (Ulp1) protease (produced in-house). Cleaved protein was

filtered through a 0.45 µm filter to remove protein aggregates before dilution 1:10 in diluting buffer. Diluted protein was applied to a to nickel Sepharose™ pre-packed 5ml HisTrap HP column (GE Healthcare) at 4 °C for 1 hour using a peristaltic pump and the unbound protein collected. Any remaining bound protein was removed by washing with 5 column volumes of 1M imidazole wash buffer. Eluted protein concentration was determined by diluting 1:10 in 25 mM wash buffer and reading absorbance at $280_{nm}$ ($A_{280nm}$) using the NanoDrop 1000 (Thermo Scientific). Protein was concentrated to >0.5 mg/mL using a Vivaspin 10,000 MWCO spin concentrator (Sartorius). Composition of buffers used are described in 2.1.4.1.

#### 2.2.2.5 Insoluble protein isolation

Each 1 L of insoluble pellet was resuspended in 30 mL of IB wash buffer I and incubated on ice for 10 minutes. Sonication was carried out on ice using 3 cycles of 10 seconds on and 10 seconds off at 6 micron amplitude followed by centrifugation at 20,000 **g** for 15 minutes at 4 °C. Pellet was resuspended in 30 mL of IB wash buffer II and incubated on ice for 10 minutes. Sonication was carried out on ice using 3 cycles of 10 seconds on and 10 seconds off at 6 micron amplitude followed by centrifugation at 20,000 **g** for 15 minutes at 4 °C. Pellet was resuspended in 30 mL of IB wash buffer III and centrifuged at 20,000 **g** for 15 minutes at 4 °C. Remaining pellet was resuspended in IB solubilisation buffer overnight at 4 °C with rotation to dissolve inclusion bodies. Dissolved protein was centrifuged at 20,000 **g** for 45 minutes at 4 °C to remove undissolved protein. Supernatant contains dissolved insoluble protein and was filtered through 0.45 µm filter to remove large protein aggregates and remaining cell debris. Composition of buffers used are described in 2.1.4.2.

#### 2.2.2.6 Nickel affinity chromatography purification of insoluble SOEV $NP_{core}$

Gu-HCl dissolved insoluble protein purified from inclusion bodies was applied to Super Ni-NTA Agarose Resin (Generon) pre-washed in 25 mM imidazole wash buffer and incubated at 4 °C for 2 hours with rotation before applying to a gravity-flow column. Resin was washed successively with IB refolding buffers I-V of increasing imidazole concentration and decreasing Gu-HCl

concentration to refold protein on the column. Resin was incubated with 50 mL of 25 mM imidazole wash buffer containing 10 U Ulp1 protease at 4 °C for 4 hours with rotation before applying to a gravity-flow column and collecting the flow-through containing the cleaved protein. Resin was washed with 5 x 10 mL of 25 mM imidazole wash buffer followed by 2 x 10 mL of 100 mM imidazole wash buffer to remove any remaining unbound protein. Any remaining bound protein was removed from the resin by washing with 20 mL of 1 M imidazole wash buffer. A sample of the resin was collect to analyse remaining bound protein. Eluted protein concentration was determined by diluting 1:10 in 25 mM wash buffer and reading $A_{280nm}$ using the NanoDrop 1000 (Thermo Scientific). Protein was concentrated to >0.5 mg/mL using a Vivaspin 10,000 kDa molecular weight cut offspin concentrator (Sartorius). Composition of buffers used are described in 2.1.4.2.

#### 2.2.2.7 Antibody production and validation

The identity of purified SEOV $NP_{core}$ was confirmed using mass spectrometry carried out by the mass spectrometry facility (University of Leeds). Purity of SEOV $NP_{core}$ was confirmed to be >85% using densitometry (ImageJ). Protein samples were sent to Alta Biosciences in 0.25 mg aliquots on dry ice. A goat was inoculated with give injections of antigen were carried out over 6 month programme. Sera was collected one week after each booster injection of antigen. Polyclonal antibody was validated by testing by western blot against recombinant SEOV $NP_{core}$, TULV infected cell lysates, transfected TULV NP cell lysates and by examination of infected and TULV NP transfected cells by indirect immunofluorescence (Figure 21).

### 2.2.3 Affimer Production and Purification

#### 2.2.3.1 Generating BAP-tagged protein

The purification of SEOV $NP_{core}$ specific affimers through phage display using streptavidin-coated strips required the production of purified biotinylated SEOV $NP_{core}$. In order to generate this biotinylated protein, a biotin accepter peptide tag was engineered to the C-terminus coding-region of the SEOV $NP_{core}$ protein. This was achieved by introducing a unique restriction cleavage site, HindIII, at the C-terminus of SEOV $NP_{core}$ and generating an BAPtag insert with between a HindIII and XhoI restriction enzyme site by PCR amplification. The BAPtag was then sub-cloned into the pET28(a)-SUMO-SEOV $NP_{core}$ vector which was then used for subsequent protein expression and purification as described previously (2.2.3.8)

#### 2.2.3.2 Affimer panning – Round One

Panning and selection for SEOV $NP_{core}$ specific affimers was carried out by phage display in accordance with protocols developed at the University of Leeds. Target protein (SEOV $NP_{core}$) produced with BAPtag was enzymatically biotinylated during production in expression *E. coli* cells and checked by western blot using an streptavidin conjugated Alexa Fluor 647 antibody.

Streptavidin coated (high binding capacity (HBC)) 8-well strips (Thermo Fisher Scientific) were incubated overnight at 37 °C with 300 µL of 2 X casein blocking buffer (BB) diluted in PBS supplemented with 0.1 % Tween-20 (PBST). Each well was washed three times in 300 µL of PBST before adding 100 µL of 2 X BB. To pre-pan the phage 5 µL of the phage library (University of Leeds) was added to the first pre-pan well and incubated on a vibrating platform shaker (Heidolph) for 40 minutes. Buffer containing phage library was pre-panned three times. To the final well, 20 µL of SEOV $NP_{core}$ + BAPtag was added and incubated for 1 hour at room temperature on a vibrating platform shaker before washing six times with 200 µL PBST. Buffer containing pre-panned phage library was added to well containing streptavidin-bound target and incubated for 2 hours at room temperature on a vibrating platform shaker. An 8 mL culture of ER2738 *E. coli* cells were set up by diluting an overnight culture of ER2738 cells 1:15 and incubating for 1 hour at 37 °C with shaking.

Panning wells were washed twenty-seven times in 300 µL PBST and bound phage were eluted by adding 100 µL 0.2 M glycine pH 2.2 and incubating for 10 minutes at room temperature. Glycine was neutralised by adding 100 µL of 1 M Tris-HCl pH 9.1 and eluted phage immediately added to the ER2738 cells. To elute remaining phage triethylamine (Sigma-Aldrich) diluted 1:70 with PBS was added to the well and incubated for 6 minutes at room temperature. Triethylamine was neutralised by adding 50 µL of 1 M Tris-HCl pH 7 and immediately added to ER2738 cells. ER2738 cells with phage were incubated for 1 hour at 37 °C without shaking before plating LB agar plate supplemented with 100 µg/mL ampicillin (LB-Amp) and incubated overnight at 37 °C.
Colonies were counted and found to be 2.96 x $10^5$ cells per 8 mL. Colonies were scraped into 7 mL of 2YT media supplemented with 100 µg/mL carbenicillin. Absorbance at 600nm ($A_{600nm}$) was measured and culture was diluted so $A_{600nm}$ = 0.2 in 2YT media and incubated for 1 hour at 37 °C with shaking. 3.2 x $10^{10}$ M13K07 helper phage was added to culture and incubated for 30 minutes at 37 °C with shaking at 90 revolutions per minute (rpm). Kanamycin was added to 25 mg/mL and incubated overnight at 25 °C. Cultures were centrifuged at 3500 **g** for 10 minutes at room temperature and supernatant containing phage was transferred to fresh tubes and retained for a second panning round.

#### 2.2.3.3 Affimer panning – Round Two

A 20 µL aliquot of Dynabeads® MyOne™ Streptavidin T1 (Invitrogen) were blocked by incubating overnight at room temperature with 100 µL of 2 X BB on a Stuart SB2 rotor at 20 rpm. For panning, wells of a deep well 96-well plate (Thermo Scientific) were blocked using 1 mL 2 X BB for panning or 300 µL of 2 X BB for elution for 2 hours at 37 °C. The pre-blocked Streptavidin beads were centrifuged at 800 **g** for 1 minute at room temperature before immobilising on a magnet. Streptavidin beads were resuspended in 100 µL fresh 2 X BB. To pre-pan the phage, 125 µL of phage-containing supernatant from the first panning round was mixed with 125 µL of 2 X BB and 25 µL of pre-blocked Streptavidin beads in Protein LoBind Tubes (Eppendorf) and incubated for 1 hour at room temperature with rotation. Streptavidin beads were centrifuged for 800 **g** for 1 minute at room temperature and immobilised

on a magnet. Pre-panning was repeated. A 15 µL aliquot SEOV $NP_{core}$ + BAPtag was mixed with 200 µL of 2 X BB and 50 µL of pre-blocked Streptavidin beads and incubated for 30 minutes at room temperature with rotation. Streptavidin beads bound to target were centrifuged at 800 **g** for 1 minute at room temperature and immobilised on a magnet and washed three times in 500 µL 2 X BB. Beads were centrifuged at 800 **g** for 1 minute at room temperature and supernatant containing pre-panned phage was added and transferred to the pre-blocked deep well 96-well plate. The KingFisher Flex (Thermo Scientific) was used for panning following the standard phage display protocol as described below.

Streptavidin beads were collected and bound by fast mixing for 10 seconds followed by slow mixing for 1 minute. Beads were washed in four times in 2 X BB with slow mixing for 1 minute. Phage was eluted from the beads by slow mixing for 7 minutes and 30 seconds in 100 µL of 0.2 M Glycine pH 2.2 and remaining phage was eluted by slow mixing for 3 minutes and 30 seconds in 100 µL in triethylamine diluted 1:70 in PBS.

An 8 mL culture of ER2738 *E. coli* cells were set up by diluting an overnight culture of ER2738 cells 1:15 and incubating for 1 hour at 37 °C with shaking. Phage elutions were neutralised as previously described in 2.2.3.2 before mixing to the ER2738 cells and incubated for 1 hour at 37 °C without shaking before plating onto LB-Amp and incubated overnight at 37 °C. Phage were prepared as previously described in 2.2.3.2.

#### 2.2.3.4 Affimer panning – Round Three

NeutrAvidin coated HBC 8-well strips (Thermo Fisher Scientific) were incubated overnight at 37 °C with 300 µL of 2 X BB. Each well was washed three times in 300 µL of PBST before adding 200 µL of 2 X BB. To pre-pan the phage, 200 µL of phage-containing supernatant from the second panning round was added to one well with 20 µL of 10 X BB and incubated for 1 hour at room temperature on a vibrating platform shaker. Pre-panning was repeated three times. To the final well, 10 µL of SEOV $NP_{core}$ + BAPtag was added with 100 µL of 2 X BB and incubated for 1 hour at room temperature on a vibrating platform shaker. Target well and the negative control blank pre-blocked well were washed three times with 200 µL PBST. A 100 µL aliquot

pre-panned phage was transferred to the target and negative control wells and incubated for 30 minutes at room temperature with shaking. An 8 mL culture of ER2738 *E. coli* cells were set up by diluting an overnight culture of ER2738 cells 1:15 and incubating for 1 hour at 37 °C with shaking. Panning wells were washed twenty-seven times in 300 µL PBST and bound phage were eluted by adding 100 µL 0.2 M glycine pH 2.2 and incubating for 10 minutes at room temperature. Glycine was neutralised by adding 100 µL of 1 M Tris-HCl pH 9.1 and eluted phage immediately added to the ER2738 cells. To elute remaining phage triethylamine (Sigma-Aldrich) diluted 1:70 with PBS was added to the well and incubated for 6 minutes at room temperature. Triethylamine was neutralised by adding 50 µL of 1 M Tris-HCl pH 7 and immediately added to ER2738 cells. ER2738 cells with phage were incubated for 1 hour at 37 °C without shaking before plating on LB-amp plates and incubated overnight at 37 °C.

#### 2.2.3.5 Preparing individual phage binders

A 200 µL aliquot of 2TY media supplemented with 100 µg/mL carbenicillin was aliquoted into a deep well 96-well plate. From the final panning round of phage display (2.2.3.4) 48 individual colonies were used to inoculate each well and incubated overnight at 37 °C with shaking. 200 µL of 2TY media supplemented with 100 µg/mL carbenicillin was aliquoted into a deep well 96-well plate and 25 µL of overnight cultures were added and incubated for 1 hour at 37 °C with shaking. 1 x $10^9$ M13K07 helper phage in 2YT media were added to each well and incubated for 30 minutes at room temperature with shaking. A 10 µL aliquot of kanamycin (1.25 mg/mL) was added to each well and incubated overnight at room temperature with shaking. The phage-infected culture plate was centrifuged at 3500 **g** for 10 minutes at room temperature. Phage-containing supernatant was collected.

#### 2.2.3.6 Phage ELISA

Lyophilised streptavidin was reconstituted in distilled water to a final concentration of 5 mg/mL and then diluted to 5 µg/mL in PBS. 50 µL of streptavidin solution was added to each well of F96 Maxisorp Nunc-Immuno Plate (Thermo Scientific) and incubated for 4 hours at room temperature.

Streptavidin coated wells were blocked overnight at 37 °C with 200 µL of 2 X BB and washed once with 300 µL PBST. SEOV $NP_{core}$ + BAPtag was diluted 1:1000 in 2 X BB and 50 µL was aliquoted into 48 wells of the 96-well plate. For the negative control, 50 µL of 2 x BB was added to the remaining 48 wells of the 96-well plate and incubated for 1 hour at room temperature with shaking. Wash once with 300 µL of PBST before aliquoting 10 µL of 10 X BB per well. To each well, 40 µL of phage containing supernatant was added and incubated for 1 hour at room temperature with shaking. Wells were washed once with 200 µL of PBST and 50 µL of anti-Fd-bacteriophage-HRP diluted 1:2000 in 2 X BB was added per well and incubated for 1 hour at room temperature with shaking. Wells were washed ten times with 300 µL of PBST and 50 µL of SeramunBlau® fast 3,3',5,5'-tetramethylbenzidine (TMB) substrate solution (Seramun) was added per well and allowed to develop for around 3 minutes. Absorbance at 620nm ($A_{620nm}$) was measured. $A_{620nm}$ was compared between target and negative control wells to identify unique binders.

#### 2.2.3.7 Unique Binders

The first set of panning rounds did not produce unique anti-SEOV NP binding affimers a second set was carried out by Dr Christian Tiede, University of Leeds, which produced two unique binders.

#### 2.2.3.8 Batch nickel affinity chromatography purification of affimers

Affimers selected were identified by sequencing (GeneWiz) and cDNA inserts generated by PCR amplification. Inserts were sub-cloned into pET11a expression vector, confirmed by sequencing (GeneWiz). Protein expression and soluble protein isolation was carried out as previously described (2.2.2.1, 0, 2.2.2.3). Clarified bacterial supernatant containing soluble protein was applied to 150 µL Super Ni-NTA Agarose Resin (Generon) pre-washed in 20 mM imdazole wash buffer and incubated at room temperature for 2 hours with rotation before centrifugation at 1000 **g** for 1 minute to remove unbound protein. Resin was washed in 1 mL 25 mM wash buffer until $A_{280nm}$ using the NanoDrop 1000 (Thermo Scientific) was below 0.01. To elute affimers, resin

was resuspended in 500 µL 300 mM elution buffer and incubated for 5 minutes at room temperature. Resin was centrifuged at 1000 **g** for 1 minute to sediment resin. Eluted protein concentration was reading $A_{280nm}$ using the NanoDrop 1000 (Thermo Scientific). Composition of buffers used are described in 2.1.4.1.

## 2.2.4 Cell Culture Methods

### 2.2.4.1 Continuous cell culture

Vero E6 cells were cultured in DMEM with 10% v/v FBS and supplemented penicillin and streptomycin, referred to as complete media. Vero E6 cells were sub-cultured when approaching confluency using trypsin-EDTA (Sigma) to detach cells from flask. Detached cells were gently pelleted by centrifugation at 500 g at 4 °C for 5 minutes and resuspended in fresh complete media. Cells were seeded at the following densities; 96-well plate (5 x $10^4$ cells/well), 12-well plate (105 cells/well), 6-well plate (5 x $10^5$ cells/well), 75 $cm^2$ flask ($10^5$ – 2 x $10^6$ cells/flask) and 175 $cm^2$ flask (5 x $10^5$ – $10^6$ cells/flask). Glass coverslips were sterilised by submerging in 100% ethanol and washing in sterile PBS prior to seeding for immunofluorescence (IF) experiments. Cells were maintained in a humidified incubator at 37 °C with 5 % $CO_2$

### 2.2.4.2 Freezing and thawing cells

Cells were frozen for long-term storage at -80 °C. Cells were trypsinised and washed 3-times in PBS with centrifugation at 500 **g** at 4 °C for 5 minutes between each wash step. Cells were counted and resuspended in ice-cold FBS supplemented with 10% DMSO to a final concentration of 5 x $10^6$ cells/mL. Cell suspension was aliquoted into cryovials which were cooled in an isopropanol chamber to -80 °C overnight. Frozen cells were rapidly thawed at 37 °C and added to 10 mL complete media then centrifuged at 500 **g** at 4 °C for 5 minutes. Cell pellet was gently resuspended in complete media and transferred to a 25 $cm^2$ flask. After 48 hours incubation in a humidified incubator at 37 °C with 5 % $CO_2$, cell culture medium was removed and attached cells gently washed in PBS before addition of fresh complete media. Cell cultures were expanded when cells reached 80% confluency.

### 2.2.5 Transfections

#### 2.2.5.1 Lipofectamine mediated transfection of Vero E6 cells with pcDNA3.1 (+)-TULV NP

Vero E6 cells were transfected with pcDNA3.1(+)-TULV NP cells for both IF, protein analysis by western blot. Lipofectamine 2000 (Life Technologies) was used to mediate transfection. Cells were seeded in 12-well plates (for IF), 6-well plates (for protein analysis) and 75 $cm^3$ flasks (for transfection) 24 hours before transfection so cell confluency was 60-80 % confluent. For 12- and 6-well plates, 1 µg DNA was added to 100 µL Opti-MEM (Gibco) and in a separate microfuge tube 3 µL lipofectamine 2000 was added to 100 µL Opti-MEM. For 75$cm^2$ flasks, 25 µg DNA was added to 2.5 mL Opti-MEM and in a separate tube, 60 µL lipofectamine 2000 was added to 2.5 mL Opti-MEM. Solutions were mixed and allowed to equilibrate for 5 minutes. The Opti-MEM-DNA solution was added to the Opti-MEM-lipofectamine 2000 solution and mixed gently. Opti-MEM-DNA-lipofectamine 2000 solution was incubated at room temperature for 20 minutes before being added dropwise to cells that have been prewashed in PBS. After 4 hours of incubation in a humidified incubator at 37 °C with 5 % $CO_2$, medium was removed and cells washed with PBS. Complete media was added and cells incubated overnight in a humidified incubator at 37 °C with 5 % $CO_2$. After 18 hours, cells were harvested for analysis either by fixation of coverslips in 100 % methanol (IF) or by cell lysis (protein analysis and IP).

### 2.2.6 Virological Techniques

#### 2.2.6.1 Virus infection and propagation by sub-culturing infected Vero E6 cells

Infectious TULV was diluted to the desired MOI (0.1-1.0) in serum free DMEM (SFM) and added to Vero E6 cells which had been washed once in sterile PBS. Cells were incubated with TULV at 37 °C with gentle rocking for 90 minutes to allow TULV to adsorb to cells. After adsorption, DMEM with 2 % FBS and supplemented with 100 U/mL penicillin and 100 µg streptomycin (2% DMEM) was added to cells and cultures were incubated in a humidified incubator at 37 °C with 5 % $CO_2$. Mock infections were carried out as described above, but omitting the addition of TULV.

TULV was propagated in Vero E6 cells seeded in a 175 $cm^2$ flask and when cells reached 70-80 % confluency they were infected as above with TULV at an MOI of 0.01. When infected cells reached 90% confluency they were sub-cultured as described previously (2.2.4.1) but retaining cell culture growth medium. Cells and cell culture growth medium were seeded at 1:5 into fresh 175 $cm^2$ flasks supplemented with fresh 2% DMEM. When infected cells reached 90% confluency they were sub-cultured as described into fresh 175 $cm^2$ flasks. When infected cells reached 100% confluency, TULV was harvested by freeze-thawing at -80 °C for a minimum of 1 hour and then incubating 37 °C for 1 hour. Cell culture medium was removed and clarified by centrifuging at 4000 **g** for 30 minutes at 4 °C. Supernatant was collected and aliquoted into 1 mL, 5 mL or 10 mL aliquots and stored at -80 °C. Clarified supernatants were used for the infection of Vero E6 cells. Typical yields from virus propagation experiments were between 1 x $10^4$ – 1 x $10^5$ immunofluorescent units (IU)/mL.

#### 2.2.6.2 TULV titre determination by neutral red uptake plaque assay

Neutral red uptake plaque assays were performed in duplicate in 6-well plates seeded with 5 x $10^5$ cells/well. TULV was serially diluted into 450 µL SFM to generate $10^{-1}$-$10^{-4}$ dilutions. As described in 2.2.6.1, 200 µL of these dilutions were used to infect Vero E6 monolayers. After TULV adsorption, cells were overlaid with 2% media diluted 1:1 with 4 % agarose (w/v). The agarose overlay prevented TULV migration through the media and ensured released virus would only infect cells neighbouring the previously infected cell. After agarose overlay had set, 2 mL of 2 % media was added on top of overlay to prevent agarose overlay from drying out. Cells were incubated for 7 days in a humidified incubator at 37 °C with 5 % $CO_2$. After 7 days, the liquid overlay was removed and replaced with 3 mL of 2 % media diluted 1:1 with 4 % agarose (w/v) supplemented with 0.16 mM neutral red. After agarose overlay had set, 2 mL of 2 % media was added on top of overlay and cells were incubated for 3 days in a humidified incubator at 37 °C with 5 % $CO_2$. Cells were examined each day for the formation of plaques. TULV is not cytopathic therefore neutral red uptake was used as a measure of cell viability to define

plaques. Neutral red uptake assay utilises the ability of cells to incorporate and bind the dye. Neutral red dye binds to anionic sites in lysosomes through electrostatic hydrophobic bonds. Damaged and dead cells do not retain the neutral red dye and therefore can be distinguished from viable cells through a lack of red colour (Borenfreund and Puerner, 1985).

$$virus\ titre\ \left(\frac{pfu}{mL}\right) = \frac{number\ of\ plaques}{dilution\ factor\ x\ volume\ (mL)}$$

#### 2.2.6.3 TULV titre determination by immunofluorescent assay

Immunofluorescent assays were performed in triplicate in 96-well plates seeded with 5 x $10^4$ cells/well. TULV was serially diluted into 350 µL SFM to generate $10^{-1}$-$10^{-5}$ dilutions. 100 µL of these dilutions were used to infect Vero E6 cells as described in 2.2.6.1. After TULV adsorption, 100 µL of 2 % media was added. Cells were incubated for 72 hours in a humidified incubator at 37 °C with 5 % $CO_2$ and then fixed and permeabilised in ice-cold methanol at -20 °C for at least 1 hour. Cells were washed in 1 X PBS before staining by immunofluorescence. Cells were blocked in 1 X PBS with 5 % bovine serum albumin (BSA) for 1 hour before probing with 50 µL anti-SEOV NP primary antibody diluted 1:2000 in 1 X PBS with 1 % BSA for 1 hour. Cells were washed three times 1 X PBS before probing with 50 µL donkey anti-sheep Alexa Fluor 488 secondary antibody diluted 1:1000. Cells were washed three times in 1 X PBS. Cells were imaged using the Incucyte Zoom instrument (Essen Bioscience) using a 10x objective lens. The Incucyte ZOOM software was used to calculate the number of infected cells per well by extrapolating an average value from three fluorescent images of each well. As infectious often form several foci within a cell which can each be counted separately, quantified virus is represented as an immunofluorescent unit per mL (IU/mL).

$$virus\ titre\ \left(\frac{IU}{mL}\right) = \frac{average\ fluorescent\ count\ per\ well}{dilution\ factor\ x\ volume\ (mL)}$$

#### 2.2.6.4 TULV sample collection

TULV-infected cell cultures were harvested for analysis by scraping cell monolayers into supernatant after desired infection time and collected into 2 mL cryovial and stored at -80 °C until analysis and for freeze-thaw lysis. For analysis, cell cultures were incubated at 37 °C for 1 hour. Sample volumes were adjusted to 2 mL to account for evaporation and centrifuged at 13,000 **g** for 10 minutes at 4 °C to pellet cells. Supernatants were analysed for viral RNA by qRT-PCR or infectious virus particles by immunofluorescent assay. Cell pellets were resuspended in 25 µL 1 x PBS and analysed for TULV NP by western blot.

#### 2.2.6.5 Routine Mycoplasma Testing

TULV stocks were routinely tested and confirmed to be mycoplasma free using MycoAlert™ (Lonza). Mycoplasma testing was carried out by Carsten Zothner.

#### 2.2.6.6 Metabolic labelling viral RNA using 5-Ethynyl Uridine

TULV viral RNA was labelled using the Click-iT® RNA Imaging kit (Invitrogen) utilising click chemistry. 5-ethynyl uridine (5-EU) is an alkyne-modified nucleoside is incorporated into nascent RNA and is detected utilising chemoselective ligation (“click” reaction) with an azide-conjugated Alexa Fluor. In order to specifically label only viral RNA, actinomycin D (ActD) was used to inhibit transcription of host cell DNA into RNA. ActD binds to DNA and inhibits RNA synthesis by interfering with elongation of RNA chains by the RNA polymerase (Sobell, 1985). TULV RNA is generated from an RNA template and so neither TULV replication nor transcription is inhibited by ActD. Vero E6 cells were seeded onto coverslips as described in 2.2.4.1 and infected with TULV MOI 0.1 as described in 2.2.6.1. One hour before the specified time-point cell culture medium was replaced with 250 µL 2 % media supplemented with 10 µg/mL actinomycin D and incubated for 1 hour at 37 °C. A 250 µL aliquot of 2% media supplemented with 2 mM 5-EU and incubated for 3 hours in an humidified incubator at 37 °C with 5 % $CO_2$. Media was removed and replaced with 1 mL 4 % formaldehyde (BHD Chemicals) diluted in 1 X PBS and incubated at room temperature for 20 minutes. To

check incorporation of 5-EU, mock Vero E6 cells were treated with 5-EU without addition of ActD. Cells were permeabilised by incubating with 0.5 % Triton X-100 diluted in 1 X PBS for 15 minutes. The click-iT® reaction cocktail was prepared according to the manufacturers' instructions and contained 1 X Click-iT® RNA reaction buffer, 4 mM copper (II) sulphate, 1 X Alexa Fluor® 594 azide and 20 mg/mL Click-iT® reaction buffer additive. The click-iT® reaction cocktail was added immediately to each well and incubated for 30 minutes at room temperature with protection from light. Reaction cocktail was removed and each well washed with 1 mL click-iT® reaction rinse buffer before washing with 1 mL PBS. Nuclei were stained by incubating with 300 nM 4',6-Diamidino-2-Phenylindole (DAPI) (Thermo Fisher) for 3 minutes at room temperature. Coverslips were mounted onto microscope slides using antifade mounting medium (Vectashield).

### 2.2.7 Immunofluorescence

#### 2.2.7.1 Seeding persistently infected Vero E6 cells

Persistent infections were carried out in Vero E6 cells seeded into 75 $cm^2$ flasks as described in section 2.2.6.1. Infections were carried out for 7 or 30 days post infection. At 24 hours before desired time point, cells were trypsinised and pelleted by centrifuging at 500 **g** for 5 minutes at 4 °C. The cell culture supernatant was retained. TULV infected Vero E6 cells were seeded onto coverslips at 5 x $10^5$ cells per well along with 1:100 dilution of infected cell culture supernatant diluted in 2 % media. Cells were incubated overnight in an humidified incubator at 37 °C with 5 % $CO_2$ and fixed in 4 % formaldehyde for 20 minutes and permeabilised in ice-cold methanol for at least 1 hour.

#### 2.2.7.2 Indirect immunofluorescence

Immunofluorescence experiments were used to visualise the subcellular localisation of host cell proteins and TULV NP. Vero E6 cells were grown on coverslips as described in 2.2.4.1 and 2.2.7.1. Media was removed from cells before fixation in 4 % formaldehyde diluted in 1 X PBS for 20 minutes at room temperature. Cells were permeabilised in ice-cold methanol for at least 1 hour. For long-term storage, cells were stored in 100% methanol in 12-well plates

at -20 °C wrapped in parafilm to prevent evaporation. Permeabilised cells were washed twice in 1 X PBS, then blocked in 5 % (w/v) BSA for 1 hour.

After blocking, cells were incubated with 50 µL of primary antibody diluted to the appropriate concentration for 2 hours at room temperature or overnight at 4 °C. Incubations were carried out in humidified chambers on droplets on parafilm. Cells were washed three times in 1 X PBS and incubated with 200 µL fluorescently labelled antibody for 1 hour at room temperature with shaking, protected from light. Cells were washed three times in 1 x PBS before incubating with 300 nM DAPI for 3-5 minutes at room temperature. Cells were washed four times in 1 X PBS and once in distilled water before mounting onto glass microscope slides using hard-set antifade mounting media (Vectashield). Slides were cured for 15 minutes at room temperature and stored at 4 °C overnight until visualisation, protected from light.

Concentrations of antibodies used are provided in Table 9 and Table 10.

#### 2.2.7.3 RNA fluorescent in-situ hybridisation (FISH)

IF was carried out as described in section 2.2.7.2 with reduced incubation times. Cells were blocked for 30 minutes and antibody incubations were carried out 1 hour each. After IF, cells were fixed in 4 % formaldehyde for 20 minutes. Formaldehyde was replaced with 1 x PBS treated with 0.1% diethylpyrocarbonate (DEPC) and cells were stored at 4 °C overnight, protected from light.

FISH probes were reconstituted to 12.5 mM in RNase free 1 X TE buffer (10 mM Tris-HCl, 1 mM EDTA pH 8.0 (G Biosciences) diluted in UltraPure™ DNase/RNase-Free Distilled water (Thermo Fisher Scientific) and stored at -20 °C. Probes were warmed to room temperature and thoroughly mixed. For each coverslip, 1 µL probe stock was used per 100 µL hybridisation buffer (Stellaris® RNA FISH hybridisation buffer (2B Scientific) diluted with deionised formamide (Severn Biotech LTD) in 9:1 ratio).

Cells were incubated in wash buffer A (Stellaris® RNA FISH wash buffer A diluted with deionized formamide and UltraPure™ DNase/RNase-Free Distilled water in a 2:7:1 ratio) for 5 minutes at room temperature. 100 µL hybridisation buffer with probes was dispensed into a droplet onto parafilm in a humidified chamber. Coverslips were incubated cell-side down onto probe mix for 4 hours at 37 °C, protected from light. Cells were incubated in 1 mL wash buffer A for 30 minutes at 37 °C, protected from light and then incubated in 1 mL wash buffer A with 300 nM DAPI for 5 minutes at room temperature. Buffer was removed and cells were incubated in 1 mL wash buffer B (Stellaris® RNA Fish wash buffer B) for 5 minutes before mounting onto glass microscope slides using hard-set antifade mounting media (Vectashield). Slides were cured for 45 minutes at room temperature, protected from light, and imaged within 24 hours.

### 2.2.8 RNA Generation and Quantification

#### 2.2.8.1 Viral RNA isolation

TULV RNA was isolated from 140 µL of clarified freeze-thawed cell culture supernatant using the QIAamp® viral RNA mini kit (Qiagen) following the manufacturers' instructions. Viral RNA was eluted with 50 µL nuclease-free water and stored at -80 °C.

#### 2.2.8.2 Reverse transcriptase PCR (RT-PCR)

TULV S segment cDNA was transcribed from viral RNA isolated in 2.2.8.1 using the ProtoScript® II First Strand cDNA synthesis kit (NEB) where 5 µL TULV RNA was mixed with 5 mM oligo $d(T)_{23}$ VN (V: A, G or C and N: A, G, C or T), 1 X ProtoScript® II Reaction Mix and 1 X ProtoScript® II Enzyme Mix in a total reaction volume of 20 µL. Reaction mix was incubated at 42 °C for 1 hour followed by incubating at 80 °C for 5 minutes to inactivate enzymes. cDNA generated from RT-PCR was amplified through PCR as described in 2.2.1.1 using TULV S Segment primers shown in Table 7.

#### 2.2.8.3 In-vitro RNA transcription

TULV S Segment cDNA isolated in 2.2.8.2 was sub-cloned into pcDNA3.1 (+) vector under the control of the T7 RNA polymerase. pcDNA3.1 (+) + TULV S Segment was linearized using Xho1, located immediately after the S segment ORF stop codon, following conditions described in 2.2.1.3. RNA was transcribed using the MEGAscript® T7 Transcription Kit following the manufacturer's instructions; 1.5 µg linear DNA was mixed with 2 µL of ATP, GTP CTP and UTP stock solutions (75 mM), 2µl of T7 enzyme mix, 1 X reaction buffer in a total volume of 20 µL. Reaction mix was incubated at 37 °C for 3 hours followed by incubation with 2 U of TURBO DNase for 15 minutes at 37 °C. RNA was purified using the RNeasy Mini Kit (Qiagen) following the manufacturer's instructions and eluted in 30 µL RNase-free water and stored at -80 °C. Quantity of RNA was assessed through spectrophotometry using a NanoDrop 1000.

#### 2.2.8.4 RNA agarose gel electrophoresis

Separation of RNA fragments for assessment of RNA was carried out using 1 % agarose 1 X 4-morpholinepropanesulfonic acid (MOPS) gel (1 % agarose, 1 X MOPS, 4.7 % formaldehyde) with SYBR Safe stain diluted 1:10,000. RNA samples were diluted 1:10 and mixed with 1 X RNA gel loading dye (New England Biolabs) and denatured by incubating at 65 °C for 5-10 minutes. before loading onto gel. Ambion Millenium™ RNA marker (Thermo Fisher) was used as a molecular maker. Electrophoresis was carried out at 80 V for

80 minutes in 1 X MOPS buffer. Blue light transillumination was used for the visualisation of RNA. Purity of RNA was assessed by examining RNA MOPS gel for contaminating bands or smears.

#### 2.2.8.5 Generating RNA standards

RNA generated through *in-vitro* transcription was adjusted to 138.2 ng/µL RNA by diluting in RNase-free water and quantifying using a NanoDrop 1000. 138.2 ng/µL RNA is equivalent to $10^{12}$ copies of TULV S segment RNA per 5 µL based on the molecular weight of the TULV S segment RNA ORF. RNA was further diluted to $10^8$, $10^6$, $10^4$, $10^2$ genome copies/5 µL to generate a standard curve.

#### 2.2.8.6 Quantitative reverse transcriptase real-time PCR (qRT-PCR)

Quantitative reverse transcriptase real-time PCR was carried out in accordance with previously described methods with adaptions to the GoTaq® 1-step RT-qPCR kit (Promega) (Kramski et al., 2007). Briefly, each reaction contained 1 X reaction buffer, 625 nM forward primer, 625 nM reverse primer, 1 X RT enzyme mix, mixed thoroughly. To each reaction mix 5 µL sample RNA or standard RNA was added to each well. The PCR thermal cycle used was as follows: 37 °C for 10 minutes, 95 °C for 10 minutes, 45 cycles of 95 °C for 10 seconds, 60 °C for 40 seconds and 72 °C for 30 seconds. Cycle threshold (Ct) values were measured at the end of each cycling step. For each qRT-PCR run the following standards of TULV S segment RNA were used: $10^8$, $10^6$, $10^4$, $10^2$ genome copies/5 µL. These standards were used to generate a standard curve from which sample relative genome copies per mL could be calculated.

| Primer Name | Primer Sequence 5' – 3' |
|---|---|
| TULV S Forward | GCCGACCCRGATGATGTTAA |
| TULV S Reverse | CAAGYTGYCTCTTGAADTCTGCCA |

**Table 8 Primer sequences used for qRT-PCR.**

### 2.2.9 Analysis of Protein Expression

#### 2.2.9.1 Preparation of cell lysates

Mammalian cells were collected by centrifugation at 20,000 **g** for 10 minutes at 4 °C and resuspended in 50 µL PBS. Bacterial protein samples were collected in 50 µL at each stage of purification for analysis by SDS-PAGE. An equal volume of 2 X loading buffer (4 X NuPage loading buffer (Thermo Fisher Scientific), 10 X DTT, water) was added and samples heated to 95 °C for at least 5 minutes. Samples were centrifuged at 10,000 **g** for 10 minutes at room temperature to pellet debris.

#### 2.2.9.2 SDS polyacrylamide gel electrophoresis (SDS-PAGE)

Cell lysates were analysed by SDS-PAGE. SDS-PAGE gels were made with either 10%, 12 % or 15 % resolving gels (10/12/15 % bis-acrylamide, 750 mM Tris-HCl pH 8.8, 0.1% (w/v) SDS, 0.1% (w/v) ammonium persulphate (APS), 0.001% (v/v) tetramethylethylenediamine (TEMED)) and a 5 % stacking gel (5 % bis-acrylamide, 126 mM Tris-HCl pH 6.8, 0.1% (w/v) SDS, 0.1% (w/v) APS, 0.001% (v/v) TEMED). Electrophoresis was carried out in a 1 X SDS running buffer (25 mM Tris, 192 mM glycine, 0.1 % (w/v) SDS) at 180 V for 60-90 minutes. Colour Prestained Protein Standard, Broad Range (11–245 kDa) (New England Biolabs) molecular weight marker was used. Proteins were visualised by colloidal Coomassie stain or by western blot.

#### 2.2.9.3 Colloidal Coomassie stain

SDS-PAGE gels to be visualised by colloidal Coomassie were fixed in gel fixative solution (40 % ethanol, 10 % acetic acid) for at least 30 minutes at room temperature and replaced with colloidal Coomassie stain (20 % methanol, 8 % (w/v) ammonium sulphate, 1.6 % phosphoric acid, 0.08 % coomassie brilliant blue G250). Gels were stained overnight at room temperature with rocking before being de-stained with 1 % acetic acid overnight with rocking.

#### 2.2.9.4 Western blot analysis

Protein samples separated by SDS-PAGE were transferred to an Immobilon-FL polyvinylidene difluoride (PVDF) membrane (Merck Millipore) using the

Trans-Blot semi-dry cell (Bio-Rad) in Towbin buffer (25 mM Tris, 192 mM glycine, 20 % (v/v) methanol) at 20 V for 90-120 minutes. Membranes were blocked for 1 hour at room temperature in Odyssey® Blocking buffer (LI-COR) diluted 1:1 in PBS. Membranes were probed with primary antibody (see Table 9) in Odyssey® Blocking buffer diluted 1:4 in PBS for 1-16 hours. Membranes were washed 3-5 times in PBS before probing with secondary antibodies (Table 8) in Odyssey® Blocking buffer diluted 1:4 in PBS for 1 hour. Membranes were washed 3-5 times in PBS before drying. Protein samples were visualised using the Odyssey Sa imaging system (LI-COR).

### 2.2.10 Immunoprecipitations

#### 2.2.10.1 Preparation of cell lysates

Three T175 $cm^3$ flasks of Vero E6 cells were infected at MOI 0.1. Cells were harvested by centrifugation at 4000 **g** for 10 minutes at 4 °C. The cell pellet was washed in ice-cold PBS and pellet collected by centrifugation at 4000 **g** for 10 minutes at 4 °C. Cells were lysed by resuspending in ice-cold 100 µL RIPA buffer (50 mM Tris-HCl pH 8.0, 150 mM NaCl, 1 % NP-40 alternative, 0.1 % sodium dodecyl sulphate, 1 X protease-inhibitor cocktail EDTA-free (Roche)) and incubated on ice for 30 minutes. Lysate was clarified by centrifugation at 1000 **g** for 10 minutes at 4 °C.

#### 2.2.10.2 Dynabead™ IPs

Immunoprecipitation (IP) was carried out using the Dynabead™ Protein G immunoprecipitation kit (Thermo Fisher Scientific). A 50 µL aliquot of Dynabeads™ were bound to TULV NP antisera by incubating with NP antisera diluted 1:200 in PBS with rotation for 1 hour at 4 °C. Beads were immobilised using a magnet and antisera removed. Beads were washed once in 200 µL PBS before adding clarified lysate and incubating overnight at 4 °C with rotation. Beads were immobilised using a magnet and cell lysate removed before washing three times in 200 µL Washing Buffer. 2 X protein loading buffer (see section 2.2.9.1) was added directly to beads in an equal volume before heating to 95 °C for 5 minutes. Samples were centrifuged at 10,000 **g** for 5 minutes to pellet beads before loading onto a 12-15 % SDS-PAGE gel. Immunoprecipitated protein was analysed by western blot.

### 2.2.11 Inhibitor Studies

#### 2.2.11.1 Inhibition of intermediate filaments

Vero E6 were infected with TULV at MOI of 0.5 as previously described in sections 2.2.6.1 and 2.2.7.1 in a 6-well plate. Infected cells were harvested for immunofluorescent at 72 hours p. i. and harvested for immunofluorescent and qRT-RT PCR analysis at 30 days p. i. (see sections 2.2.7.2 and 2.2.8.6). Prior to harvesting, cells were treated with the following cytoskeletal inhibitors; 10 µM cytochalasin D (CytD) for 60 minutes, 17 µM nocodazole (NOC) for 60 minutes, 100 µM erythro-9-(2-hydroxy-3-nonyl)adenine (EHNA) for 24 hours, and 400 nM okadaic acid (OA) for 30, 60 or 90 minutes. Infected Vero E6 cells treated with OA were also recovered by removing inhibitor and incubating overnight with fresh media before harvesting. Mock treatments were carried out using an equal volume of solvent (dimethyl sulfoxide (DMSO)/ethanol).

### 2.2.12 Microscopy

#### 2.2.12.1 Laser scanning confocal microscopy

Laser scanning confocal imaging was carried out using the Zeiss LSM700 confocal microscope using the 40X/1.3 Oil DIC Plan Apochromat, M27 objective lens with the diode 405 nm, 488 nm, 55 nm and 639 nm lasers or the Zeiss LSM880 + Airyscan upright confocal microscope using the Plan-Apochromat 40X/1.4 Oil DIC objective lens with the diode 405 nm, argon 488 nm, DPSS 561 nm and HeNe 633 nm lasers. Image analysis was carried out in Fiji is just ImageJ (FIJI).

#### 2.2.12.2 Widefield fluorescence deconvolution microscopy

Widefield fluorescence deconvolution microscopy was carried out using the Delta Vision widefield deconvolution microscope using the 100X/1.4 Oil Iris, U Plan Apo objective lens with the following filter sets; DAPI, FITC, TRITC and Cy5. Image analysis was carried out in FIJI.

## 2.3 List of Antibodies

### 2.3.1 Primary antibodies used in western blot and/or IF

| Target | Vendor | WB Dilution | IF Dilution | Incubation Temperature |
|---|---|---|---|---|
| SEOV NP Goat | In house | 1:2000 | 1:2000 | 4 °C overnight RT 1-2 hours |
| GAPDH (GT239) Mouse | GeneTex | 1:10 000 | N/A | 4 °C overnight RT 1-2 hours |
| Rab5 #2143 Rabbit | NEB | 1:200 | 1:50 | 4 °C overnight RT 1-2 hours |
| Rab7 (D95F2) XP® Rabbit | NEB | 1:200 | 1:50 | 4 °C overnight RT 1-2 hours |
| Rab11 (D4F5) XP® Rabbit | NEB | 1:200 | 1:50 | 4 °C overnight RT 1-2 hours |
| LAMP1 (D2D11) XP® Rabbit | NEB | 1:200 | 1:50 | 4 °C overnight RT 1-2 hours |
| DCP1a (56-Y) Mouse | Santa Cruz | 1:200 | 1:50 | 4 °C overnight RT 1-2 hours |
| TIA-1 (G-3) Mouse | Santa Cruz | 1:200 | 1:50 | 4 °C overnight RT 1-2 hours |
| Golgi Marker (AE6) Mouse | Santa Cruz | 1:200 | 1:50 | 4 °C overnight RT 1-2 hours |
| Concanavalin A, Alexa Fluor 594 | Thermo Fisher | 1:200 | 1:30 | 4 °C overnight RT 1-2 hours |
| Vimentin (D21H3) XP® Rabbit | NEB | 1:200 | 1:50 | 4 °C overnight RT 1-2 hours |
| β-Tubulin (9F3) Rabbit | NEB | 1:200 | 1:100 | 4 °C overnight RT 1-2 hours |
| β-Actin (D6A8) Rabbit | NEB | 1:200 | 1:100 | 4 °C overnight RT 1-2 hours |
| Caspase-3 (D3R6Y) Rabbit | NEB | 1:200 | n/a | 4 °C overnight RT 1-2 hours |
| Cleaved Caspase-3 (Asp175) (5A1E) Rabbit | NEB | 1:200 | 1:50 | 4 °C overnight RT 1-2 hours |
| Cleaved PARP (Asp214) (D64E10) XP® Rabbit | NEB | 1:200 | n/a | 4 °C overnight RT 1-2 hours |

**Table 9 Primary antibodies used for western blot or immunofluorescence.**

### 2.3.2 Secondary antibodies used in western blot and/or IF

| Target | Vendor | WB Dilution | IF Dilution | Incubation Temperature |
|---|---|---|---|---|
| IRDye680RD donkey anti-mouse IgG (H+L) | LI-COR | 1:10,000 | n/a | RT 1-2 hours |
| IRDye800CW donkey anti-goat IgG (H+L) | LI-COR | 1:10,000 | n/a | RT 1-2 hours |
| IRDye800CW donkey anti-rabbit IgG (H+L) | LI-COR | 1:10,000 | n/a | RT 1-2 hours |
| Donkey anti-Goat IgG (H+L), Alexa Fluor 488 | Thermo Fisher | n/a | 1:500-1:1000 | RT 1-2 hours |
| Donkey anti-Rabbit IgG (H+L), Alexa Fluor 647 | Thermo Fisher | n/a | 1:500 | RT 1-2 hours |
| Donkey anti-Mouse IgG (H+L), Alexa Fluor 647 | Thermo Fisher | n/a | 1:500 | RT 1-2 hours |
| Donkey anti-Rabbit IgG (H+L), Alexa Fluor 555 | Thermo Fisher | n/a | 1:500 | RT 1-2 hours |
| Donkey anti-Mouse IgG (H+L), Alexa Fluor 555 | Thermo Fisher | n/a | 1:500 | RT 1-2 hours |

**Table 10 Secondary antibodies used for western blot or immunofluorescence.**

# Chapter 3 : Development of molecular tools for the detection and quantification of orthohantaviruses

## 3.1 Chapter Introduction

This chapter describes the development of molecular tools used to explore the lifecycle of the orthohantaviruses in cultured cells. As funding for this project was obtained by agreement to produce an anti-SEOV NP antibody for Public Health England (PHE), recombinant SEOV NP was bacterially expressed, purified and used as an antigen for the generation of both antibodies and non-antibody binding proteins known as Affimers. Generated antibody was provided to PHE to be used in the surveillance of SEOV in the UK. In addition, a reliable, fast and high-throughput virus titration assay was developed to permit the quantification of infectious virus as well as modifying an existing qRT-PCR assay to allow numerical quantitation of viral RNA.

## 3.2 Results: Generation of polyclonal anti-SEOV NP antibody

### 3.2.1 Introduction to bacterial-expression of recombinant proteins

Antigen for the generation of a polyclonal anti-SEOV NP antibody was produced utilising an *E. coli* based expression system. Modified pET vectors (pET28a(+) and pET11a) containing viral sequences were transformed into expression competent *E. coli* strains, and used for the inducible expression of recombinant viral protein. These vectors contain the promotor region for bacteriophage T7 RNA polymerase paired with the *lac* operator, which together control the T7 RNA polymerase-driven transcription of the target gene (i.e. SEOV NP). The *lac* repressor (*lacI*) represses transcription of the T7 RNA polymerase at the *lac* UV5 promoter and at the *lac* operator to block transcription by any basally produced T7 RNA polymerase in the *E. coli* expression host (Dubendorf and Studier, 1991).

Expression vectors were transformed into BL21 (DE3) *E. coli* expression strains which carry the T7 RNA polymerase ORF under control of the *lac* UV5

promotor. In the presence of an inducer (e.g. IPTG), T7 RNA polymerase is produced and begins expression of the target gene. The BL21 (DE3) expression strains also contain the pLysS plasmid which encodes a T7 lysozyme which acts to reduce basal expression of the T7 RNA polymerase (Studier and Moffatt, 1986).

SEOV NP ORF was cloned into the pET28a(+) expression vector in-frame with a 6x His SUMO tag fused to its amino terminus. The 6x His-tag allows purification of the expressed protein via metal affinity chromatography (nickel or cobalt). The small ubiquitin-related modifier (SUMO) fusion tag has been documented to increase the solubility of bacterially expressed proteins. The 6x His-SUMO tag is removed using the Ulp1 protease which recognises the tertiary structure of SUMO and cleaves at the C-terminus of the molecule (Mossessova and Lima, 2000; Malakhov et al., 2004).

Other systems can be utilised for recombinant protein expression such as yeast, baculovirus-infected insect cells and mammalian cells. Advantages of *E. coli* recombinant protein expression over these options include fast growth, high density cultures, inexpensive growth medias and easy transformation. However, there are several disadvantages of using a prokaryotic system to produce eukaryotic proteins. One issue can be the lack of proper folding leading to the formation of insoluble protein aggregates known as inclusion bodies. Some proteins require specific post-translational modifications such as N- and O-linked glycosylation, phosphorylation, methylation and ubiquitination. However, *E. coli* expression systems do not support all required modifications and lack of proper post-translational modification could lead to protein aggregation and misfolding (Cain et al., 2014). Another issue is the codon usage bias where if the gene to be expressed uses codons rare in *E. coli*, only suboptimal expression will be achieved. However, this issue can be overcome, in part, by the use of codon optimisation and by using *E. coli* strains such as Rosetta or Codon Plus, which encode for some of these rare codons.

### 3.2.2 Expression and purification of SEOV NP

#### 3.2.2.1 Cloning SEOV NP ORF into the pET28a(+) expression vector

A cDNA representing the full-length SEOV NP ORF optimised for bacterial expression was synthesized and subsequently used to generate a second

truncated cDNA named SEOV $NP_{core}$ comprising NP residues 111-399 using PCR. Full-length SEOV NP and truncated SEOV $NP_{core}$ cDNA fragments were isolated by agarose gel electrophoresis and ligated into an empty pET28(+) SUMO vector to generate pET28a(+) SUMO + SEOV NP and pET28a(+) SUMO + SEOV $NP_{core}$ expression plasmids, designed to express either full-length or SEOV $NP_{core}$ with their respective N-termini fused to 6x His, and SUMO tags (Figure 15).

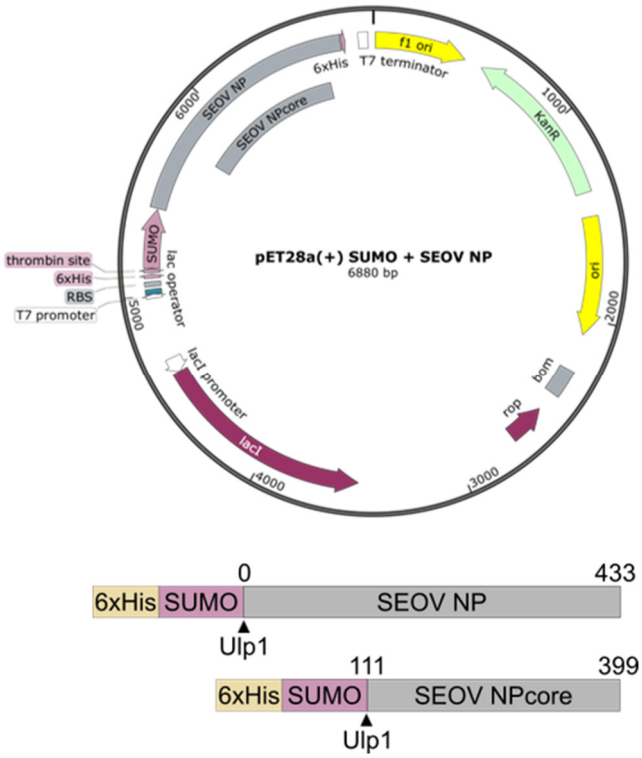


**Figure 15 Plasmid map of the pET28a(+) SUMO + SEOV NP constructs.** Schematic of SEOV NP constructs displaying Ulp1 cleavage site after the 6x His SUMO tag at the N-terminus of the SEOV NP construct. Plasmid map was generated using SnapGene® software.

### 3.2.2.2 Optimising expression of SEOV NP

To identify the optimal expression conditions for recombinant full-length SEOV NP and the truncated SEOV $NP_{core}$ derivative, first, the most suitable expression host strain was chosen by examining expression of soluble or insoluble protein in a variety of *E. coli* strains, namely Gold, Star, Rosetta, Rosetta 2 and Codon Plus (Table 3; Figure 16A, Figure 17A). His-SUMO SEOV NP was predicted to have a mass of ~61.2 kDa (Figure 16) and a band of this size was clearly detected in the insoluble fraction from all strains, although only a minor amount of soluble protein with this mass was

expressed. Rosetta cells were identified as producing the most full-length protein (Figure 16A) and were carried forward to test if alteration of IPTG concentration or temperature could further increase the quantity of soluble protein (Figure 16B and C). IPTG concentrations of 0.5 mM, 0.4 mM, 0.3 mM, 0.2 mM and 0.1 mM were tested at both 18 °C and 12 °C, with 12 °C and induction with 0.2 mM IPTG concentration resulting in optimal soluble protein expression.

The SEOV $NP_{core}$ expression construct was designed to express a truncated version of NP in which the N- and C- terminal oligomerisation domains were removed to leave the compact globular core domain (residues 111-399), based on the previously described crystal structure of the Sin Nombre virus and Andes virus NP (Guo et al., 2016). Optimal conditions for the expression of His-SUMO SEOV $NP_{core}$ were determined as described for the full length SEOV NP construct, above, with the expected mass of the His-SUMO SEOV $NP_{core}$ protein predicted to be ~45.4 kDa. Codon Plus cells were identified as producing the largest quantity of His-SUMO SEOV $NP_{core}$ (Figure 17A), and optimal conditions for expression was identified to be incubation at 18 °C with expression induced with 0.5 mM IPTG (Figure 17B, C).

In addition to optimising conditions for expression, nickel-affinity purification of His-SUMO SEOV NP and His-SUMO SEOV $NP_{core}$ was carried out using small-scale cultures. Following SDS-PAGE analysis of eluted proteins, the abundance of His-SUMO SEOV $NP_{core}$ was significantly higher than that of full-length His-SUMO SEOV NP. Based on this, only large-scale purification of SEOV $NP_{core}$ was attempted. Other methods used to produce larger amounts of soluble protein included using a glutathione S-transferase (GST) solubility tag and expression using autoinduction (data not shown).

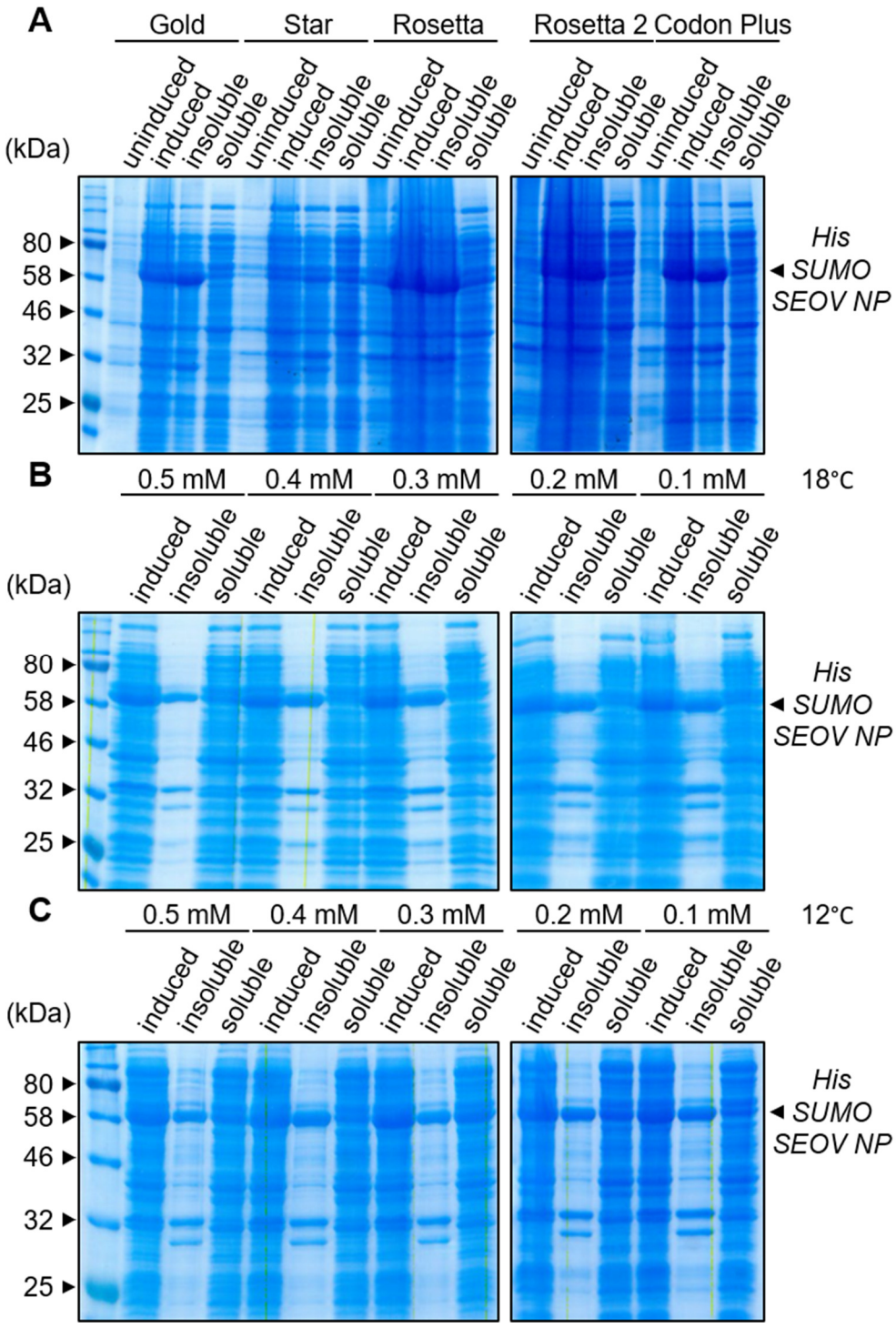


**Figure 16 Expression profile of His-SUMO SEOV NP.**

Analysis of His-SUMO SEOV NP expression by SDS-PAGE followed by colloidal Coomassie staining A) Expression of His-SUMO SEOV NP in various *E. coli* strains, B) Expression of His-SUMO SEOV NP in Rosetta cells at 18 °C with altered IPTG concentration C) Expression of His-SUMO SEOV NP in Rosetta cells at 12 °C with altered IPTG concentration. His-SUMO SEOV NP has a predicted mass of ~61.2 kDa

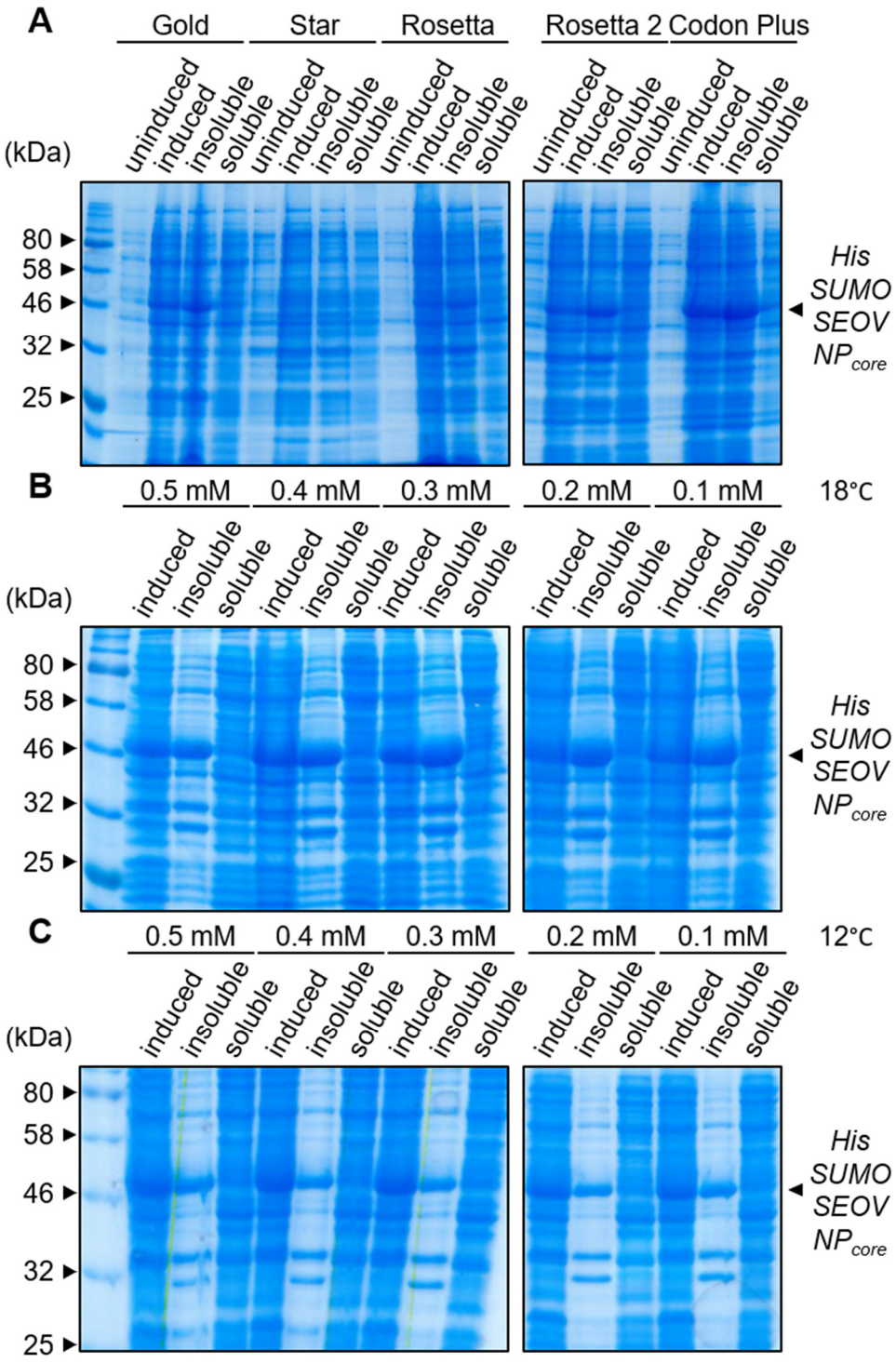


**Figure 17 Expression profile of His-SUMO SEOV $NP_{core}$.**

Analysis of His-SUMO SEOV $NP_{core}$ expression by SDS-PAGE followed by colloidal Coomassie staining A) Expression of His-SUMO SEOV $NP_{core}$ in various *E. coli* strains, B) Expression of His-SUMO SEOV $NP_{core}$ in Codon Plus cells at 18 °C with altered IPTG concentration C) Expression of His-SUMO SEOV $NP_{core}$ in Codon Plus cells at 12 °C with altered IPTG concentration. His-SUMO SEOV $NP_{core}$ has a predicted mass of ~45.4 kDa

### 3.2.2.3 Metal affinity purification of soluble SEOV $NP_{core}$

His-SUMO SEOV $NP_{core}$ was expressed by overnight induction with 0.5 mM IPTG at 18 °C in Codon Plus cells. Soluble recombinant protein was harvested from cell lysates by applying the clarified supernatant fraction containing soluble His-SUMO SEOV $NP_{core}$ to nickel sepharose (6% agarose) resin, with binding for 1 hour at 4 °C. Contaminating proteins were removed by washing with increasing concentrations of imidazole wash buffer (Figure 18A) and subsequently the His-SUMO SEOV $NP_{core}$ was eluted using elution buffer containing imidazole at 500 mM (Figure 18B). All fractions were analysed by SDS-PAGE and visualised using colloidal Coomassie (Figure 18). Fractions containing His-SUMO SEOV $NP_{core}$ were pooled and incubated with Ulp1 protease overnight to cleave the His-SUMO tag from SEOV $NP_{core}$. Cleaved SEOV $NP_{core}$ has a predicted molecular weight of 32.3 kDa (ProtParam) and was further purified away from any uncleaved His-SUMO SEOV $NP_{core}$, His-SUMO and the Ulp1 protease (containing a His-tag) by a second round of nickel affinity chromatography, with pooled fractions diluted 1:10 in low imidazole buffer prior to applying to nickel sepharose resin (Figure 18C). Alternatively, dialysis of fractions as a means to reduce imidazole concentration was tested prior to application to nickel sepharose resin, but was found to cause precipitation of the protein. Flow-through, containing purified SEOV $NP_{core}$, was collected (Figure 18C) and concentrated to 0.82 mg/mL using a spin concentrator. This resulted in the isolation of >85% pure SEOV $NP_{core}$, as analysed by densitometry of Coomassie-stained proteins following SDS-PAGE (Figure 18D). Purification of soluble SEOV $NP_{core}$ was also attempted using batch purification on loose nickel agarose resin (7.5% agarose), however, SEOV $NP_{core}$ was found to bind directly to agarose resin and with only a small percentage of protein recovered during elution (data not shown). Other methods of purifying SEOV $NP_{core}$ were attempted including cationic exchange chromatography and size exclusion chromatography, but these were judged to be unsuccessful (data not shown).

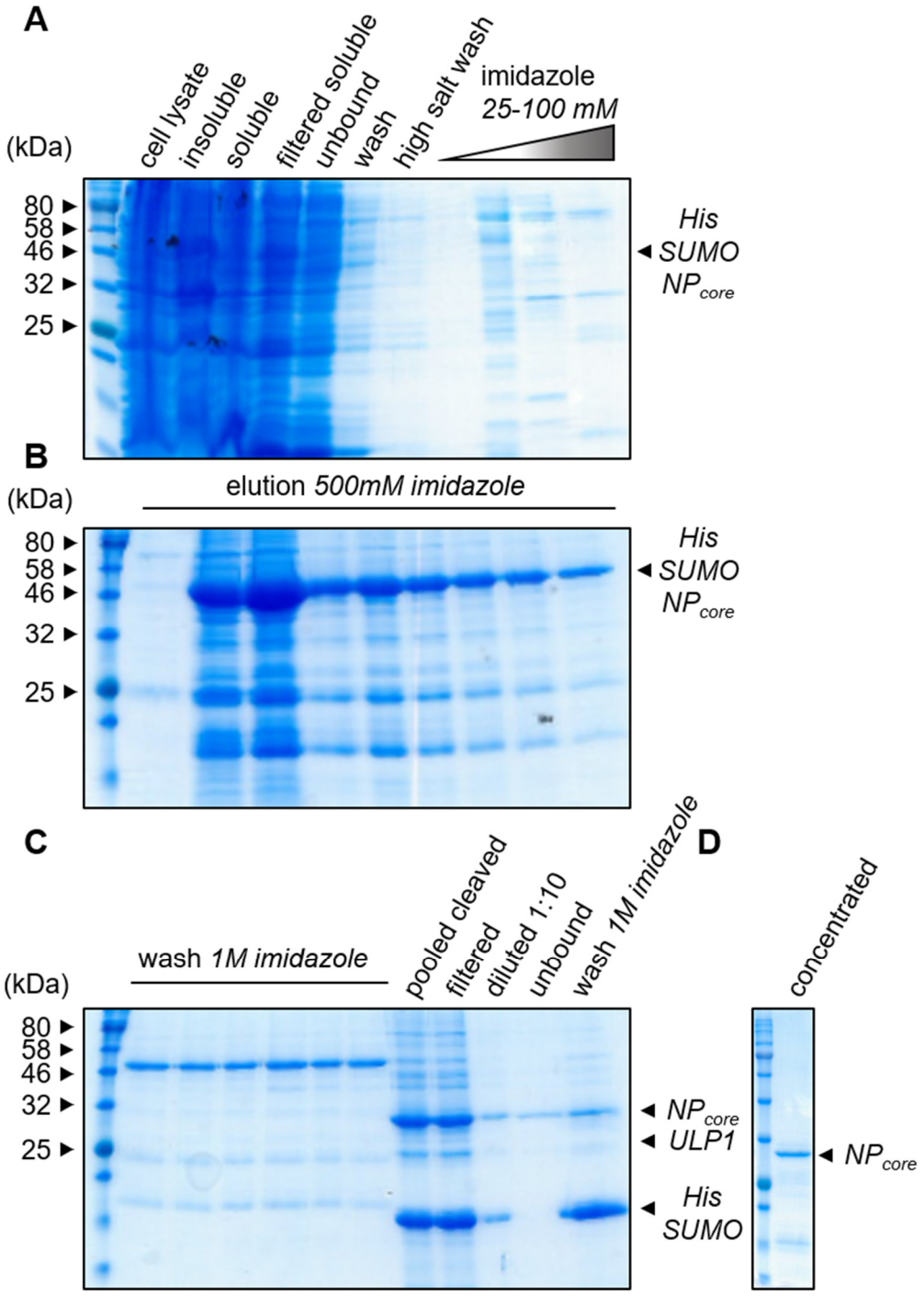


**Figure 18 Purification of soluble His-SUMO SEOV $NP_{core}$ using nickel affinity chromatography.**

Analysis of purified His-SUMO SEOV $NP_{core}$ expression by SDS-PAGE followed by colloidal Coomassie staining A-B) Purification of His-SUMO SEOV $NP_{core}$ using nickel affinity chromatography and subsequent cleavage of the His-SUMO tag using Ulp1 protease. C) A second nickel affinity chromatography step was used to remove 6x His tagged contaminants, which resulted in >85 % purification of SEOV $NP_{core}$. D) Purified SEOV $NP_{core}$ was concentrated to >0.82 mg/mL.

#### 3.2.2.4 Metal affinity purification of insoluble SEOV $NP_{core}$

As the majority of His-SUMO SEOV $NP_{core}$ was found to be insoluble, an alternative purification protocol was adopted in which recombinant protein was purified from inclusion bodies. Inclusion bodies were isolated by centrifugation of the cell lysate and collection of the insoluble pellet (Figure 19A, left panel). His-SUMO SEOV $NP_{core}$ was solubilised by dissolving in 8M GuHCl and applied to loose nickel agarose resin in batch. His-SUMO SEOV $NP_{core}$ was refolded on the column in combination with removal of contaminating proteins by washing in increasing imidazole and decreasing GuHCl wash buffers (Figure 19A, right panel). To remove the His-SUMO tag, refolded His-SUMO SEOV $NP_{core}$ bound to resin was incubated with Ulp1 protease overnight and SEOV $NP_{core}$ was eluted by washing in low imidazole wash buffer. Any protein remaining bound to resin was removed using high concentration imidazole wash buffers and resin was examined for remaining protein (Figure 19B). As seen in Figure 19B, a high amount of cleaved SEOV $NP_{core}$ remained bound to the resin. Fractions containing purified SEOV $NP_{core}$, were pooled and concentrated to 0.8 mg/mL using a spin concentrator. This resulted in the isolation of >85% pure SEOV $NP_{core}$ determined by densitometry (Figure 19C).

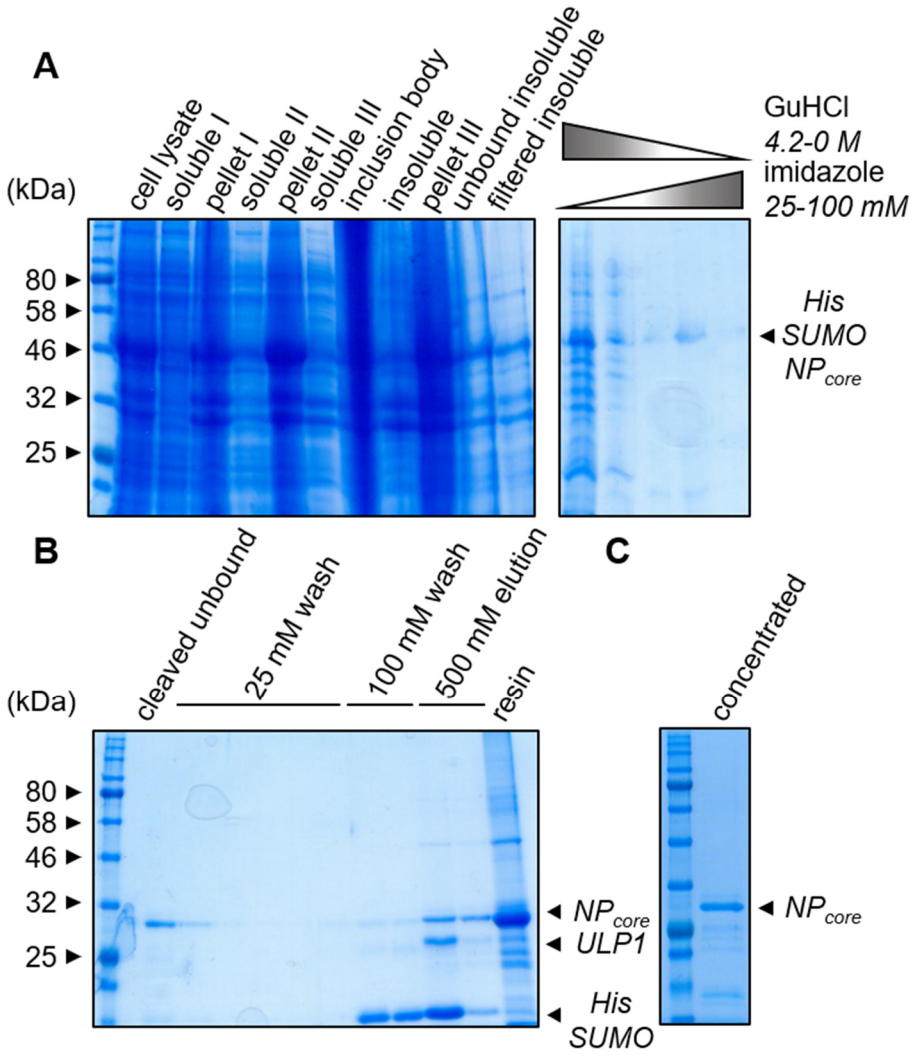


**Figure 19 Purification of insoluble His-SUMO SEOV $NP_{core}$ using nickel affinity chromatography.**

Analysis of insoluble His-SUMO SEOV $NP_{core}$ purification by SDS-PAGE followed by colloidal Coomassie staining A) Insoluble His-SUMO SEOV $NP_{core}$ was isolated by harvesting inclusion bodies from bacterial cells, followed by solubilisation using GuHCl and purification using nickel affinity chromatography and on-column refolding. B) Cleavage of the His-SUMO tag using Ulp1 protease on column overnight followed elution from the column to produce >85 % pure SEOV $NP_{core}$. C) Purified SEOV $NP_{core}$ was concentrated to >0.8 mg/mL.

### 3.2.3 Anti-SEOV NP antibody

#### 3.2.3.1 Generating polyclonal anti-SEOV NP antisera

Prior to immunization of animals for antibody production, the identity of purified SEOV $NP_{core}$ protein was confirmed using mass spectrometry (Figure 20). Subsequently, 1.25 mg of purified soluble SEOV $NP_{core}$ was used as antigen to produce a polyclonal antisera against SEOV $NP_{core}$ utilizing an immunization regimen comprising five spaced injections of a goat with SEOV $NP_{core}$. Goat sera was collected one week after each booster immunisation, and samples were tested for the ability to specifically recognise SEOV NP.

#### 3.2.3.2 Validating the anti-SEOV NP antisera

Anti-SEOV NP polyclonal antisera was validated by measuring reactivity against a panel of various antigens, namely, purified SEOV $NP_{core}$ (Figure 21A), transfected recombinant TULV NP (Figure 21B), TULV-infected Vero E6 cell lysates (Figure 21C) and by laser-scanning confocal microscopy (LSCM) utilising immunofluorescence of TULV infected monolayers (Figure 21D). The generated antibody displayed good reactivity to SEOV NP and also showed cross-reactivity to TULV NP, which belongs a different phylogroup of the orthohantaviruses (Chapter One, Figure 2, Chapter Three Figure 21).


**Figure 20 Mass spectrometry analysis of purified SEOV NP$_{core}$.**

Mass spectrometry was carried out on purified His-SUMO SEOV NP$_{core}$ resolved by SDS-PAGE and stained using InstantBlue™. The SEOV NP$_{core}$ band was excised from the gel prior to analysis by mass spectrometry. The start and end of the SEOV NP$_{core}$ sequences is highlighted and reads covering this region are shown.

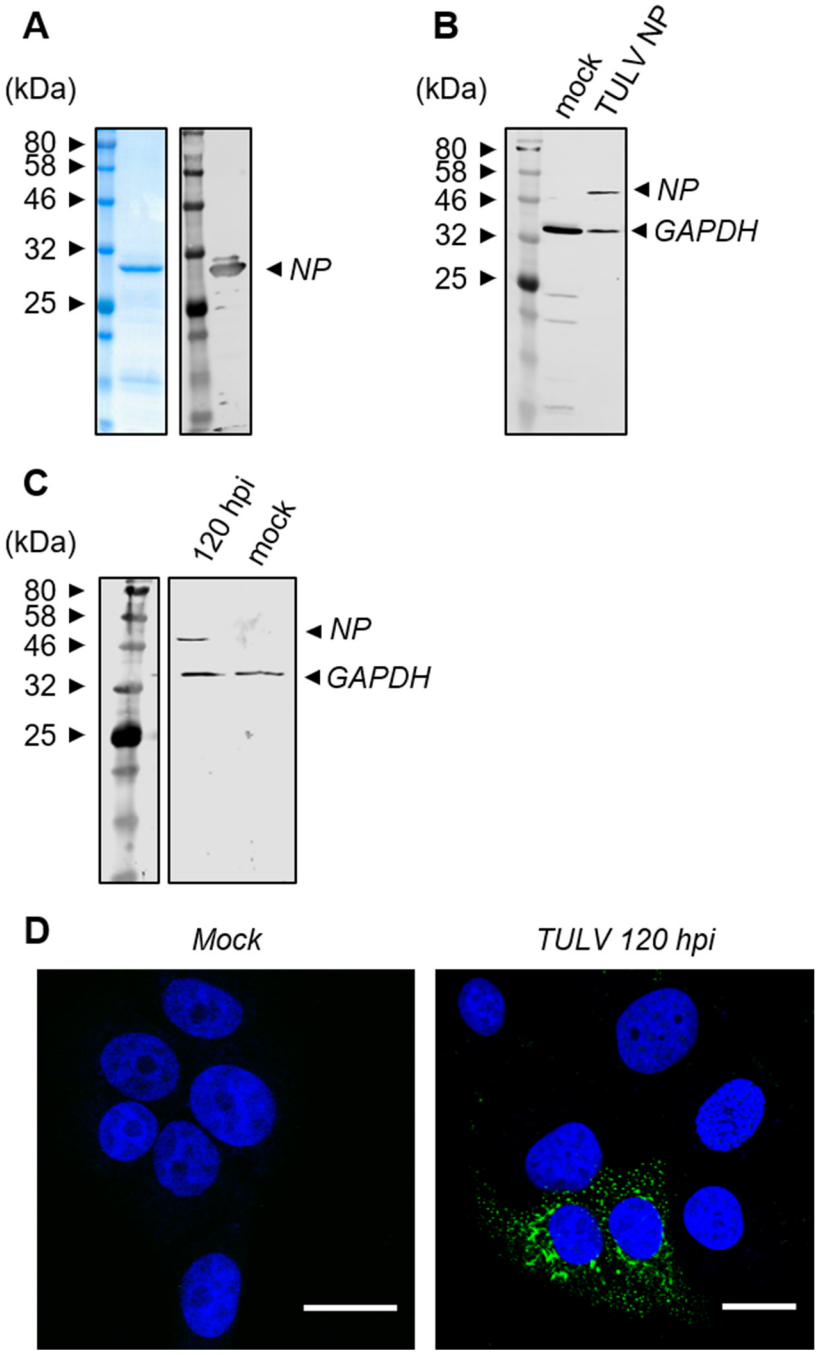


**Figure 21 Validation of anti-SEOV NP polyclonal antibody.**

A) Analysis of purified SEOV $NP_{core}$ by SDS-PAGE followed by colloidal Coomassie staining and western blotting. B) Western blot analysis of transfected TULV NP cell lysates. C) Western blot analysis of TULV infected cell lysates at 120 hpi. D) Indirect immunofluorescence of TULV infected monolayers at 120 hpi. The white bar represents 30 µm.

### 3.2.4 Section summary

This section describes the generation of SEOV NP antisera, to be used to facilitate the analysis of orthohantavirus infection kinetics, to identify the location of NP within infected cells, and for the precipitation of NP from infected cells to study its binding partners. Expression and purification of recombinant SEOV NP from *E. coli* cells was optimised and SEOV NP was used as an antigen in the production of a polyclonal antibody. This antibody proved to be cross-reactive against *E. coli* expressed SEOV $NP_{core}$ in addition to mammalian cell transfected TULV NP and TULV NP in TULV-infected cell lysates and in fixed Vero E6 monolayers.

## 3.3 Results: Generation of an anti-SEOV NP Affimer

### 3.3.1 Introduction to Affimers

Polyclonal antibodies can be generated against specific antigens and used as an important tool in research and diagnostic assays and for immunotherapies. In the context of this current study, the production of virus-specific antibodies can be used as a measure of virus multiplication, to identify the location of viral components within infected cells, and as a means to purify virus components with a view to studying virus-host interactions. Polyclonal antibodies can be generated by inoculation of various animals (e.g. sheep, rabbits, goats, chickens) with antigen over a specified time frame. Serum is collected after each antigen booster inoculation. Antibodies have several disadvantages including batch-to-batch variability, reliance on animals for production and expense.

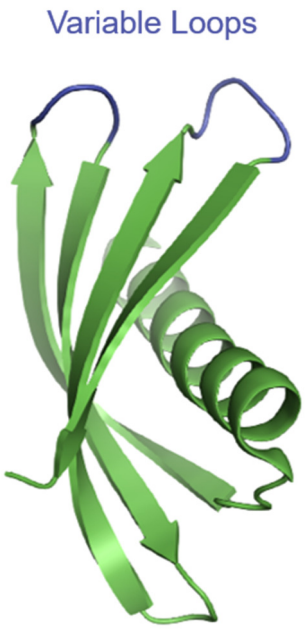


**Figure 22 Crystal structure of an Affimer protein.**

Crystal structure of the Affimer protein (PDB: 4N6T) (Tiede et al., 2014). Variable loops are highlighted in blue. Structure was generated using PyMOL.

Affimers are non-antibody binding scaffold proteins with two randomised peptide loops which can be selected for to provide high-specificity binding against the target antigen (Figure 22). Affimers display several advantages over traditional antibodies: Their production does not involve the use of animals, but instead relies on expression from cloned cDNAs, most commonly using a prokaryote-based expression system. Affimers are relatively small and tend to be both highly soluble, and highly thermostable, allowing heat purification and no requirement for cold storage. Affimers can also be biotin- or fluorescently-labelled by utilising an incorporated C-terminal cysteine residue, proving especially useful for super-resolution microscopy (Tiede et al., 2014; Tiede et al., 2017).

### 3.3.2 Expression and purification of SEOV $NP_{core}$ + BAP tag

#### 3.3.2.1 Cloning BAP tag into the pET28a(+) SUMO + SEOV $NP_{core}$ expression vector

To act as bait for the selection of Affimers by phage display the SEOV $NP_{core}$ was first appended to a BAP tag at its C-terminus, which allows attachment to a streptavidin coated binding matrix. The SEOV $NP_{core}$ insert was amplified through PCR using the SEOV $NP_{core}$ BAP tag Forward and SEOV $NP_{core}$ BAP tag Reverse primers allowing addition of a *Hind* III site upstream of the Xho1 site with the generated fragmented ligated into the pET28a(+) SUMO vector. The BAP tag sequence was synthesised by PCR amplification with Forward and Reverse BAP tag primers containing *Hind* III and *Xho* I restriction sites and the subsequently generated fragment was ligated into *Hind* III and *Xho* I sites within the previously described plasmid pET28a(+) SUMO + SEOV $NP_{core}$ (Figure 23)

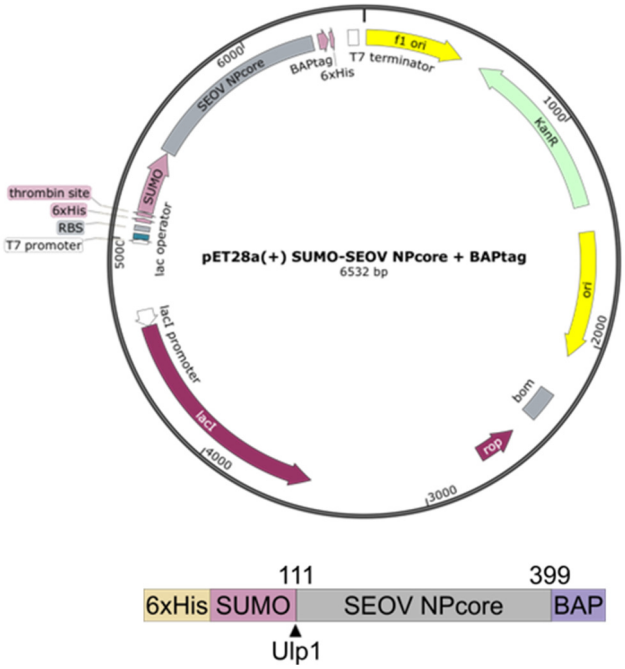


**Figure 23 Plasmid map of the pET28a(+) SUMO + SEOV $NP_{core}$ + BAP tag constructs.**

Schematic of SEOV $NP_{core}$ + BAP tag construct displaying Ulp1 cleavage site after the 6xHis SUMO tag at the N-terminus of the SEOV $NP_{core}$ construct and displaying the BAP tag at the C-terminus of SEOV $NP_{core}$. Plasmid map was generated using SnapGene® software.

### 3.3.2.2 Metal affinity purification of soluble SEOV $NP_{core}$ + BAP tag

Expression of His-SUMO SEOV $NP_{core}$ + BAP tag was performed using the same optimized expression conditions identified for His-SUMO SEOV $NP_{core}$, namely overnight expression at 18°C in Codon Plus cells, with induction using 0.5 mM IPTG. Soluble protein was isolated from lysed cells by centrifugation and the clarified soluble protein from the supernatant was bound to nickel resin for 1 hour at 4 °C. Contaminating proteins were removed by washing with increasing concentrations of imidazole wash buffer (Figure 24A), and the His-SUMO SEOV $NP_{core}$ + BAP tag was eluted using an elution buffers containing 1M imidazole (Figure 24B). Eluted protein was pooled and incubated with Ulp1 protease overnight to remove the His-SUMO tag, after which cleaved protein was diluted 1:10 in low imidazole buffer and re-applied to a pre-packed nickel resin column. Flow-through containing purified SEOV $NP_{core}$ + BAP tag was collected (Figure 24C) and concentrated to 0.93 mg/mL using a spin concentrator, and all fractions were analysed by SDS-PAGE, followed by colloidal Coomassie staining. The predicted masses of cleaved

and un-cleaved forms of the His SUMO + SEOV $NP_{core}$ + BAP tag were predicted to be 47.9 kDa and 34.8 kDa, respectively, and bands corresponding to these products were identified in the appropriate lanes (Figure 9C and D). Purified and concentrated SEOV $NP_{core}$ + BAP tag protein showed good reactivity for streptavidin (essential for phage display panning) by western blot analysis using a streptavidin-conjugated antibody (Figure 24D).

### 3.3.3 Phage display selection of unique Affimers binders

#### 3.3.3.1 Phage display panning for Affimers

Affimers which displayed unique SEOV NP binding were selected using three consecutive rounds of phage display. A phage-display library generated from the phagemid vector pBSTG1-Adh (Tiede et al., 2014), containing an Affimer library of $10^{10}$ random binding sequences, were incubated with the target protein SEOV $NP_{core}$ + BAP tag. Phages which do not bind to the target protein were washed away, whereas binders were eluted using glycine (pH 2.2) and triethylamine. Each consecutive panning round was carried out utilising a different binding matrix to reduce off-target binding. The first round used streptavidin coated strips, the second round used streptavidin dynabeads and the third round used NeutrAvidin coated strips. Selected phage were transformed into ER2738 cells and plated onto LB-agar, with each resulting colony representing an individual phage binder. Individual binders were tested for specific binding by phage ELISA against either a blank well or a well bound with SEOV $NP_{core}$ + BAP tag. Binding was confirmed by probing using an anti-Fd-bacteriophage-HRP in conjugation with 3,3′,5,5′-Tetramethylbenzidine (TMB) SeraminBlau®, which produces a soluble blue product which can be quantified by measuring absorbance at 620nm, with comparison between target and negative control wells. A total of 10 phages were identified that displayed greater binding to the target protein than the negative control wells, although sequence analysis revealed 9 of the 10 binders comprised the same binding sequences (Figure 25A). The two unique Affimer sequences and resulting proteins are referred to as Affimer 2 and Affimer 16, and their sequences are displayed in Figure 25B.

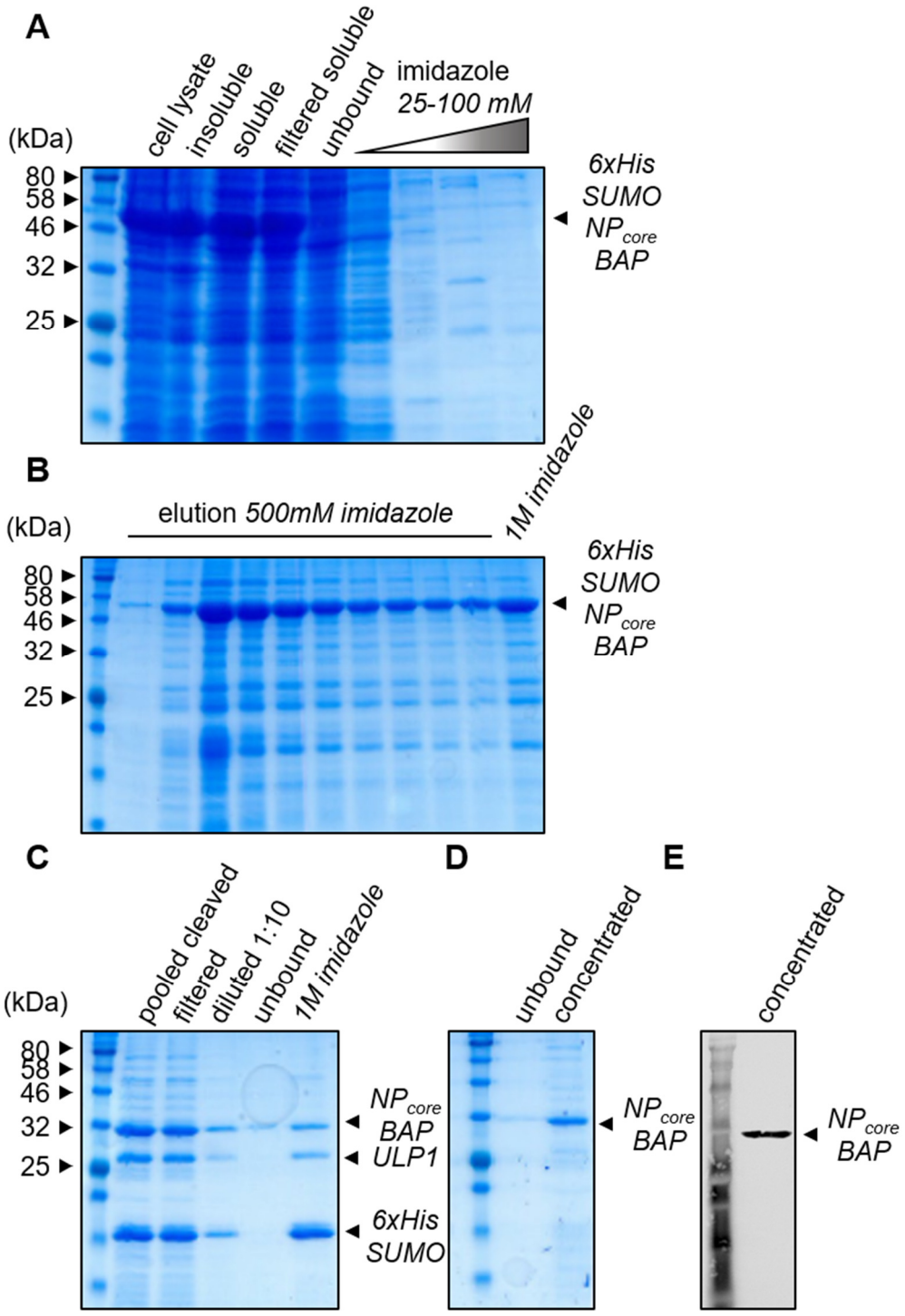


**Figure 24 Purification of SEOV $NP_{core}$ + BAP tag using nickel affinity chromatography.**

Analysis of His-SUMO SEOV $NP_{core}$ + Bap tag purification by SDS-PAGE followed by colloidal Coomassie staining (A-D) or western blot E) Purification of His SUMO + SEOV $NP_{core}$ + BAP tag using nickel affinity chromatography and subsequent cleavage of the His SUMO tag using Ulp1 protease followed by a second nickel affinity chromatography step to remove his tagged contaminants E) Purified SEOV $NP_{core}$ + BAP tag was tested for streptavidin reactivity by western blot

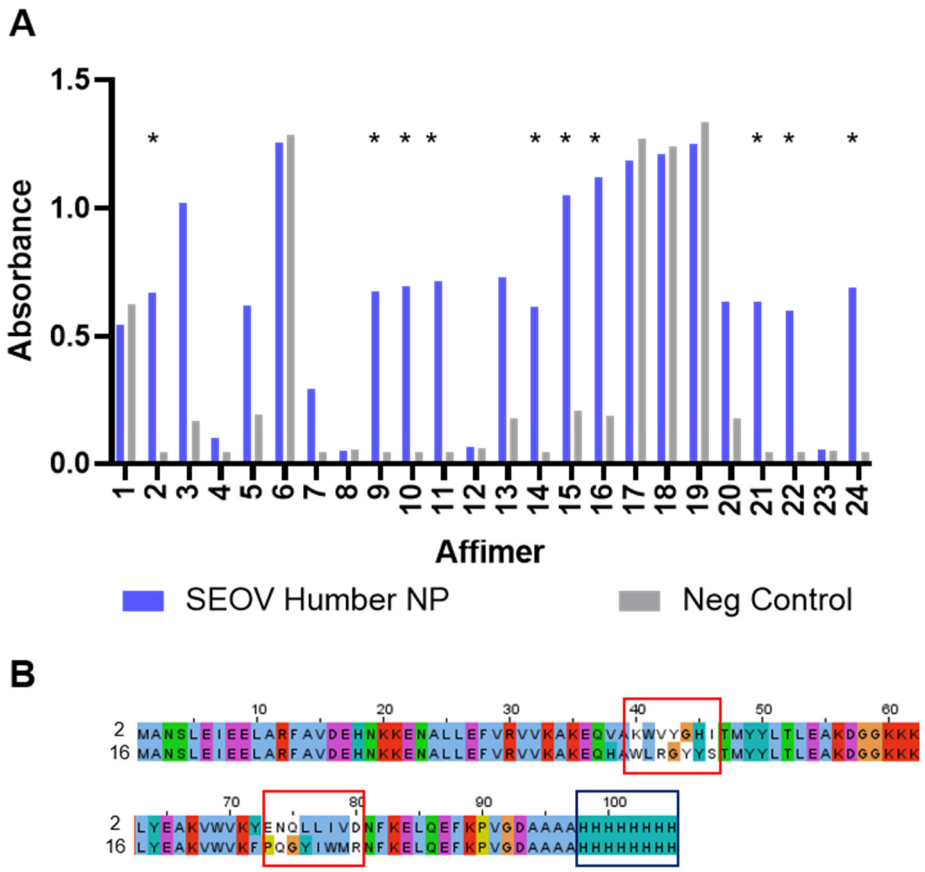


**Figure 25 Phage ELISA of 24 randomly picked Affimers after 3 consecutive panning rounds to select for SEOV Humber NP binders.**

A) Affimers were tested against target SEOV Humber NP and a negative control (no target). Unique binders showing more binding to target wells compared to negative wells are highlighted with an asterix. B) Pairwise sequence alignment of uniquely binding Affimers, boxes denote the variable loops (red) and 8 X His-tag (blue). Sequences were aligned in ClustalW and the schematic generated using Jalview software.

### 3.3.4 Expression and purification of Affimers

#### 3.3.4.1 Cloning Affimer into the pET11a expression vector

The cDNAs encoding Affimers were synthesised by PCR amplification of Affimer sequences within a phagemid vector using Affimer Forward and Reverse primers (Table 7) and resulting fragments were sub-cloned into an empty pET11a vector utilising the *Not* I and *Nhe* I restriction sites. The pET11a + Affimer vector resulted in the expression of a C-terminal 8x His tagged Affimer (Figure 26).

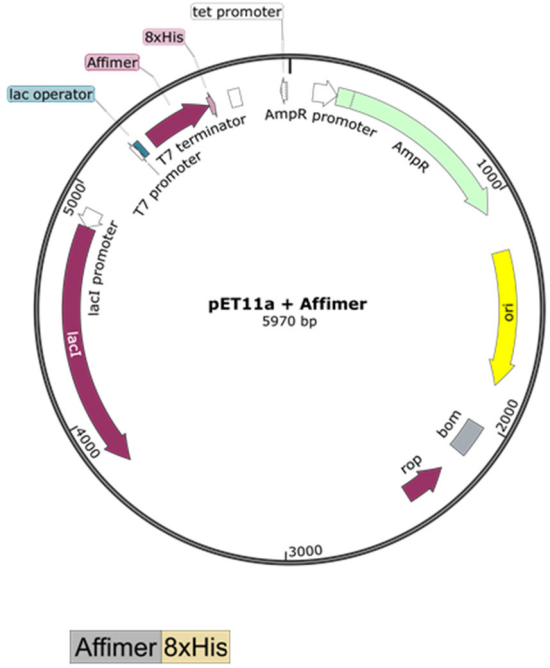


**Figure 26 Plasmid map of the pET11a Affimer construct.**.
Schematic of Affimer construct with 8x His tag at the C-terminus. Plasmid map was generated using SnapGene® software

#### 3.3.4.2 Batch purification of soluble Affimers

Expression of Affimer 2 and Affimer 16 was carried out using optimal expression conditions previously defined (Tiede et al., 2014). Briefly, pET11a + Affimer vectors were transformed into the Rosetta 2 *E. coli* expression strain and induced using 0.1 mM IPTG at 25 °C for 6 hours. Clarified supernatants containing soluble protein was applied to loose nickel resin and allowed to bind for 1 hour. Resin was washed in 20 mM imidazole wash buffer and Affimers were eluted using 300 mM elution buffer. Eluted Affimers were found to be 0.9 mg/mL (Affimer 2) and 2.1 mg/mL (Affimer 16). SDS-PAGE analysis followed by colloidal Coomassie staining identified purification of Affimers with

a predicted weight of 12.5 kDa (Figure 27). Further purification and analysis may be carried out at a later time.

### 3.3.5 Section summary

This section describes the expression and purification of a BAP-tagged recombinant SEOV NP from *E. coli* cells. This purified protein was used as a target in three successive Affimer panning rounds and two unique Affimer binders were selected for. The selected Affimers were sub-cloned into a pET expression vector and purified.

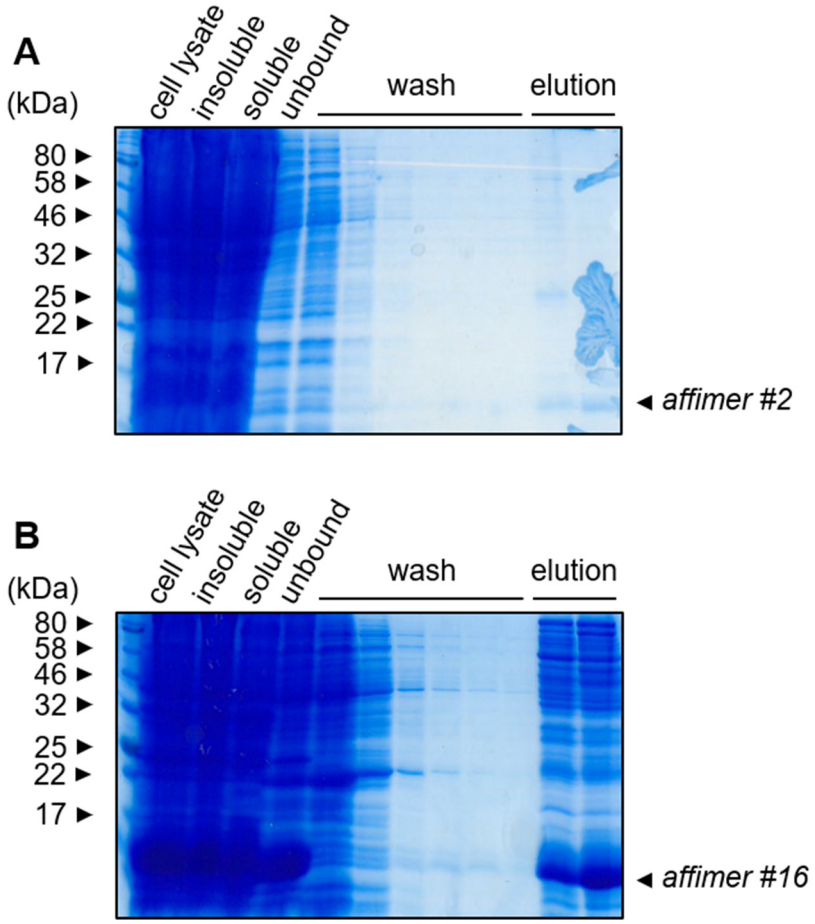


**Figure 27 Purification of Affimers using nickel affinity chromatography.** Purification of Affimer 2 (A) and Affimer 16 (B) through nickel affinity chromatography. Predicted weight of Affimers is ~12.5 kDa.

## 3.4 Results: Quantitative RT-PCR assay to detect TULV RNA

### 3.4.1 Introduction to quantitative RT-PCRs

Along with the measurement of virus infectivity, the ability to quantify the abundance of products of viral RNA replication is of fundamental importance in the study of virus multiplication cycles. Measurement of specific viral RNA can be achieved in real-time by quantifying reverse transcribed cDNA as a proxy, utilising a variety of fluorescent compounds in a PCR reaction to measure the amplification of DNA at the end of each thermal cycle, called qRT-PCR. This reporter can either be a fluorescent dye which is incorporated into double stranded DNA (e.g. SYBR Green; Life Technologies or BRYT Green; Promega) or by using a fluorescently- and quencher-labelled oligonucleotide primer specific to target (e.g. 6-Carboxyfluorescein (6-FAM) and Black Hole Quencher® (BHK) dye). The fluorescent oligonucleotide is quenched when unbound to DNA, but upon binding a fluorescent signal is emitted due to separation of the fluorescent label from the quencher.

A specific and sensitive diagnostic real-time reverse transcriptase PCR (RT PCR) has been developed allowing specific detection of different hantaviruses (Kramski et al., 2007). Here, this protocol was modified to allow the quantification of TULV genomes throughout the course of both single step cycles of virus multiplication, and also long-term infection time courses.

### 3.4.2 Comparison of laboratory TULV strain S segment ORF to wild type sequences

TULV was propagated in Vero E6 cells and total viral RNA isolated from cell culture medium using viral RNA mini kit (Qiagen). Sequencing of the S segment was carried out to confirm the identity of the orthohantavirus species used in all experiments. TULV S Segment ORF was amplified from viral RNA using S segment specific primers (Chapter Two, Table 7) and inserted into the pcDNA3.1 (+) vector. The S Segment ORF was sequenced using the T7 and T7Term primers (GeneWiz). NCBI nucleotide blast revealed the closest related sequence to be from Tula/Moravia/5302v/95 (GeneBank: Z69991). Sequence alignment revealed 1 amino acid substitution: R311A (Figure 28)

and 3 nucleotide substitutions: A24G, C931G, G932C (Figure 29). The R311A substitution is within a conserved region of the orthohantavirus sequence but is located within the NP ORF (Figure 30). The impact of this mutation is not known. As infectious virus particles have been isolated from this strain this mutation does not affect the essential functions of the NP.

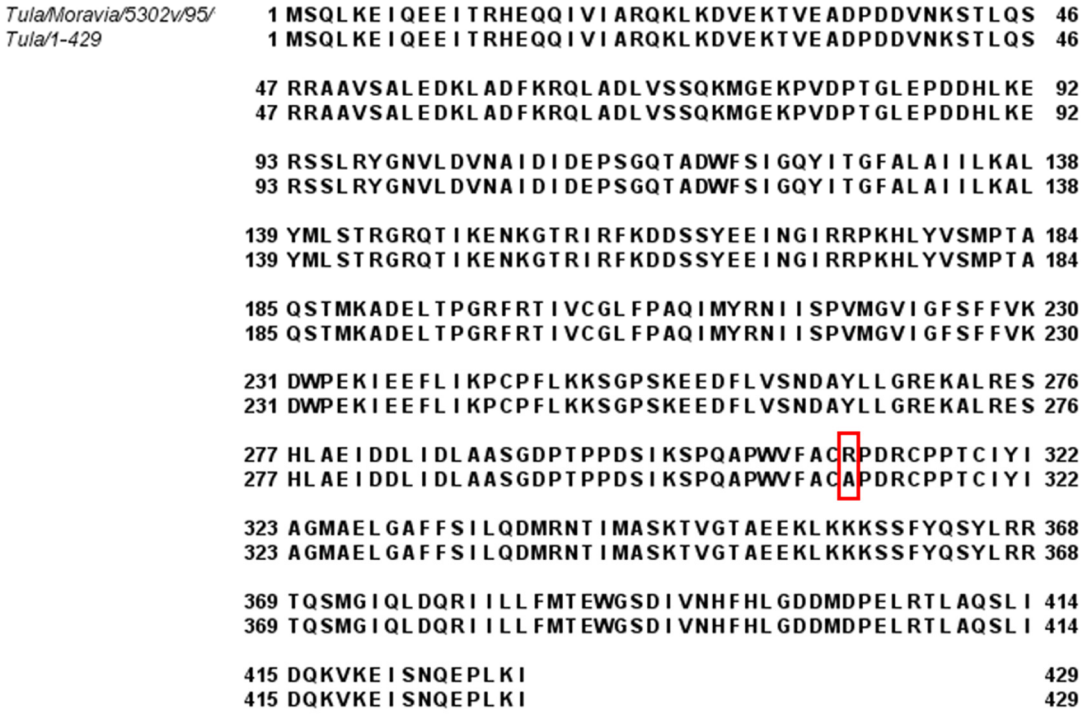


**Figure 28 Alignment of laboratory strain and wild type TULV S segment residues.**

Alignment was carried out using ClustalW, with the mismatched residues denoted with red box. Schematic generated using Jalview software.

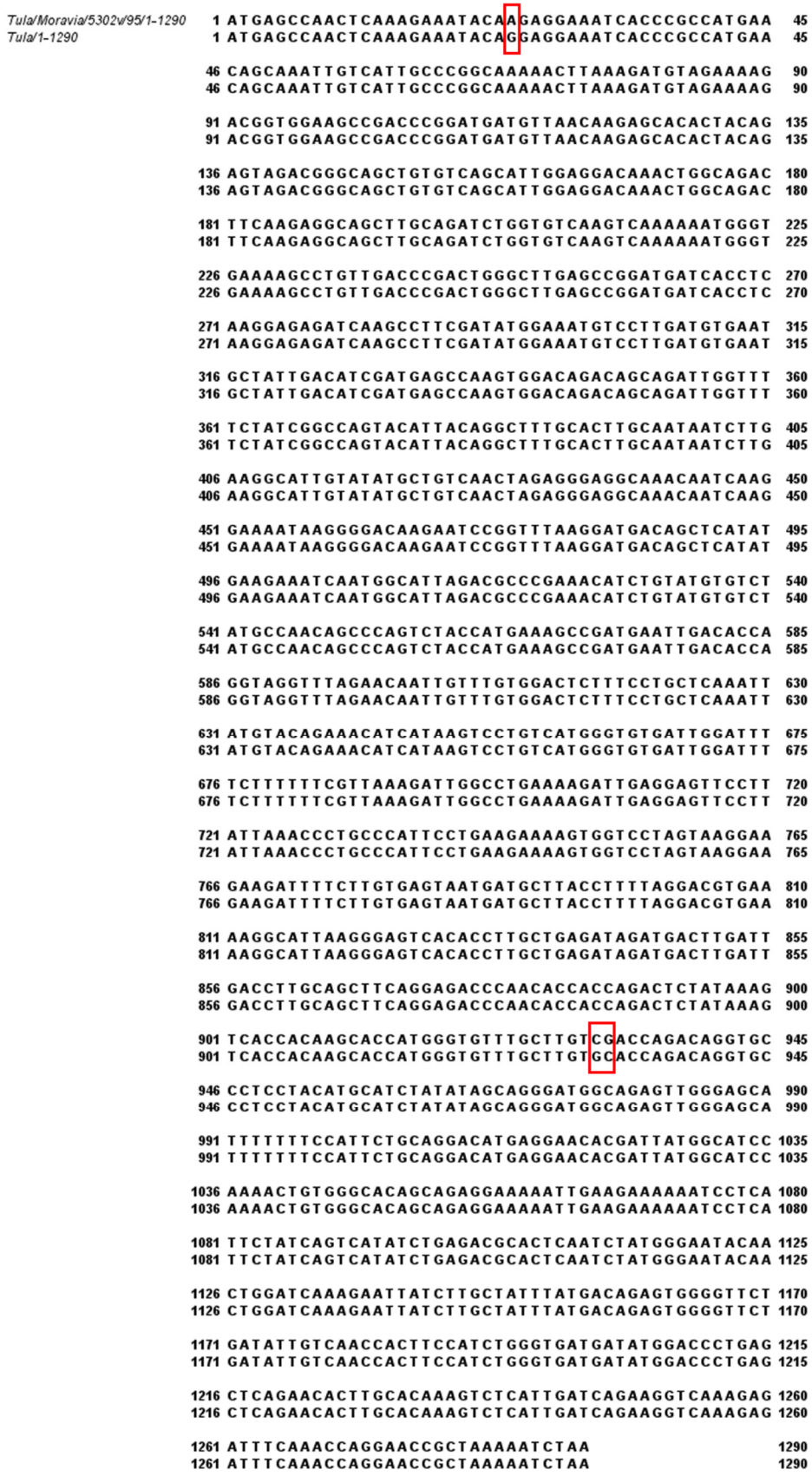


**Figure 29 Alignment of laboratory strain and wild type TULV S segment nucleotide sequences.**

Alignment was carried out using ClustalW, with the mismatched residues denoted with red box. Schematic generated using Jalview software

**Figure 30 Location of TULV NP R311A mutation within the orthohantavirus NP structure.**

HTNV nucleocapsid protein (PDB: 6I2N) residues 80-429. A311 is highlighted in red.

### 3.4.3 Generating a standard curve

TULV S segment RNA was *in vitro* transcribed from the pCDNA3.1 (+) + TULV S segment ORF vector utilising the upstream T7 RNA polymerase. Transcribed RNA was analysed by agarose gel electrophoresis to estimate purity (Figure 31). TULV S segment RNA was diluted to estimated $10^8$, $10^6$, $10^4$ and $10^2$ copies/5 µL and used in qRT-PCR to generate a standard curve with an Rsq value of >0.9 (Figure 32). These standards were used for every qRT-PCR analysis which allowed quantification of TULV in relative genomes copies/mL and comparison between separate qRT-PCR reactions. qRT-PCR were carried out based on previously described protocols (Kramski et al., 2007) adapted to using the BYRT green fluorescent dye as a way of quantification of genome copies. Briefly, 5 µL of sample RNA was mixed with qRT-PCR mix. Reverse transcriptase was carried out followed by 45 PCR cycles. Cycle threshold (Ct) values were obtained for each sample and genome copies per 5 µL sample were calculated from the standard curve. Genome copies per mL cell culture supernatant was calculated.

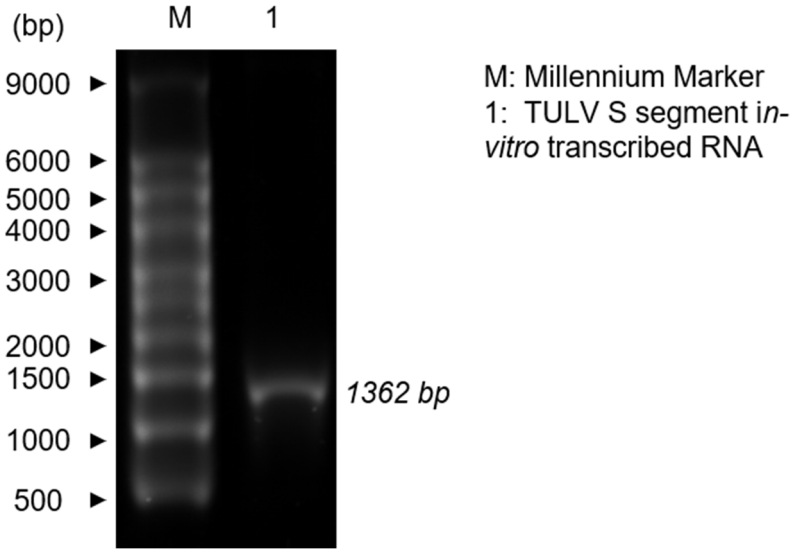


**Figure 31 Electrophoresis of *in vitro* transcribed TULV S segment RNA.** TULV S segment RNA generated through *in vitro* RNA transcription was analysed by agarose gel electrophoresis.

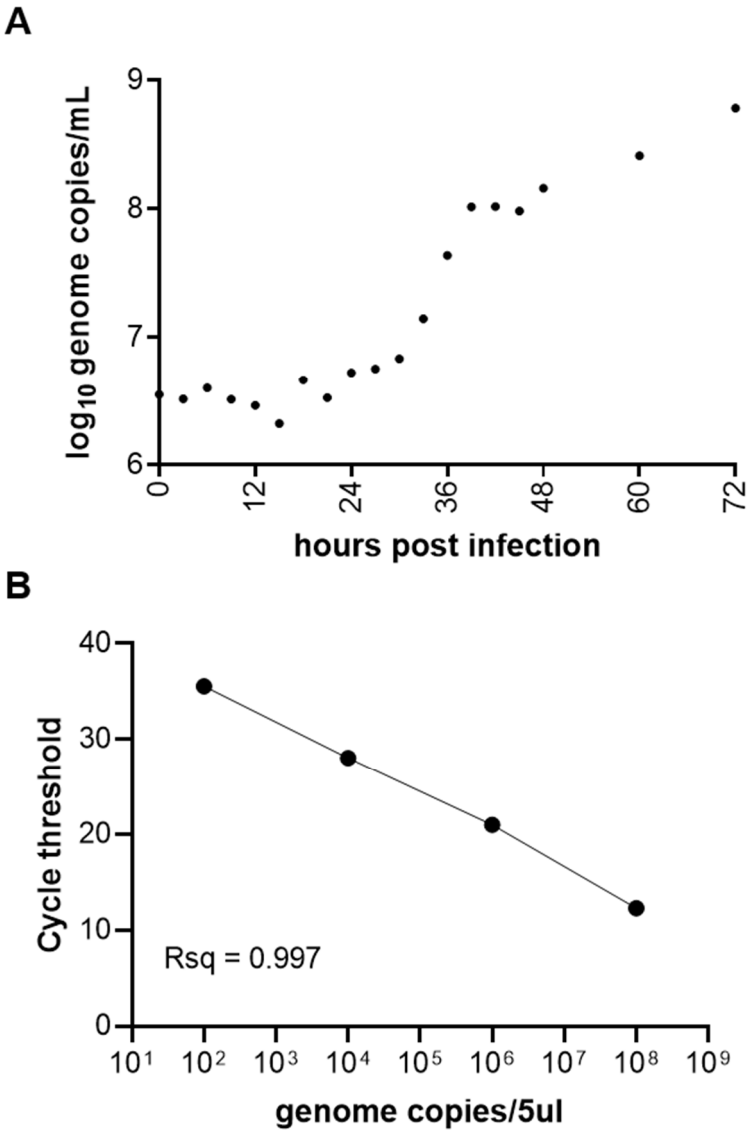


**Figure 32 Example qRT-PCR detection of TULV RNA and example standard curve generated from *in vitro* transcribed TULV S segment RNA**.

A) Example time course of TULV RNA production during infection of Vero E6 cells at MOI 0.1 B) Example standard curve based on serially diluted *in vitro* transcribed TULV S segment RNA generated through qRT-PCR. Graphs are for demonstrative purposes and are based of one replicate.

### 3.4.4 Section summary

This section describes the development of a rapid PCR based assay for the quantitative detection of TULV RNA replication products by generating a calibration curve from *in vitro* transcribed RNA allowing fast, accurate and specific detection of TULV RNA. This standardised calibration curve will allow

reliable comparison of TULV S segment RNA quantities even obtained through separate qRT-PCR runs. As the numerical value of each sample is quantified against a standard curve the values obtained are unlikely to be exact. However as every condition remains the same, save the initial template RNA concentration, this assay is a reliable method of detecting TULV RNAs under experimental conditions. Further applications of this method, for viral diagnostics, would require further quality control mechanisms such as detection of an endogenous housekeeping or reference gene for example GAPDH (Panina et al., 2018).

## 3.5 Results: Developing assays to detect infectious TULV

### 3.5.1 Introduction to virus titration assays

There are many different methods used for the quantification of infectious virus. Traditional methods include tissue culture infective dose assay (TCID50), focus forming assay (fluorescence or colourimetric), crystal violet plaque assay, neutral red uptake plaque assay, flow cytometry based assay and focus reduction neutralisation (FRNT) assay (Cooper, 1962; McCormick et al., 1982; Tanishita et al., 1984; Gavrilovskaya et al., 1998; Bharadwaj et al., 2000; Tischler et al., 2005; Ramanathan et al., 2007; Barriga et al., 2013; Baer and Kehn-Hall, 2014).

Orthohantaviruses are not known to cause lytic infections *in vitro* or *in vivo* (Vapalahti et al., 1996; McElroy et al., 2004; Mackow et al., 2014; Ermonval et al., 2016). This prevents the use of traditional plaque assays in which areas of cell death are counted, as measured by the appearance of plaques against a densely-stained crystal violet monolayer. However, orthohantaviruses-infected cells show growth impairment, and can be stained using the neutral red uptake plaque assay, in which growth-impairment can be visualized by reduced uptake of the stain compared to un-infected cells (McElroy et al., 2004). However, this assay is time-consuming (10-17 days) with plaques that are not easily distinguishable from surrounding cells (especially in comparison to the crystal violet plaque assays) (Schmaljohn et al., 1983; McElroy et al., 2004). Here, a fast and high-throughput immunofluorescence-based assay was developed utilising the polyclonal antisera generated against SEOV NP, which displayed cross-reactivity against TULV NP allowing discrete infectious centres to be stained and counted.

### 3.5.2 Neutral red uptake plaque assay

Neutral red uptake plaque assay is a common method used for the titration of orthohantaviruses. Plaque assays were performed in duplicate in 6-well plates using TULV serially diluted from $10^{0}$-$10^{-4}$. After adsorption, monolayers were overlaid with using a 2 % agarose overlay. After 7 days of incubation, a second overlay containing neutral red was added. Cells were checked for plaques 1-

3 days post staining. A typical TULV stock was estimated to have a titre of 1.2 x $10^5$ pfu/mL (Figure 33).

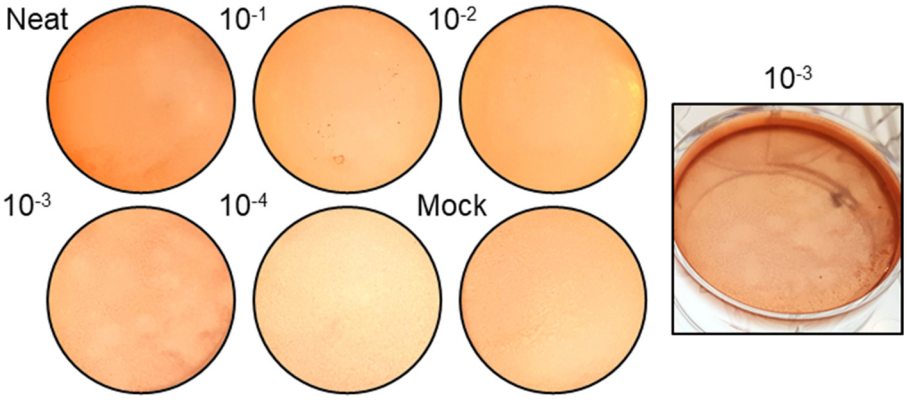


**Figure 33 Example neutral red uptake plaque assay.**

TULV viral titres were assessed using neutral red uptake plaque assay. Plaques were counted in the well containing TULV diluted $10^{-3}$ where plaques are most easily distinguished.

### 3.5.3 Immunofluorescent assay

The neutral red uptake plaque assay method is time-consuming, taking over 10 days, and produces poorly-visible plaques. An improved immunofluorescence-based assay was developed based on detection of viral NP for the titration of TULV, for TULV infection kinetics and for measuring virus production. The immunofluorescence assay was carried out in triplicate in 96-well plates using TULV serially diluted from $10^0$-$10^{-5}$. After adsorption, 2 % media was added to each well and infection was carried out for 72 hours. Cells were fixed and stained for indirect immunofluorescence using SEOV NP antisera. Infected cells were imaged using the Incucyte ZOOM software and quantified using masking software (Figure 34). An example TULV dilution series was examined by this method and was shown to describe a linear range with an Rsq value of 0.9862 (Figure 34). This methods allows accurate, high-throughput and fast titration of TULV.

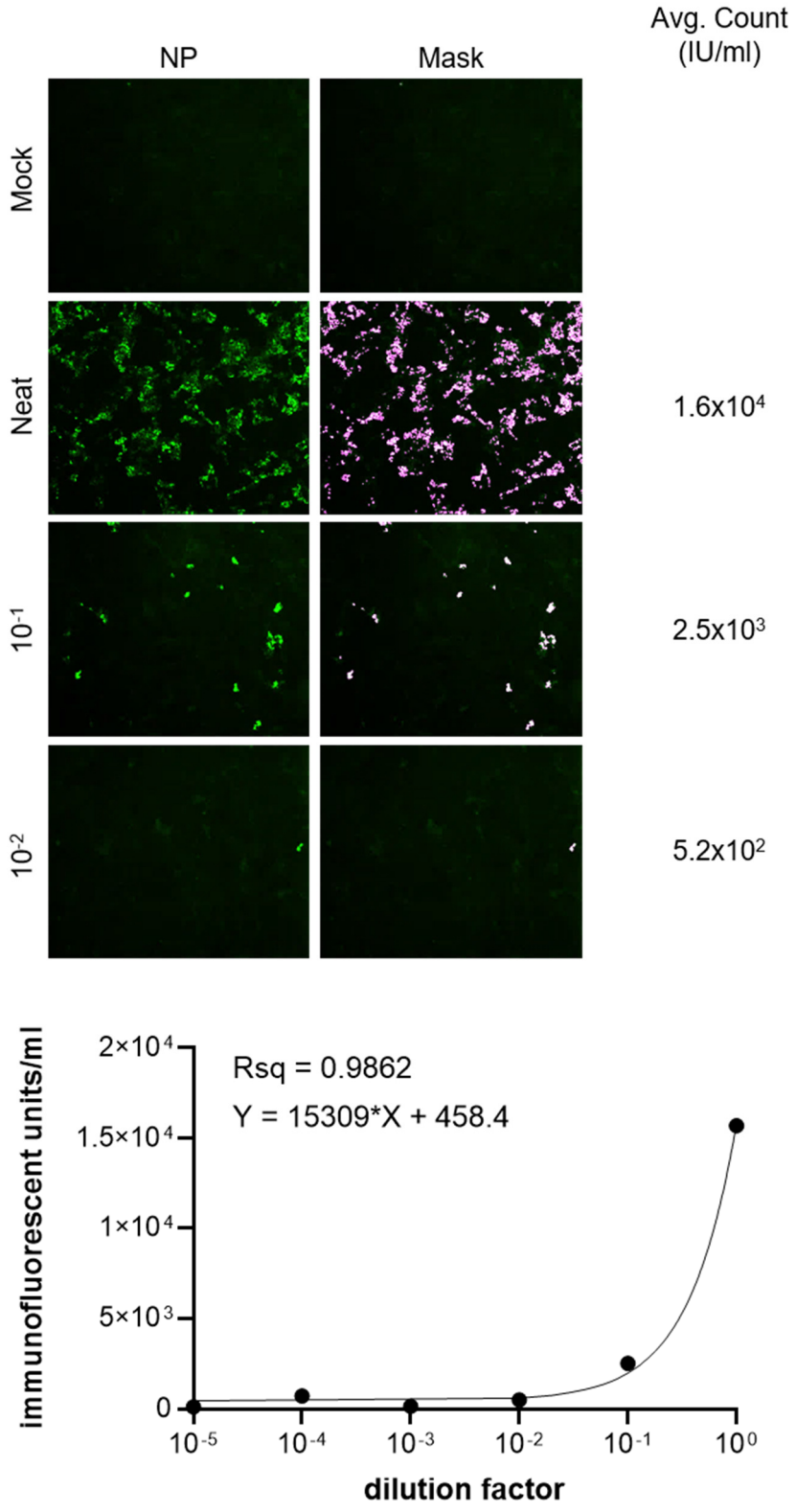


**Figure 34 Example immunofluorescence assay.**

Example images of infected or mock wells used for the immunofluorescence assay using the Incucyte ZOOM instrument and showing subsequent analysis using masking software to count immunofluorescent units per well. The linear range describing the dilution factor is shown.

### 3.5.4 Section summary

This section describes development of methods to titrate infectious TULV. A neutral red uptake plaque assay (Schmaljohn et al., 1983) and an immunofluorescence assay were developed in order to facilitate the titration of infectious TULV.

# Chapter 4 : Examining the life cycle and persistence of TULV

## 4.1 Chapter Introduction

The previous chapter described the development of molecular tools to allow examination of the TULV lifecycle based on the detection of both viral RNA and protein products, specifically the nucleocapsid protein (NP). Here, these tools are exploited to examine the kinetics of TULV multiplication within cultured cells, in which TULV establishes a long-term infection. The localisation of TULV NP during early, peak and persistent stages of infection was examined along with the ability of NP to interact with various host-cell proteins using IF analysis.

## 4.2 Results: Quantification of TULV replication products

### 4.2.1 Introduction to the orthohantavirus lifecycle

The lifecycle of the orthohantaviruses is poorly understood and many fundamental questions surrounding their multiplication still remain unanswered. Important questions include where is the site of the replication factory within the cytosol, what is the identity of host-cell components that are required for formation of the viral factory, and what mediates hantavirus persistence *in vivo* and *in vitro*?

During infection of the host cell, viruses often induce the formation of viral factories where the production of viral RNA and protein components take place, and in some but not all cases, virus particles are assembled. These cellular inclusions often comprise specific cell organelles or modified membranes where host proteins are recruited, which may aid the virus replication cycle and protect the virus from the host immune responses. For orthohantaviruses the location and composition of the viral factory is still unknown. It is likely that the NP is a major structural component of the hantaviral factory, being the most abundant protein that builds up the RNP, which acts as the template for all viral RNA synthetic activities. NP may also have a role in establishment of the factory, based on the observation that NP-

host interactions are required for formation of viral factories (Ding et al., 2016). Examining the interaction of NP with host cell components in cells may reveal the specific requirements for establishment of the orthohantavirus replication factory as well as provide information about its location.

Examining NP interactions may also aid understanding of why orthohantavirus infections in cell culture and the natural rodent hosts leads to persistence, particularly in view of the increasing body of evidence showing the hantaviral NP possesses anti-apoptotic functions. However, the molecular and cellular basis for orthohantavirus persistence both *in vivo* and *in vitro* is poorly understood.

#### 4.2.1.1 Orthohantavirus life cycle *in vivo*

Viral persistence in a natural host or reservoir may be an evolutionary adaptation developed by the viruses after millions of years of virus-host co-evolution. Syrian hamsters, macaques (rhesus and cynomolgus), ferrets and marmosets have all be used as a model of orthohantavirus infection *in vivo*. Infection with HFRS-causing orthohantaviruses (e.g. HTNV/PUUV) leads to a similar disease to humans in macaques (Groen et al., 1995), whereas infection in Syrian hamsters, ferrets and marmosets, while susceptible to HTNV and PUUV infection, showed asymptomatic infections with either no symptoms of infection or subclinical manifestations of pathogenesis (Perley et al., 2019). These asymptomatic infections of animal models show little evidence of systemic viremia despite a detectable immune response and the detection of virus in organs and excretions of infected animals (Perley et al., 2019). Asymptomatic models of HFRS-infection are similar to orthohantavirus infection of rodents, the natural host, and can be a model for viral persistence in the host animal (Sanada et al., 2011). However, immunosuppression of Syrian hamsters and ferrets leads to the development of a disease phenotype for HFRS- and HCPS-causing orthohantaviruses suggesting immune involvement is required for the regulation of asymptomatic, persistent infection (Hooper et al., 2001; Brocato et al., 2014; Vergote et al., 2017; Perley et al., 2019).

In the orthohantavirus reservoir host, asymptomatic virus infections follow distinctive kinetics. Viremia peaks between 10-20 dpi and during this period

virus shedding in excreta is high. The acute phase is followed by a persistent phase of reduced virus replication and shedding but with high antibody titres. These kinetics have been experimentally demonstrated for HFRS/NE and HCPS with mice, voles and rats. Virus can be detected in excreta up to at least a year post infection (detected at experimental end point). Orthohantaviruses can persist and remain infectious in the environment for significant periods, which allow efficient transmission to rodent or human hosts (Kallio et al., 2006). Horizontal transfer due to exposure and inhalation of infective excreta appears to be the common way virus is transmitted (Lee et al., 1981; Gavrilovskaya et al., 1990; Hutchinson et al., 1998; Botten et al., 2002). Hantavirus maintenance in reservoir hosts is likely due to a combination of exposure to infected excreta through bedding, grooming and fighting (Ermonval et al., 2016). Vertical transfer has been shown not to occur as the placenta acts as a barrier to transmission. The progeny of infected mothers have shown congenital and post-natal immunity to orthohantavirus infection for at least 20 days post birth (Yanagihara et al., 1985).

Virus persistence may be due to a specific immune response induced in the reservoir host. The development of regulatory T cells and production of TGF-β may limit a pro-inflammatory response and prevent viral clearance, as seen in persistent (but not acute) orthohantavirus infections of Norway rats. In contrast, during human orthohantavirus infection pro-inflammatory cytokines such as TNFα, IFNγ and IL-2 are upregulated in addition to increased numbers of CTLs implicated in inflammatory responses and viral pathogenesis (Schountz et al., 2007; Easterbrook and Klein, 2008; Spengler et al., 2013). Orthohantaviruses can be separated into clades which correlate well with host-species and pathogenicity in humans (Chapter One, Figure 2, Table 2). Persistent infection of the host allows greater opportunity for reassortment and genetic drift which are beneficial traits for overcoming any deleterious mutations introduced during viral replication (Plyusnin et al., 1996; Plyusnin et al., 2002). Several other zoonotic viruses have displayed persistent phenotypes in their reservoir hosts such as simian immunodeficiency virus (SIV) infections of primates and arenavirus (e.g. Lassa and Junín viruses) infection of rodents by inducting regulatory immune mechanisms (Vitullo et al., 1987; Mandl et al., 2015; Mariën et al., 2017).

#### 4.2.1.2 Orthohantavirus life cycle *in vitro*

The replication kinetics of orthohantavirus infections and their persistence in cell culture has not been described in detail. Several studies have been conducted examining either genome production, infectious virion production or viral protein production but few have studied these in combination. For both New World and Old World orthohantaviruses, reports have described a slow but steady increase in viral replication products from 24 hpi up to 10 dpi by observing levels of infectious virus, viral genomes or levels of viral NP (Jin et al., 2001; Li et al., 2010; Shim et al., 2011; I.N. Gavrilovskaya et al., 2012; Witkowski et al., 2017). In addition to lifecycle kinetics, the localisation of orthohantavirus NP has been briefly assessed. Orthohantavirus NP has been described to form puncta at early time points and perinuclear “crescents” or “filaments” at later time points (Vapalahti et al., 1996; Ramanathan and Jonsson, 2008).

Orthohantaviruses have been implicated in both the induction and evasion of apoptosis in cell culture. The lack of cytopathology in cell culture is well described through the inability to titrate the virus through traditional crystal violet methods and development of alternative non-lytic based methods of virus titration have been developed (McElroy et al., 2004). Infectious virus and viral RNA have been detected up to 139 dpi from SEOV infected Vero E6 cells (Meyer and Schmaljohn, 2000) and up to 55 dpi from TULV infected Vero E6 cells without observing cytopathic effects (Vapalahti et al., 1996). Additionally, endothelial cells are known to be the primary sites of orthohantavirus multiplication but are not associated with cell lysis (Cosgriff, 1991).

The evasion of host cell apoptosis may be mediated through several mechanisms. The NSs protein, encoded by several members of the *Orthohantavirus* genus, is capable of suppressing antiviral immune responses and can reduce IFNβ expression which contributes to virus survival (Jääskeläinen et al., 2007; Jääskeläinen et al., 2008). Additionally, defective interfering particles (DIs) have been suggested to be a factor in viral persistence. DIs have been identified within the majority of RNA and DNA families and are virus-like particles with mutated or shortened genomes which render them incapable of autonomous replication. They infect cells simultaneously with a helper virus and interfere with its replication by

competing for host resources (Strauss and Strauss, 2008). DIs are associated with increased IFN production, which may aid the development of persistent infections through reduction of the inflammatory response (Sekellick and Marcus, 1978; Manzoni and López, 2018). However, as of yet, no role for DIs in orthohantavirus persistence has been demonstrated and instead persistence has been linked to accumulation of terminally deleted RNAs which still are capable of replication (Meyer and Schmaljohn, 2000). This suggests that other mechanisms, alternative to DIs, are involved in the induction of orthohantavirus persistence.

### 4.2.2 Introduction to laser scanning confocal microscopy (LSCM) and widefield fluorescence deconvolution microscopy (WFDM)

Florescent microscopy is a powerful technique which can be utilised for the examination of the localisation of subcellular structures. Fluorescent microscopy relies on the use of antibodies which target the protein of interest and use a conjugated fluorophore to provide a localised signal. LSCM or WFDM can be used for visualisation of fluorophore signal.

In LSCM, a laser of a specific wavelength is used as a light source with fluorescent emission detected through a specific filter set. The emitted light is passed through a pinhole (aperture) reducing the amount of light reaching the light detector (photomultiplier). This reduces the out-of-focus light giving a sharply focused image of one focal plane of the specimen (Ferrando and Spiess, 2000; Földes-Papp et al., 2003; Nwaneshiudu et al., 2012). Widefield fluorescent deconvolution microscopy (WFDM) in contrast utilises either light-emitting diodes (LEDs), mercury or xenon arc-lamps as a light source, with both excitation and emission filters used. In WFDM, the entire specimen is illuminated by the light source and as a result the emitted light can be scattered producing a blurred image. No pinhole is employed in WFDM and instead a mathematical algorithm, deconvolution, is used where out-of-focus light is returned to its estimated point source. Images are recorded over a series of focal planes and deconvolution is applied to give an image with higher contrast and resolution than the raw data would normally allow (Shaw, 2006; Wilson, 2017). Advantages of WFDM over LSCM include speed of

image capture, higher resolution, sensitivity and improved signal-to-noise ratio. The advantages of LSCM are sharper optical sectioning, reduced background, increased cross talk elimination and capture of more than one fluorophore simultaneously. However, with LSCM there is usually a trade-off between image quality, speed and light intensity (Shaw, 2006; Sanderson, 2008).

### 4.2.3 TULV RNA replication kinetics in Vero E6 cells through a 10 day time course

The multiplication of TULV in Vero E6 cells was examined over an extended time course when incubated at 37 °C. Growth of TULV in Vero E6 cells 32 °C was examined due to previous work carried out on Hazara virus where 32 °C growth achieved significantly higher viral titres (Emma Punch, unpublished data). Vero E6 cells were infected with TULV at MOI 0.1 and the supernatants and cell lysates were collected at specified time points and assessed separately for production of viral RNA and infectious particles. Analysis of sense and anti-sense RNA from 37 °C culture lysates using qRT-PCR revealed a lag phase of up to 30 hpi where no increase in viral RNA replication products was detected. This lag-period was followed by an exponential phase of rapid viral RNA production which lasted for around 12 hours (Figure 35A, B, Figure 36A, B). This was followed by a period with a much slower RNA replication rate, eventually leading to a plateau in RNA abundance at around 168 hpi at 37 °C (Figure 36B). This plateau was not reached during the 32 °C time course, with quantities continuing to rise, suggesting slower replication kinetics (Figure 35B).

The production of infectious virus particles was also examined to assess whether infectious virus production reflected increasing genome abundance. This measurement would also allow us to examine whether our measurement of viral RNA was influenced by the production of defective RNA genomes within DIs, a known characteristic of RNA virus infections (Rima et al., 1977; Sekellick and Marcus, 1978). Assessment of infectivity was performed using the same time points as previously used for RNA analysis, which revealed the overall pattern of infectious virus release mirrored that of viral RNA abundance as measured by qRT-PCR. There was an initial lag period of around 48 hpi at 37 °C (Figure 36C) and 60 hpi at 32 °C (Figure 35C) followed by a period of increased infectious virus production up to 144 hpi at 37 °C (Figure 36C) and 168 hpi at 32 °C (Figure 35C). As viral genomes and infectious virus concentrations follow similar growth patterns this suggests that there may be no production of DIs during long-term orthohantavirus infection. DI contamination of infective virus stocks leads to a decreased viral titre

compared to viral protein or viral genome levels as demonstrated with LCMV (Thompson and Yin, 2010; Perelygina et al., 2015; Ziegler et al., 2016).

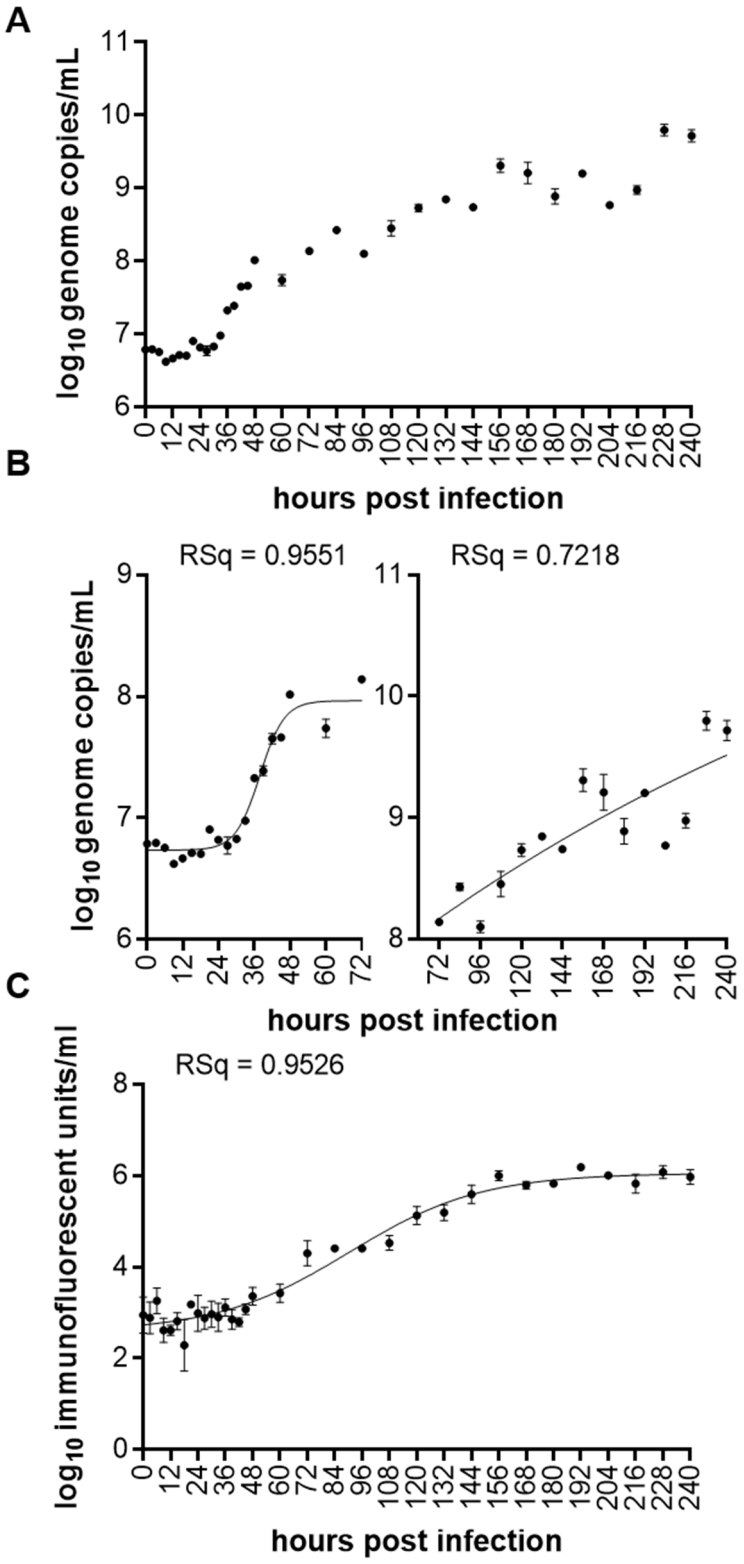


**Figure 35 Examination of TULV replication kinetics in Vero E6 cells at 32 °C by qRT-PCR and IF assay.**

A) TULV infectious titres/mL determined by IF assay using SEOV NP antisera B) TULV RNA genome copies/mL determined by qRT-PCR C) TULV RNA genome copies/mL displaying lag and exponential phase separate from slow/plateau phase

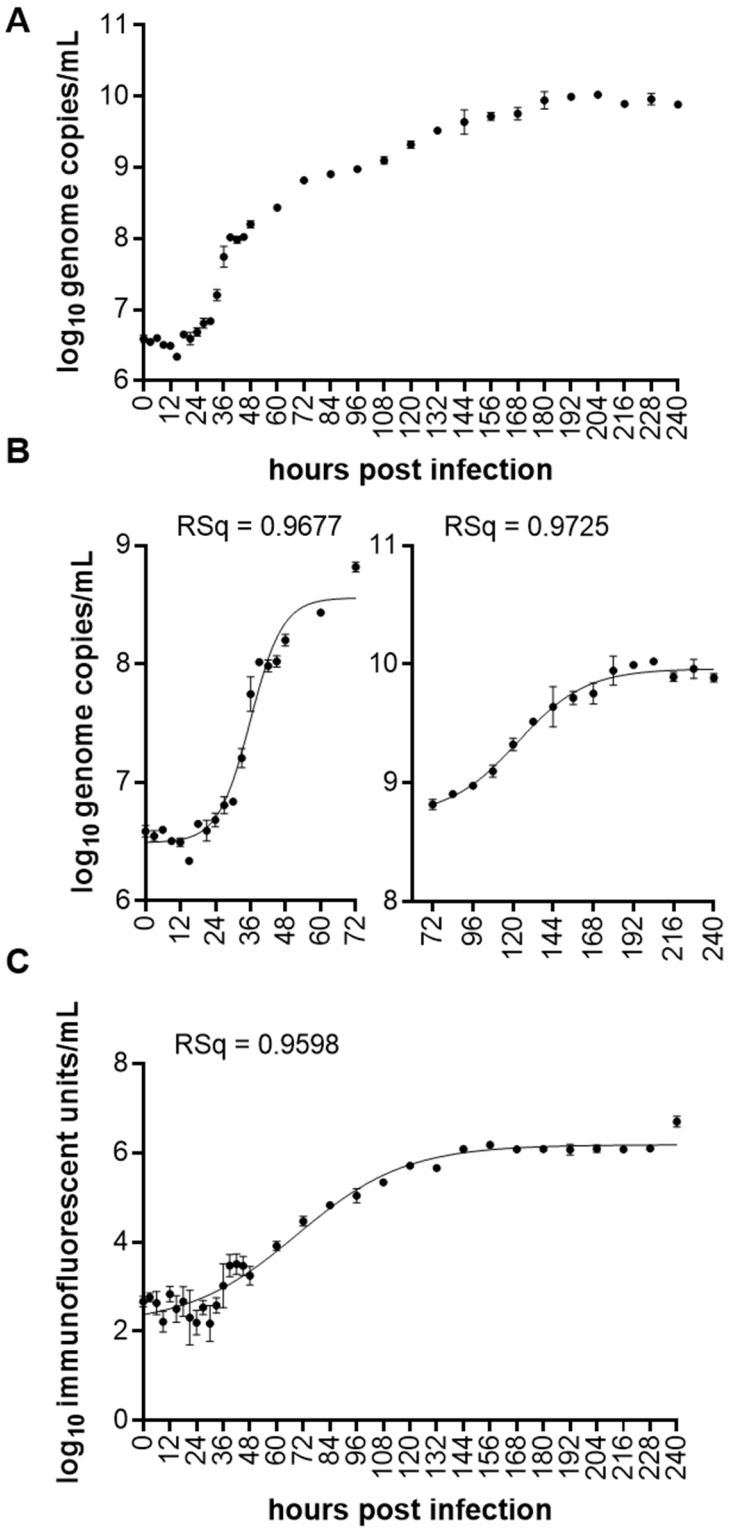


**Figure 36 Examination of TULV replication kinetics in Vero E6 cells at 37 °C by qRT-PCR and IF assay.**

A) TULV infectious titres/mL determined by IF assay using SEOV NP antisera B) TULV RNA genome copies/mL determined by qRT-PCR C) TULV RNA genome copies/mL displaying lag and exponential phase separate from slow/plateau phase

During TULV infection the concentration of viral RNAs compared to infectious viral particles decreases as infection progresses, the opposite to what is expected with DIs contamination (Figure 37).

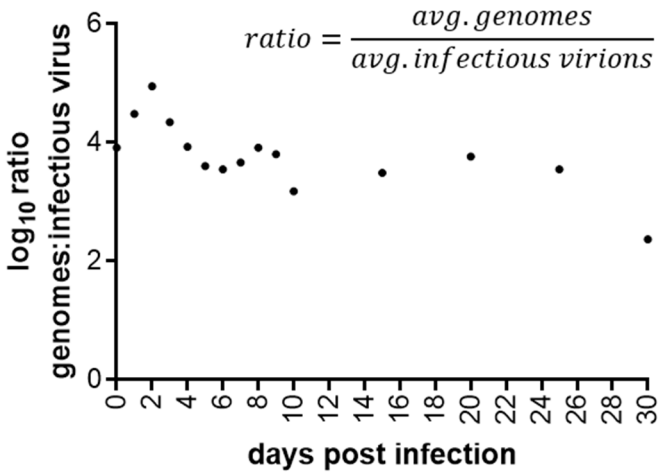


**Figure 37 Ratio of viral genomes to titre in Vero E6 cells at 37°C.**
Ratio of viral RNA genomes and infectious virus detected over 30 days post infection in Vero E6 cells at 37°C

Alongside the quantification of TULV replication, SEOV NP antisera was used to assess TULV NP accumulation in Vero E6 cells infected at MOI 0.1 by western blotting of cell lysates. Intracellular NP was detected 36-48 hpi (1.5-2 dpi) with a significant increase in NP detection occurring between 60 (2.5 dpi) and 72 hpi (3 dpi). NP could be detected in cell lysates at consistent levels up until the final harvest of the time course of 240 hpi (10 dpi) (Figure 39). Taken together, these results suggest that the replication of TULV genomes and production of infections TULV particles is relatively slow when compared to other RNA viruses. For example, Nipah virus begins exponential replication of genomes 8 hpi and reaches peak virus production at around 32 hpi (Chang et al., 2006) and influenza virus begins genome replication very soon after infection and reaches peak virus levels at 4-10 hpi after which virus genomes and virus titres decrease (Schulze-Horsel et al., 2009; Frensing et al., 2016). This immediate decrease in replication products after peak production is not observed during orthohantavirus infection of Vero E6 cells. Instead a plateau phase is reached after peak virus production where the rate of production of RNA products and infectious particles continues but remained static. This may

be due to the lack of CPE induced by orthohantaviruses. Viruses displaying decrease in viral genomes and infectious particles after peak virus production often induce apoptosis to aid virus dissemination, such as during influenza virus infection (Herold et al., 2012).

### 4.2.4 TULV replication during persistent infections

As TULV replication products and infectious TULV could be detected in an extended time course of up to 240 hpi (10 dpi) , the time course was extended up to 30 dpi to assess TULV replication in persistently infected cell cultures. After 10 dpi, there was a slow decreases in viral RNA up to the end of the time course at 30 dpi but genome levels still remain approximately one log higher than initial values (Figure 38B). Assessment of infectious TULV also revealed a slow decrease in infectious particle counts from 10-30 dpi (Figure 38A). The larger decrease in viral genomes compared to infectious virus particles is not distinctive of persistence induced by the presence of DIs where the ratio would be expected to be reversed (Ziegler et al., 2016) suggesting an alternative mechanism for viral persistence.

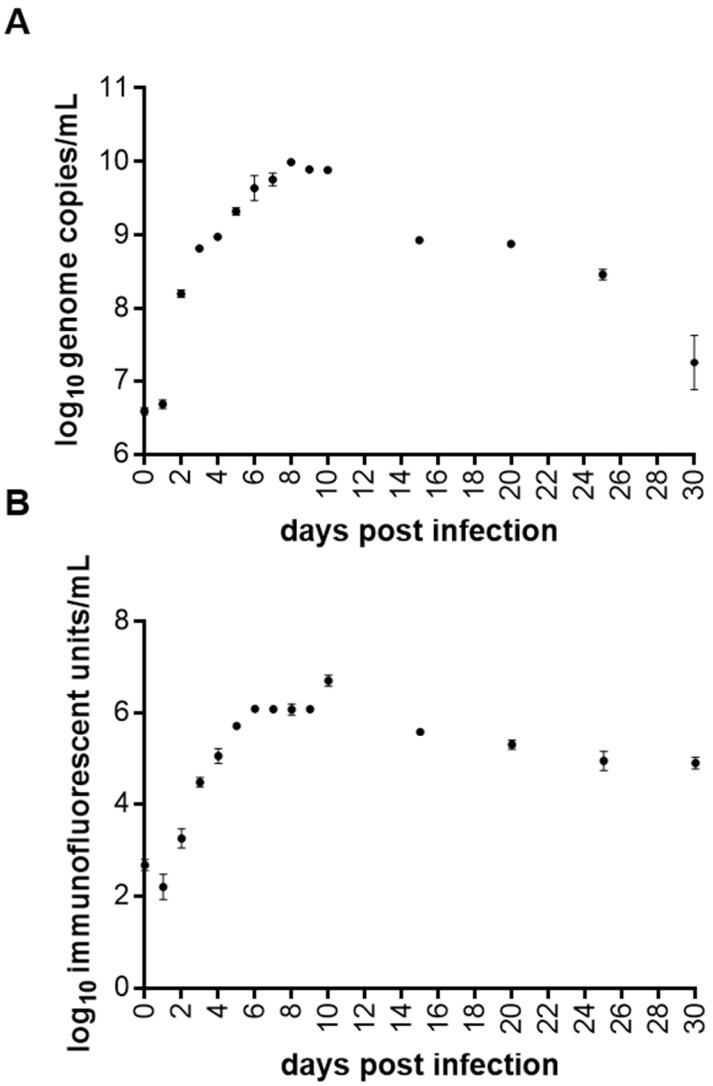


**Figure 38 Examination of persistent TULV infection replication kinetics in Vero E6 cells at 37°C by qRT-PCR and IF assay.**

A) TULV infectious titres/mL determined by IF assay using SEOV NP antisera B) TULV RNA genome copies/mL determined by qRT-PCR

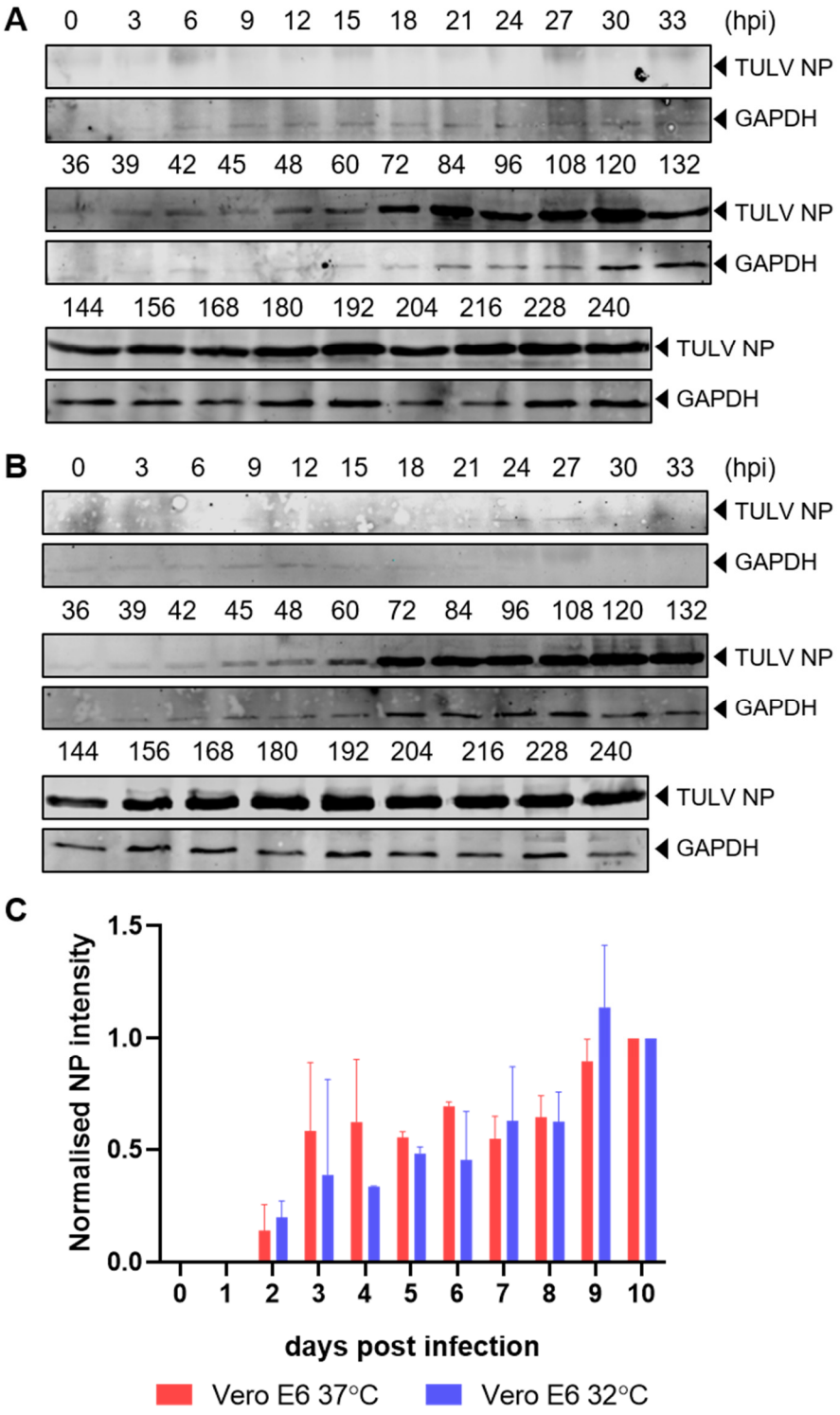


**Figure 39 Examination of TULV replication kinetics at 32 °C and 37 °C by western blot**

A) Accumulation of NP in TULV infected Vero E6 cell lysates at 32 °C assessed by western blot using SEOV NP antisera alongside a GAPDH loading control. B) Accumulation of NP in TULV infected cell lysates at 37 °C assessed by western blot C) Normalised NP values as a percentage of 10 dpi, an average of two separate experiments

### 4.2.5 Detection of TULV NP localisation in infected and transfected cell cultures

#### 4.2.5.1 Localisation of TULV NP in infected Vero E6 cell cultures

The location of TULV NP in TULV infected cells at 36 hpi (early), 7 dpi (peak) and 30 dpi (persistent) was examined by IF analysis using SEOV NP antisera. LSCM revealed at least three distinct patterns of NP accumulation at these specific time points. At 36 hpi, NP was observed throughout the cytoplasm as predominantly punctate bodies, 0.3-2.7 µm diameter, and also thin tubular structures, with dimensions of approximately 4-7.5 µm long and 0.5-1.5 µm in width (Figure 40, top panel). At 7 dpi, NP was observed in the cytoplasm as punctate bodies (0.3-2.7 µm) in addition to an accumulation of NP as filaments in the perinuclear region. At 7 dpi, TULV NP filaments are around 6.0-20.0 µm in length and 0.5-5.0 µm in diameter (Figure 40, middle panel). At 30 dpi, the location of NP was similar to that observed at 7 dpi, forming large filaments and macromolecular complexes in the perinuclear region, and punctate bodies in the cytoplasm. TULV NP filaments in persistently infected cells were 6.0-25.0 µm in length and 2.0-6.0 µm in diameter and puncta ranged between 1.0-3.5 µm in diameter. Though NP filaments and puncta gradually increase in size throughout infection their locations remain fairly consistent with tubular NP localising in the perinuclear region and punctate NP throughout the cytoplasm. Due to the resolution limits of LSCM it was not determined whether TULV NP filaments were composed of multiple thin filaments of NP or were larger accumulations or aggregations of NP. However, the increased size of these large structures as the infection progressed through the time course suggests they may represent important sites of viral activity, and are candidates for the viral factory. Viral NP found in punctate form may be contained within membranous vesicles such as endosomes or lysosomes, but will require further analysis to confirm their identity.

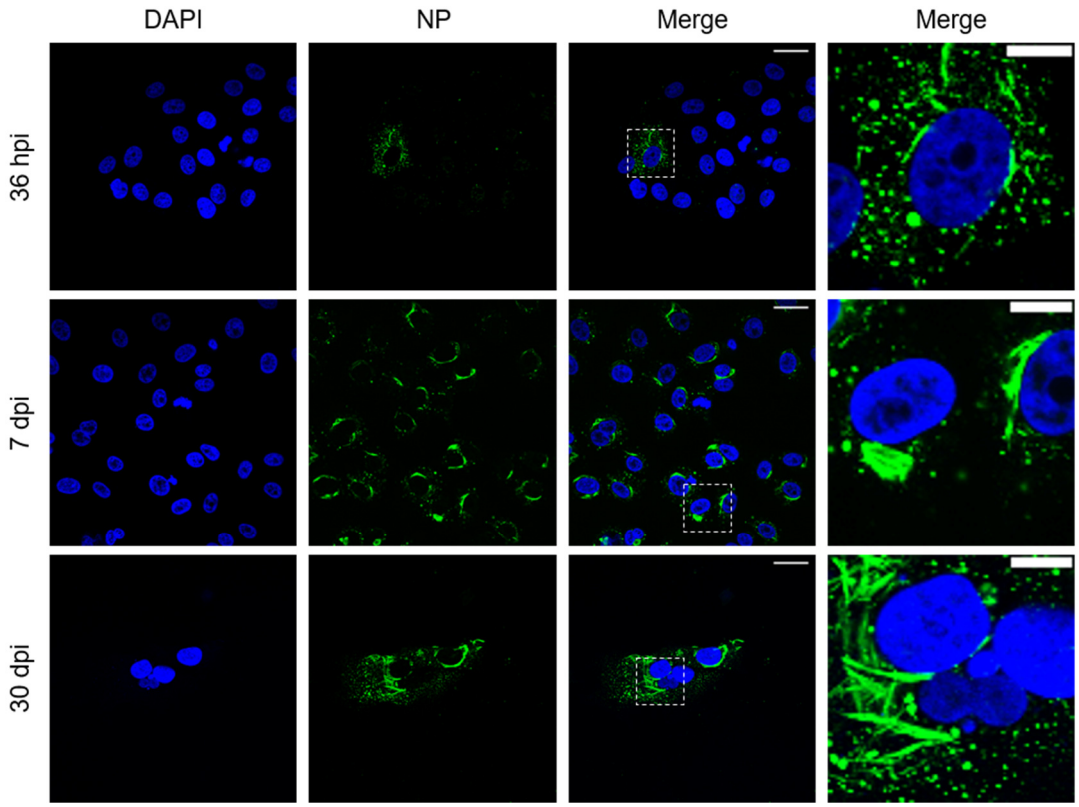


**Figure 40 Detection of TULV NP in early, peak and persistently infected Vero E6 cells.**

LSCM images of TULV infected cells at 36 hpi, 7 dpi and 30 dpi using 40 X magnification. Characteristic punctate and tubular NP staining at these time points is shown. The white bar represents 30 µm and 10 µm in zoomed images. Nuclei were stained with DAPI (blue) and TULV NP detected using NP antisera (green)

#### 4.2.5.2 Persistent TULV infection induces syncytia

To confirm the appearance of syncytia in 30 dpi persistently infected cell cultures the use of differential interference contrast (DIC) microscopy was employed where visualisation of cells using polarized light allows increased contrast and the perception of depth. In the context of this experiment, DIC microscopy allowed cell boundaries to be more easily identified, and revealed that while some cells were uninucleate (Figure 41, black arrow) others were clearly multinucleate (Figure 41, white arrow) with evidence of a single membrane around multiple nuclei (Figure 41, bottom panel). Large structures of NP within multinucleate cells were often found localised between the nuclei within the multinucleate cell (Figure 41, bottom panel).

To assess whether the ratio of cells to nuclei changes throughout infection, the ratio of cell counts to nuclei counts was determined; an equal number of

cells to nuclei would give a ratio of 1, whereas increased nuclei per cell would result in a ratio of <1. A total of 18 cells were counted at 36 hpi, 132 counted at 7 dpi and 35 counted at 30 dpi (Figure 42). At 36 hpi, no multinucleate cells were observed, at 7 dpi the majority of cells were uninucleate with a few cells containing two nuclei. At 30 dpi a high proportion of multinucleate cells contained 2-3 nuclei (but sometimes upward of 4) and displayed mostly normal nuclear morphology, but with some nuclei occasionally appearing as fragmented (Figure 40, bottom panel, Figure 41).

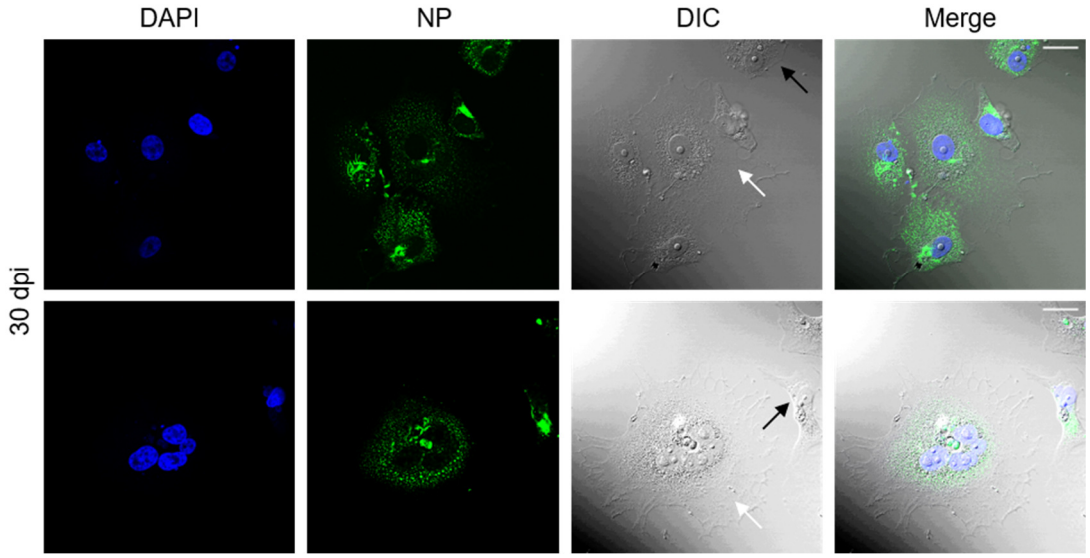


**Figure 41 Formation of multinuclear cells during persistent TULV infections in Vero E6 cells.**

LSCM images with DIC microscopy using 40 X magnification to assess formation of multinuclear cells during persistent infections in Vero E6 cells. The white bar represents 30 µm. White arrows point to multinucleate cells and black arrows point to uninucleate cells. Nuclei were stained with DAPI (blue), TULV NP detected using NP antisera (green) and differential interference contrast (grey).

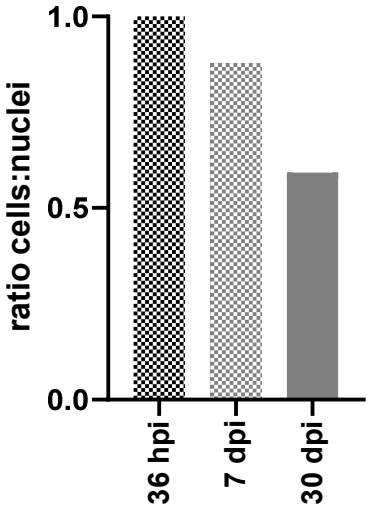


**Figure 42 Histogram of the ratio of cells to nuclei in early, peak and persistently TULV infected Vero E6 cells.**

The ratio of the number of cells to the number of nuclei identified is displayed for TULV infected cells at 36 hpi, 7 dpi and 30 dpi. Cells were counted from LSCM images. 169 cells were counted in total (18 (36 hpi), 132 (7 dpi) and 35 (30 dpi).

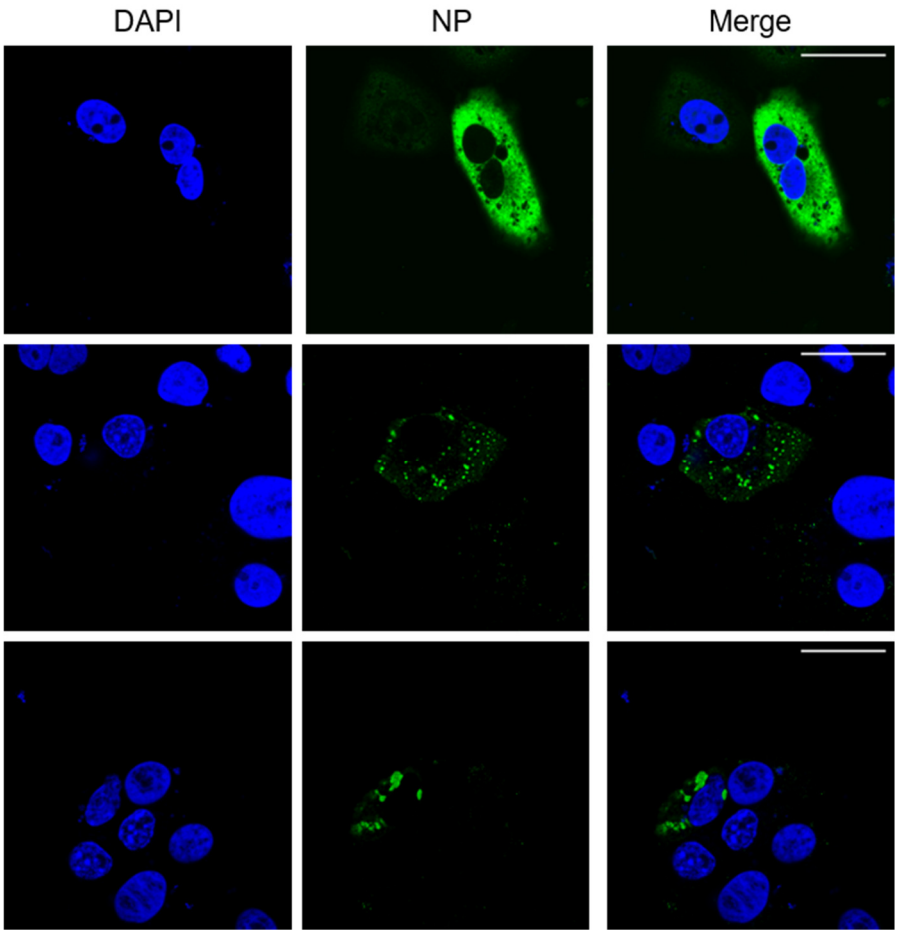


**Figure 43 Distribution of TULV NP in transfected Vero E6 cells.**

LSCM images taken of Vero E6 cells transfected with pcDNA3.1 (+) TULV NP at 18 hours post transfection using 63 X magnification. Three distinct phenotypes of recombinantly expressed TULV NP are shown. The white bar represents 30 µm. Nuclei were stained with DAPI (blue) and TULV NP detected using NP antisera (green).

#### 4.2.5.3 Localisation of TULV NP in transfected Vero E6 cells

The phenotype of TULV NP in Vero E6 cells transfected with pcDNA3.1 (+) TULV NP was examined by IF analysis. LSCM revealed several distinct patterns of NP accumulation in transfected cells. Recombinantly expressed TULV NP was observed in the cytoplasm either dispersed (Figure 43, top panel), in discrete puncta (Figure 43, middle panel) or in large structures in the perinuclear region (Figure 43, bottom panel). This is similar to observations of TULV infected cells, apart from disperse NP phenotype, suggesting the formation of these structures is not reliant on the expression of the other viral proteins, such as the viral glycoprotein or polymerase.

### 4.2.6 Section summary

This section describes the distribution of TULV NP in Vero E6 cells during early, peak and persistent infections and in TULV NP transfected cells. TULV NP shows distinct localization phenotypes at early, peak and persistent stages on infection notably the formation of large tubular structures in the perinuclear region in addition to the establishment of multinucleate cells. TULV NP transfected cells show similar NP phenotypes to infected cells at 36 hpi and 7 dpi but lack the distinct filamentous structures found at 30 dpi.

## 4.3 Results: Analysis of TULV NP co-localisation with host cell components

### 4.3.1 Introduction to orthohantavirus NP co-localisation with cellular components

The previous section described the appearance and distribution of TULV NP in both infected and transfected cells. Next, the location of TULV NP in relation to cellular components was examined. This would provide information that would aid in identifying and characterising interactions between TULV NP and various cellular components and, in addition, improve understanding of where within the infected cell the various stages of the hantavirus life cycle occur. Little is known of how hantavirus NP interacts with other cellular components, and the site of hantavirus replication factories remains elusive. Previous work by others has shown hantavirus NP localises in punctate granules in the cytoplasm at early stages of infection but by later time points, NP localises to the ER-Golgi intermediate compartment (ERGIC) in the perinuclear region. HTNV, SEOV, BCCV and ANDV NPs have been described to traffic after entry along microtubules with a requirement of the molecular motor dynein for transportation to the perinuclear region (Ramanathan et al., 2007; Ramanathan and Jonsson, 2008). BCCV NP may utilise transport along actin filaments for assembly and release, however this may not be ubiquitous over all orthohantavirus species as HTNV NP transportation post-entry shows no requirement for actin filaments, but instead actin may be necessary for early entry and replication (Ravkov et al., 1998; Ramanathan and Jonsson, 2008). Orthohantavirus NP has also been reported to co-localise with processing (P) bodies, which are the sites of sequestered cellular mRNAs. Recombinantly expressed SNV NP was found to co-localise with the P body marker, DCP1a in addition to co-immunoprecipitation of this host protein with orthohantavirus NP (Mir et al., 2008). Additionally, HTNV and SEOV NP have been described to localise to the ER/*cis*-Golgi which is important for viral replication (Li et al., 2010).

### 4.3.2 Interactions of TULV NP with the host cell cytoskeleton

#### 4.3.2.1 TULV NP co-localisation with actin, tubulin and vimentin

There are three major types of cytoskeletal filaments in the cell; actin filaments, microtubules and intermediate filaments. These are organised into a highly ordered network which controls cell shape and directs the movement of cellular components. Actin filaments are involved in cell motility and cell-to-cell communication and as a result constantly reassembles as directed through cell signalling. Microtubules are made up of α- and β-tubulin units and form rigid linear tracks throughout the cell. These tracks are used for trafficking of cellular components by molecular motors such as dynein. Intermediate filaments, as the name suggests, are intermediate in diameter (10 nm) between actin (7 nm) and tubulin (25 nm) and are formed from a diverse collection of filament proteins that share the ability to polymerize into long chains. The intermediate filaments are the least rigid of the cytoskeletal elements and are involved in diverse cellular roles including providing structural support, organelle tethering, cell signalling, and resistance to cellular stresses (Fletcher and Mullins, 2010). Previous results have suggested orthohantaviruses utilise the host cytoskeleton post-entry for trafficking, assembly and release (Ravkov et al., 1998; Ramanathan et al., 2007; Ramanathan and Jonsson, 2008).

To assess the interaction of the host cell cytoskeleton with TULV NP the intracellular localisation of actin filaments, microtubules and the intermediate filament, vimentin, was examined alongside TULV NP by IF analysis and fluorescent line scan. Line scan was chosen as a method of choice for co-localisation analysis. There is previous precedent for using the line-scan technique for both viral protein localisation (King et al., 2017) and cellular compartments (Bolte and Cordelières, 2006). Antisera against the β-actin subunit, the β-tubulin subunit and intermediate filament protein vimentin (residues surrounding Arg45 of vimentin) were used for analysis. The distribution of NP generated during TULV infection was examined at early (36 hpi), peak (7 dpi) and persistent (30 dpi) infection time points for co-localisation with host cytoskeleton components.

At 36 hpi, staining for TULV NP, actin, tubulin and vimentin revealed low levels of co-localisation (Figure 44). However, at the 7 dpi and 30 dpi, tubular NP

structures but not punctate NP displayed high levels of co-localisation with tubulin and vimentin (Figure 45, Figure 46, middle panels). Fluorescent line scan analysis of vimentin and tubular TULV NP co-localisation at 7 dpi (Figure 45) reveals near-perfect co-localisation suggesting close interaction of NP with this intermediate filament component at peak (7 dpi) infection. Later in infection, at 30 dpi, staining with vimentin showed low levels of co-localisation and instead large ultrastructural assemblies of vimentin were observed surrounding multimeric NP structures (Figure 46). Spatial distribution analysis of cytoskeletal proteins and TULV NP revealed low counts of co-localisation with actin filaments and vimentin at all time points. The low count number with vimentin at 7 dpi is due to a large amount of NP found in punctate form which does not co-localise well with vimentin staining, whereas the few tubular structures of NP co-localise well with vimentin (Figure 48).

Next, the location of NP expressed from a recombinant source was examined. pcDNA 3.1 (+) TULV S ORF was transfected into Vero E6 cells resulting in the expression of recombinant TULV NP. As above, co-localisation of the host cytoskeleton with recombinantly expressed TULV NP was assessed using IF analysis. In agreement with observations above with peak and persistently TULV infected Vero E6 cells, co-localisation was observed between TULV NP structures or tubules with tubulin but not with actin. Additionally, recombinantly expressed TULV NP co-localises with vimentin but without the observation of the vimentin “cage” around sites of NP accumulation suggesting a requirement for other viral proteins for efficient cage formation (Figure 47).

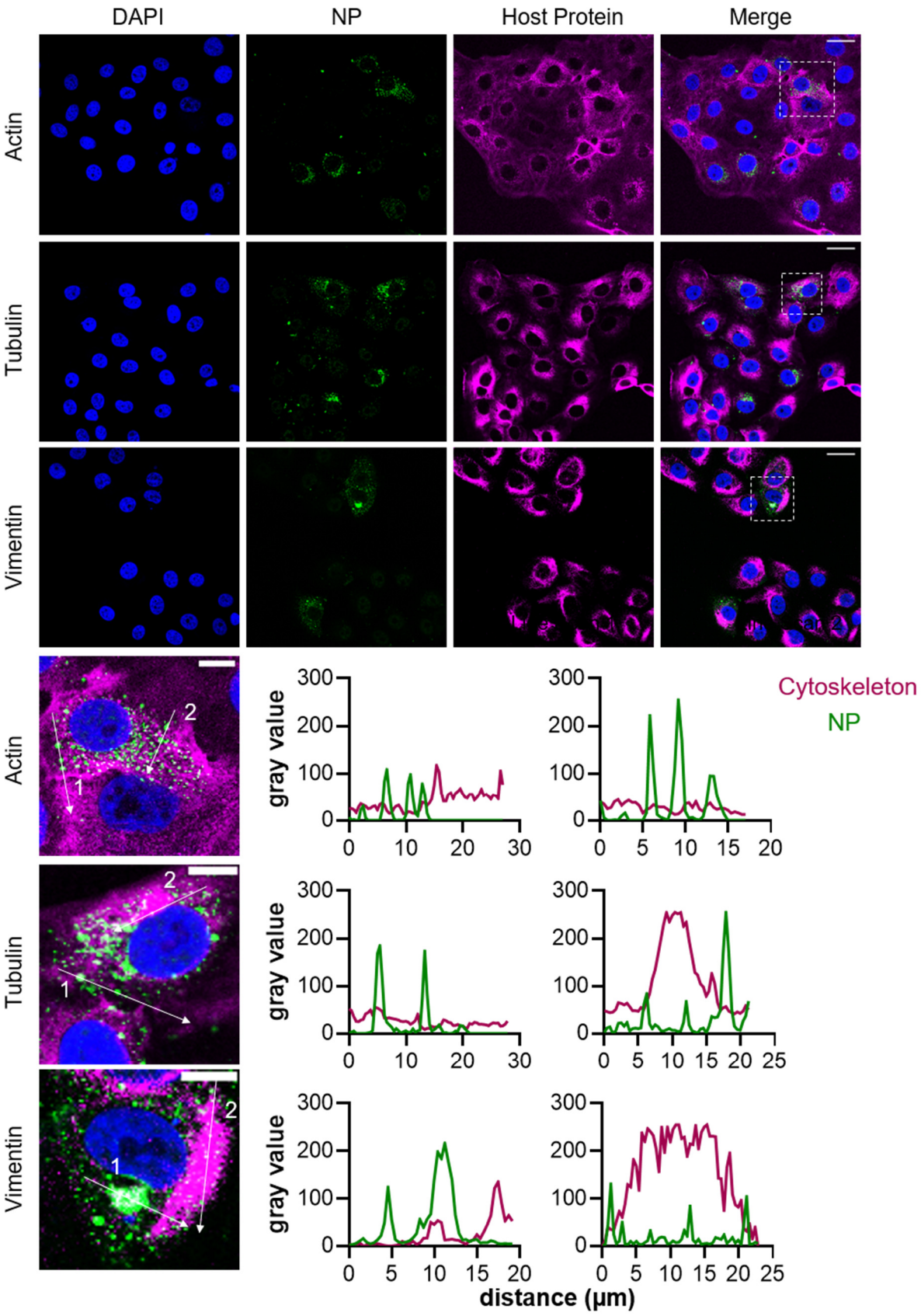


**Figure 44 Co-localisation of actin filaments, microtubules and vimentin with TULV NP in Vero E6 cells at 36 hpi.**

**Figure 44 Co-localisation of actin filaments, microtubules and vimentin with TULV NP in Vero E6 cells at 36 hpi.**

The spatial distribution of the cytoskeletal markers (magenta) was observed alongside TULV NP (green) in TULV infected Vero E6 cells (MOI 0.1) at 36 hpi by LSCM at 40 X magnification. The white bar represents 30 µm and 10 µm (zoom). Fluorescent line scans taken using Fiji software. Nuclei were stained with DAPI (blue), TULV NP detected using NP antisera and cytoskeleton detected using antibodies against β-actin, β-tubulin and vimentin

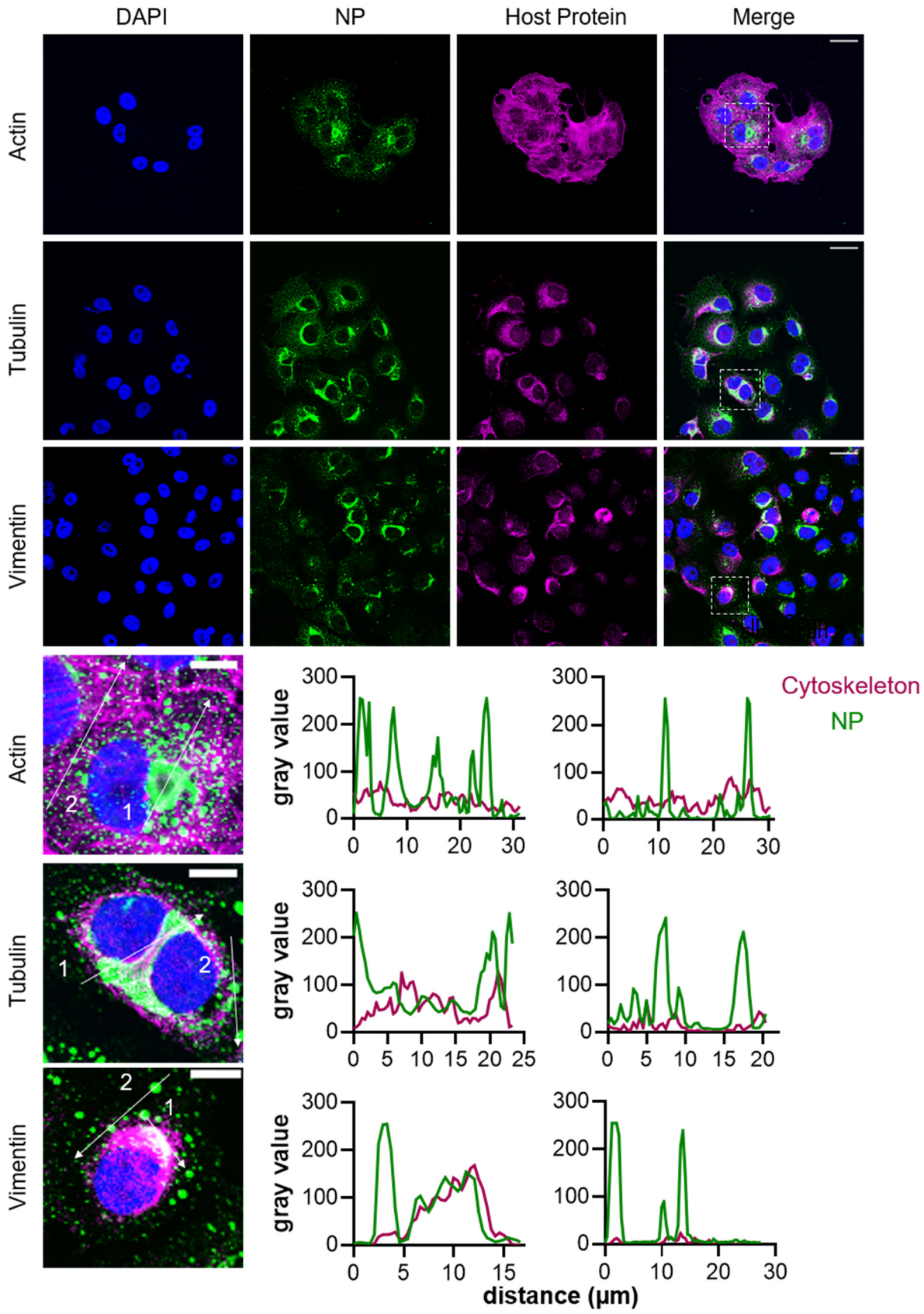


**Figure 45 Co-localisation of actin filaments, microtubules and vimentin with TULV NP in Vero E6 cells at 7 dpi.**

**Figure 45 Co-localisation of actin filaments, microtubules and vimentin with TULV NP in Vero E6 cells at 7 dpi.**

The spatial distribution of the cytoskeletal markers (magenta) was observed alongside TULV NP (green) in TULV infected Vero E6 cells (MOI 0.1) at 7 dpi by LSCM at 40 X magnification. The white bar represents 30 µm and 10 µm (zoom). Fluorescent line scans taken using Fiji software. Nuclei were stained with DAPI (blue), TULV NP detected using NP antisera and cytoskeleton detected using antibodies against β-actin, β-tubulin and vimentin.

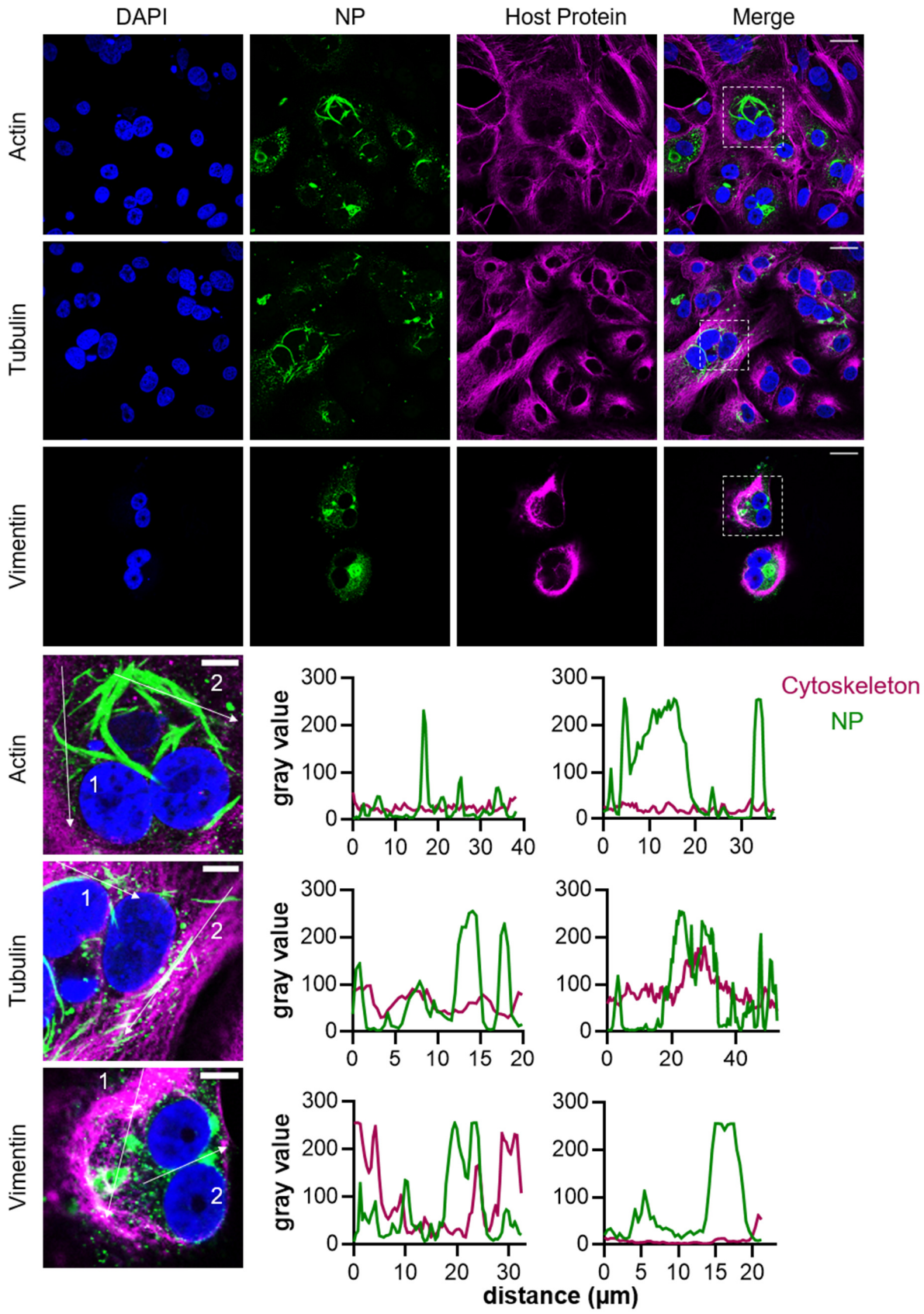


**Figure 46 Co-localisation of actin filaments, microtubules and vimentin with TULV NP in persistently infected Vero E6 cells.**

**Figure 46 Co-localisation of actin filaments, microtubules and vimentin with TULV NP in persistently infected Vero E6 cells.**

The spatial distribution of the cytoskeletal markers (magenta) was observed alongside TULV NP (green) in TULV infected Vero E6 cells (MOI 0.1) at 30 dpi by LSCM at 40 X magnification. The white bar represents 30 µm and 10 µm (zoom). Fluorescent line scans taken using Fiji software. Nuclei were stained with DAPI (blue), TULV NP detected using NP antisera and cytoskeleton using antibodies against β-actin, β-tubulin and vimentin.

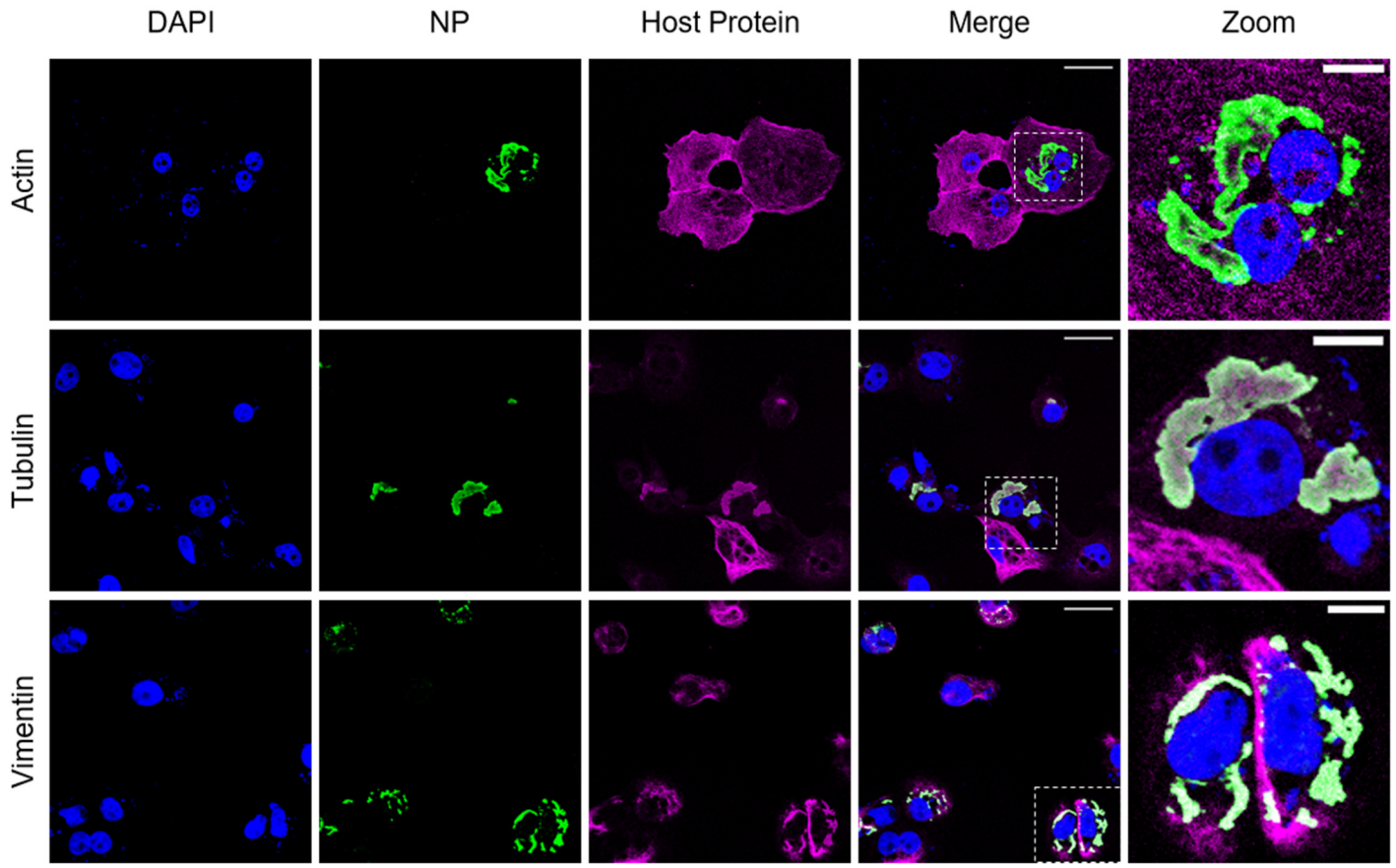


**Figure 47 Location of cytoskeletal markers and transfected TULV NP within Vero E6 cells.**

LSCM images of Vero E6 cells transfected with pcDNA3.1 (+) TULV NP at 18 hours post transfection using 40 X magnification. The white bar represents 30 µm. Nuclei were stained with DAPI (blue), TULV NP detected using NP antisera (green) and cytoskeleton detected using antibodies against β-actin, β-tubulin and vimentin (magenta).

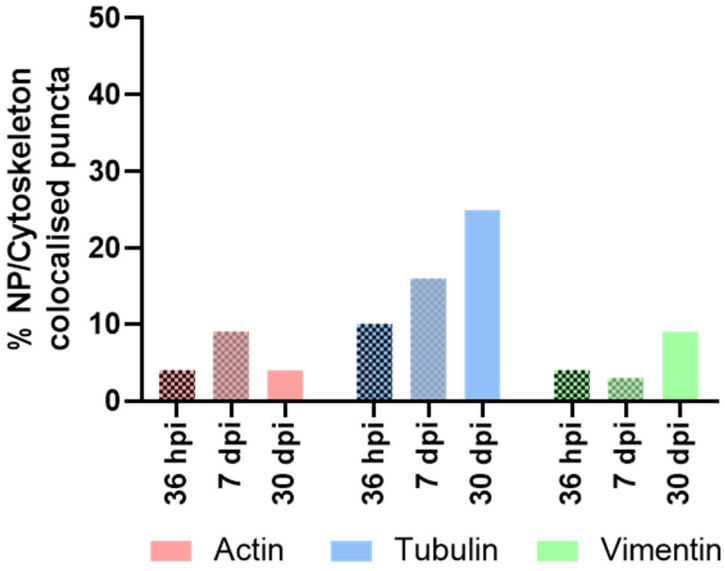


**Figure 48 Quantification of TULV NP puncta and structures co-localising with cytoskeletal markers.**

Co-localisation was assessed using Fiji software. For each time point (36 hpi, 7 dpi and 30 dpi) at least 100 TULV NP puncta/filaments were examined for co-localisation with actin, tubulin or vimentin

#### 4.3.2.2 Inhibition of actin polymerisation and degradation on TULV NP localisation

To further examine the interaction of the actin cytoskeleton on TULV NP localisation, TULV infected Vero E6 cells were treated for 60 minutes with 10 µM cytochalasin D (CytD) and examined for TULV NP and actin co-localisation by IF analysis. CytD causes severe disruption of the actin network by breaking down actin filaments into smaller fragments and binding to filament ends preventing re-polymerisation (Schliwa, 1982). CytD treated Vero E6 cells displayed cellular retraction and arborisation (branching) previously described (Schliwa, 1982) for CytD treatment as well as displaying disrupted actin network organisation where actin appear aggregated and discontinuous in comparison to DMSO treated cells. TULV infected Vero E6 cells displayed less dispersed punctate NP when treated with CtyD in comparison to DMSO mocks. TULV NP perinuclear structures were still observed but appeared more condensed and less tubular in nature (Figure 49). This suggests actin is involved in localisation of TULV NP despite displaying little co-localisation by IF analysis.

#### 4.3.2.3 Inhibition of tubulin polymerisation on TULV NP localisation

To further examine the interaction of the tubulin cytoskeleton on TULV NP localisation, TULV infected Vero E6 cells were treated for 60 minutes with 17 µM nocodazole (NOC) and examined for TULV NP and tubulin localisation by IF analysis. Nocodazole causes the depolymerisation of tubulin by binding to tubulin and preventing polymerisation (Vasquez et al., 1997). NOC treated Vero E6 cells displayed a reduction in tubulin staining and showed a decrease in microtubule structure in comparison to DMSO treated cells. NOC did not appear to have significant impact on TULV localisation as TULV NP was still observed in discrete puncta in addition to compact and tubular macromolecular structures as observed in mock treated Vero E6 cells (Figure 50). This suggests there is no reliance on microtubules for the localisation of TULV NP despite the co-localisation with tubulin in IF. It is likely that multiple mechanisms of TULV NP localisation are employed where if microtubule transportation is inhibit another mechanism may be able to compensate.

#### 4.3.2.4 Inhibition of the motor protein dynein on TULV NP localisation

Dynein, a cytoskeletal motor protein, transports various cargos along microtubules. To examine if dynein had an impact on the localisation of TULV NP, TULV infected Vero E6 cells were treated with 100 µM of EHNA for 24 hours and examined by IF . EHNA is an adenosine deaminase inhibitor which blocks ATPase function of dynein (Bouchard et al., 1981). EHNA treatment did not appear to have a significant impact on the cytoplasmic distribution of TULV NP or tubulin (Figure 51).

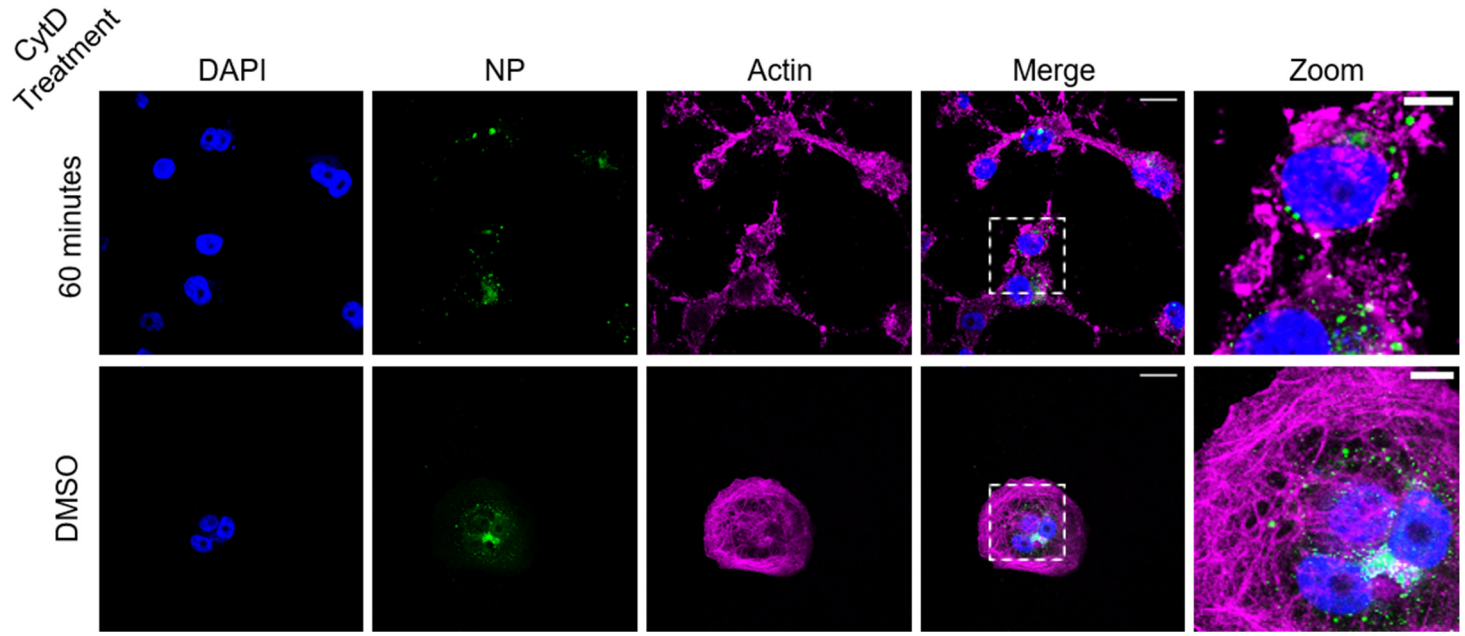


**Figure 49 Actin filament depolymerisation and degradation may impact TULV NP localisation at 30 dpi.**

Actin filaments were depolymerised and degraded by treating Vero E6 cells with 10 μM cytochalasin D (CytD) and observing the effect of this on TULV NP localisation using LSCM at 40 X magnification. The white bar represents 30 μm and 10 μm in zoomed images. Nuclei were stained with DAPI (blue), TULV NP detected using NP antisera (green) and actin filaments detected using antibodies against β-actin (magenta).

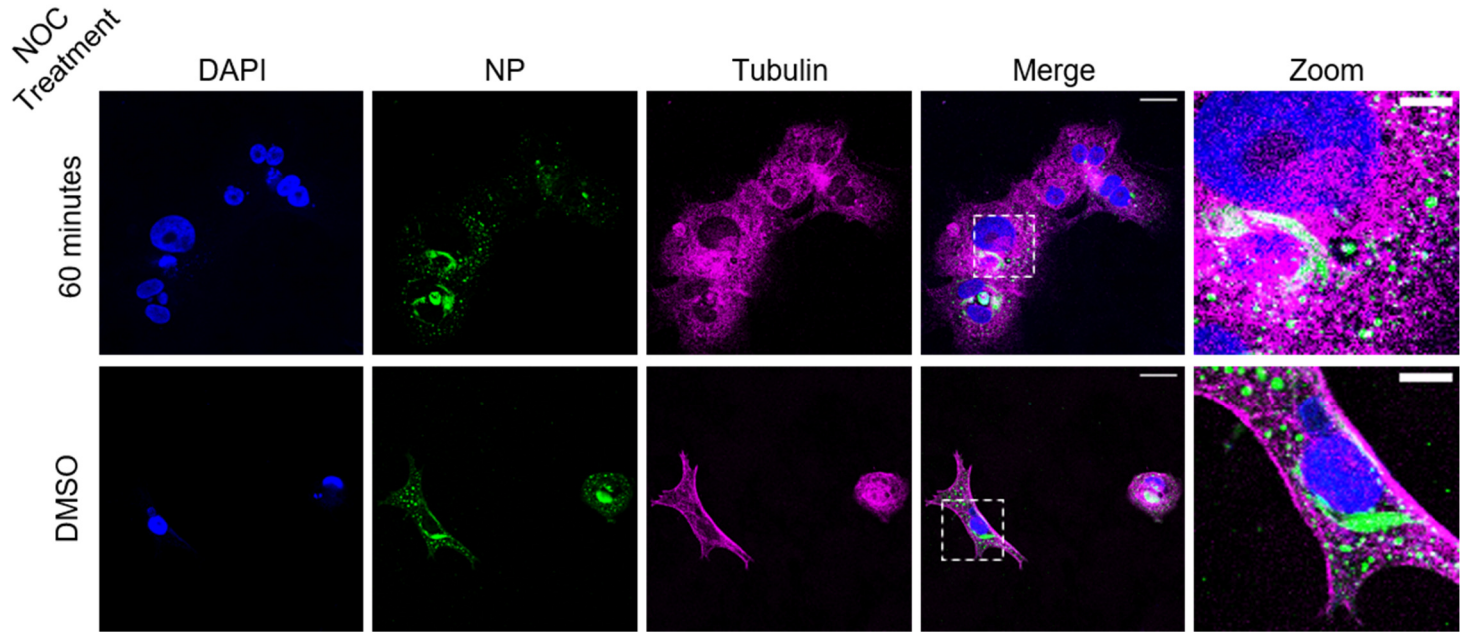


**Figure 50 Microtubule depolymerisation does not alter TULV NP localisation at 30 dpi.**

Microtubules were depolymerised by treating Vero E6 cells with 17 μM for 60 minutes. The effect of TULV NP localisation under these conditions was assessed by LSCM at 40 X magnification. The white bar represents 30 μm and 10 μm in zoomed images. Nuclei were stained with DAPI (blue), TULV NP detected using NP antisera (green) and microtubules detected using antibodies against β-tubulin (magenta).

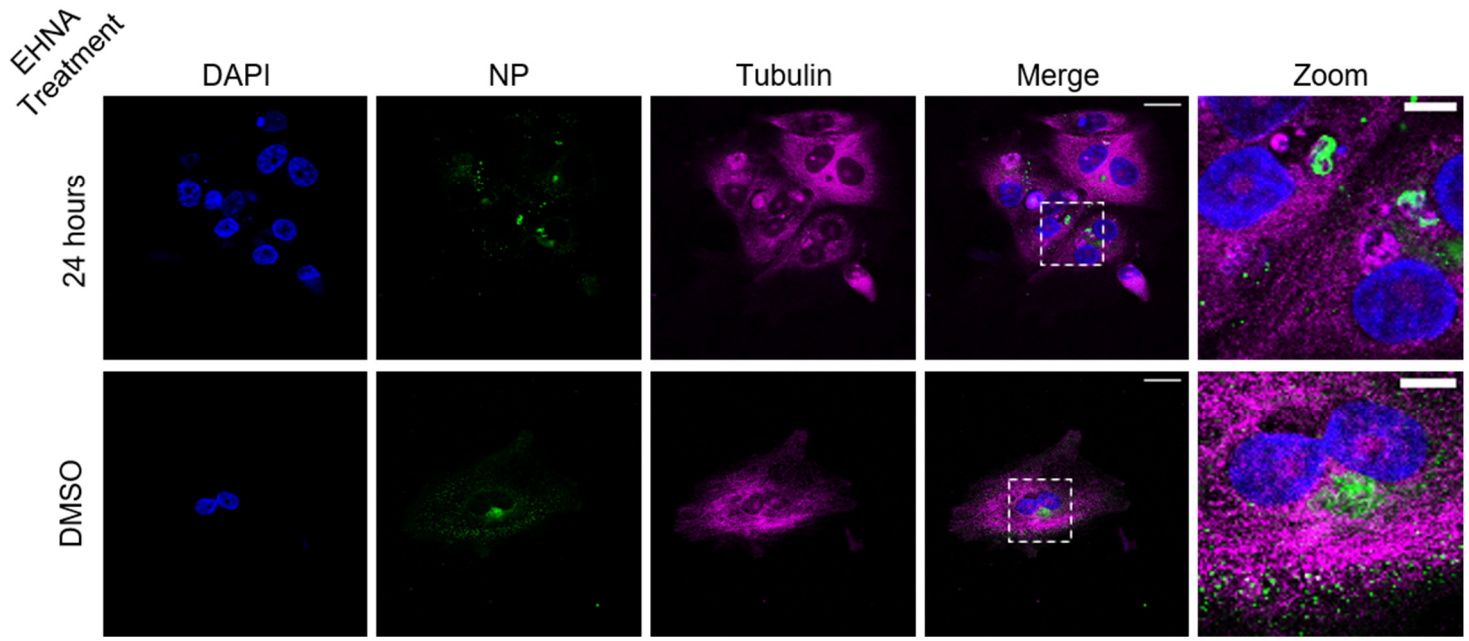


**Figure 51 Inhibition of dynein does not alter TULV NP localisation at 30 dpi.**

The function of the motor protein dynein was inhibition by treating Vero E6 cells with 100 µM erythro-9-(2-hydroxy-3-nonyl)adenine (EHNA) for 24 hours. The effect of TULV NP localisation was examined using LSCM at 40 X magnification. The white bar represents 30 µm and 10 µm in zoomed images. Nuclei were stained with DAPI (blue), TULV NP detected using NP antisera (green) and microtubules detected using antibodies against β-tubulin (magenta).

#### 4.3.2.5 Effect of vimentin reorganisation on TULV NP localisation

To further examine the interaction between vimentin filaments and TULV NP, and how this association influences NP localisation, TULV infected Vero E6 cells were treated with 400 nM okadaic acid (OA) and examined for TULV NP and vimentin localisation by IF analysis at 0, 60 and 90 minutes and after recovery by removal of OA. OA is a 38-carbon polyether monocarboxylic acid which induces increased phosphorylation of vimentin Ser56 by inhibiting cellular phosphatases (potentially protein phosphatase 1) which induces a reorganisation of the vimentin network. OA mode-of-action is reversible and after OA removal vimentin filaments have been shown to return to normal cellular morphology (Lee et al., 1992; Candenas et al., 1992).

OA had a significant impact on vimentin organisation and caused reorganisation of the intermediate filament at 60 and 90 minutes post treatment as vimentin filaments appeared disassembled and vimentin staining was concentrated around the cell nucleus instead of in organised filaments throughout the cell. Vero E6 cells were recovered by removing OA and growing for 18 hours in 2% media. Recovered cells displayed a more normal phenotype of vimentin organisation where staining was less concentrated around the cell nucleus and the reappearance of vimentin filaments was observed (Figure 52). Depolymerisation of vimentin had a significant impact on TULV NP localisation; at 60 and 90 minutes post-treatment, the characteristic perinuclear structures of NP observed at 0 minutes post-treatment and in untreated cells were no longer apparent. Tubular structures of TULV NP could no longer be seen and there was a marked reduction in the number of punctate NP in the cytoplasm and puncta appeared less dispersed in the cytoplasm. These results suggest vimentin filaments are required for the maintenance of TULV NP filaments and macromolecular structures.

OA treatment also resulted in a marked reduction in cytoplasmic punctate TULV NP. NP distribution was less perinuclear and instead was located towards the outer part of the cytoplasm. When OA was removed, vimentin filaments re-polymerised and TULV NP regained its punctate distribution and reformed perinuclear tubular structures. Interestingly, these NP structures appear to be within a vimentin “cage”. This suggests vimentin may be required for the

formation and maintenance of multimeric NP structures and filaments (Figure 52).

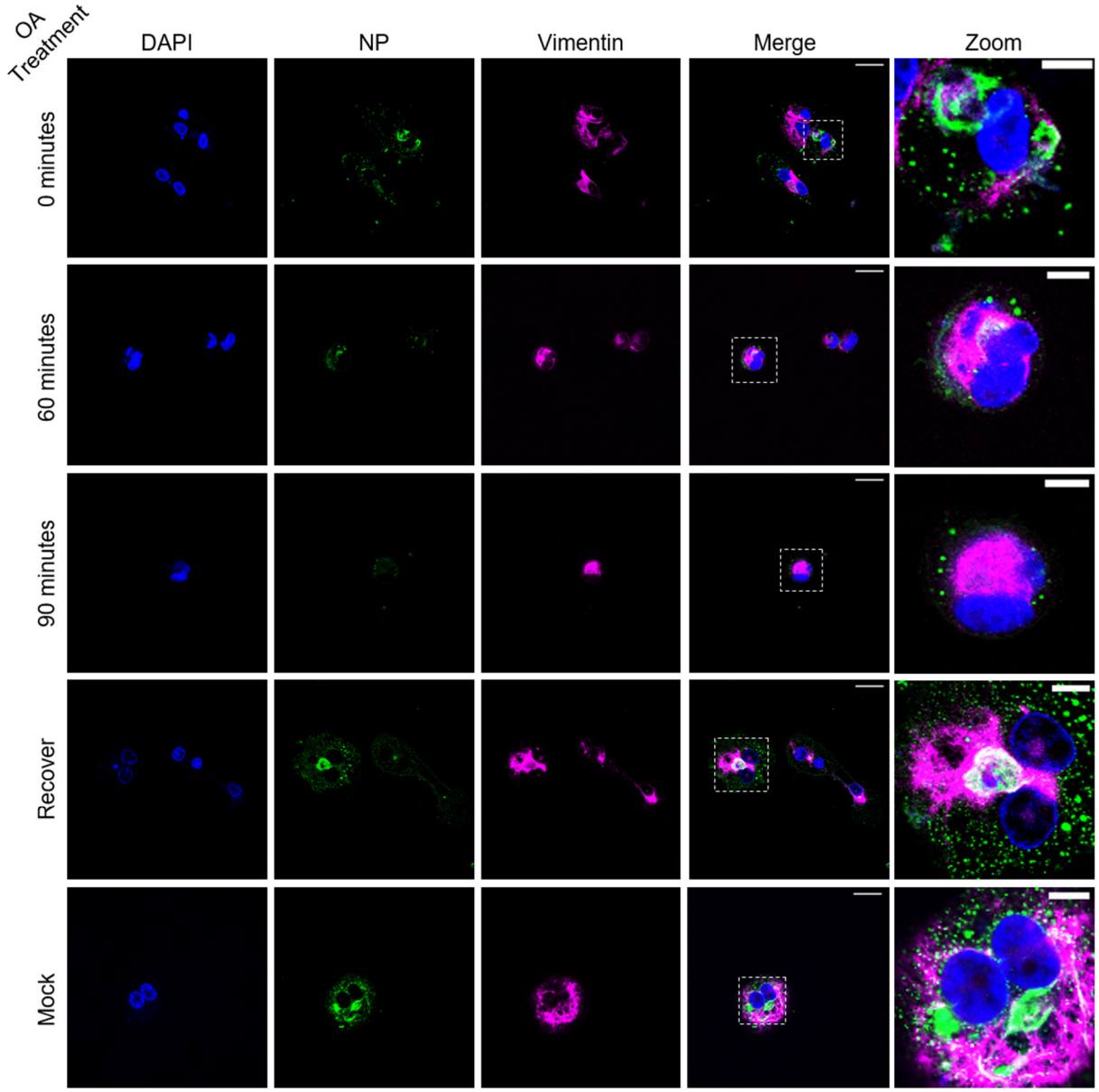


**Figure 52 Vimentin dissassembly and reorganisation alters the localisation of TULV NP.**

Vimentin filaments were disassembled by treatment with 400 nM okadaic acid (OA) for 60 and 90 minutes. Recovery of vimentin filaments was induced by removal of OA. Inhibition of vimentin using okadaic acid (OA) on TULV NP localisation using LSCM at 40 X magnification. The white bar represents 30 µm and 10 µm in zoomed images. Nuclei were stained with DAPI (blue), TULV NP detected using NP antisera (green) and vimentin (magenta).

#### 4.3.2.6 Section Summary

This section describes the co-localisation and interaction of TULV NP with components of the host cell cytoskeleton; actin, tubulin and vimentin. The interaction of TULV NP with components of the host cell cytoskeleton was examined through co-localisation analysis and fluorescent line scan. TULV NP was found to strongly co-localise with microtubules. Actin filaments showed no co-localisation with TULV NP, at any of the time points tested. Vimentin filaments showed high levels of co-localisation with TULV NP during peak infections (7dpi). These results suggests TULV NP is transported through cells on microtubules. However, inhibition of host-cell cytoskeletal components revealed microtubule depolymerisation did not alter the localisation of TULV NP. Instead, actin filament depolymerisation showed slight alteration in TULV NP localisation where NP was less dispersed in the cytoplasm. This suggests that TULV NP may be transported along microtubules but the maintenance of the TULV NP compartments may require actin in either a transient or indirect manner.

The disassembly of vimentin filaments had the most striking impact on the localisation of NP, where formation of perinuclear tubular structures of NP were completely abrogated and the number of cytoplasmic puncta reduced. Recovery of the vimentin network lead to the reformation of cytoplasmic NP structures. Taken together these results suggest that the vimentin network is highly important for the formation and maintenance of TULV NP structures.

### 4.3.3 Interaction of TULV NP with host cell organelles

#### 4.3.3.1 Interaction between TULV NP and the ER and Golgi network

To assess the interaction of host organelles with TULV NP, the intracellular localisation of the endoplasmic reticulum (ER) and Golgi network was examined alongside TULV NP by IF analysis and fluorescent line-scan. TULV infected Vero E6 cells were examined at predefined early (36 hpi), peak (7 dpi) and persistent (30 dpi) time points. To identify the location of the ER, a fluorescently labelled ER stain Concanavalin A (ConA) was used. ConA is a lectin which binds selectively to $\alpha$-mannopyranosyl and $\alpha$-glucopyranosyl residues in the ER. ER staining by ConA displays characteristic staining at all time points and no co-localisation between the ER and TULV NP was observed when examined by IF analysis and fluorescent line scan (Figure 53, Figure 54, Figure 55).

The Golgi network displayed characteristic Golgi staining at 36 hpi when using the Golgi marker and did not co-localise with TULV NP (Figure 53). At 7 dpi, the Golgi network retained some characteristic staining but also large perinuclear structures were observed which co-localised with TULV NP staining. In addition, some punctate NP bodies were observed to co-localise with Golgi staining (Figure 54). At 30 dpi, this effect was more pronounced with infected Vero E6 cells displaying no typical Golgi network stain and instead strong co-localisation with TULV NP (Figure 55). Vero E6 cells showing high concentration of TULV NP were observed alongside several Vero E6 displaying no infection or very low level TULV infection (Figure 55B). Comparison between TULV-infected and uninfected cells revealed TULV infection induces a decrease in granular Golgi staining and increase in aggregated, tubular staining which co-localises well with TULV NP. This suggesting that TULV infection may interfere with, or remodel, organisation of the Golgi network. Analysis of the spatial distribution of the Golgi network alongside TULV NP revealed increasing co-localisation as infection progressed. At early time points, very little co-localisation was observed but by 7 dpi around 50 % of the total punctate bodies of NP displayed co-localisation with the Golgi stain (Figure 56).

Recombinantly expressed TULV NP achieved by transfection of Vero E6 cells with pcDNA 3.1 (+) TULV S ORF was examined for co-localisation with the ER and Golgi network by IF analysis. In agreement with previous results from TULV infected Vero E6 cells, there was no co-localisation between TULV NP and the

ER. However, recombinant TULV NP co-localized with the Golgi network, however only non-typical Golgi staining was observed. The morphology of Golgi staining in transfected cells was the same as described for persistently infected cell cultures. Neighbouring, non-transfected, cells displayed the normal granular phenotype expected for the Golgi. This suggests that TULV NP alone is involved in altering the organisation of the Golgi network (Figure 57).

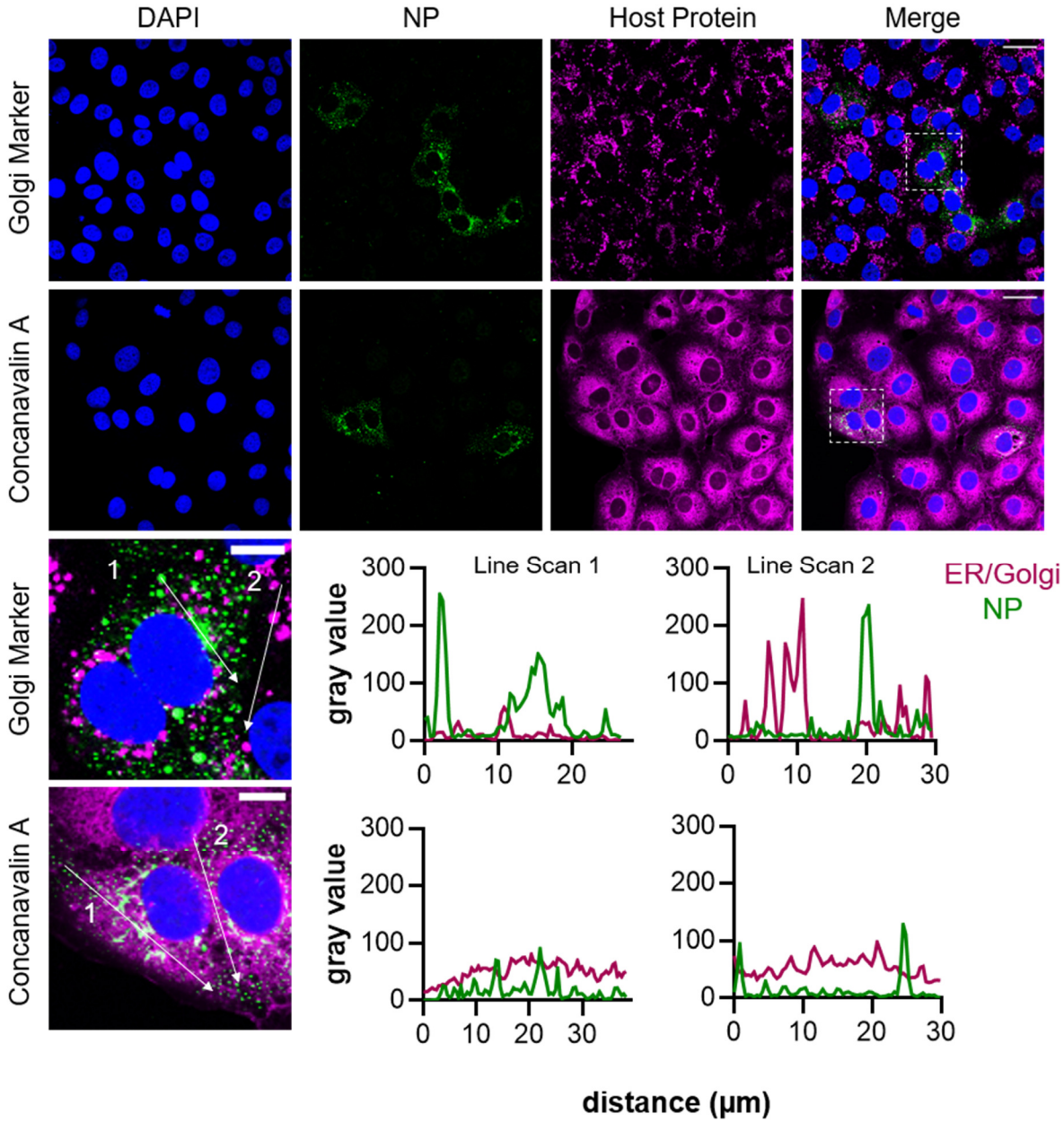


**Figure 53 Co-localisation between TULV NP, Endoplasmic reticulum and Golgi network in Vero E6 cells at 36 hpi.**

The spatial distribution of the endoplasmic reticulum and the Golgi network (magenta) was observed alongside TULV NP (green) in TULV infected Vero E6 cells at 36 hpi using LSCM at 40 X magnification. Vero E6 cells were infected at MOI 0.1. The white bar represents 30 µm and 10 µm in zoomed images. Fluorescent line scans taken using Fiji software. Nuclei were stained with DAPI (blue), TULV NP detected using NP antisera, endoplasmic reticulum was detected using ConA stain and Golgi network detect using Golgi Marker antibody

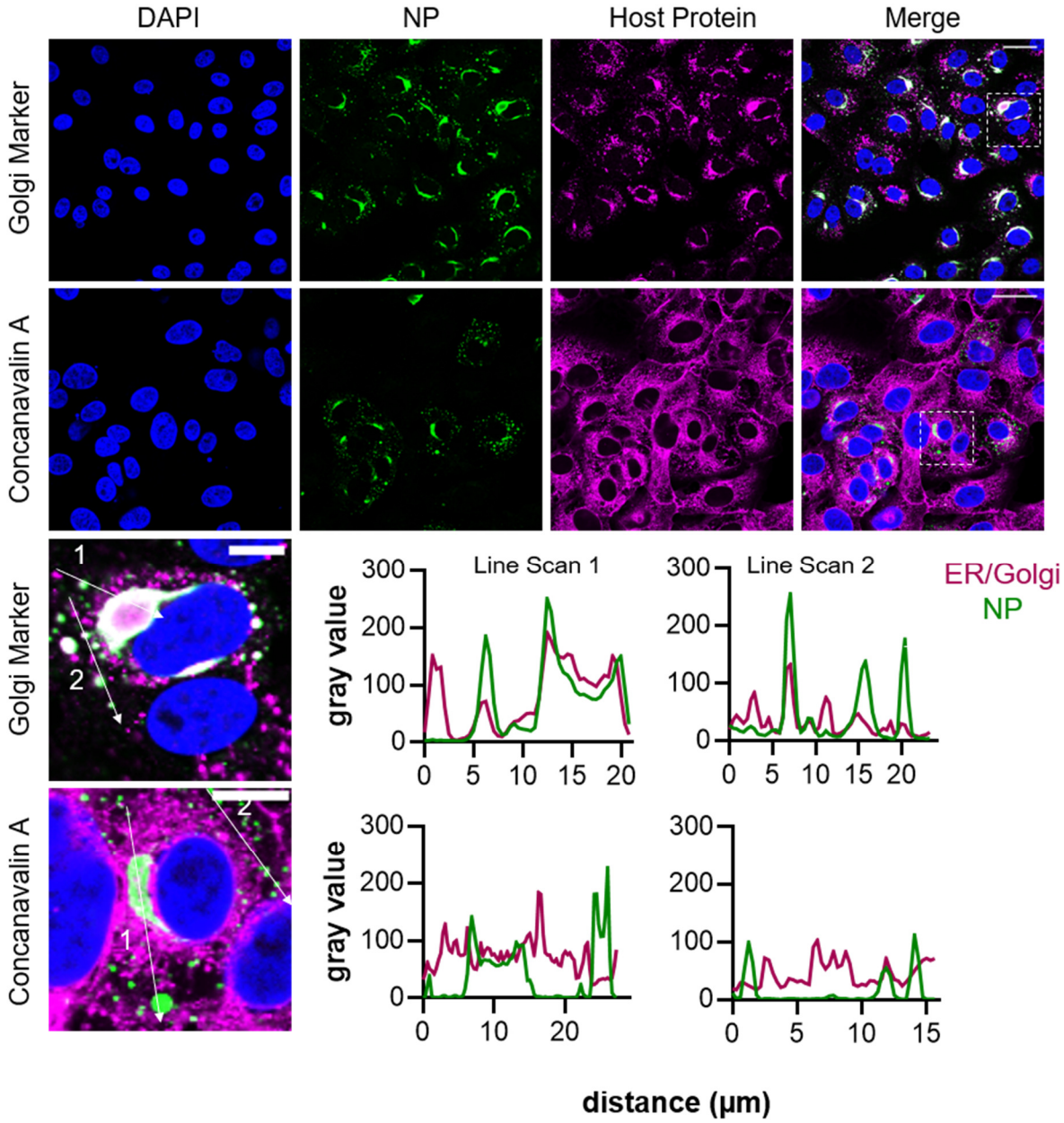


**Figure 54 Co-localisation between TULV NP, Endoplasmic reticulum and Golgi network in Vero E6 cells at 7 dpi.**

The spatial distribution of the endoplasmic reticulum and the Golgi network (magenta) was observed alongside TULV NP (green) in TULV infected Vero E6 cells at 7 dpi using LSCM at 40 X magnification. Vero E6 cells were infected at MOI 0.1. The white bar represents 30 µm and 10 µm in zoomed images. Fluorescent line scans taken using Fiji software. Nuclei were stained with DAPI (blue), TULV NP detected using NP antisera, endoplasmic reticulum was detected using ConA stain and Golgi network detect using Golgi Marker antibody

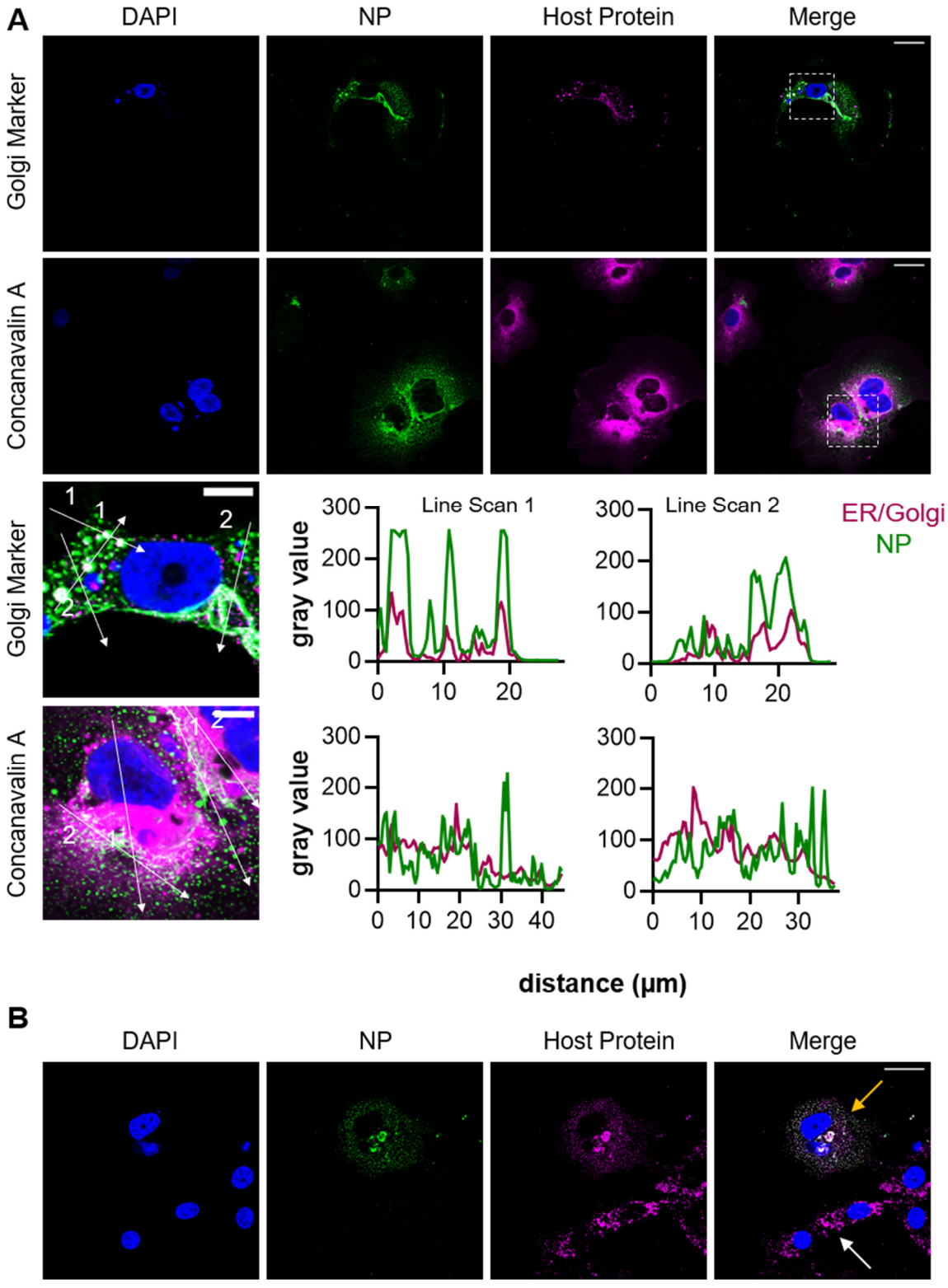


**Figure 55 Co-localisation between TULV NP, Endoplasmic reticulum and Golgi network in Vero E6 cells during persistent infection.**

**Figure 55 Co-localisation between TULV NP, Endoplasmic reticulum and Golgi network in Vero E6 cells during persistent infection.**

A) The spatial distribution of the endoplasmic reticulum and the Golgi network (magenta) was observed alongside TULV NP (green) in TULV infected Vero E6 cells at 30 dpi using LSCM at 40 X magnification. Vero E6 cells were infected at MOI 0.1. B) TULV infected Vero E6 cells at 30 dpi displaying a population of uninfected cells (white arrow) alongside an infected cell (yellow arrow) The white bar represents 30 µm and 10 µm in zoomed images. Fluorescent line scans taken using Fiji software. Nuclei were stained with DAPI (blue), TULV NP detected using NP antisera, endoplasmic reticulum was detected using ConA stain and Golgi network detect using Golgi Marker antibody

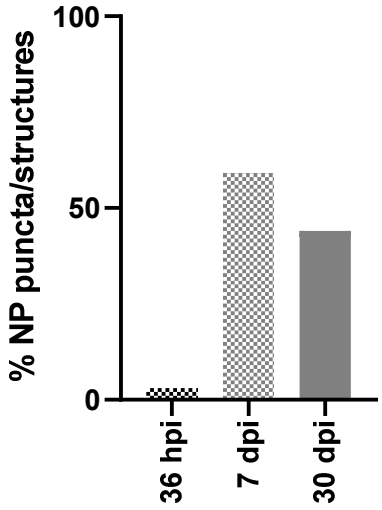


**Figure 56 Quantification of TULV NP puncta and structures co-localising with Golgi markers.**

Co-localisation was assessed using Fiji software. For each time point (36 hpi, 7 dpi and 30 dpi) at least 100 TULV NP puncta/filaments were examined for co-localisation with Golgi Marker

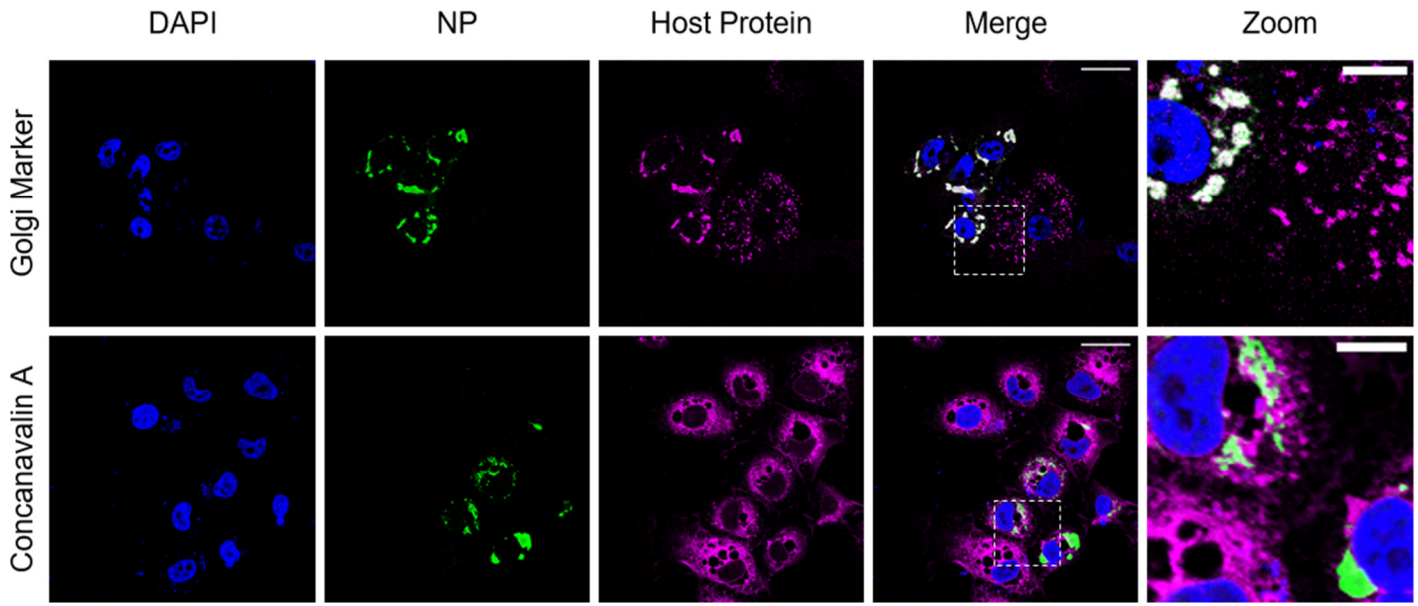


**Figure 57 Location of endoplasmic reticulum and Golgi network with transfected TULV NP within Vero E6 cells.**

LSCM images of Vero E6 cells transfected with pcDNA3.1 (+) TULV NP at 18 hours post transfection using 40 X magnification. The white bar represents 30 µm. Nuclei were stained with DAPI (blue), TULV NP detected using NP antisera (green), endoplasmic reticulum was detected using ConA stain and Golgi network detect using Golgi Marker antibody (magenta)

### 4.3.4 Interaction of TULV NP with host cell stress granules and P bodies

#### 4.3.4.1 Co-localisation between TULV NP, stress granules and P bodies

TIA-1 is one of several proteins involved in the formation of stress granules and therefore can be used as a stress granule marker whereas DCP1a is an mRNA decapping enzyme and can be used as a positive marker for P bodies. Previous studies on orthohantaviruses have suggested NP localises to P bodies and binds to the capped 5'-ends of host cell mRNAs. The capped mRNAs are used as a substrate by the RdRp to act as primers for viral transcription. As TULV NP forms multiple puncta in the cytoplasm during infection it is likely a percentage of these puncta co-localise with P bodies to carry out this "cap-snatching" role (Garcin et al., 1995; Mir and Panganiban, 2010; Cheng and Mir, 2012). In addition, stress granule formation is a known response to viral infection. Several viruses have been shown to interact with components of stress granules such as DENV, CHIKV and WNV (Emara and Brinton, 2007; Fros et al., 2012).

To examine the possibility of interaction between TULV NP with either stress granules or P bodies, IF examination and fluorescent line scan analysis was carried out on TULV infected Vero E6 cells using specific antisera for NP, DCP1a and TIA-1.

Throughout all time points examined, DCP1a retained its characteristic punctate distribution throughout the cytoplasm (Figure 58,Figure 59,Figure 60). TIA-1 signal was barely detectable at early time points suggesting initial infection does not upregulate expression of TIA-1 (Figure 58) which is also consistent with the ability of TULV to avoid or supress host cell pathogen surveillance mechanisms. However, the TIA-1 signal increased throughout peak and persistent infection time points suggesting TULV infection had upregulated TIA-1 expression as infection progressed (Figure 59, Figure 60). The upregulation of TIA-1 is indicative of a cell undergoing the stress response due to viral infection.

At 36 hpi, very little co-localisation was observed between TULV NP and the signal for DCP1a and TIA-1 (Figure 58). At 7 and 30 dpi, IF analysis showed TIA-1 co-localised with TULV NP, especially in condensed TULV NP structures in the perinuclear region. TIA-1 structures observed in the cytoplasm during infection are punctate and granular which phenotypically resembles stress granules (Sola et al., 2011). However, we were unable to co-localise TIA-1 and G3BP1 (G3BP

Stress Granule Assembly Factor) in these locations which would have led to positive identification of stress granule formation (data not shown). G3BP1 is a DNA-unwinding enzymes which localises to stress granules along with TIA-1.

In contrast, DCP1a signals did not co-localise with TULV NP structures at either 7 or 30 dpi time points, although DCP1a puncta were proximal to TULV NP puncta, as shown by fluorescent line scan (Figure 59, Figure 60). The distribution of DCP1a as distinct puncta throughout the cytoplasm remained constant throughout infection suggesting TULV infection does not upregulate formation of P bodies.

In order to provide a quantitative measurement of the extent of co-localization, TULV NP in both puncta and macromolecular structures were examined for co-localisation with TIA-1 or DCP1a by fluorescent line scan and counted. This revealed that low levels of TULV NP co-localised with DCP1a at all time points with little increase over the time course. However, TIA-1 co-localised with around 40 % of TULV NP structures and puncta at 7 dpi and 30 dpi (Figure 59, Figure 60).

Recombinantly expressed TULV NP in Vero E6 was examined for interaction with stress granule marker, TIA-1, and P body marker, DCP1a, by IF analysis. In agreement with previous results from TULV infected Vero E6 cells, there was no co-localisation of recombinant TULV NP with DCP1a. However, recombinant TULV NP did co-localise with TIA-1 suggesting that TULV NP alone interacts with TIA-1 and may induce the formation of stress granules or stress granule like vesicles without the need for additional viral components or activities (Figure 61).

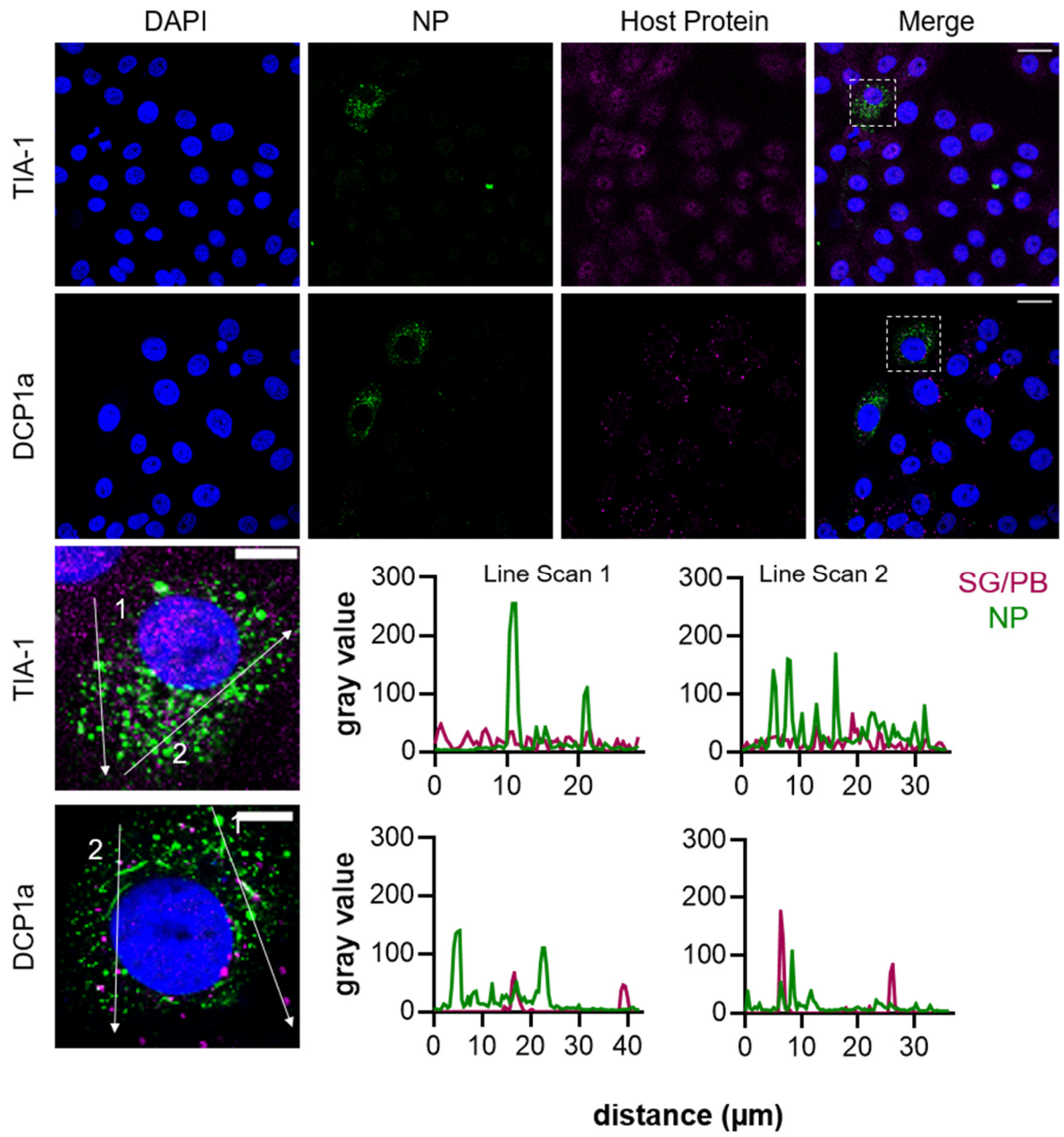


**Figure 58 Co-localisation of stress granules and P bodies with TULV NP in Vero E6 cells at 36 hpi.**

The spatial distribution of stress granules (TIA-1) and P bodies (DCP1a) (magenta) was observed alongside TULV NP (green) in TULV infected Vero E6 cells at 36 hpi by LSCM at 40 X magnification. Vero E6 cells were infected at MOI 0.1. The white bar represents 30 µm and 10 µm in zoomed images. Fluorescent line scans taken using Fiji software. Nuclei are stained with DAPI (blue), TULV NP detected using NP antisera and cytoskeleton detected using antibodies against TIA-1 and DCP1a

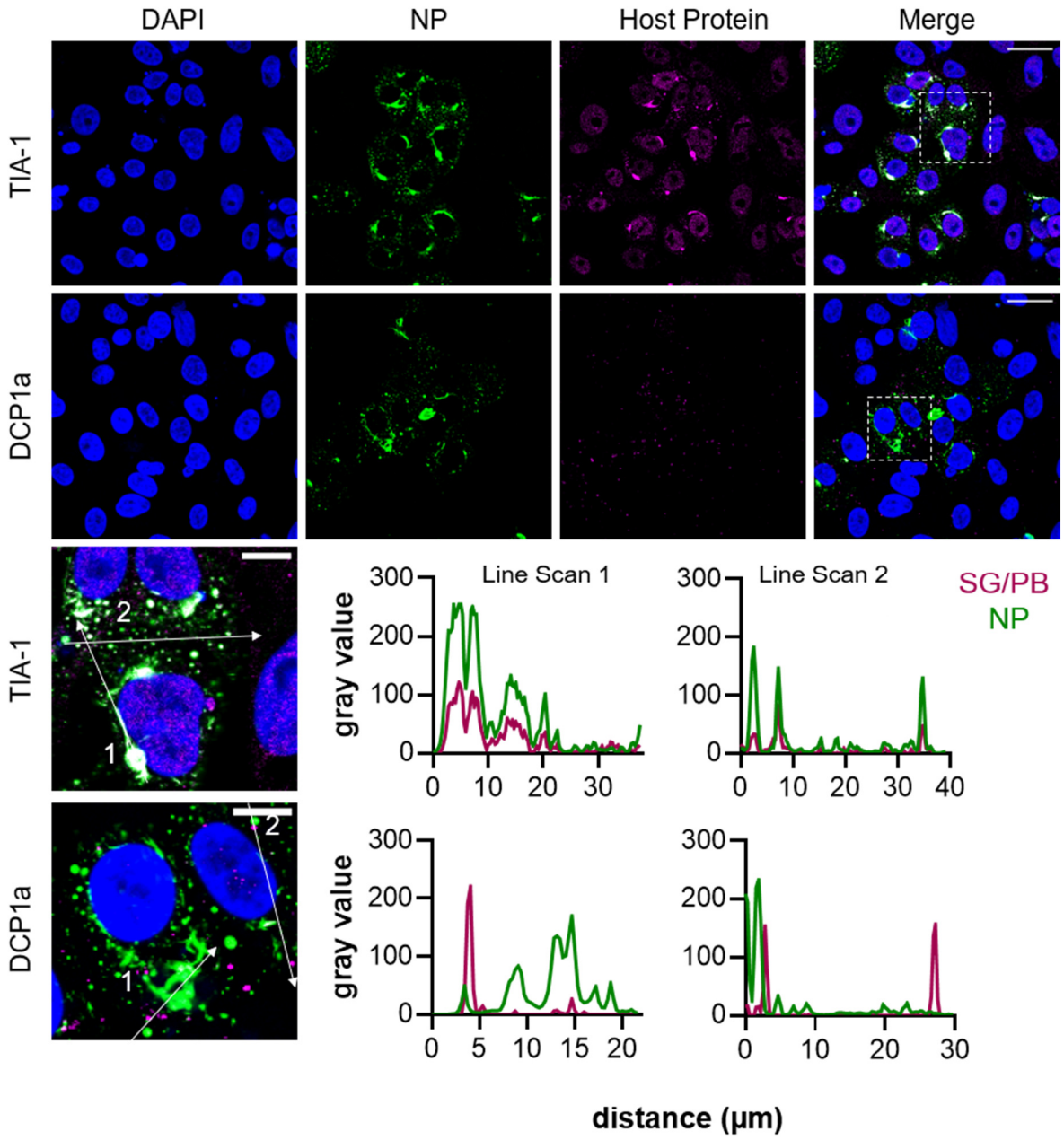


**Figure 59 Co-localisation of stress granules and P bodies with TULV NP in Vero E6 cells at 7 dpi.**

The spatial distribution of stress granules (TIA-1) and P bodies (DCP1a) (magenta) was observed alongside TULV NP (green) in TULV infected Vero E6 cells at 7 dpi by LSCM at 40 X magnification. Vero E6 cells were infected at MOI 0.1. The white bar represents 30 µm and 10 µm in zoomed images. Fluorescent line scans taken using Fiji software. Nuclei are stained with DAPI (blue), TULV NP detected using NP antisera and cytoskeleton detected using antibodies against TIA-1 and DCP1a

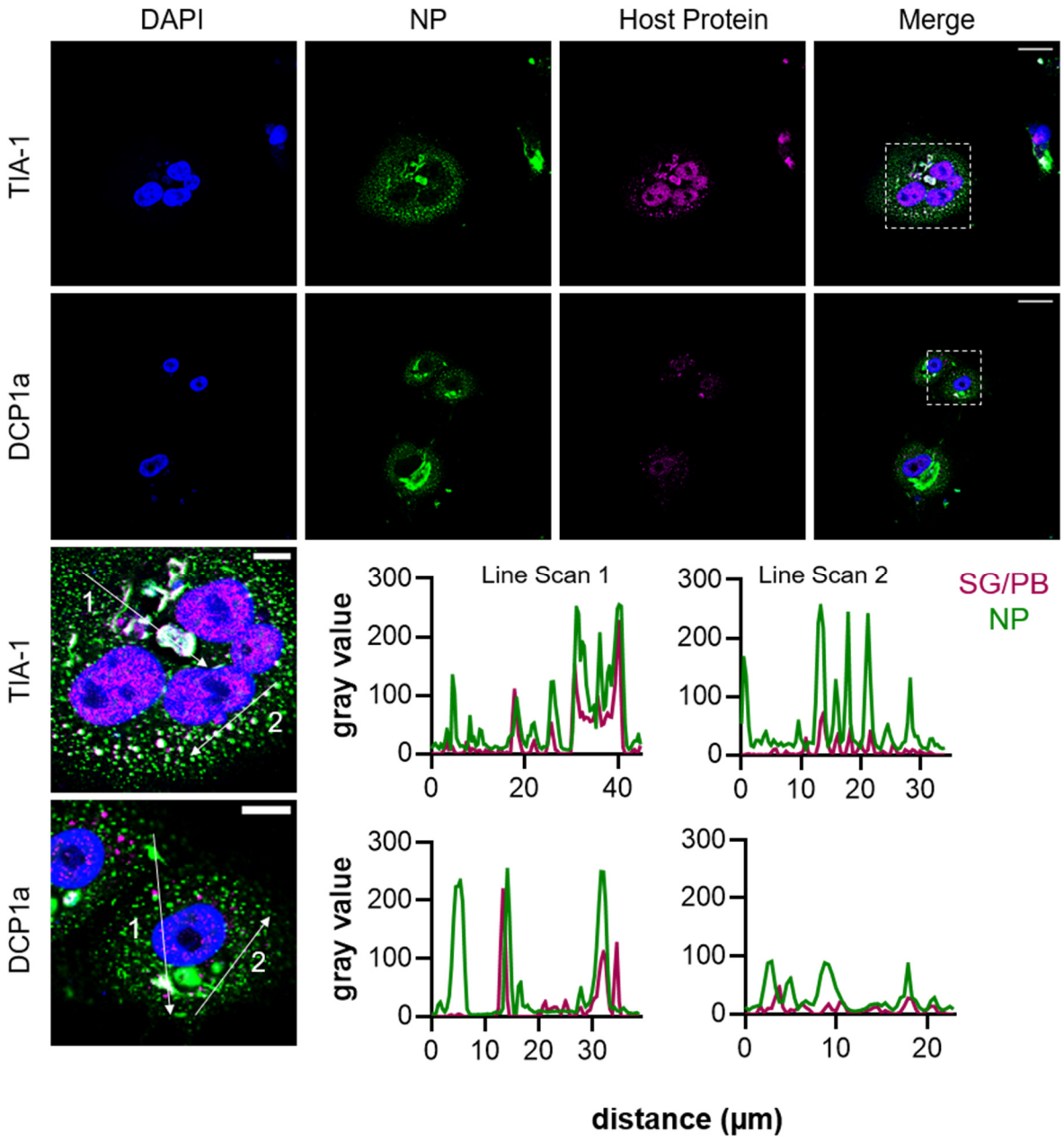


**Figure 60 Co-localisation of stress granules and P bodies with TULV NP in Vero E6 cells during persistent infections.**

The spatial distribution of stress granules (TIA-1) and P bodies (DCP1a) (magenta) was observed alongside TULV NP (green) in TULV infected Vero E6 cells at 30 dpi by LSCM at 40 X magnification. Vero E6 cells were infected at MOI 0.1. The white bar represents 30 µm and 10 µm in zoomed images. Fluorescent line scans taken using Fiji software. Nuclei are stained with DAPI (blue), TULV NP detected using NP antisera and cytoskeleton detected using antibodies against TIA-1 and DCP1a

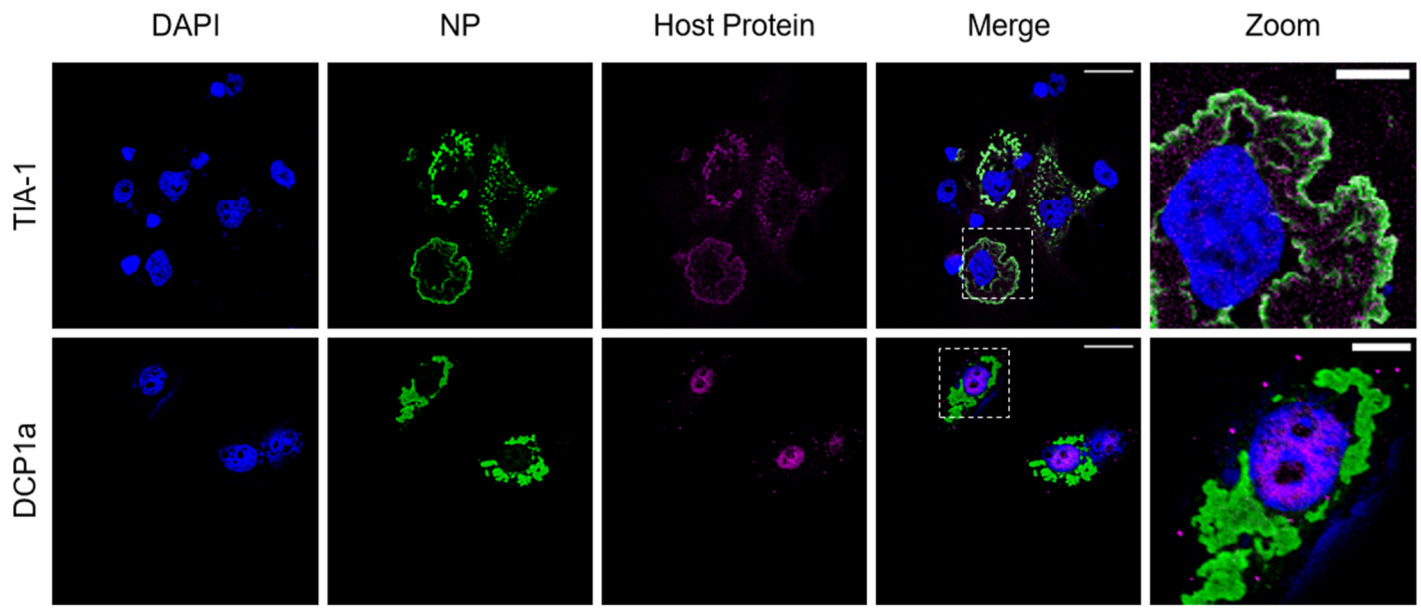


**Figure 61 Detection of stress granule and P body markers and transfected TULV NP.**

LSCM images of Vero E6 cells transfected with pcDNA3.1 (+) TULV NP at 18 hours post transfection using 40 X magnification. The white bar represents 30 µm. Nuclei were stained with DAPI (blue), TULV NP detected using NP antisera (green) and stress granule and P body markers (magenta).

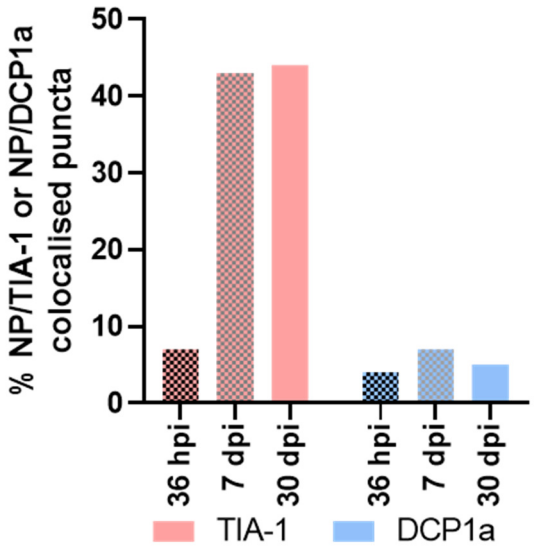


**Figure 62 TULV NP puncta and structures co-localising with stress granule or P body markers.**

Co-localisation was assessed using Fiji software. For each time point (36 hpi, 7 dpi and 30 dpi) at least 100 puncta/structures were counted

### 4.3.5 Interaction of TULV NP with host cell trafficking proteins

#### 4.3.5.1 Co-localisation between TULV NP and endosomes, lysosomes and transport vesicles

To further assess the intracellular location of TULV NP and examine whether it associated with trafficking proteins, IF analysis and fluorescent line scan analysis was carried out of TULV NP and the trafficking proteins Rab5 (early endosomes), Rab7 (early to late endosomes), Rab11, (early, late and recycling endosomes), LAMP1 (lysosomes) and clathrin (clathrin-coated vesicles).

At 36 hpi and 30 dpi these various trafficking markers showed characteristic granular straining patterns expected of trafficking vesicles (Figure 63, Figure 65). At 36 hpi, some puncta of TULV NP displayed co-localisation of puncta of Rab5, Rab11 and clathrin suggesting that these proteins may be utilised for the trafficking of TULV NP at early stages in the lifecycle. Co-localisation with Rab5, Rab11 and clathrin was only observed within cytoplasmic puncta and not within tubular structures in the perinuclear region (Figure 63

**Figure 63 Co-localisation of trafficking proteins with TULV NP in Vero E6 cells at 36 hpi.**

, Figure 64). No co-localisation was observed for TULV NP with Rab7 or LAMP1. The lack of co-localisation with LAMP suggests, for TULV infections, entry into lysosomes is not required during the virus lifecycle (Figure 63, Figure 64). At 30 dpi, clathrin displayed co-localisation with a few TULV NP puncta within the cytoplasm. Puncta co-localising with clathrin tended to be larger in size. Clathrin vesicles observed in uninfected cells were on average ~ 0.7 µm in diameter whereas the diameter of clathrin vesicles co-localising with TULV NP were 1.5-2.5 µm diameter. No other trafficking proteins were observed to co-localise with NP at the 30 dpi time point (Figure 65, Figure 66).

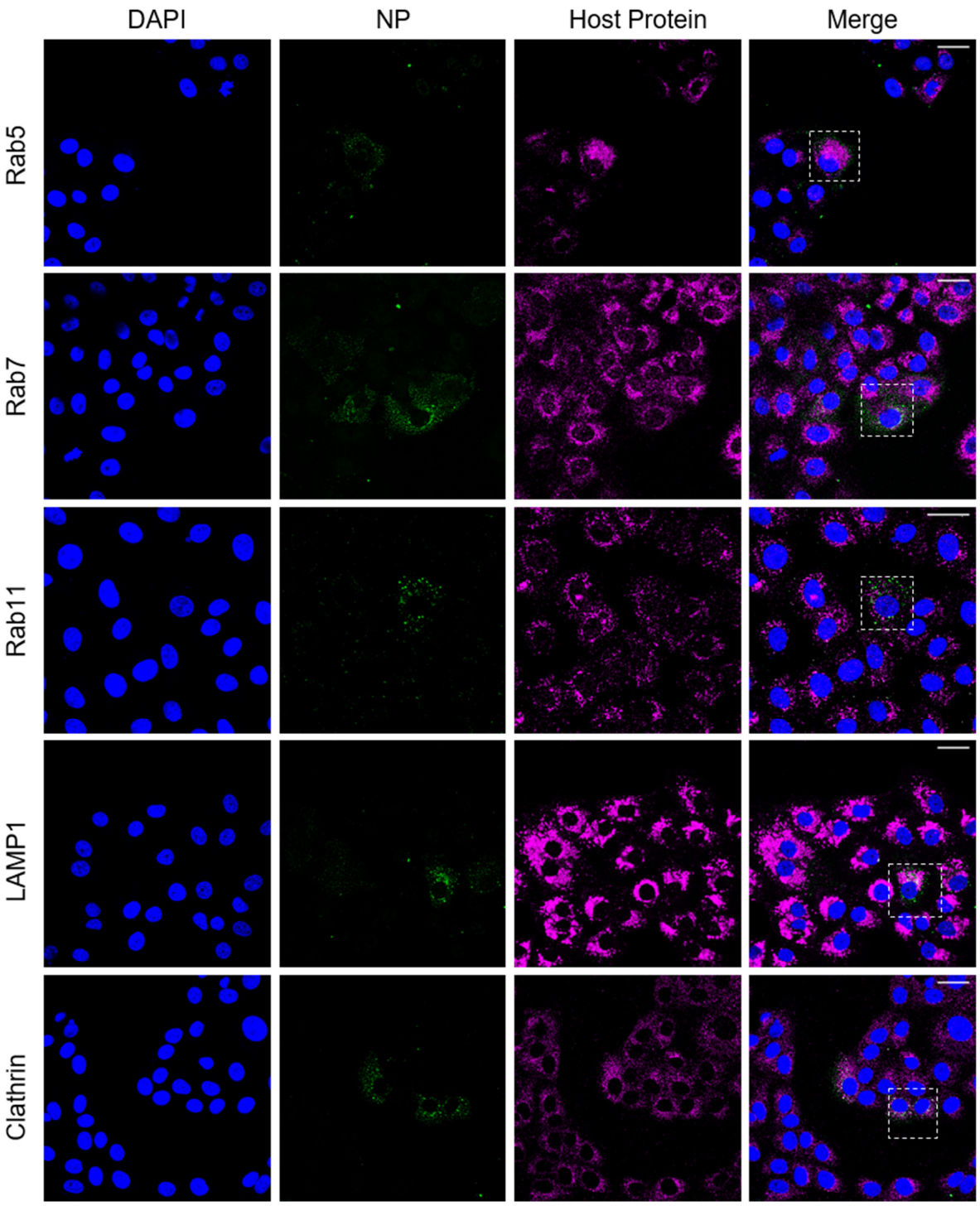


**Figure 63 Co-localisation of trafficking proteins with TULV NP in Vero E6 cells at 36 hpi.**

**Figure 63 Co-localisation of trafficking proteins with TULV NP in Vero E6 cells at 36 hpi.**

The spatial distribution of the trafficking proteins; Rab5 (early endosome), Rab7 (early/late endosome), Rab11 (early late, recycling endosome), LAMP1 (lysosome) and clathrin (coated vesicles) (magenta) was observed alongside TULV NP (green) in TULV infected Vero E6 cells at 36 hpi by LSCM at 40 X magnification. Vero E6 cells were infected at MOI 0.1. The white bar represents 30 µm. Nuclei are stained with DAPI (blue), TULV NP detected using NP antisera and trafficking proteins detected using antibodies against Rab5, Rab7, Rab11, LAMP1 and clathrin.

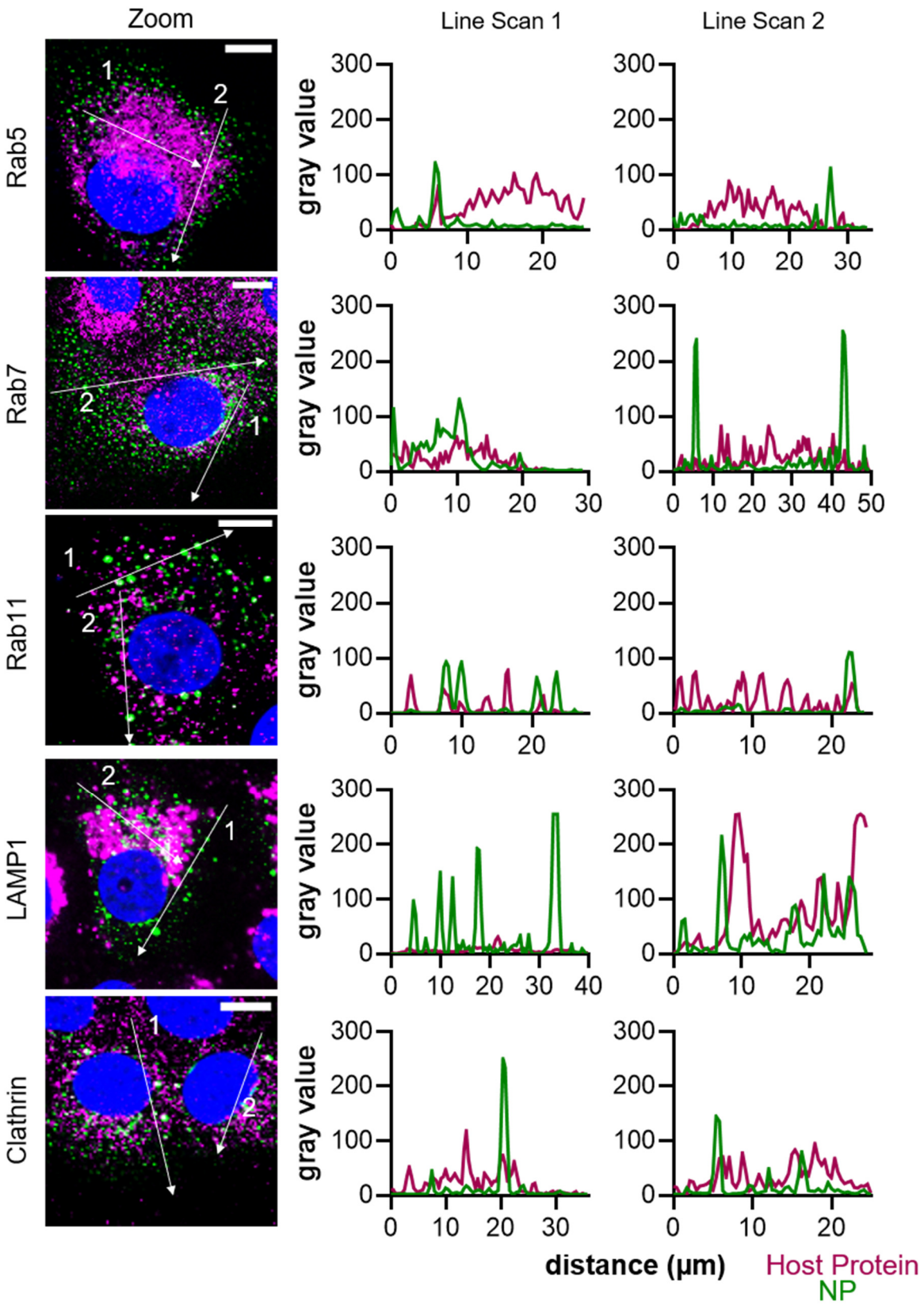


**Figure 64 Co-localisation of trafficking proteins with TULV NP in Vero E6 cells at 36 hpi.**

**Figure 64 Co-localisation of trafficking proteins with TULV NP in Vero E6 cells at 36 hpi.**

The spatial distribution of Rab5, Rab7, Rab11, LAMP1 and clathrin (magenta) was observed alongside TULV NP (green) in TULV infected Vero E6 cells at 36 hpi by LSCM at 40 X magnification. Images are zoom versions of co-localisations seen in Figure 63. The white bar represents 10 µm. Fluorescent line scans taken using Fiji software. Nuclei are stained with DAPI (blue), TULV NP detected using NP antisera and trafficking proteins detected using antibodies against Rab5, Rab7, Rab11, LAMP1 and clathrin.

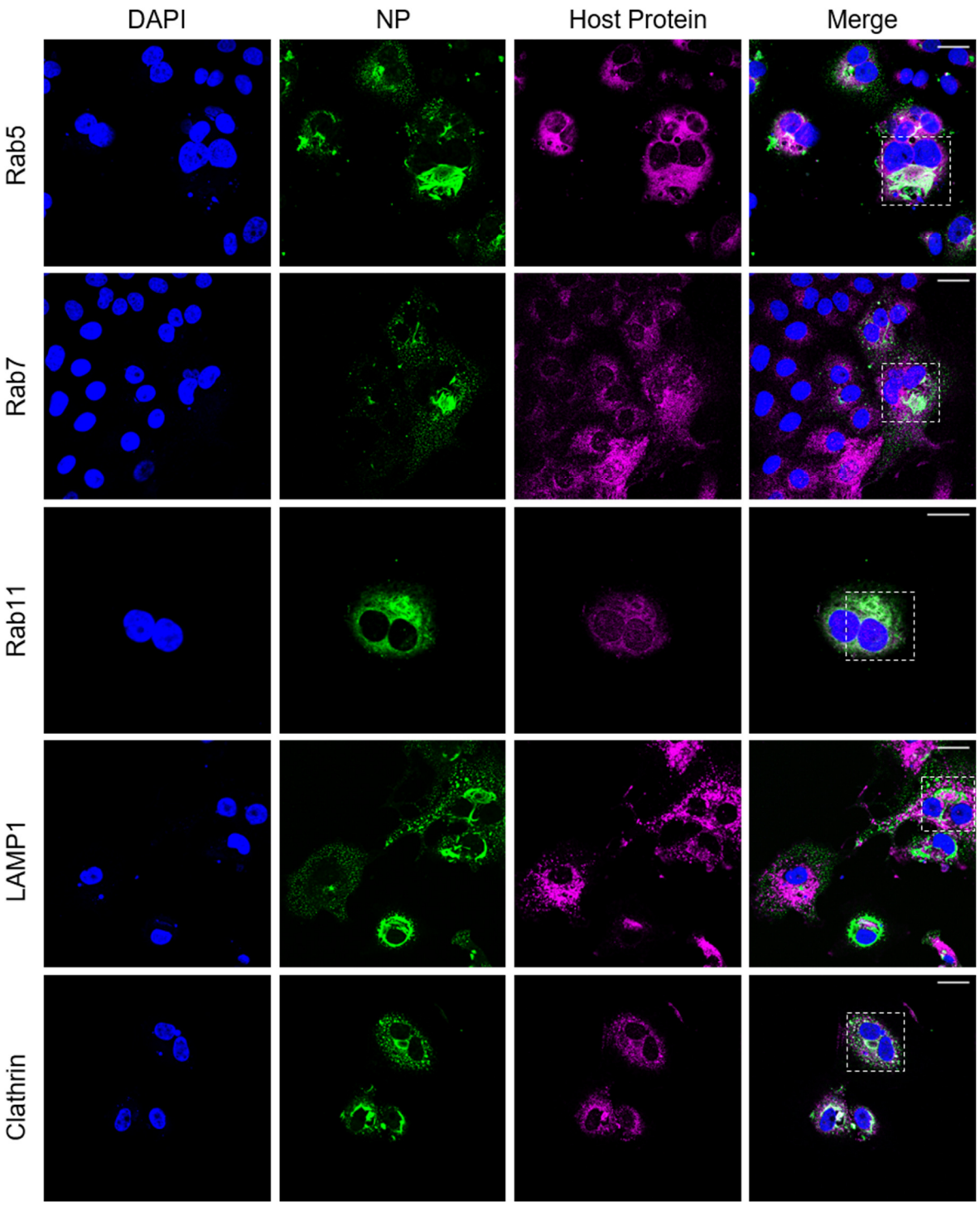


**Figure 65 Co-localisation of trafficking proteins with TULV NP in Vero E6 cells during persistent infections.**

**Figure 65 Co-localisation of trafficking proteins with TULV NP in Vero E6 cells during persistent infections.**

The spatial distribution of the trafficking proteins; Rab5 (early endosome), Rab7 (early/late endosome), Rab11 (early late, recycling endosome), LAMP1 (lysosome) and clathrin (coated vesicles) (magenta) was observed alongside TULV NP (green) in TULV infected Vero E6 cells at 30 dpi by LSCM at 40 X magnification. Vero E6 cells were infected at MOI 0.1. The white bar represents 30 µm. Nuclei are stained with DAPI (blue), TULV NP detected using NP antisera and trafficking proteins detected using antibodies against Rab5, Rab7, Rab11, LAMP1 and clathrin.

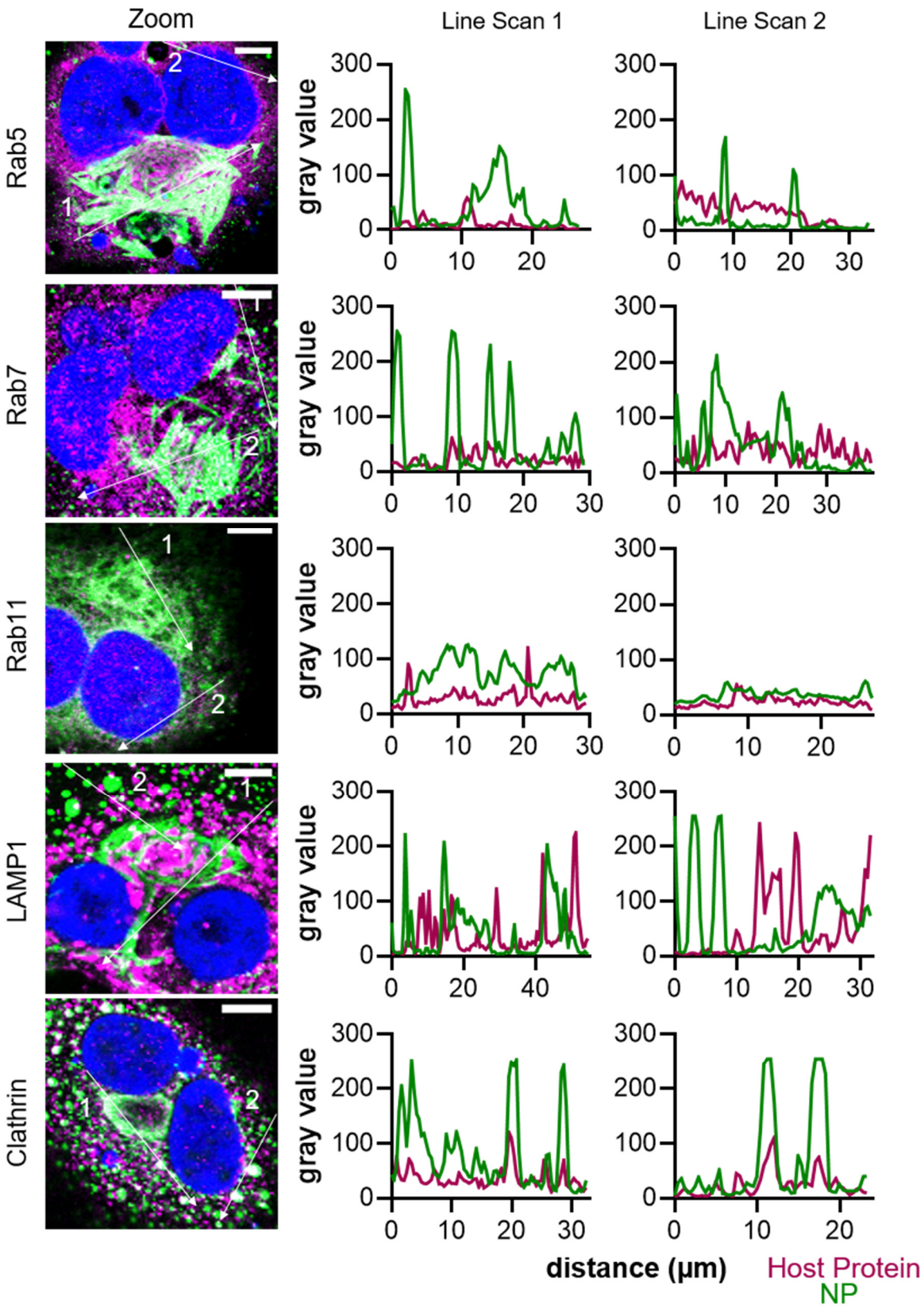


**Figure 66 Co-localisation of trafficking proteins with TULV NP in Vero E6 cells during persistent infections.**

**Figure 66 Co-localisation of trafficking proteins with TULV NP in Vero E6 cells during persistent infections.**

The spatial distribution of Rab5, Rab7, Rab11, LAMP1 and clathrin (magenta) was observed alongside TULV NP (green) in TULV infected Vero E6 cells at 30 dpi by LSCM at 40 X magnification. Images are zoom versions of co-localisations seen in Figure 65. The white bar represents 10 µm. Fluorescent line scans taken using Fiji software. Nuclei are stained with DAPI (blue), TULV NP detected using NP antisera and trafficking proteins detected using antibodies against Rab5, Rab7, Rab11, LAMP1 and clathrin

### 4.3.6 Interaction of TULV NP with host cell cleaved caspase-3

#### 4.3.6.1 TULV infection interferes with apoptotic induction

To examine the apoptotic response of Vero E6 cells to TULV infection, cell lysates were collected every 24 hpi up to 10 dpi and again at 30 dpi and examined for the presence of the apoptotic markers caspase-3 (casp-3), cleaved caspase-3 (casp-3C) and cleaved poly (ADP-ribosome) polymerase (PARP-C). Caspase-3 was detected in cell lysates and increased in abundance in later time points consistent with the GAPDH loading control. Active casp-3C, indicative of apoptosis induction, was detected in TULV cell lysates from 5-6 dpi and increased in abundance up to the final time point of 30 dpi. This suggested that TULV was an inducer of apoptosis in cell culture, however a lack of PARP-C was evident at 6-10 dpi and only a moderate amount of PARP-C observed at 30 dpi. This further suggests, that although the apoptotic marker casp-3C was present in TULV infected cell cultures, it failed to trigger cell death. One possibility was that the activity of a TULV component suppressed or blocked the induction of apoptosis (Figure 67).

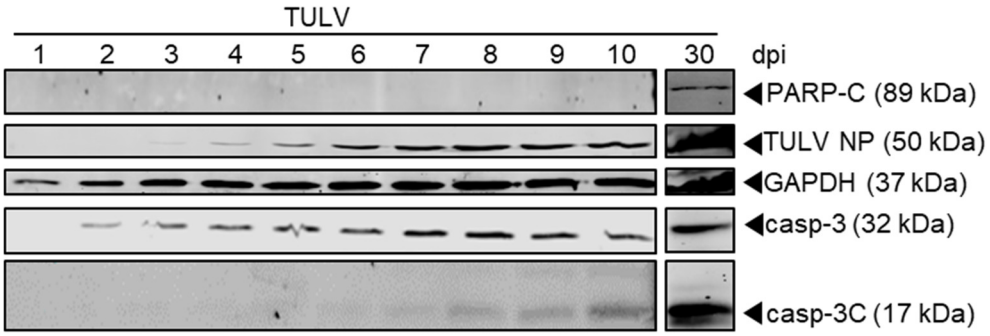


**Figure 67 Detection of TULV NP with caspase 3 and PARP during TULV infection.**

Left hand panel displays TULV cell lysates collected from 0-10 dpi and 30 dpi examined for the presence on casp-3, casp-3C, PARP-C and TULV NP alongside a GAPDH loading control.

#### 4.3.6.2 Interaction between active caspase-3 and TULV NP

The results described above suggest that the activity of the executioner casp-3C may be supressed in TULV-infected cells. Thus, the intracellular location of both active caspase-3 and TULV NP was examined in individual TULV infected Vero E6 cells using indirect IF and fluorescent line scan analysis within cells at early, peak and persistent infection time points. At 36 hpi, TULV NP staining was abundant within infected cells whereas minimal signal for casp-3C was observed. However, casp-3C was abundant in uninfected bystander cells suggesting apoptotic induction (Figure 68, Figure 70). This may be due to these bystander cells receiving indirect recognition signals from adjacent TULV-infected cells, thus inducing an apoptotic state. Fluorescent line-scan analysis revealed clear segregation of TULV NP staining from casp-3C staining in the adjacent TULV-infected and bystander cells (Figure 68). To quantify this observation, the number of infected (TULV NP stained) cells and uninfected cells were counted, which revealed casp-3C staining in over 60 % of bystander cells but only in 4 % of TULV-infected cells (Figure 70). This is supported by imaging of TULV infected cells using WFDM where increased signal for casp-3C can be detected in uninfected bystander cells and low signal casp-3C is detected in TULV infected cells (Figure 69A).

At 7 dpi and 30 dpi, TULV NP punctate bodies and perinuclear cytoplasmic structures exhibited co-localisation staining with casp-3C, and fluorescent line scan analysis revealed that this co-localisation was consistent between the two markers (Figure 68). Further examination of co-localisation of TULV NP and casp-3C in persistently infected cells was carried out using WFDM to enhance detection sensitivity. WFDM revealed that TULV infected cells exhibited casp-3C staining within discrete cytoplasmic puncta. While some casp-3C staining were distinct from TULV NP localisation, a high level of co-localisation was observed to be contained within TULV puncta. Analysis of the spatial distribution of the two proteins using fluorescent line scan revealed confirmed co-localising signals. Interestingly, TULV NP puncta display the characteristic ‘M’ shape of a hollow vesicle with casp-3C localising within this vesicle (Figure 69).

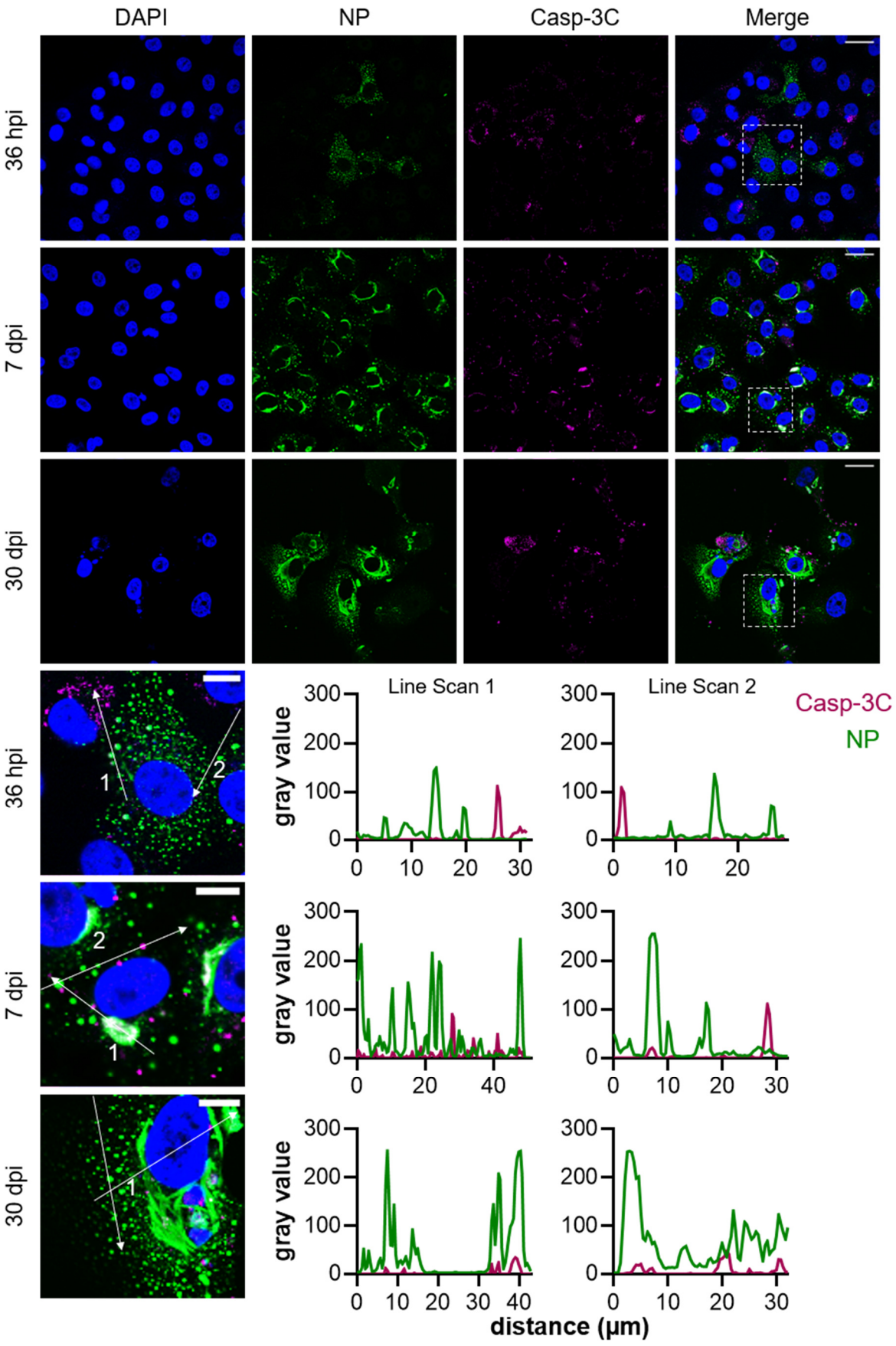


**Figure 68 Co-localisation of cleaved caspase 3 with TULV NP in Vero E6 cells.**

**Figure 68 Co-localisation of cleaved caspase 3 with TULV NP in Vero E6 cells.**

The spatial distribution of casp-3C (magenta) observed alongside TULV NP (green) in TULV infected Vero E6 cells at 36 hpi, 7 dpi and 30 dpi by LSCM at 40 X magnification. Cells infected at MOI 0.1. The white bar represents 30 µm and (10 µm). Fluorescent line scans taken using Fiji software. Nuclei are stained with DAPI (blue), TULV NP detected using NP antisera and active capase-3 detected with casp-3C antibody.

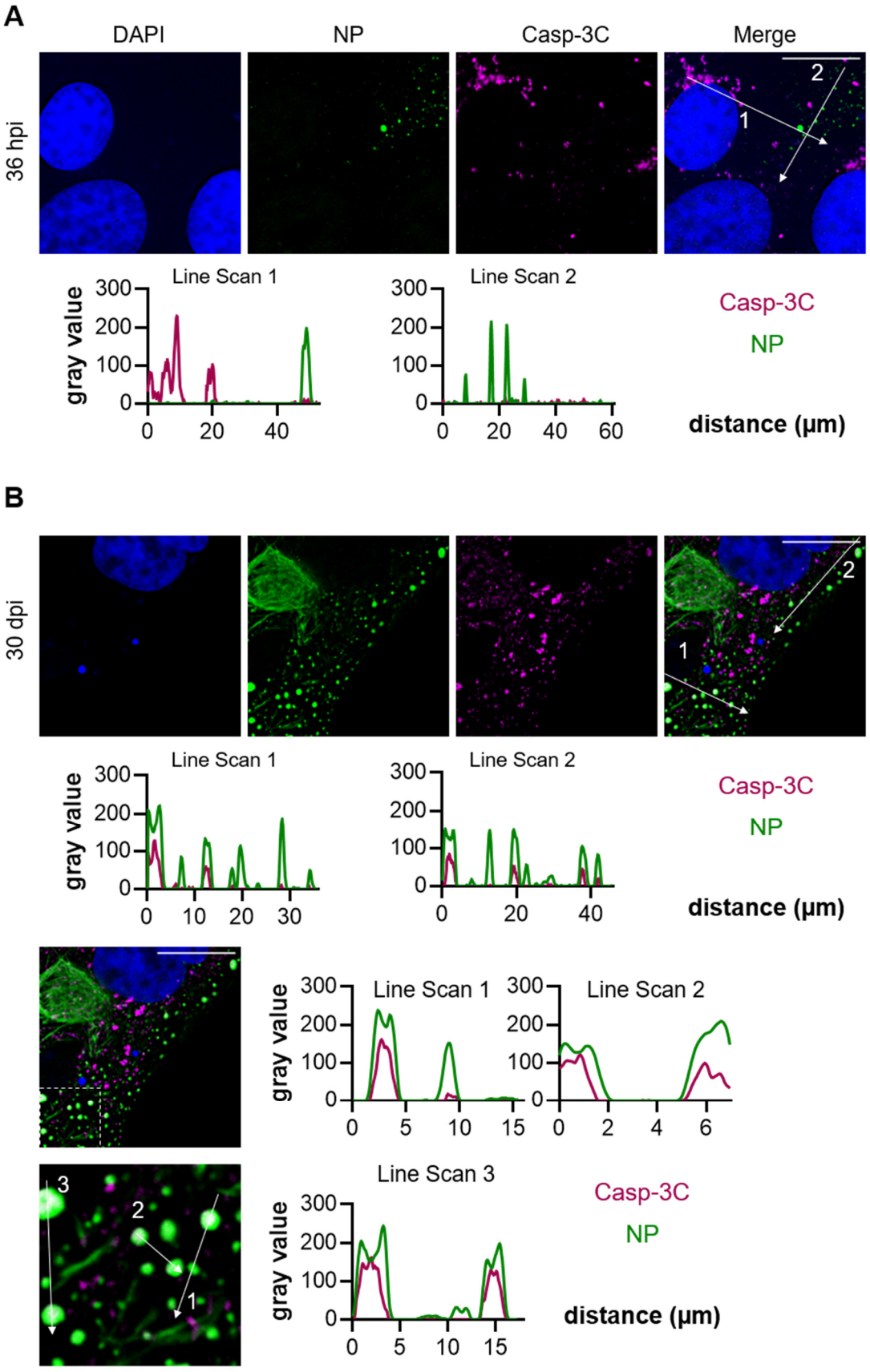


**Figure 69 Co-localisation of cleaved caspase 3 with TULV NP in Vero E6 cells during early and persistent infections through WFDM.**

**Figure 69 Co-localisation of cleaved caspase 3 with TULV NP in Vero E6 cells during early and persistent infections through WFDM.**

The spatial distribution of casp-3C (magenta) observed alongside TULV NP (green) in TULV infected Vero E6 cells at 36 hpi and 30 dpi WFDM 100 X magnification. Cells were infected at MOI 0.1. The white bar represents 30 µm and (10 µm zoom). Fluorescent line scans taken using Fiji software. Nuclei are stained with DAPI (blue), TULV NP detected using NP antisera and active capase-3 detected with casp-3C antibody

#### 4.3.6.3 TULV NP is cleaved in infected cells and associates with casp-3C

The interaction of TULV NP and casp-3C is not unique among the hantaviruses. For other orthohantavirus species; ANDV, DOBV and PUUV, recombinant casp-3C has been shown to mediate cleavage of NP in cell-free assays (Solà-Riera et al., 2019). For ANDV, casp-3C cleaves ANDV at the sequence, $DLID_{285}$, which conforms to the DXXD consensus motif for caspase-3 cleavage (Gupta et al., 2013). Analysis of the TULV NP sequence, revealed the presence of an identical DLID motif. However, while this DLID motif was represent in the NP sequence from ANDV and TULV it was absent in HTNV, PHV and SEOV (Figure 71A). Cleavage at this site was predicted to generate TULV NP fragments of approximately 32 kDa and 16 kDa. TULV cell lysates were examined for NP-derived cleavage products by western blotting using anti-NP antisera which revealed the presence of NP cleavage products matching the predicted masses (Figure 71B). The 16 kDa fragment was detected with high abundance from 3 dpi suggesting NP cleavage occurs early during TULV infection. This represents the first detection of caspase-mediated hantavirus NP cleavage in infected cells.

To further examine the TULV NP and casp-3C interaction, co-immunoprecipitation analysis was performed. Western blot analysis revealed the presence of full-length NP and the NP cleavage products (32 kDa and 16 kDa) along with abundant casp-3C (Figure 72) suggesting that the interaction between casp-3C and TULV NP is highly stable.

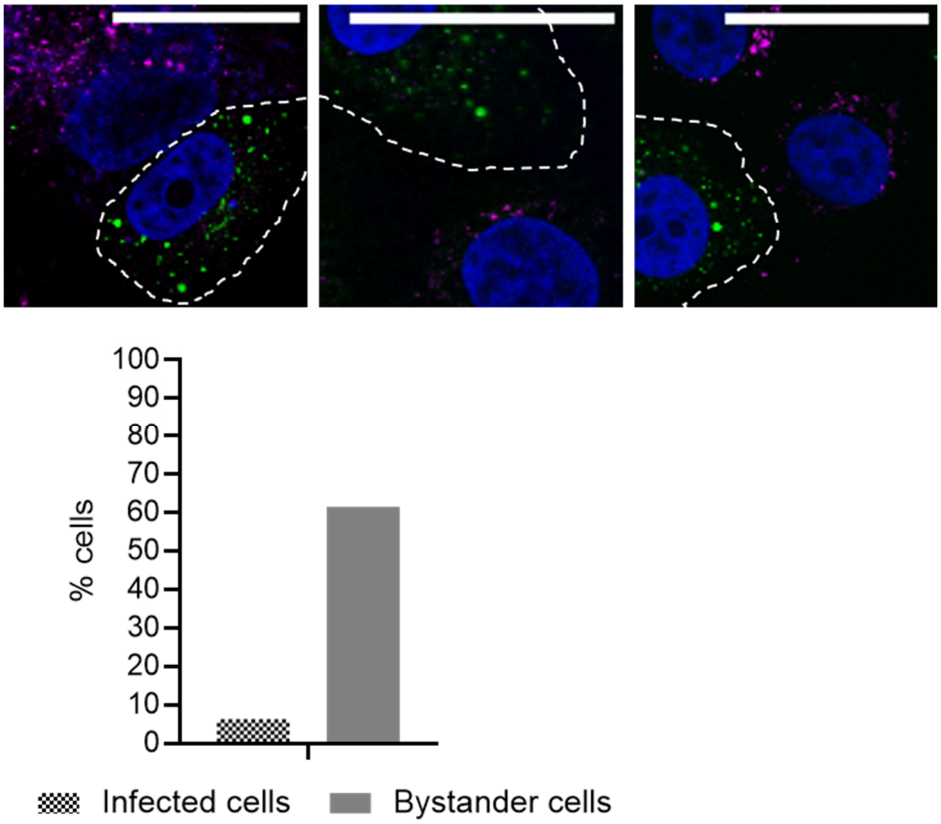


**Figure 70 Bystander cells display signal for cleaved caspase 3.**

LSCM images of TULV infected cells examined for cleaved caspase 3 signal at 36 hpi. The white bar represents 30 µm. Nuclei were stained with DAPI (blue), TULV NP detected using NP antisera (green) and casp-3C (magenta). TULV infected cells are highlighted using the dotted white line. Percentage of TULV infected cells and bystander cells displaying cleaved caspase 3 signal are shown as a histogram.

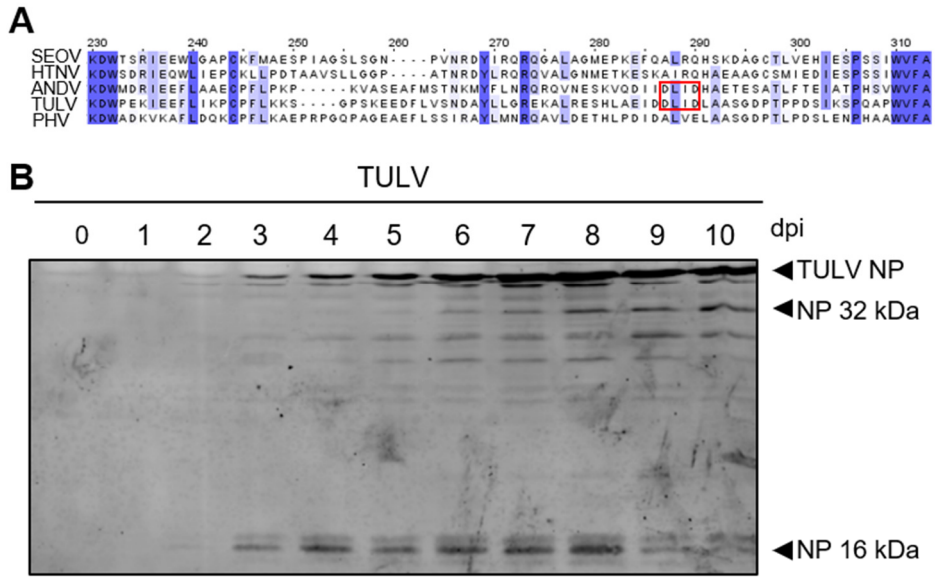


**Figure 71 TULV NP possesses a caspase-3 cleavage site.**

A) Multiple sequence alignment of TULV, SEOV, HTNV, PHV and ANDV NP protein sequences carried out in Clustal W and analysed using Jalview software. Red box highlights the identified caspase-3 cleavage sites B) TULV cell lysates examined for the presence of TULV NP (FL NP) and the cleavage products at 32.4 kDa (*) and 16 kDa (**) assessed by western blot using SEOV NP antisera

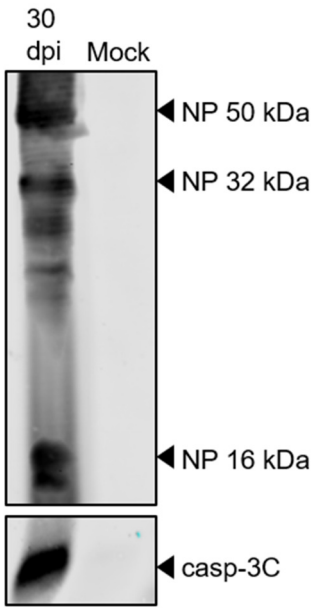


**Figure 72 Co-immunoprecipitation of TULV NP with cleaved caspase-3.**

Co-immunoprecipitation of full length TULV NP and NP cleavage products from cell lysates from TULV 30 dpi and mock-infected cells. Full length NP (FL NP) (50 kDa) and casp-3C (17 kDa) were detected, along with TULV NP cleavage products with molecular masses of 32.4 kDa (*) and 16 kDa (**) assessed by western blot using SEOV NP antisera and casp-3C antibody

### 4.3.7 Section summary

This section describes the co-localisation and interaction of TULV NP with host cell components including the endoplasmic reticulum, Golgi network, Stress granules, P bodies and trafficking proteins. TULV NP forms distinct punctate granules throughout the cytoplasm of infected cells and additionally forms filaments in the perinuclear region. These structures are likely to co-localise with compartments, vesicles or organelles within the host cell as viruses are required to co-opt host cell functions in order to carry out their lifecycles. In order to explore which host cell components might interact with these NP structures and co-localisation analysis. It was found that perinuclear TULV NP structures and some punctate NP co-localised with the Golgi network through early, peak and persistent time points. During later time points, the characteristic granular Golgi network staining was reduced in infected cells and instead co-localised with tubular formations of TULV NP. This suggests that NP may accumulate in and alter the organisation of the Golgi. Additionally, NP was found to co-localise with the stress granule marker, TIA-1, which may act to sequester TIA-1 away from other components required for stress granule formation and in doing so inhibit the cellular stress response to infection.

TULV infected cell lysates were found to contain the presence of casp-3C from 5-6 dpi but not the presence of PARP-C suggesting a block in the apoptotic cascade. TULV NP was found to co-localises with casp-3C and sequesters it in NP-coated vesicles which may spatially separate it from its downstream effector PARP and delay apoptosis. Additionally, the TULV NP ORF was found to contain the casp-3C consensus motif ‘DLID’ and to form predicted cleavage products of ~32 kDa and ~16 kDa. These results suggest TULV NP may inhibit the induction of cellular apoptosis by binding to and sequestering casp-3C.

# Chapter 5 : Identifying the replication sites of TULV *in vitro*

## 5.1 Chapter introduction

This chapter describes an investigation into the location of orthohantavirus replication factories, where viral RNA synthesis and possibly virion assembly takes place. In order to identify these replication sites, the localisation of newly synthesised TULV RNA was attempted by labelling viral RNA using click-chemistry to incorporate an alkyne-tagged uridine analogue (5EU) which could be detected using an aldehyde-tagged fluorophore. In addition to this, the localisation of accumulated viral RNAs was identified using RNA-FISH probes designed against the sense and anti-sense TULV S segment RNA sequences. Furthermore, TULV infected Vero E6 cells were analysed for the localisation of RNA and TULV NP alongside target host components identified in the previous chapter, namely the Golgi network marker and stress granule marker TIA-1.

## 5.2 Results: Identification of TULV replication sites

### 5.2.1 Introduction to methods for labelling viral RNA

#### 5.2.2 Click-IT(TM) RNA Imaging

Click-IT™ RNA imaging utilises click chemistry, which relies upon an azide-alkyne coupling reaction to specifically label nascent RNA within cells (Jao and Salic, 2008). This is achieved using an alkyne-labelled nucleoside, 5-ethynyl uridine (5EU) that is recognised by cellular and viral RNA polymerases and is metabolically-incorporated into growing RNA strands. The subsequent addition of an azide-labelled fluorophore allows the location of the newly synthesised 5EU-incorporated RNA to be identified by confocal microscopy within fixed and permeabilized cells (Jao and Salic, 2008) (Figure 73). As 5EU is recognized as a substrate by both cellular and viral RNA polymerases, selective incorporation into viral transcripts is achieved by incubating cells with actinomycin D to inhibit host cell DNA-directed RNA synthesis. The azide-alkyne coupling reaction rate is low, so catalytic amounts of copper (Cu(I) or Cu(II)) are added which increases reaction rates significantly and improves

reaction selectivity (Rostovtsev et al., 2002; Breinbauer and Köhn, 2003). This method has been previously used for the labelling of coronavirus RNA (a positive sense RNA virus) and hRSV RNA (a non-segmented negative-sense RNA virus) (Hagemeijer et al., 2012; Rincheval et al., 2017).

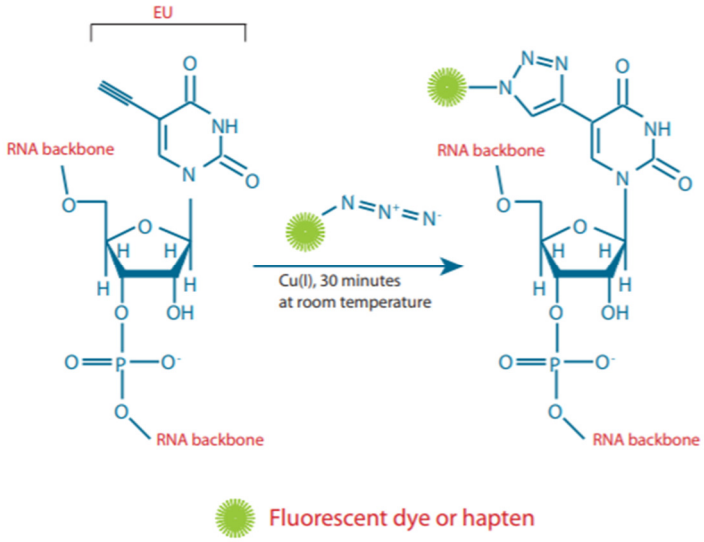


**Figure 73 Click chemistry reaction between alkyne-modified EU and azide-modified fluorophore.**

Click chemistry reaction between alkyne-modified EU and azide-conjugated fluorophore in the presence of copper for the labelling of nascent RNAs. Taken from Invitrogen, Thermo Fisher Scientific

#### 5.2.2.1 RNA FISH

The visualisation of RNA molecules can be achieved through the use of RNA fluorescent *in situ* hybridisation (FISH). The system used here depends on the ability of custom designed DNA oligonucleotide probes complementary to the RNA molecule of interest, which in this case was the sense and anti-sense TULV S segment RNA sequences. Each probe set targets a specific RNA and comprises a minimum of 25 individually labelled oligonucleotides that hybridize at non-overlapping locations on the same RNA target, thus allowing molecule-specific detection with a high signal to noise ratio. Fixed cells are permeabilised before incubating with a probe set and probes can be visualised using LSCM or WFDM (Raj et al., 2008) (Figure 74).

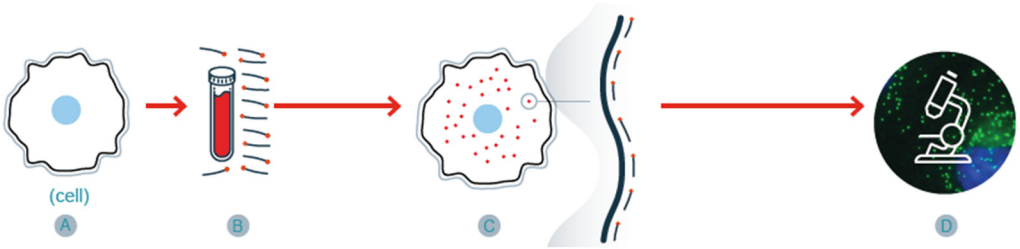


**Figure 74 Labelling cells through RNA-FISH hybridisation.**
A) Cells are fixed and permeabilised with alcohol. B) Probes are mixed and added to cells. C) RNA-FISH probes hybridise to target RNAs within cell at complementary regions D) Cells are imaged using fluorescent microscopy. Taken from Stellaris®

#### 5.2.2.2 Identifying viral replication factories by RNA labelling

The location of several viral replication factories have been identified through the use of RNA labelling techniques. Cytoplasmic inclusion bodies (IBs) were identified as replication sites for hRSV through the use of 5EU labelling via click-chemistry. These IBs were further characterised by RNA FISH and it was found they contained exclusively viral genomes, whereas viral mRNAs were concentrated instead within alternative granular structures located elsewhere in the cytoplasm (Rincheval et al., 2017). RNA-FISH was also used to show that rabies virus replication factories were located within Negri bodies (NBs), in which all viral transcripts as well as genomic RNAs were located. The NBs were also shown to be the sites of on-going RNA synthesis, identified through the metabolic incorporation of bromo-uridine triphosphate (Br-UTP), an alternative strategy for detection of incorporated nucleotides that relies on subsequent immunological detection (Lahaye et al., 2009). Labelling of LCMV genomes by RNA-FISH identified early endosomes as a scaffold for viral replication (King et al., 2017). Taken together, these reports provide precedence for both the use of FISH and the metabolic incorporation of modified nucleotides for the identification of the orthohantavirus replication site.

### 5.2.3 Utilising click-IT chemistry for labelling nascent TULV RNA

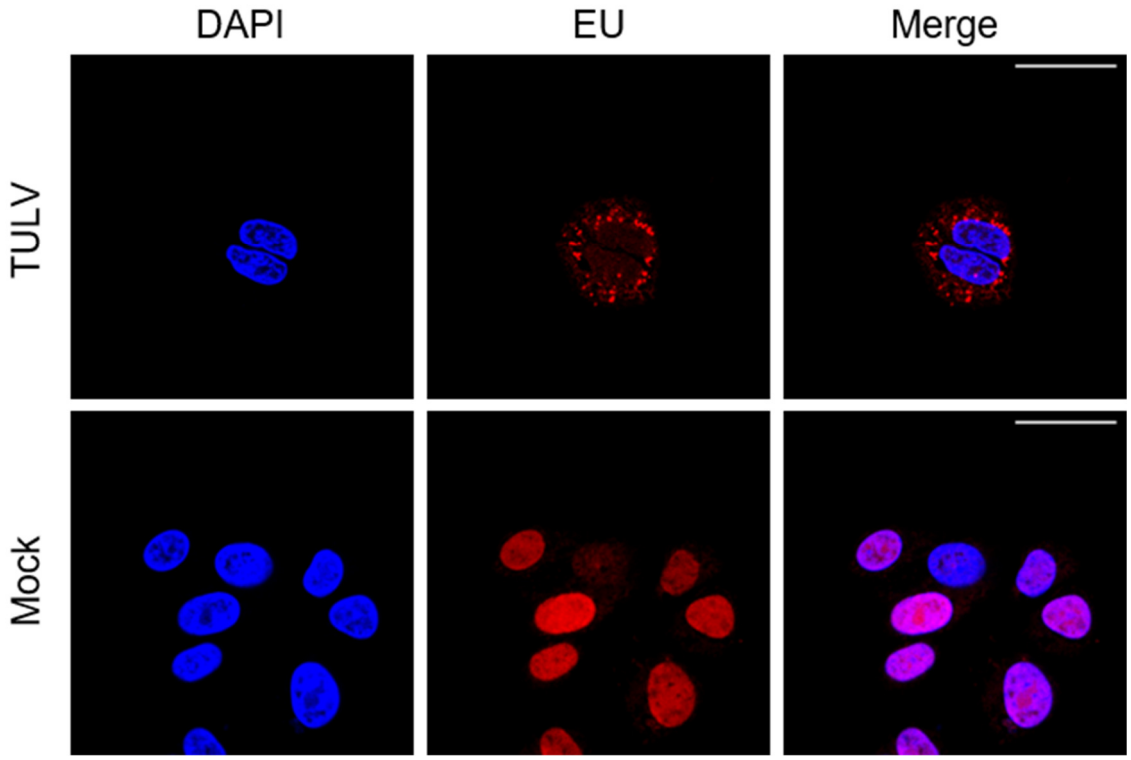


**Figure 75 Labelling newly synthesised TULV RNA utilising 5EU in Vero E6 cells at 4 dpi.**

Nascent TULV RNA labelled using click-iT™ chemistry. White bar represents 30 µm. LSCM of TULV infected Vero E6 cells (MOI 0.1) at 4 dpi using 40X magnification. Nuclei stained using DAPI (blue) and newly synthesised RNA labelled with azide-conjugated fluorophore (red).

#### 5.2.3.1 Nascent TULV RNA visualised using click-iT™ chemistry

To identify orthohantavirus replication sites of *in vitro*, 5EU was incorporated during viral replication into nascent viral RNAs and these were detected using an azide-conjugated fluorophore. Sites of viral replication were detected using LSCM. Discrete puncta of fluorescence was detected in the perinuclear region of TULV infected Vero E6 cells (Figure 75, top panel). These puncta were around 0.5-1.5 µm in diameter. Actinomycin D untreated cells were used as a positive control to display effectiveness of the 5EU incorporation. As seen in Figure 75, bottom panel, nuclei were stained red showing labelling of host cell RNA during the DNA-dependant RNA polymerization of mRNA transcripts. Attempts were made to co-stain TULV infected cells with 5EU and NP anti-sera but were unsuccessful (data not shown).

### 5.2.4 Co-localisation of sense and anti-sense TULV S segment RNA with TULV NP

#### 5.2.4.1 TULV S segment RNA co-localises with TULV NP

Metabolic labelling provided information on the location of newly produced viral RNAs however there was no discrimination between RNAs involved in replication or transcription. Therefore RNA-FISH probes were designed specifically to recognise either sense (transcription/replication) or anti-sense (replication) S segment RNA and provide greater resolution to the localisation of RNAs involved in replication and transcription. The localisation of sense or anti-sense TULV S segment RNA alongside the signal for TULV NP was examined using RNA-FISH and NP antisera by LSCM and WFDM. The TULV anti-sense RNAs generated during infection comprises exclusively genomic RNAs, thus the anti-sense signal corresponds to viral RNA replication. In contrast, TULV sense RNAs will include both anti-genomic replication products and also mRNA transcripts. However, previous work with other bunyaviruses shows the abundance of antigenomic replication products is likely several orders of magnitude less than mRNAs, (Barr et al., 2003) thus the vast majority of the sense RNA signal will represent mRNA transcription products. TULV NP is the major structural component of the RNP, which forms the template for both mRNA transcription and also RNA replication, thus detection of NP is predicted within regions where all forms of viral RNAs are being made.

At 36 hpi the majority of sense and anti-sense TULV S segment RNA closely co-localised with TULV NP in strand-like structures, with the morphology of the stained areas of both RNA and NP being superimposable. These strands were 4.0-8.5 µm in length with a diameter of ~ 0.7 µm and were dispersed throughout the cytoplasm. Anti-sense RNA also co-localised with larger punctate NP structures in the cytoplasm with an average diameter of ~1.5 µm (Figure 76, Figure 79A), and as described above for the strand-like structures, the areas staining for both RNA and NP were essentially superimposable. Not all TULV NP co-localised with TULV RNA, which is in agreement with previous studies stating TULV NP possesses alternative roles in addition to its role as the major structural component of the RNP (Reuter and Krüger, 2018).

At 7 dpi, the distribution of TULV RNA was similar to that observed at 36 hpi, however, there was little evidence of NP-RNA structures dispersed throughout the cytoplasm. Instead, sense and anti-sense RNA co-localised with filamentous and tubular NP structures in the perinuclear region within either large accumulations of 5.0-10.0 μm diameter or in thinner arrangements of 1.0-3.0 μm in diameter and up to 25 μm in length that appear to wrap around the nucleus. Some RNA also co-localised with NP within perinuclear puncta of around 1.0-2.0 μm diameter (Figure 77, Figure 79B). These punctate NP structures contained lower quantities of sense or antisense RNA compared to perinuclear compartments as seen in Figure 77. As above, for the most part, areas of both NP and RNA staining appeared to precisely coincide within the two-dimensional section, strongly suggesting these components occupy the same three-dimensional space. Also, in agreement with observations at 36 hpi, not all TULV NP co-localised with TULV RNA, suggestive of additional roles for NP outside of RNP assembly. This is also shown through the co-localisation threshold overlap score (TOS), where the overlap value of viral RNA and NP increases as the infection progresses, consistent with accumulation of viral RNA. However the TOS never reaches a score of 1 which would indicate every NP signal colocalised with S segment RNA (Figure 80).

In persistently infected cells at 30 dpi, accumulation of sense and anti-sense S segment RNA was also observed in the macromolecular tubular filamentous NP structures. These tubular structures, similarly to 7 dpi, existed as either extensive bundles of filaments up to 25 μm in diameter or as a few individual thinner strands of ~0.7 μm in diameter (Figure 78, Figure 79). These structures either appear to be individual filamentous structures or tubes as seen in the 3D projection of stacked optical sections (Figure 81).

TULV RNA also co-localised with larger some punctate NP in the cytoplasm. The majority of these puncta occurring within the cytoplasm but close to the plasma membrane. Most TULV NP puncta containing TULV RNA were 1.0-1.8 μm in diameter with some puncta as large as 2.0 μm in diameter (Figure 78, Figure 79C). Additionally, the concentration of RNA in large punctate NP appears to be much higher and similar to the concentration found in perinuclear tubular structures as seen in Figure 78. As observed previously

by qRT-PCR analysis (Chapter 4, Figure 38), accumulation of both sense or anti-sense S segment RNAs increased with time up to 10 dpi, as did NP abundance. Through IF analysis, all signals corresponding to TULV RNAs closely co-localised with TULV NP at each time point examined (36 hpi, 7 dpi and 30 dpi). There was no apparent difference in the localisation of sense or anti-sense RNA as both localise to perinuclear NP structures and cytoplasmic NP puncta.

In summary, both sense and anti-sense TULV RNA localized within two distinct morphological structures, namely punctate bodies and filamentous structures. Both these types of structures were present in all time points, and both closely colocalized with NP such that their signals were overlapping. However, a fraction of the punctate NP structures did not colocalize with RNA, thus suggesting TULV NP possesses one or more alternative roles other than RNP formation. The size of RNA and NP colocalizing structures increased throughout the time course, and at the 30 dpi time points, the RNA-NP assemblies occupied a significant proportion of the cell volume, approaching that of the nucleus.

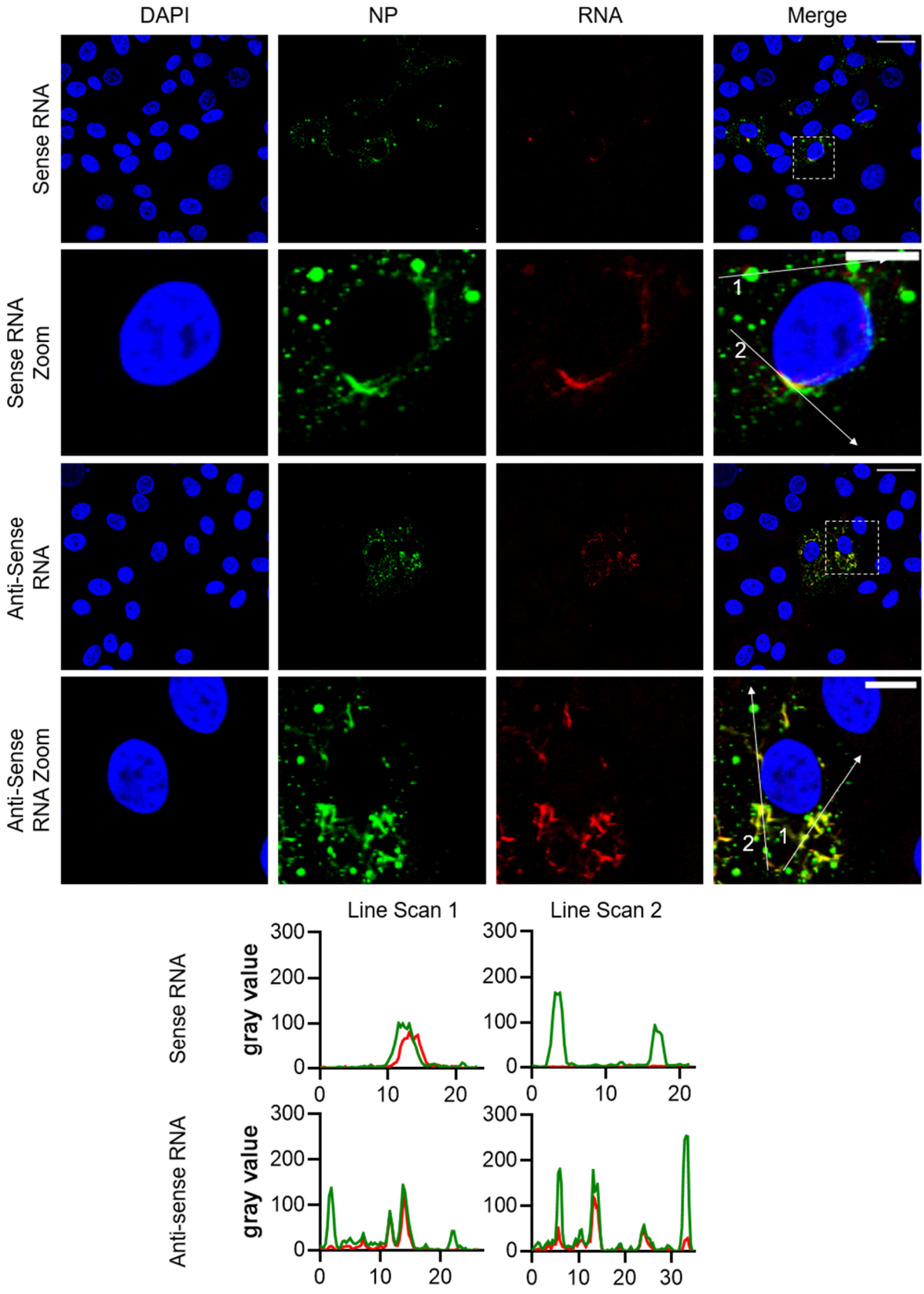


**Figure 76 Co-localisation between TULV NP and TULV S segment RNA in Vero E6 cells at 36 hpi.**

**Figure 76 Co-localisation between TULV NP and TULV S segment RNA in Vero E6 cells at 36 hpi.**

The spatial distribution of TULV NP (green) and S segment RNA (red) was observed at 36 hpi using LSCM at 40 X magnification. Vero E6 cells were infected at MOI 0.1. The white bar represents 30 µm and 10 µm (zoom). Fluorescent line scans taken using Fiji software. Nuclei are stained with DAPI (blue), TULV NP detected using NP antisera and S segment RNA detected using sense or anti-sense RNA FISH probes.

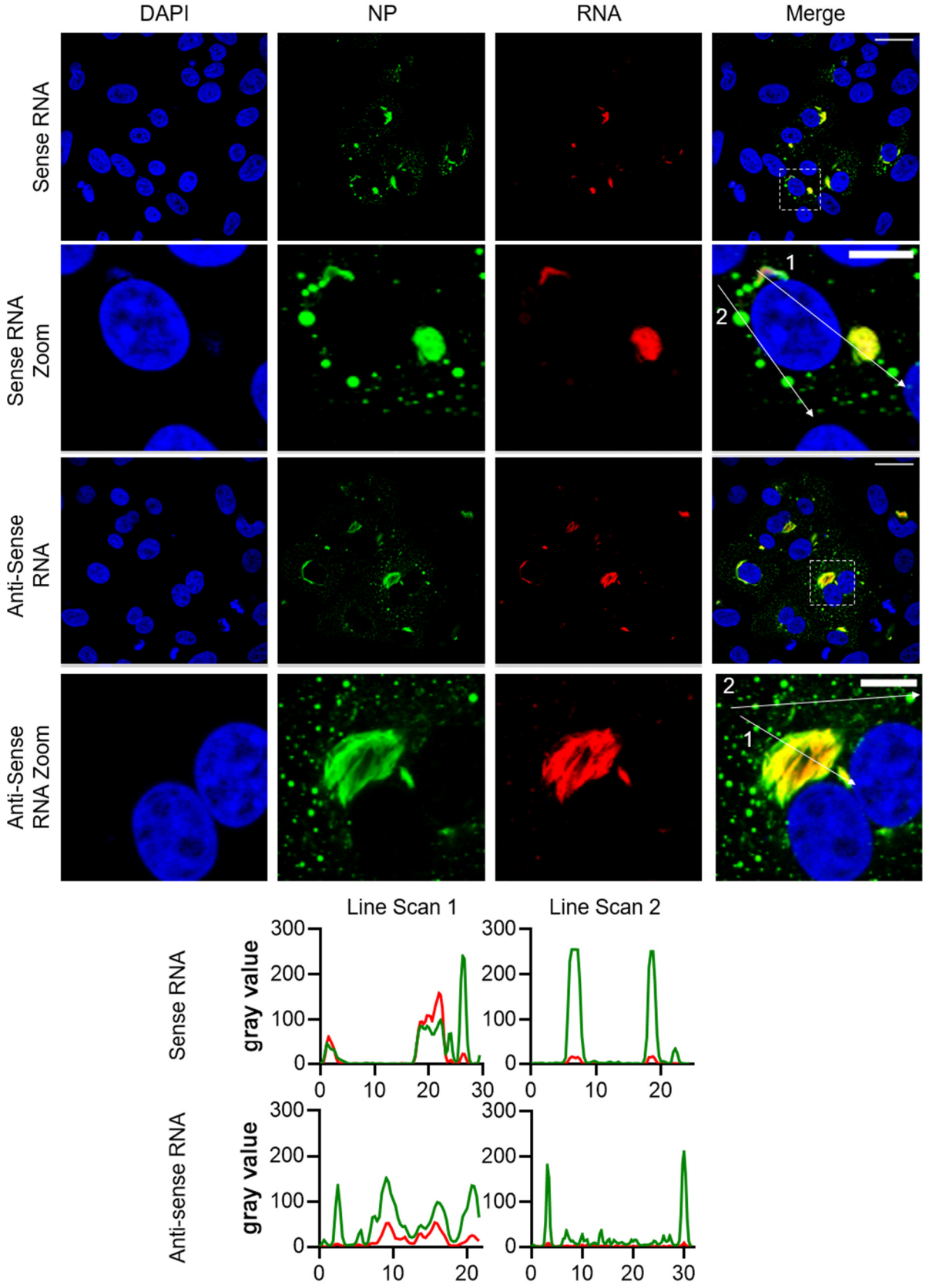


**Figure 77 Co-localisation between TULV NP and TULV S segment RNA in Vero E6 cells at 7 dpi.**

**Figure 77 Co-localisation between TULV NP and TULV S segment RNA in Vero E6 cells at 7 dpi.**

The spatial distribution of TULV NP (green) and S segment RNA (red) was observed at 7 dpi using LSCM at 40 X magnification. Vero E6 cells were infected at MOI 0.1. The white bar represents 30 µm and 10 µm (zoom). Fluorescent line scans taken using Fiji software. Nuclei are stained with DAPI (blue), TULV NP detected using NP antisera and S segment RNA detected using sense or anti-sense RNA FISH probes.

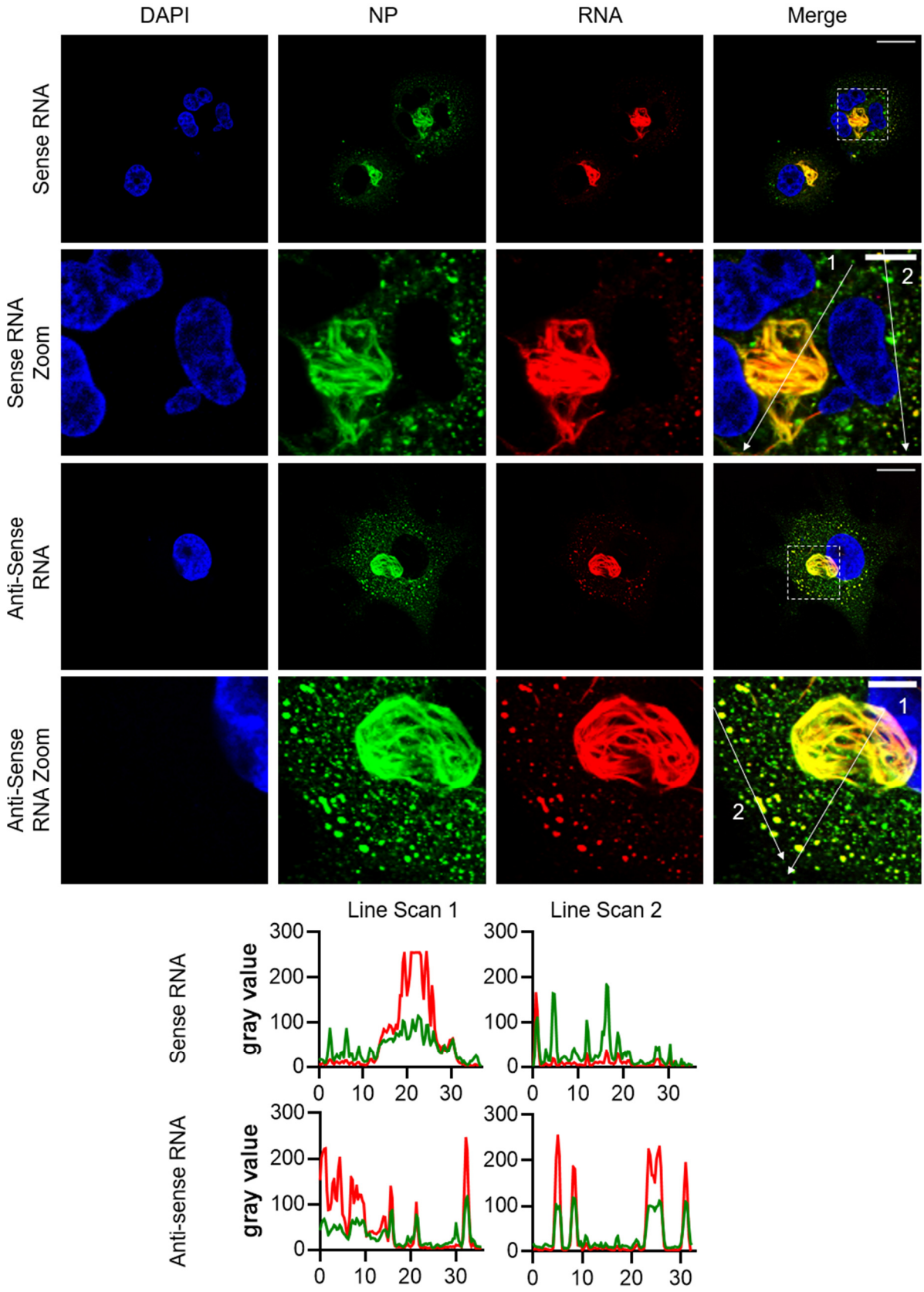


**Figure 78 Co-localisation between TULV NP and TULV S segment RNA in Vero E6 cells at 30 dpi.**

**Figure 78 Co-localisation between TULV NP and TULV S segment RNA in Vero E6 cells at 30 dpi.**

The spatial distribution of TULV NP (green) and S segment RNA (red) was observed at 30 dpi using LSCM at 40 X magnification. Vero E6 cells were infected at MOI 0.1. The white bar represents 30 µm and 10 µm (zoom). Fluorescent line scans taken using Fiji software. Nuclei are stained with DAPI (blue), TULV NP detected using NP antisera and S segment RNA detected using sense or anti-sense RNA FISH probes.

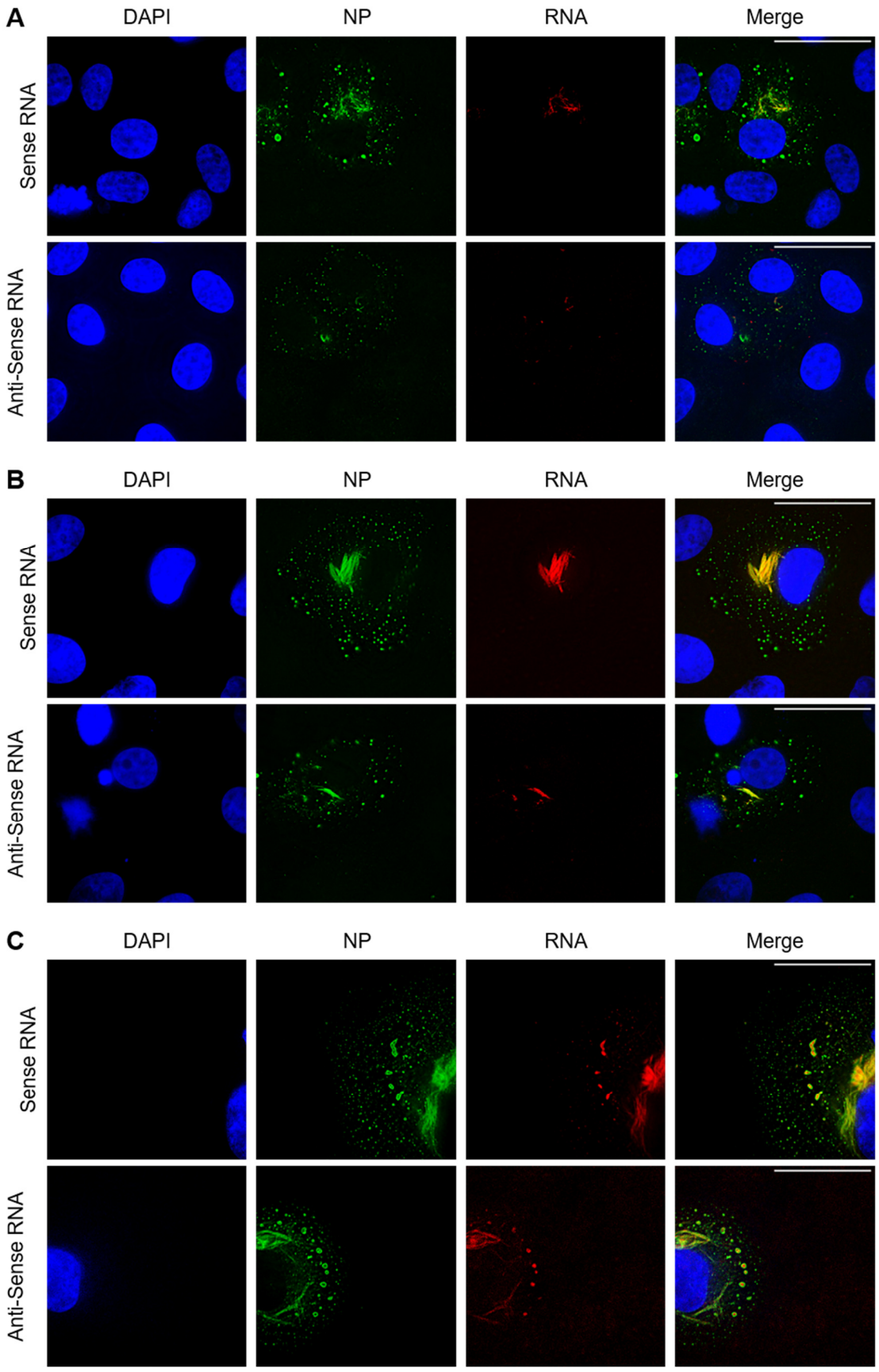


**Figure 79 Co-localisation between TULV NP and TULV S segment RNA in Vero E6 cells using WFDM.**

**Figure 79 Co-localisation between TULV NP and TULV S segment RNA in Vero E6 cells using WFDM.**

The spatial distribution of TULV NP (green) and S segment RNA (red) was observed during early, peak and persistent infection using WFDM at 100 X magnification. Vero E6 cells were infected at MOI 0.1. The white bar represents 30 µm (zoom). Nuclei are stained with DAPI (blue), TULV NP detected using NP antisera and S segment RNA detected using sense or anti-sense RNA FISH probes. A) Vero E6 cells at 36 hpi, B) Vero E6 cells at 7 dpi C) Vero E6 cells at 30 dpi

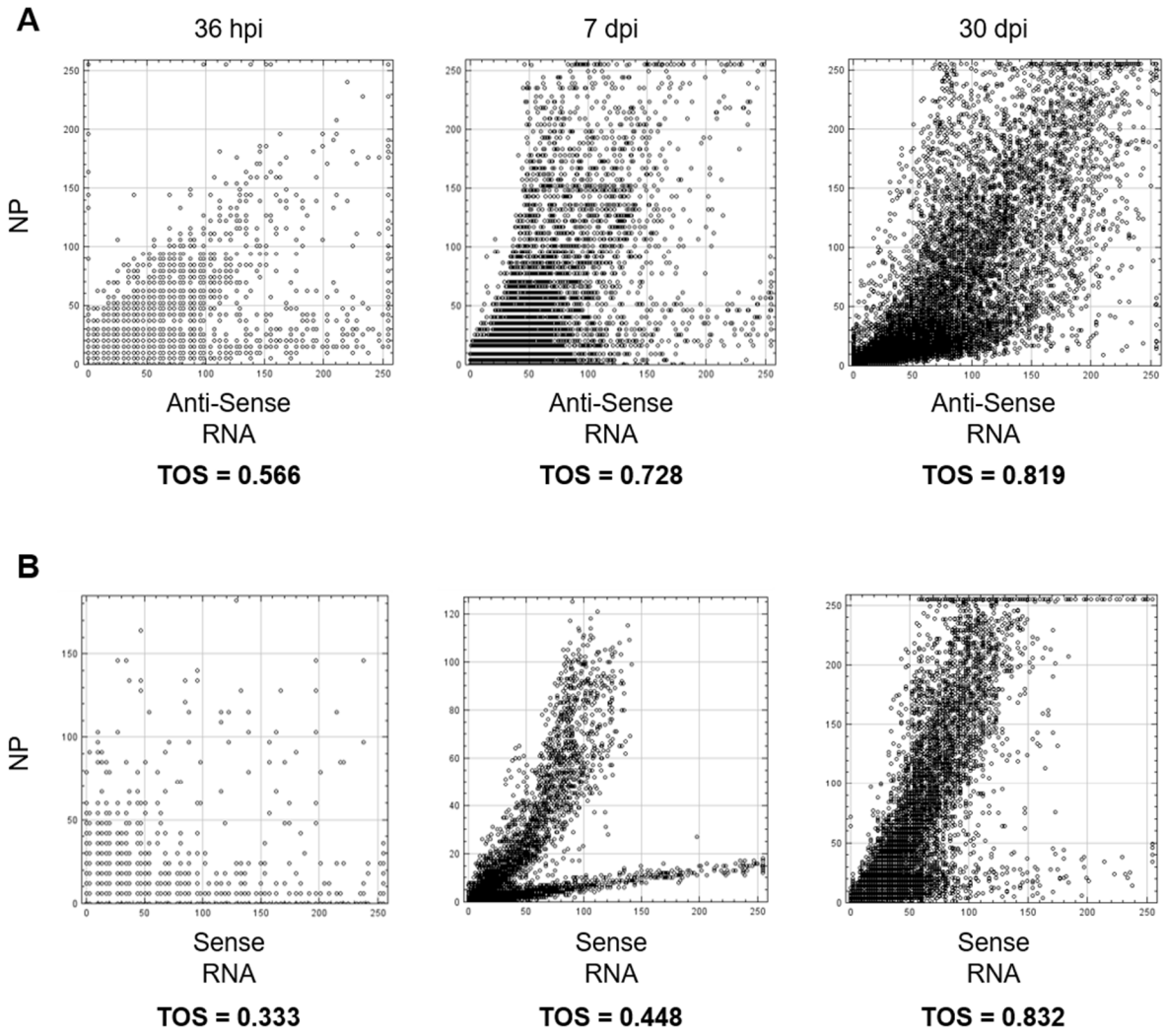


**Figure 80 Co-localisation analysis of TULV NP and S Segment RNA.**

Co-localisation of Figure 76, Figure 77 and Figure 78 were analysed using FIJI plugin EzColocalization. Scatter plots pictorially representing co-localisation were produced and the threshold overlap score (TOS) demonstrates level of co-localisation (Stauffer et al., 2018).

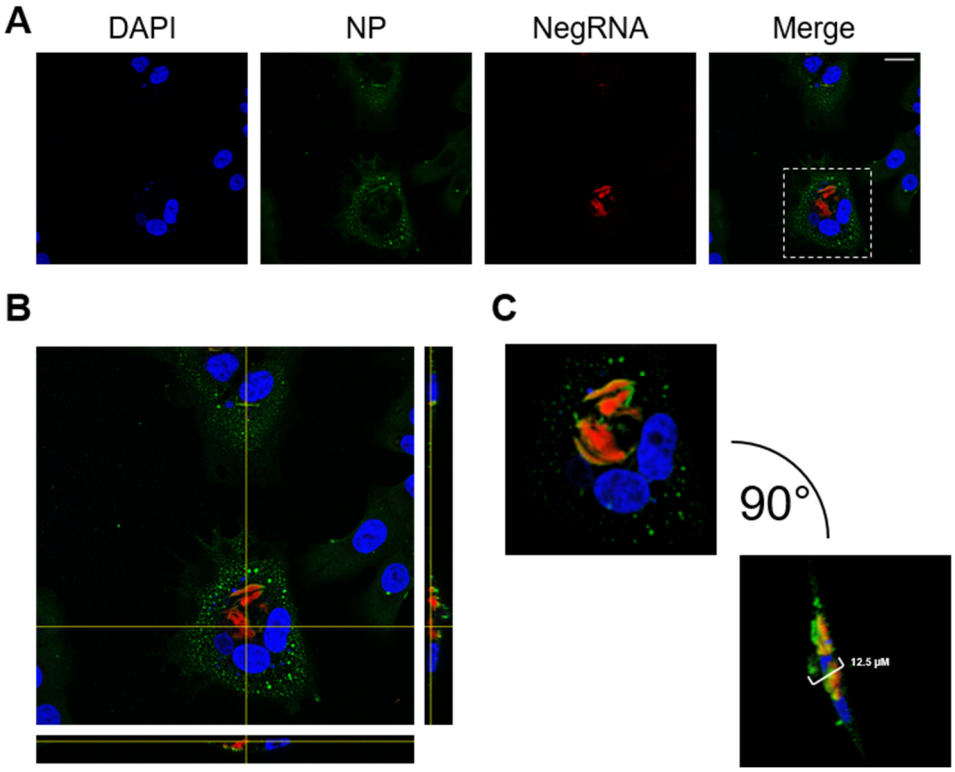


**Figure 81 Three-dimensional co-localisation of TULV NP and anti-sense S segment RNA in persistently infected cells.**

LSCM of TULV infected cells at 30 dpi using 40 X magnification. The white bar represents 30 µm. Nuclei are stained with DAPI (blue), TULV NP detected using NP antisera (green) and S segment RNA detected anti-sense RNA FISH probes (red). Images were taken on 40 different focal planes and stacked. A) Represents one focal plane of the hyper-stack, section 9 of 40, B) Orthogonal view of hyper-stacked images using Fiji software C) 3D reconstruction of persistently infected cells using 3D viewer in Fiji, depth of NP structure within cell calculated to be ~ 12.5 µm.

### 5.2.5 Disruption of multimeric NP has a negative effect on production of TULV RNA

#### 5.2.5.1 Okadaic acid treatment of TULV persistently infected Vero E6 cells reduces viral genome copies

As previously shown in Chapter Four, section 4.3.2.5, treatment with okadaic acid (OA) resulted in the depolymerisation of vimentin filaments and disruption of the perinuclear tubular/filamentous NP structures. The accumulation of sense and anti-sense TULV S segment RNA with tubular NP structures suggests that viral replication and possibly storage of viral RNAs may occur within these regions. Consequently, disruption of these tubular NP structures would be predicted to cause a reduction in total cellular RNA genome copy number, either due to abrogated genome replication and/or release of viral RNA into the cytoplasm followed by its degradation.

Vero E6 cells were infected with TULV and at either 3 dpi or 30 dpi were treated with 400 nM OA and incubated for 30, 60 and 90 minutes before harvesting. As a drug treatment control, the effect of 17 μM NOC on viral genome copy numbers was also assessed. As NOC did not appear to significantly affect the structure of tubular NP, it was expected this would not reduce viral copy numbers but would give a measure of control for drug-induced cytopathology. The number of TULV genome copies in the cytoplasm were assessed by qRT-PCR. As expected, treatment with OA at 30, 60 and 90 minutes reduced TULV genome copies/mL relative to NOC treatment which did not reduce TULV genome copies/mL when compared to mock-treated cells. This effect could be replicated at both 3 dpi and 30 dpi (Figure 82). This suggests vimentin polymerisation is important for the accumulation of viral RNAs in the cytoplasm.

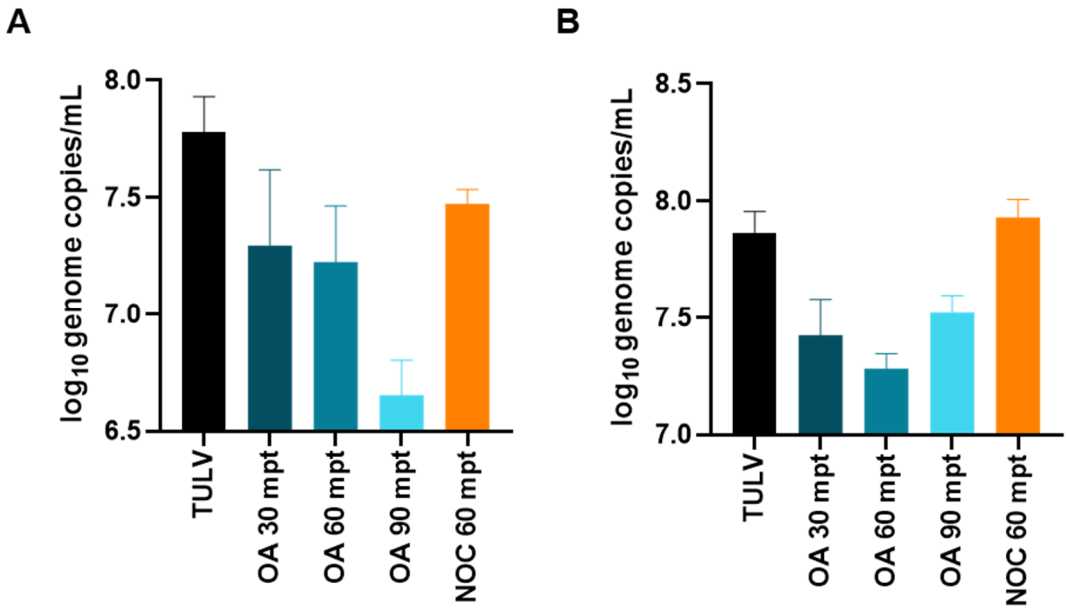


**Figure 82 Okadaic acid treatment of TULV infected Vero E6 cells decreases viral genome copies.**

TULV infected Vero E6 cells at 3 dpi (A) and 30 dpi (B) were treated with 400 nM okadaic acid (OA) for 30, 60 or 90 minutes or 17 µM nocodazole (NOC) for 60 minutes. After harvesting, cell lysates were examined for TULV genome copies by qRT-PCR.

### 5.2.6 Co-localisation of sense and anti-sense TULV S segment RNA with TULV NP, stress granule marker and Golgi network marker

#### 5.2.6.1 TULV S segment RNA co-localises with TULV NP and Golgi network marker

The results of the previous section showed TULV NP and TULV S segment RNA (both sense and anti-sense) co-localised within both punctate and filamentous/sheet/tubular structures. Interestingly, morphologically-similar filamentous sheet tubular structures were previously identified as co-localizing sites for TULV NP and the Golgi apparatus (Chapter Four, Figure 55). Therefore, to confirm colocalization of all three components, TULV infected Vero E6 cells were stained using FISH for TULV S segment RNAs, as well as antisera specific for TULV NP, and the Golgi network. IF and fluorescent line-scan analysis revealed sense and anti-sense TULV S segment RNA displayed precise co-localisation with the Golgi marker as well as both perinuclear tubular forms of TULV NP (Figure 83). Taken together, this finding

strongly implicates the Golgi network as a site of viral RNA synthesis and accumulation.

#### 5.2.6.2 TULV S segment RNA co-localises with TULV NP and stress granule marker TIA-1

The results of section 4.3.4 showed TULV NP and the stress granule marker TIA-1 co-localised within punctate bodies. The size and distribution of these puncta were similar to many of the structures where TULV S segment RNA and NP localise (Chapter Four, Figure 60). Therefore, to confirm co-localization of all three components, the intracellular localisation of TULV S segment RNA was visualized by IF analysis and fluorescent line scan alongside that of TULV NP and TIA-1.

Staining associated with TULV and anti-sense RNAs exhibited precise colocalization with both TIA-1 and NP in structures that were both punctate and filamentous in appearance (Figure 84). Sense RNAs also displayed high levels of co-localisation with punctate NP and TIA-1 (Figure 85). NP puncta displaying co-localisation with TIA-1 and S segment RNA were on average 1.7 μm in diameter (Figure 84, Figure 85). Sense RNA however, while co-localising with some areas of filamentous NP and TIA-1 co-localisation was completely absent from other areas of perinuclear NP and TIA-1 co-localisation. Additionally, some perinuclear areas of high levels of TULV NP and sense RNA displayed low levels of TIA-1 staining (Figure 85), consistent with the TOS determined for TULV NP, sense S segment and TIA-1 being lower than the TOS for TULV NP, anti-sense S segment and TIA-1, being TOS=0.696 and TOS=0.775 respectively (Figure 86). This suggests there may be difference in the perinuclear localisation of sense and anti-sense RNA. Areas in which sense RNAs are absent may be sites of viral assembly or transport to the plasma membrane as predominately for negative-sense RNA viruses only anti-sense RNA is required in the mature virus particle, with the exceptions of RVFV and UUKV (Simons et al., 1990; Ikegami et al., 2017).

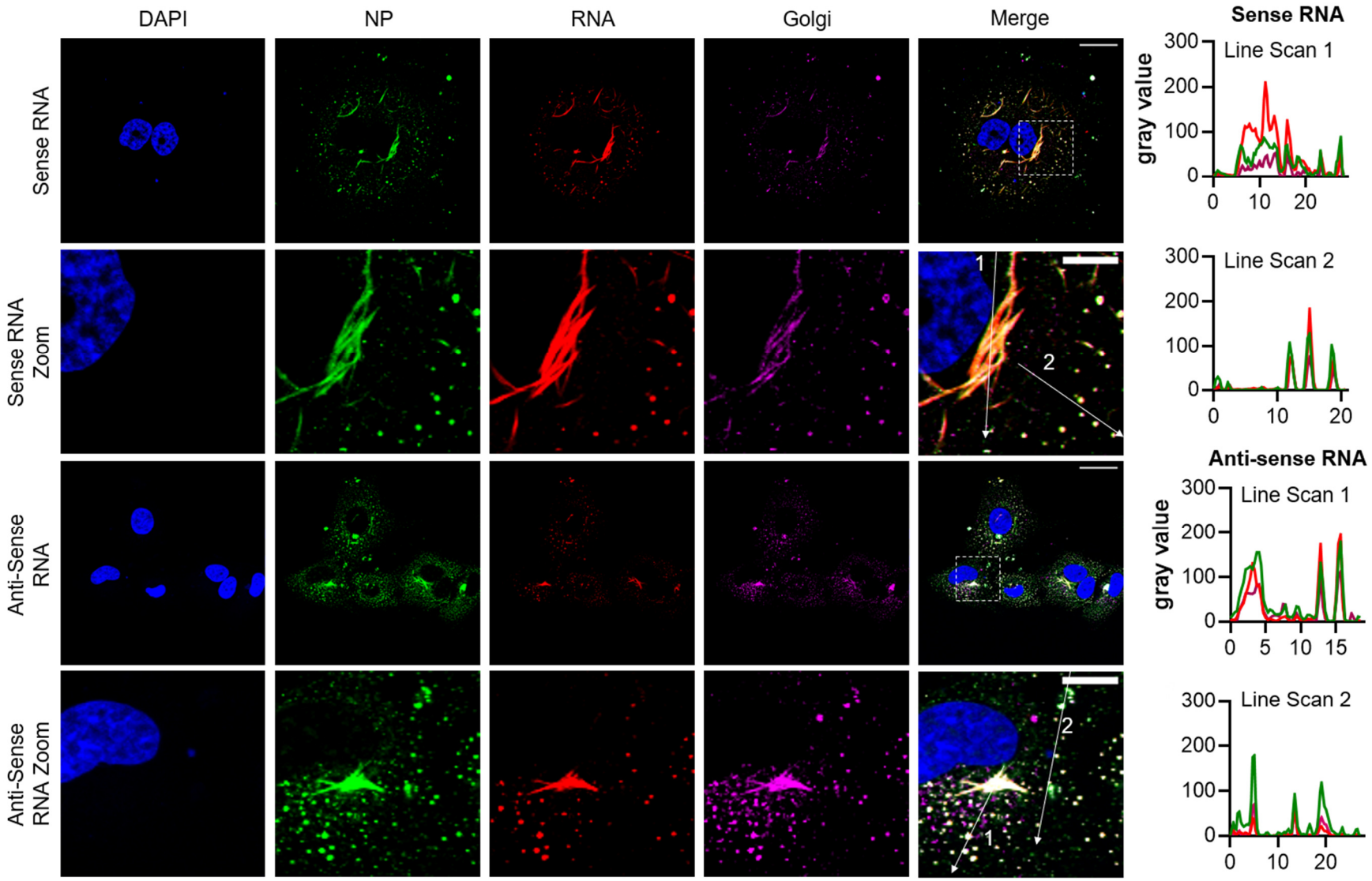


**Figure 83 Co-localisation between TULV NP, TULV S segment RNA and the Golgi network in Vero E6 cells during persistent infections.**

**Figure 83 Co-localisation between TULV NP, TULV S segment RNA and the Golgi network in Vero E6 cells during persistent infections.**

The spatial distribution of TULV NP (green), S segment RNA (red) and the Golgi (magenta) was observed during persistent infections using LSCM at 40 X magnification. Vero E6 cells were infected at MOI 0.1. The white bar represents 30 µm and 10 µm (zoom). Fluorescent line scans taken using Fiji software. Nuclei are stained with DAPI (blue), TULV NP detected using NP antisera, S segment RNA detected using sense or anti-sense RNA FISH probes and Golgi detected using Golgi marker antibody

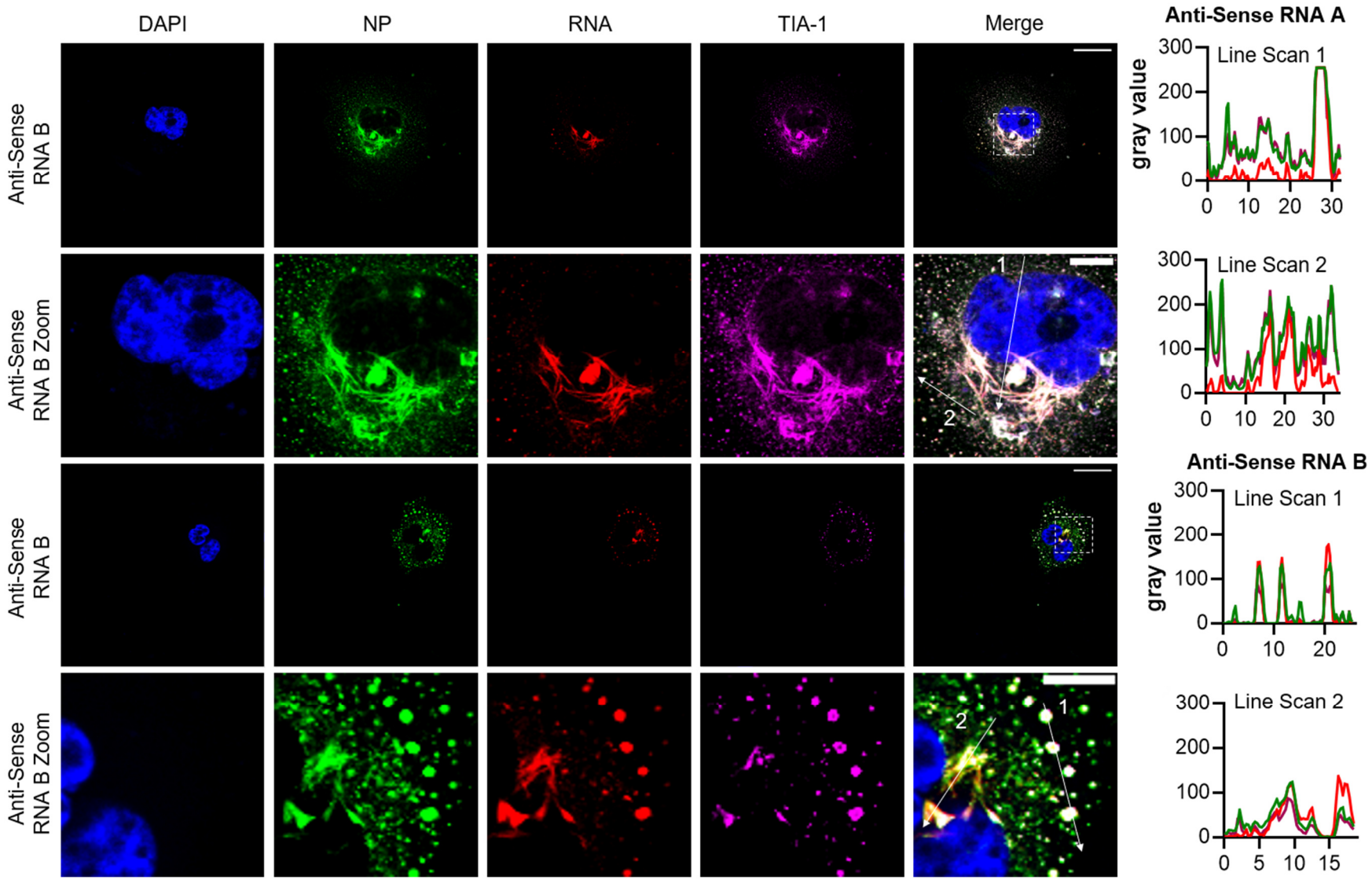


**Figure 84 Co-localisation between TULV NP, TULV anti-sense S segment RNA and TIA-1 in Vero E6 cells during persistent infections.**

**Figure 84 Co-localisation between TULV NP, TULV anti-sense S segment RNA and TIA-1 in Vero E6 cells during persistent infections.**

The spatial distribution of TULV NP (green), S segment RNA (red) and TIA-1 (magenta) was observed during persistent infections using LSCM at 40 X magnification. Vero E6 cells were infected at MOI 0.1. The white bar represents 30 µm and 10 µm (zoom). Fluorescent line scans taken using Fiji software. Nuclei are stained with DAPI (blue), TULV NP detected using NP antisera, S segment RNA detected using sense or anti-sense RNA FISH probes and TIA-1 detected using TIA-1 antibody.

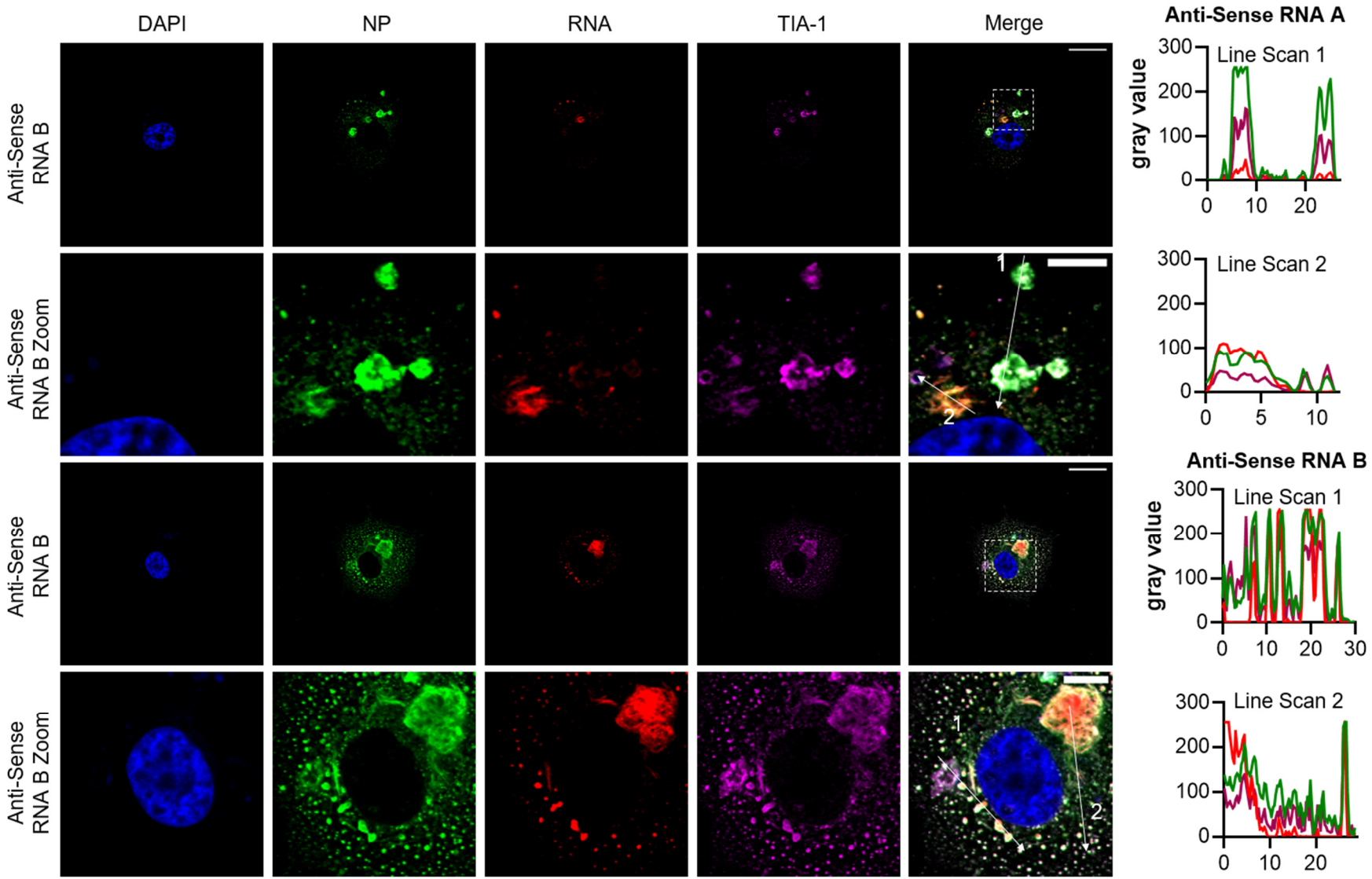


**Figure 85 Co-localisation between TULV NP, TULV sense S segment RNA and TIA-1 in Vero E6 cells during persistent infections.**

**Figure 85 Co-localisation between TULV NP, TULV sense S segment RNA and TIA-1 in Vero E6 cells during persistent infections.**

The spatial distribution of TULV NP (green), S segment RNA (red) and TIA-1 (magenta) was observed during persistent infections using LSCM at 40 X magnification. Vero E6 cells were infected at MOI 0.1. The white bar represents 30 µm and 10 µm (zoom). Fluorescent line scans taken using Fiji software. Nuclei are stained with DAPI (blue), TULV NP detected using NP antisera, S segment RNA detected using sense or anti-sense RNA FISH probes and TIA-1 detected using TIA-1 antibody.

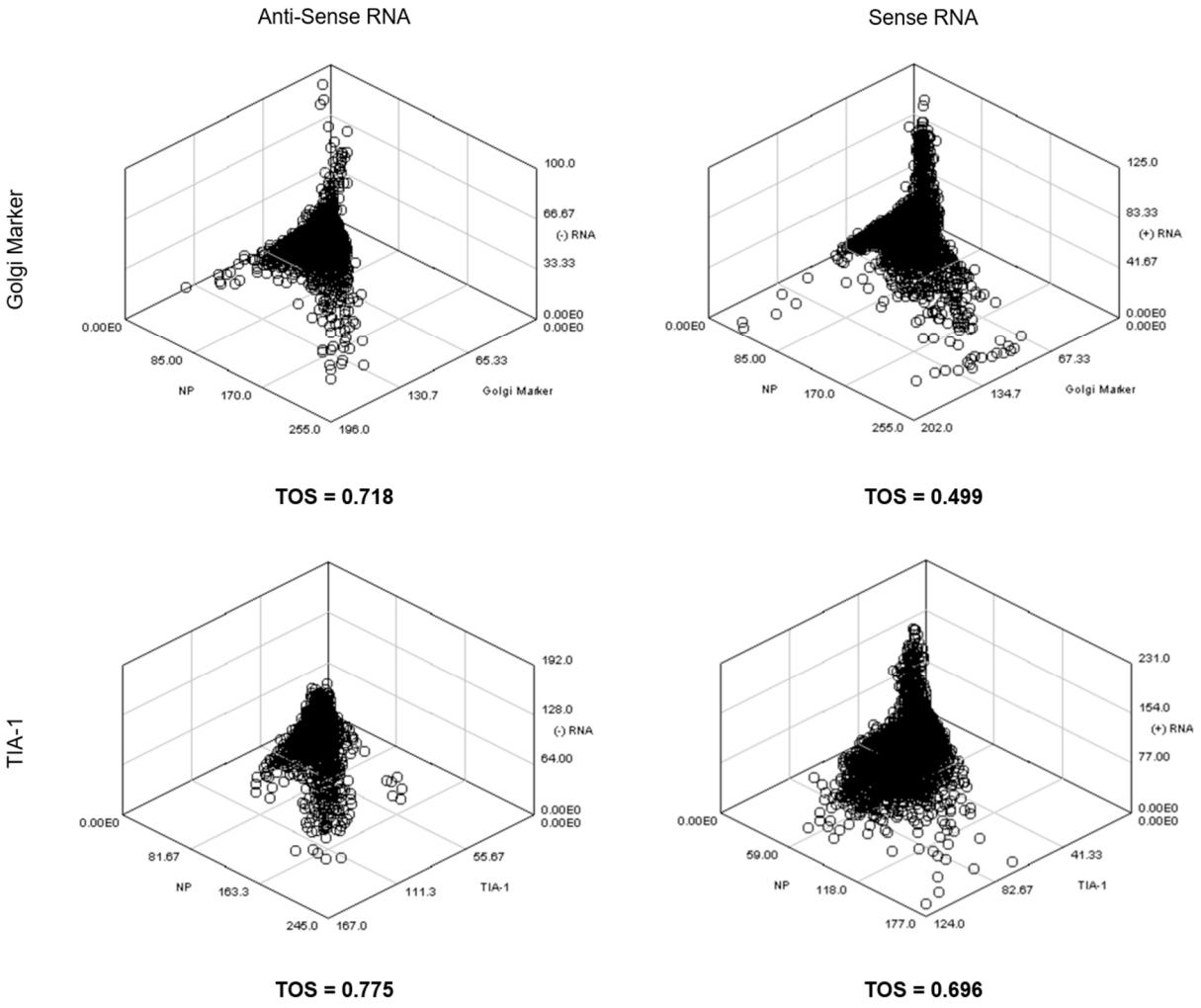


**Figure 86 Co-localisation of TULV NP, S Segment RNA with the host protein TIA-1 or Golgi.**

Co-localisation of confocal images shown in Figure 83, Figure 84 and Figure 85 were analysed using FIJI plugin EzColocalization. Scatter plots pictorially representing co-localisation were produced and the threshold overlap score (TOS) demonstrates level of co-localisation. The average TOS from three separate analyses is shown (Stauffer et al., 2018).

### 5.2.7 Section Summary

This section describes the spatial localisation of TULV S segment RNA within TULV infected Vero E6 cells during early, peak and persistent infection. The localisation of TULV RNA and interaction with TULV NP and host cell components, Golgi and TIA-1, was assessed by IF analysis. TULV RNA co-localised exclusively with TULV NP. At early stages of infection RNA co-localised with strand-like TULV NP within the perinuclear region whereas in peak and persistent infections RNA co-localised with perinuclear tubular accumulations and large cytoplasmic puncta.

A clear target for the replication site of TULV was the perinuclear region as TULV RNA localised here at early time points and nascent RNAs was detected in the perinuclear region. As previously described in Chapter Four, the disassembly of vimentin filaments by treatment with OA disrupted the perinuclear formations of TULV NP. If these perinuclear areas are required for virus replication and storage of RNAs as suspected, OA treatment should have a detrimental effect on the genome copy number of TULV. OA was shown to reduce the genome copy number TULV providing further evidence for location of the orthohantavirus replication site.

To further the identification of this site, target components of the host cell which co-localise with TULV NP within this region was used for IF analysis. It was found that TULV NP, RNA and Golgi marker showed high levels of co-localisation with early, peak and persistently infected cells suggesting that the Golgi may be the site of viral replication and transcription. Additionally, it was found that puncta NP containing sense or anti-sense RNAs co-localised with stress granule component TIA-1, but while perinuclear filaments containing anti-sense RNA displayed high levels of co-localisation with TIA-1 this was not reflected for sense RNA. With some areas of TULV NP and TIA-1 co-localisation displaying no RNA signal. This indicates there may difference in the locations of sense and anti-sense RNA which may indicate a site of viral assembly separate to replication and transcription.

# Chapter 6 : Discussion

## 6.1 Expression and purification of recombinantly expressed orthohantavirus nucleocapsid protein

The orthohantavirus nucleocapsid protein is multifunctional and is associated with roles in the encapsidation of viral RNA, viral transcription, viral translation and immune evasion. As the orthohantavirus NP is a relatively small (50 kDa) protein, an interesting research question is how the NP performs and regulates these multiple functions. High resolution structural studies are a powerful approach to answer this question, however, the orthohantavirus NP proven problematical to recombinantly express and purify in the full-length form. Several groups were able to, with difficulty, express and purify various truncated versions of the orthohantavirus NP; initial expressions of full-length SNV and ANDV NPs were unsuccessful due to solubility and stability, suggested to be due to the N- and C-terminal domains role in NP oligomerisation. Truncated NP constructs of E111-G399 were successfully expressed, purified and used to solve the structure of the NP core domain (Guo et al., 2016). Olal and Daumke 2016 were able to solve the structure of a similar truncated HTNV NP, containing the NP core region and the N-terminal domain from residues 113-429. This construct was fused to maltose binding protein to aid solubility, but still had problems due to the intrinsic flexibility of NP and its tendency to oligomerise. These previous studies utilised bacterial expression for production of NP.

In this current study, bacterial expression was utilised to produce SEOV NP. Like Guo et al., 2016 and Olal and Daumke 2016, full-length SEOV NP displayed poor expression and stability despite multiple attempts to optimise expression and purification conditions. A truncated SEOV $NP_{core}$ was produced, based on conditions described by Guo et al., and low concentrations (0.5 mg/mL) of SEOV $NP_{core}$ was produced at >85% purity while unsuitable for X-ray crystallography was acceptable for antibody generation. Recently, full length HTNV NP was purified utilising a baculovirus-insect cell expression system (Arragain et al., 2019). This suggests that orthohantavirus NP may require post-translational modification that cannot be

achieved through bacterial cell expression. As a high percentage of SEOV $NP_{core}$ was found in inclusion bodies this suggests improper folding during expression which may be due to a lack of post-translational modification. It has also been suggested that solubility problems may arise due to slow proline isomerisation, improper reduction/oxidation of cysteine residues and the lack of essential component such as RNA or ribonucleases (Spiropoulou, 2001). Due to time constraints of the project, attempts to further purify SEOV NP were discontinued and focused instead on the molecular mechanisms of the orthohantavirus lifecycle.

## 6.2 Development of molecular tools for the quantification of the orthohantavirus lifecycle

Orthohantaviruses are traditionally titrated using the neutral red uptake plaque assays or by genomic counts using qRT-PCR. The neutral red uptake is a commonly used measurement of cytotoxicity and provides a measure of cell health. Healthy cells will incorporate and retain the neutral red dye within lysosomes whereas unhealthy cells will not (Borenfreund and Puerner, 1985; Repetto et al., 2008). This assay has been adapted to virus quantification by counting areas of viral infection where neutral red dye is not retained, forming “plaques”. This is an acceptable method for the quantification of non-cytolytic viruses, such as orthohantavirus, which do not cause cell lysis but instead establish latent infections that cause an overall reduction in host cell health. A major drawback of this method of orthohantavirus titration is the prohibitively long assay time, which includes up to 7 days to establish the Vero E6 monolayers followed by 7-14 days for viral infection and 1-5 days for viral plaque formation after addition of the neutral red dye (French et al., 1981; Schmaljohn et al., 1983; Hooper et al., 2001; McElroy et al., 2004). Together, these time requirements are prohibitive for many experimental systems, where high throughput readouts of virus multiplication are needed.

Other methods to give a measure of viral amounts have been developed such as qRT-RT PCR, which is a much faster method for the quantification of orthohantaviruses and is the gold-standard for molecular diagnostics (Mackay et al., 2002; Jiang et al., 2013; Wigren Byström et al., 2018). However, PCR allows only the detection of viral nucleic acids and does not give information

on virion viability or number of infectious virus particles. In addition, a standard curve must be used to give absolute genome copies, so quantified values will be relative to the accuracy of the standard curve used.

Other methods of orthohantavirus detection have been developed. These include the focus reduction neutralisation assay (FRNT), tissue culture infective dose 50% (TCID50), plaque reduction neutralisation test (PRNT) in addition to various adaptations of focus-forming or infectious-virus centre assay which utilise antibody detection either in conjunction with chemiluminescent substrates or fluorescent antibodies. Orthohantavirus titration methods requiring a form of “plaque” formation require 5-18 days before a titre can be determined. Immunocytochemical or immunofluorescent assays tend to allow faster titration and can be completed in 1-5 days (Gavrilovskaya et al., 1998; Ramanathan et al., 2007; I.N. Gavrilovskaya et al., 2012). To provide a more rapid assay to measure infectious virus quantities, an immunofluorescent-based assay was developed for the titration of TULV orthohantavirus. This assay relies on orthohantavirus NP anti-sera generated in sheep against recombinantly expressed SEOV $NP_{core}$. This assay allows reliable and reproducible quantification of TULV titres within 72 hours post viral adsorption.

## 6.3 Tula orthohantavirus lifecycle kinetics and formation of multinuclear persistently infected cells

TULV multiplication, infectious virus production and replication kinetics were examined over an extended time-course using the molecular tools developed in Chapter One. This revealed TULV replication consisted of a lag-phase (0-30 hpi) where no increase in viral RNA or infectious virus was detected, followed by an exponential phase (30-42 hpi) where viral RNA production rapidly increased followed by a phase of slower viral RNA and infectious virus production, reaching an eventual plateau (6-10 dpi). Extension of the time course to 30 dpi revealed a slow decrease in viral RNA and infectious titres but remaining at least one log above initial infection values. Based on these observations distinct time points of 36 hpi, 7 dpi and 30 dpi were defined as early, peak and persistent phases of virus multiplication, respectively.

Previous studies have shown a similar pattern of orthohantavirus replication kinetics, but few studies assess infective virus, viral RNA and viral protein loads simultaneously. Assessment of orthohantavirus titres (by plaque assay and TCID50) showed a gradual increase in infective virus particles (Shim et al., 2011). One study, described an increase in ANDV titre up to 5 dpi, but a decreases in HTNV and TULV titre from 3-5 dpi (I.N. Gavrilovskaya et al., 2012). Orthohantavirus RNA analysis has previously been described with increasing viral titres up to at least 10 dpi (Witkowski et al., 2017). A more recent study showed lag phase of viral RNA replication up 24 hpi followed by a period of replication up to 2-8 dpi followed by a decrease in viral RNA concentration (Wigren Byström et al., 2018). These studies broadly agree with the lifecycle kinetics described here for TULV.

IF analysis of TULV infected Vero E6 cells displayed distinct distribution of NP at early, peak and persistent time points. Early infection was characterised by small distinct puncta and strand-like TULV NP. Peak infection was characterised by large NP puncta with NP filament crescents in the perinuclear region. At 30 dpi, infected cells displayed large macromolecular complexes of NP in the perinuclear region in addition to dispersed NP puncta, with large puncta towards the outer edge of the cell membrane. TULV has previously been described to exhibit this NP phenotype of small puncta at early stages of infection and crescent shaped tubes in the later stages of infection (Vapalahti et al., 1996). Ramanathan et al., 2007 describes condensed tubular NP structures in the perinuclear region at 5 dpi.

In addition to phenotypic localisation of TULV NP, persistent infections were characterised by the formation of multinuclear cells with upwards of two nuclei. These multinuclear cells were often found with normal nuclear morphology, but some cells displayed evidence of nuclear fragmentation. Orthohantavirus syncytia have been described previously and cell-fusion was thought to be mediated by the glycoproteins, which act as fusogens on the cell surface (Ogino et al., 2004). This cell-to-cell fusion may be induced by low pH conditions in multiple species of orthohantavirus including HTNV, PUUV and SEOV (Arikawa et al., 1985; McCaughey et al., 1999). The multinuclear phenotype was not limited to cell culture. Syrian hamsters infected with PUUV

were found to have giant, multinuclear cells in alveolar regions at 14 dpi (Sanada et al., 2011).

## 6.4 Tula orthohantavirus NP requires vimentin filaments for maintenance of NP macromolecular complexes

To examine the relationship between TULV NP and the host cell cytoskeleton, the spatial location of TULV NP and the cytoskeletal filaments; actin, tubulin and vimentin were examined by indirect immunofluorescence. The cellular localisation NP was also examined with drug-induced depolymerisation of cytoskeletal filaments. Previously, it has been shown that ANDV, BCCV, HTNV and SEOV NP co-localise with tubulin in infected Vero E6 cells. When infected Vero E6 cells were treated with NOC, NP displayed a cytoplasmic instead of perinuclear distribution. This redistribution of NP could repeated using a dynein-inhibitor, EHNA, suggesting NP was transported to the perinuclear region on microtubules via dynein motors (Ramanathan et al., 2007; Ramanathan and Jonsson, 2008). Actin filament depolymerisation was not found to affect NP subcellular localisation despite previous studies suggesting actin was required for NP intracellular transport (Ravkov et al., 1998; Ramanathan and Jonsson, 2008). However, it was found that intact actin and microtubule networks were required for efficient viral entry and potentially viral replication (Ramanathan and Jonsson, 2008). The study by Ramanathan et al., 2008 suggested that different orthohantavirus species may utilise different components of the cytoskeleton at different points throughout their lifecycles. In this study, TULV NP was not found to co-localise closely with actin but was found to co-localise with tubulin and vimentin in both infected and transfected cells. The depolymerisation of actin and tubulin were not found to drastically effect the sub-cellular localisation of TULV NP. Depolymerisation of vimentin by treatment with OA caused disruption of macromolecular NP structures. Removal of OA leading to recovery of vimentin polymerisation permitted the re-formation of macromolecular NP structures. This suggests that the vimentin cytoskeleton is involved in the maintenance and formation of TULV NP macromolecular structures, which was further supported by the observation that qRT-RT PCR measurements of OA-treated TULV infected Vero E6 cells show a reduction in viral RNA genome copies.

This suggests that the macromolecular NP complexes may be site of viral replication or viral RNA storage and the depolymerisation of vimentin may lead to viral RNA degradation due to its release or exposure into the cytoplasm. Vimentin has previously been shown to be important in the lifecycle of other viruses. For example, Dengue virus (DENV), requires an intact vimentin scaffold for the localisation and formation of viral replication complexes (Teo and Chu, 2014). The parvovirus, minute virus of mice (MVM), induces rearrangement of the vimentin network to form vimentin 'cages' in the perinuclear region and was important for MVM transport and replication (Fay and Panté, 2013). In African Swine Fever virus (ASFV) infections, the vimentin cage was found to have important roles in the formation of viral assembly sites and protection from cytoplasm (Stefanovic et al., 2005). The vimentin cage has also been identified during foot-and-mouth disease virus (FMDV) infections as being required for viral replication (Gladue et al., 2013). Ultrastructural analysis of Zika virus also revealed a requirement for remodelling of the cytoskeleton to form a cage around the replication complex (Cortese et al., 2017). These studies show that vimentin has an important role during multiple virus life cycles, such as formation of replication factories and protection from the host cell. The vimentin cage formation has been identified through multiple different virus infections as important in formation of replication sites. This gives precedent to the importance of vimentin for orthohantavirus replication and maintenance of NP coated replication sites. Therefore, the perinuclear region of the cell may be the site of orthohantavirus replication within a vimentin cage.

## 6.5 TULV orthohantavirus NP interacts with host proteins at different lifecycle stages

Orthohantavirus NP is a multifunctional protein that has been suggested to interact with multiple host cell proteins at different stages of the virus lifecycle. After entry into the host cell viral components need to be trafficked through the cell to sites of uncoating, transcription and translation. PUUV and HTNV NPs co-localise with early endosomal marker EEA-1 (early endosomal antigen-1). It was also found that HTNV NP co-localises with lysosomal marker LAMP-1 (lysosomal-associated membrane protein-1) in the

perinuclear region (Jin et al., 2002; Witkowski et al., 2017). These results suggest transport of virus particles through the endocytic pathway. In contrast, a separate study also found accumulation of HTNV NP in the perinuclear space but independent from EEA-1 and it was suggest that virus components were transported directly to the ERGIC via the microtubule network (Ramanathan et al., 2007).

TULV was found to show a small-degree of co-localisation with Rab5 (early endosome), Rab7 (early to late endosome) and Rab11 (late and recycling endosome) markers, but not LAMP-1 at early time points indicating a role in the endocytic but not lysosomal network for TULV trafficking. ANDV has been shown to associate with Rab8 and Rab11 (recycling endosomal) markers suggested to be important for transport to plasma membrane from the Golgi network (Rowe et al., 2008). However, at 30 dpi no colocalization was observed for TULV NP with any endosomal markers examined. It was expected that TULV proteins and RNA or assembled virions would be being transported from site of synthesis to the plasma membrane at this time. Instead, more co-localisation at this time point can be seen with clathrin. Orthohantaviruses may use clathrin-mediated endocytosis as a method of entering cells (Vaheri, Strandin, et al., 2013). Clathrin co-localises with some TULV NP puncta in the cytoplasm at 36 hpi and 30 dpi. It was possible that this may be some mechanism of viral transport from the Golgi to the plasma membrane within a transport vesicle. Clathrin has been implicated in regulation of exocytosis of post-Golgi vesicles and has been implicated in the transport of cargo from the trans-Golgi network where uncoating occurs near the plasma membrane (Puertollano et al., 2003; Jaiswal et al., 2009) . This function of clathrin may be utilised for orthohantavirus transport from the Golgi to the plasma membrane.

In addition to trafficking, orthohantavirus NPs have been associated with functions related to viral transcription and translation. NP has been described to localise to P bodies, sites of RNA degradation, where it binds to 5’ capped mRNAs and protects from degradation by cellular machinery it a process known as cap-snatching. These 5’ capped mRNAs are used as primers by the RdRp for viral RNA synthesis (Mir et al., 2008; Cheng and Mir, 2012). The co-localisation of TULV and P-body marker, DCP1a, was observed at a low level

within the cell during early, peak and persistent infections. This suggests that if this mechanism of cap-snatching occurs, it is not a major function of the TULV NP but may assist with increasing efficiency of viral RNA transcription.

## 6.6 TULV NP was cleaved in infected cells and may sequester activated caspase-3 during persistent infection to suppress apoptosis

The relationship between TULV infection and apoptosis induction in Vero E6 cells was examined through an extended time course. Previous studies have shown that TULV along with other hantaviruses were able to inhibit apoptosis (Li et al., 2002; Ontiveros et al., 2010; Gupta et al., 2013; Solà-Riera et al., 2019). Firstly, it was observed that casp-3C was absent from TULV infected Vero E6 cells at early phases of infection but was abundant in non-infected bystander cells. Western blot analysis of TULV-infected Vero E6 cells reveals the slow accumulation of apoptotic marker casp-3C. This was in direct conflict with previous studies in which TULV-infection was associated with the fast and abundant detection of apoptotic markers by western blotting (Markotic et al., 2003; Li et al., 2004; Li et al., 2005). Discrepancies between studies may be due to technical differences in approaches used to detect the apoptotic marker. In addition to western blot analysis, fluorescent line-scans were carried out to examine the spatial distribution of TULV NP and casp-3C in individual cells. This revealed casp-3C was predominantly located in bystander cells rather than TULV infected cells at 36 hpi, consistent with a separate study demonstrating the “bystander effect” of SEOV, HTNV, and ANDV infected cells (Markotic et al., 2003) and may be the source of apoptotic markers observed in other previous studies (Markotic et al., 2003; Li et al., 2004; Li et al., 2005). The “bystander effect” is an established phenomenon and has been described for HIV infections where the Env glycoprotein induces apoptosis in neighbouring cells (Garg et al., 2012) and has been utilised in cancer therapy by the use of “suicide genes”, which allow production of a toxic metabolite that acts deleteriously on neighbouring cells (Karjoo et al., 2016). The apoptotic casp-3C marker was not detected in infected cells at 36 hpi and but was detected in TULV infected cells at 7 dpi and 30 dpi. However, it was observed that TULV can form persistently infected cell cultures of up to 30 dpi

without significant cytopathic effect (CPE) or development of an apoptotic phenotype. Taken together, this suggest that TULV infection inhibits host cell apoptosis.

Previously, it has been shown that orthohantavirus NPs, recombinantly expressed or purified from virions, can be cleaved by recombinant activated caspase-3 in cell-free assays. TULV NP was cleaved during infection with cleavage products produced having apparent masses consistent with expected products based on an identified caspase-3 cleavage site in ANDV NP, namely DLID (Gupta et al., 2013). This cleavage site was conserved in TULV NP. The role of TULV NP cleavage by casp-3C in infected cells has yet to be determined. TULV NP could act as a 'decoy' substrate in a similar fashion to Junín arenavirus (JUNV) where the NP acts as a 'caspase sink' and prevents the cleavage of downstream effector proteins (Wolff et al., 2013). However, the ability of TULV NP to interact with casp-3C in a robust manner shown by indirect immunofluorescence and immunoprecipitation suggests an alternative mechanism. Fluorescent line-scan analysis on the spatial distribution of TULV NP and casp-3C in persistently infected cells revealed TULV NP and casp-3C do not occupy precisely the same position, with TULV NP forming a distinct boundary around casp-3C indicating TULV NP may form a viral-induced compartment in which casp-3C was physically separated from the rest of the cell. It is possible that TULV NP compartmentalises casp-3C and physically-segregates it from downstream components of the apoptotic cascade. This was supported by the immunoprecipitation of casp-3C using NP antisera and suggests a stable casp-3C/NP interaction that differs from the canonical enzyme:substrate interaction. This apparently stable interaction suggests the casp-3C/NP interaction encompasses addition residues outside of the casp-3C active site.

This mechanism of apoptotic protection has been previously demonstrated in a variety of other human diseases, and in cell homeostasis. In Alzheimer's disease, amyloid-β (Aβ) fibrils sequester caspase-3 into compartments and protects the cell from apoptosis (Chang et al., 2016). During thermotolerance, heat shock protein 27 (Hsp27) sequesters procaspase-3 and cytochrome-c which prevents the formation of the apoptosome (Concannon et al., 2001). In *Caenorhabditis elegans* the ced-9 molecule, a Bcl-2 homolog, is a well-

established example of a protein that regulates apoptosis by sequestering the caspase-activating factor ced-4, an analogue of mammalian Apaf-1, to the mitochondria, preventing non-programmed apoptosis. When the interaction between ced-9 and ced-4 is disrupted, downstream caspase cleavage and its subsequent activation result in apoptosis (Hengartner et al., 1992; Yan et al., 2005; Tan et al., 2007). These examples provide precedent for apoptotic protein sequestration acting to prevent apoptosis in both health and disease systems.

The co-localisation and co-precipitation of TULV NP and casp-3C in addition to the presence of a casp-3C recognition site suggests that TULV NP interferes with the host cell apoptotic pathway. TULV NP may bind to and sequester casp-3C in NP-coated vesicles and physically separate casp-3C from downstream effectors.

## 6.7 TULV RNA and NP co-localise with the Golgi and TIA-1 within early, peak and persistently infected Vero E6 cells

The location of the orthohantaviruses replication sites have not yet been identified. It has been suggested that like Bunyamwera virus (BUNV), replication may take place within the Golgi network (Fontana et al., 2008; Vaheri, Strandin, et al., 2013). To determine the replication site of orthohantaviruses *in vitro*, localisation of nascent and accumulated TULV RNA was examined by IF analysis. Firstly, the localisation of newly made TULV RNA was examined utilising Click-iT™ chemistry to fluorescently label newly transcribed viral RNA. Nascent TULV RNA localises to the perinuclear region of infected Vero E6 cells to a similar location to where filamentous structures of TULV NP were located during peak and persistent infection. To positively identify these fluorescent RNA puncta as replication sites, co-localisation with NP antisera was attempted. Unfortunately, attempts to visualise both nascent TULV RNA and TULV NP proved unsuccessful. Therefore, an alternative approach using RNA-FISH was used, in which fluorescent probes were designed against the sense and antisense TULV S segment sequences and used to determine their location within TULV infected cells. Early, peak and persistently TULV infected cells were probed for the localisation of S segment RNA in conjunction with visualisation of TULV NP

and markers for the host cell Golgi and TIA-1. Golgi and TIA-1 were previously identified as co-localising with TULV NP in the correct spatial location.

TULV sense and anti-sense RNA co-localise predominately within filamentous strands of NP in the perinuclear region of infected cells at early times post infection. During peak and persistent infections, TULV NP and S segment RNA co-localise in perinuclear filamentous structures but also within large TULV NP puncta toward the outer edge of the cytoplasm. Similar cytoplasmic structures have been seen in other viral infections, such as hRSV, Ebola virus and rabies virus, where viral replication factories were found within cytoplasmic inclusion bodies (Lahaye et al., 2009; Hoenen et al., 2012; Rincheval et al., 2017). However, many Bunyaviruses have replication factories associated with the Golgi network, such as Bunyamwera virus (BUNV) (Salanueva et al., 2003; Fontana et al., 2008). TULV NP puncta and perinuclear filaments containing S segment RNA exhibit very close co-localise well with the Golgi. These filament structures no longer resemble characteristic granular Golgi and instead appear to be large filament bundles or aggregations. This suggests that TULV may reorganise the Golgi structure to form the viral replication factory. Similar formations have been described previously for BUNV with viral factories were found to be located within the tubular-rearrangements of the Golgi network (Fontana et al., 2008; Shi et al., 2010). RNA-FISH analysis of Rift Valley Fever virus (RVFV) demonstrated S, M and L viral segments were recruited to the Golgi complex early in viral infection mediated by interactions with RVFV NP with the Gn cytoplasmic tail (Wichgers Schreur and Kortekaas, 2016). Uukuniemi virus (UUKV) buds through the Golgi apparatus and progressively induces vacuolisation (Kuismanen et al., 1982; Kuismanen et al., 1984). A similar phenotype was induced during TULV infection. This phenotype may be due to the accumulation of viral RNA and proteins in the Golgi. Previously, orthohantavirus glycoproteins and NP have been described to accumulate on the Golgi network membranes (Spiropoulou, 2001), suggesting the Golgi may act as one site of virus maturation. Glycoproteins have also been found to accumulate on the plasma membrane suggesting assembly occurs here rather than at the Golgi (Ravkov et al., 1997). It was likely that different orthohantavirus species use alternative mechanism with which to assemble;

old world viruses may assemble at the Golgi and new world viruses assemble at the plasma membrane. Results here, showing accumulation of sense and anti-sense RNA within Golgi network, suggests TULV (like other old-world viruses) may assemble within the Golgi before budding off into transport vesicles and transported to the plasma membrane.

TULV NP and TIA-1, stress-granule marker, were also shown to co-localise in Vero E6 infected cells. However, attempts to co-localise TULV NP and G3BP (Ras-GAP SH3 binding-domain protein) were unsuccessful suggesting either staining was unsuccessful, or stress granule formation had not occurred. TIA-1 and G3BP were both found in stress granules and detection of both markers substantiates stress granule formation. The lack of one of these suggests an alternative to stress granule formation was occurring. Chikungunya virus (CHIKV) has also been described to interfere with stress granule formation by sequestering G3BP into cytoplasmic foci (Fros et al., 2012). West Nile virus (WNV) and DENV have been shown to interfere with the formation of stress granules and interact with TIA-1 to form pseudo-stress granules which may be the site of viral RNA synthesis (Emara and Brinton, 2007). Similarly, TULV NP, TIA-1 and viral RNAs were observed to co-localise with some sense viral RNAs displaying lower levels of co-localisation with TIA-1. Areas positive for anti-sense RNA signal but negative for sense RNA signal may represent sites of viral assembly as, generally speaking, only anti-sense genomes are packaged into virus particles. Other areas displaying signal for both viral RNAs, TIA-1 and NP are areas of viral replication and transcription. Cytoplasmic puncta displaying high levels of co-localisation of TIA-1, NP, Golgi and viral RNAs may cytoplasmic bodies independent from replication or transcription in a similar manner to coronaviruses which induce the formation of cytoplasmic granules containing TIA-1, TIAR, PTB and viral RNA. These granules may be sites of RNP formation or post-transcriptional modification of viral RNAs (Sola et al., 2011). However further exploration is necessary for any definitive conclusions to be made.

These results suggest orthohantavirus replication occurs within the perinuclear region in a viral-induced compartment which may arise from a rearrangement of the Golgi network and may involve an interaction with TIA-1. Preliminary results from fluorescently labelled nascent viral RNA localising

to the perinuclear region supports this. Viral transcription may take place within NP-Golgi compartments where sense RNA was localised. This site may be part of the ER-Golgi intermediate compartment (ERGIC) as suggested by Ramanathan et al., 2008 and Li et al., 2010.

## 6.8 The TULV orthohantavirus lifecycle

The findings described in this study have been added to previously described knowledge and used to suggest an updated model for the orthohantavirus lifecycle. Orthohantavirus particles attach to the host cell via interactions with host surface proteins such as β1/β3 integrins or pro-cadherin 1. Viruses are internalised via clathrin-dependent or clathrin-independent mechanisms and are trafficked through early- to late-endosomes or to lysosomes. Orthohantavirus attachment, internalisation into the host cell and subsequent trafficking are all likely to be through species specific mechanisms. In late-endosomes and lysosomes, low pH induces a conformational change in viral glycoprotein structure which inserts into target membrane and causes a membrane fusion event releasing viral genomes and proteins into the cytoplasm. Virus components are trafficked to sites of replication and transcription which is likely to be in the perinuclear region of the cell. Alternatively, some orthohantavirus species virus particles are trafficked directly to the Golgi apparatus from the plasma membrane. Viral replication and transcription likely occur within the Golgi apparatus where viral NP are also located. Orthohantavirus NP also may interact with TIA-1 to generate replication factories and protect genomes from the host cell immune response. The formation of viral replication factories may require interaction with and the vimentin cage which maintains the viral factory. Viral RNA and protein accumulate within the reorganised Golgi compartment. New World orthohantavirus replication products and proteins are transported to the plasma membrane where viral assembly occurs. Assembly of old world orthohantaviruses occurs at the Golgi before transport of virions to plasma membrane. Assembled virions may be trafficked to the plasma membrane through recycling endosomes or clathrin-coated transportation vesicles. Mature hantaviruses bud from the plasma membrane by exocytosis. Orthohantaviruses may prolong cell-survival by sequestering the pro-

apoptotic factor, casp-3C, in NP coated vesicles and thereby preventing its downstream action in the apoptotic cascade.

## References


Abudurexiti, A., Adkins, S., Alioto, D., Alkhovsky, S. V., Avšič-Županc, T., Ballinger, M.J., Bente, D.A., Beer, M., Bergeron, É., Blair, C.D., Briese, T., Buchmeier, M.J., Burt, F.J., Calisher, C.H., Cháng, C., Charrel, R.N., Choi, I.R., Clegg, J.C.S., de la Torre, J.C., de Lamballerie, X., Dèng, F., Di Serio, F., Digiaro, M., Drebot, M.A., Duàn, X., Ebihara, H., Elbeaino, T., Ergünay, K., Fulhorst, C.F., Garrison, A.R., Gāo, G.F., Gonzalez, J.-P.J., Groschup, M.H., Günther, S., Haenni, A.-L., Hall, R.A., Hepojoki, J., Hewson, R., Hú, Z., Hughes, H.R., Jonson, M.G., Junglen, S., Klempa, B., Klingström, J., Kòu, C., Laenen, L., Lambert, A.J., Langevin, S.A., Liu, D., Lukashevich, I.S., Luò, T., Lǔ, C., Maes, P., de Souza, W.M., Marklewitz, M., Martelli, G.P., Matsuno, K., Mielke-Ehret, N., Minutolo, M., Mirazimi, A., Moming, A., Mühlbach, H.-P., Naidu, R., Navarro, B., Nunes, M.R.T., Palacios, G., Papa, A., Pauvolid-Corrêa, A., Pawęska, J.T., Qiáo, J., Radoshitzky, S.R., Resende, R.O., Romanowski, V., Sall, A.A., Salvato, M.S., Sasaya, T., Shěn, S., Shí, X., Shirako, Y., Simmonds, P., Sironi, M., Song, J.-W., Spengler, J.R., Stenglein, M.D., Sū, Z., Sūn, S., Táng, S., Turina, M., Wáng, B., Wáng, C., Wáng, H., Wáng, J., Wèi, T., Whitfield, A.E., Zerbini, F.M., Zhāng, J., Zhāng, L., Zhāng, Yànfāng, Zhang, Y.-Z., Zhāng, Yújiāng, Zhou, X., Zhū, L. and Kuhn, J.H. 2019. Taxonomy of the order Bunyavirales: update 2019. *Archives of Virology*. **164**(7), pp.1949–1965.

Ahlm, C., Alexeyev, O.A., Elgh, F., Aava, B., Wadell, G., Tarnvik, A., Juto, P. and Palo, T. 1997. High prevalence of hantavirus antibodies in bank voles (Clethrionomys glareolus) captured in the vicinity of households afflicted with nephropathia epidemica. *The American journal of tropical medicine and hygiene*. **56**(6), pp.674–8.

Alfadhli, A., Love, Z.A.C., Arvidson, B., Seeds, J., Willey, J. and Barklis, E. 2001. Hantavirus Nucleocapsid Protein Oligomerization. *Journal of virology*. **75**(4), pp.2019–2023.

Alfadhli, A., Steel, E., Finlay, L., Bächinger, H.P. and Barklis, E. 2002. Hantavirus nucleocapsid protein coiled-coil domains. *Journal of Biological Chemistry*. **277**(30), pp.27103–27108.

Alff, P.J., Sen, N., Gorbunova, E., Gavrilovskaya, I.N. and Mackow, E.R. 2008. The NY-1 Hantavirus Gn Cytoplasmic Tail Coprecipitates TRAF3 and Inhibits Cellular Interferon Responses by Disrupting TBK1-TRAF3 Complex Formation. *Journal of Virology*. **82**(18), pp.9115–9122.

Ali, H.S., Drewes, S., Weber de Melo, V., Schlegel, M., Freise, J., Groschup, M.H., Heckel, G. and Ulrich, R.G. 2015. Complete genome of a Puumala virus strain from Central Europe. *Virus Genes*. **50**(2), pp.292–298.

Alonso, D.O., Iglesias, A., Coelho, R., Periolo, N., Bruno, A., Córdoba, M.T., Filomarino, | Noemi, Quipildor, M., Biondo, E., Fortunato, | Eduardo, Bellomo, C. and Paula Martínez, V. 2019. Epidemiological description, case-fatality rate, and trends of Hantavirus Pulmonary Syndrome: 9 years of surveillance in Argentina.

Amroun, A., Priet, S., de Lamballerie, X. and Quérat, G. 2017. Bunyaviridae RdRps: structure, motifs, and RNA synthesis machinery. *Critical Reviews*

*in Microbiology*. **43**(6), pp.753–778.

Arai, S., Gu, S.H., Baek, L.J., Tabara, K., Bennett, S.N., Oh, H.-S., Takada, N., Kang, H.J., Tanaka-Taya, K., Morikawa, S., Okabe, N., Yanagihara, R. and Song, J.-W. 2012. Divergent ancestral lineages of newfound hantaviruses harbored by phylogenetically related crocidurine shrew species in Korea. *Virology*. **424**(2), pp.99–105.

Arai, S., Ohdachi, S.D., Asakawa, M., Kang, H.J., Mocz, G., Arikawa, J., Okabe, N. and Yanagihara, R. 2008. Molecular phylogeny of a newfound hantavirus in the Japanese shrew mole (Urotrichus talpoides). *Proceedings of the National Academy of Sciences*. **105**(42), pp.16296–16301.

Arai, S., Taniguchi, S., Aoki, K., Yoshikawa, Y., Kyuwa, S., Tanaka-Taya, K., Masangkay, J.S., Omatsu, T., Puentespina, R., Watanabe, S., Alviola, P., Alvarez, J., Eres, E., Cosico, E., Quibod, M.N.R.M., Morikawa, S., Yanagihara, R. and Oishi, K. 2016. Molecular phylogeny of a genetically divergent hantavirus harbored by the Geoffroy's rousette ( Rousettus amplexicaudatus ), a frugivorous bat species in the Philippines. *Infection, Genetics and Evolution*. **45**, pp.26–32.

Arikawa, J., Takashima, I. and Hashimoto, N. 1985. Cell fusion by haemorrhagic fever with renal syndrome (HFRS) viruses and its application for titration of virus infectivity and neutralizing antibody. *Archives of virology*. **86**(3–4), pp.303–13.

Arragain, B., Reguera, J., Desfosses, A., Gutsche, I., Schoehn, G. and Malet, H. 2019. High resolution cryo-EM structure of the helical RNA-bound Hantaan virus nucleocapsid reveals its assembly mechanisms. *eLife*. **8**.

Baer, A. and Kehn-Hall, K. 2014. Viral concentration determination through plaque assays: using traditional and novel overlay systems. *Journal of visualized experiments : JoVE*. (93), p.e52065.

Barr, J.N., Elliott, R.M., Dunn, E.F. and Wertz, G.W. 2003. Segment-specific terminal sequences of Bunyamwera bunyavirus regulate genome replication. *Virology*. **311**(2), pp.326–338.

Barriga, G.P., Martínez-Valdebenito, C., Galeno, H., Ferrés, M., Lozach, P.-Y. and Tischler, N.D. 2013. A rapid method for infectivity titration of Andes hantavirus using flow cytometry. *Journal of Virological Methods*. **193**(2), pp.291–294.

Barriga, G.P., Villalón-Letelier, F., Márquez, C.L., Bignon, E.A., Acuña, R., Ross, B.H., Monasterio, O., Mardones, G.A., Vidal, S.E. and Tischler, N.D. 2016. Inhibition of the Hantavirus Fusion Process by Predicted Domain III and Stem Peptides from Glycoprotein Gc D. W. C. Beasley, ed. *PLOS Neglected Tropical Diseases*. **10**(7), p.e0004799.

Battisti, A.J., Chu, Y.-K., Chipman, P.R., Kaufmann, B., Jonsson, C.B. and Rossmann, M.G. 2011. Structural Studies of Hantaan Virus. *Journal of Virology*. **85**(2), pp.835–841.

Bennett, S.N., Gu, S.H., Kang, H.J., Arai, S. and Yanagihara, R. 2014. Reconstructing the evolutionary origins and phylogeography of hantaviruses. *Trends in Microbiology*. **22**(8), pp.473–482.

Bharadwaj, M., Nofchissey, R., Goade, D., Koster, F. and Hjelle, B. 2000. Humoral Immune Responses in the Hantavirus Cardiopulmonary Syndrome. *The Journal of Infectious Diseases*. **182**(1), pp.43–48.

Bi, P., Cameron, S., Higgins, G. and Burrell, C. 2005. Are humans infected by Hantaviruses in Australia? *Internal Medicine Journal*. **35**(11), pp.672–674.

Bi, Z., Formenty, P.B.H. and Roth, C.E. 2008. Hantavirus Infection: a review and global update. *The Journal of Infection in Developing Countries*. **2**(01).

Bolte, S. and Cordelières, F.P. 2006. A guided tour into subcellular colocalization analysis in light microscopy. *Journal of Microscopy*. **224**(3), pp.213–232.

Borenfreund, E. and Puerner, J.A. 1985. A simple quantitative procedure using monolayer cultures for cytotoxicity assays (HTD/NR-90). *Journal of Tissue Culture Methods*. **9**(1), pp.7–9.

Borges, A.A., Campos, G.M., Moreli, M.L., Moro Souza, R.L., Saggioro, F.P., Figueiredo, G.G., Livonesi, M.C. and Moraes Figueiredo, L.T. 2008. Role of mixed Th1 and Th2 serum cytokines on pathogenesis and prognosis of hantavirus pulmonary syndrome. *Microbes and Infection*. **10**(10–11), pp.1150–1157.

Botten, J., Mirowsky, K., Ye, C., Gottlieb, K., Saavedra, M., Ponce, L. and Hjelle, B. 2002. Shedding and intracage transmission of Sin Nombre hantavirus in the deer mouse (Peromyscus maniculatus) model. *Journal of virology*. **76**(15), pp.7587–94.

Bouchard, P., Penningroth, S.M., Cheung, A., Gagnon, C. and Bardin, C.W. 1981. erythro-9-[3-(2-Hydroxynonyl)]adenine is an inhibitor of sperm motility that blocks dynein ATPase and protein carboxylmethylase activities. *Proceedings of the National Academy of Sciences*. **78**(2), pp.1033–1036.

Boudko, S.P., Kuhn, R.J. and Rossmann, M.G. 2007. The Coiled-coil Domain Structure of the Sin Nombre Virus Nucleocapsid Protein. *Journal of Molecular Biology*. **366**(5), pp.1538–1544.

Bouloy, M., Plotch, S.J. and Krug, R.M. 1978. Globin mRNAs are primers for the transcription of influenza viral RNA in vitro. *Proceedings of the National Academy of Sciences of the United States of America*. **75**(10), pp.4886–90.

Braun, M., Björkström, N.K., Gupta, S., Sundström, K., Ahlm, C., Klingström, J. and Ljunggren, H.G. 2014. NK Cell Activation in Human Hantavirus Infection Explained by Virus-Induced IL-15/IL15Rα Expression. *PLoS Pathogens*. **10**(11).

Breinbauer, R. and Köhn, M. 2003. Azide-Alkyne Coupling: A Powerful Reaction for Bioconjugate Chemistry. *ChemBioChem*. **4**(11), pp.1147–1149.

Bridgen, A., Dalrymple, D.A. and Elliott, R.M. 2002. Dugbe Nairovirus S Segment: Correction of Published Sequence and Comparison of Five Isolates. *Virology*. **294**(2), pp.364–371.

Brocato, R.L., Hammerbeck, C.D., Bell, T.M., Wells, J.B., Queen, L.A. and Hooper, J.W. 2014. A Lethal Disease Model for Hantavirus Pulmonary Syndrome in Immunosuppressed Syrian Hamsters Infected with Sin Nombre Virus. *Journal of Virology*. **88**(2), pp.811–819.

Brummer-Korvenkontio, M., Vaheri, A., Hovi, T., von Bonsdorff, C.H., Vuorimies, J., Manni, T., Penttinen, K., Oker-Blom, N., Lähdevirta, J., Bonsdorff, C.-H. von, Vuorimies, J., Manni, T., Penttinen, K., Oker-Blom, N. and Lähdevirta, J. 1980. Nephropathia epidemica: detection of antigen in bank voles and serologic diagnosis of human infection. *Journal of Infectious Diseases*. **141**(2), pp.131–134.

Buys, K.K., Jung, K.-H., Smee, D.F., Furuta, Y. and Gowen, B.B. 2011. Maporal Virus as a Surrogate for Pathogenic New World Hantaviruses and its Inhibition by Favipiravir. *Antiviral Chemistry and Chemotherapy*. **21**(5), pp.193–200.

Cain, J.A., Solis, N. and Cordwell, S.J. 2014. Beyond gene expression: The impact of protein post-translational modifications in bacteria. *Journal of Proteomics*. **97**, pp.265–286.

Camaioni, M., Botten, J., Hjelle, B. and Loew, S.S. 2001. Hantavirus seroconversion of wild-caught Peromyscus during quarantine. *Emerging infectious diseases*. **7**(3), pp.482–3.

Candenas, M.L., Norte, M., González, R., Arteche, E., Fernández, J.J., Borges, R., Boada, J., Advenier, C. and Martín, J.D. 1992. Inhibitory and contractile effects of okadaic acid on rat uterine muscle. *European journal of pharmacology*. **219**(3), pp.473–6.

Casals, J., Henderson, B.E., Hoogstraa, H., Johnson, K.M. and Shelokov, A. 1970. A review of soviet viral hemorrhagic fevers, 1969. *Journal of Infectious Diseases*. **122**(5), pp.437–453.

Chang, L.-Y., Ali, A.M., Hassan, S. and AbuBakar, S. 2006. Quantitative estimation of Nipah virus replication kinetics in vitro. *Virology Journal*. **3**(1), p.47.

Chang, Y.-J., Linh, N.H., Shih, Y.H., Yu, H.-M., Li, M.S. and Chen, Y.-R. 2016. Alzheimer's Amyloid-β Sequesters Caspase-3 in Vitro via Its C-Terminal Tail. *ACS Chemical Neuroscience*. **7**(8), pp.1097–1106.

Chaparro, J., Vega, J., Terry, W., Vera, J.., Barra, B., Meyer, R., Peters, C.J., Khan, A.S. and Ksiazek, T.G. 1998. Assessment of person-to-person transmission of hantavirus pulmonary syndrome in a Chilean hospital setting. *Journal of Hospital Infection*. **40**(4), pp.281–285.

Cheng, E. and Mir, M.A. 2012. Signatures of Host mRNA 5' Terminus for Efficient Hantavirus Cap Snatching. *Journal of Virology*. **86**(18), pp.10173–10185.

Cheng, E., Wang, Z. and Mir, M.A. 2014. Interaction between Hantavirus Nucleocapsid Protein (N) and RNA-Dependent RNA Polymerase (RdRp) Mutants Reveals the Requirement of an N-RdRp Interaction for Viral RNA Synthesis. *Journal of Virology*. **88**(15), pp.8706–8712.

Chiang, C.F., Flint, M., Lin, J.M.S. and Spiropoulou, C.F. 2016. Endocytic pathways used by andes virus to enter primary human lung endothelial

cells. *PLoS ONE*. **11**(10), pp.1–19.

Chinikar, S., Shah-Hosseini, N., Bouzari, S., Shokrgozar, M.A., Mostafavi, E., Jalali, T., Khakifirouz, S., Groschup, M.H. and Niedrig, M. 2016. Assessment of Recombination in the S-segment Genome of Crimean-Congo Hemorrhagic Fever Virus in Iran. *Journal of arthropod-borne diseases*. **10**(1), pp.12–23.

Chizhikov, V.E., Spiropoulou, C.F., Morzunov, S.P., Monroe, M.C., Peters, C.J. and Nichol, S.T. 1995. Complete genetic characterization and analysis of isolation of Sin Nombre virus. *Journal of virology*. **69**(12), pp.8132–6.

Chua, K.B., Koh, C.L., Hooi, P.S., Wee, K.F., Khong, J.H., Chua, B.H., Chan, Y.P., Lim, M.E. and Lam, S.K. 2002. Isolation of Nipah virus from Malaysian Island flying-foxes. *Microbes and infection*. **4**(2), pp.145–51.

Chung, D.-H., Kumarapperuma, S.C., Sun, Y., Li, Q., Chu, Y.-K., Arterburn, J.B., Parker, W.B., Smith, J., Spik, K., Ramanathan, H.N., Schmaljohn, C.S. and Jonsson, C.B. 2008. Synthesis of 1-β-d-ribofuranosyl-3-ethynyl-[1,2,4]triazole and its in vitro and in vivo efficacy against Hantavirus. *Antiviral Research*. **79**(1), pp.19–27.

Chung, D.-H., Västermark, Å., Camp, J. V, McAllister, R., Remold, S.K., Chu, Y.-K., Bruder, C. and Jonsson, C.B. 2013. The murine model for Hantaan virus-induced lethal disease shows two distinct paths in viral evolutionary trajectory with and without ribavirin treatment. *Journal of virology*. **87**(20), pp.10997–1007.

Cifuentes-Munoz, N., Barriga, G.P., Valenzuela, P.D.T. and Tischler, N.D. 2011. Aromatic and polar residues spanning the candidate fusion peptide of the Andes virus Gc protein are essential for membrane fusion and infection. *Journal of General Virology*. **92**(3), pp.552–563.

Cifuentes-Muñoz, N., Salazar-Quiroz, N. and Tischler, N.D. 2014. Hantavirus Gn and Gc envelope glycoproteins: key structural units for virus cell entry and virus assembly. *Viruses*. **6**(4), pp.1801–22.

Cimica, V., Dalrymple, N.A., Roth, E., Nasonov, A. and Mackow, E.R. 2014. An Innate Immunity-Regulating Virulence Determinant Is Uniquely Encoded within the Andes Virus Nucleocapsid Protein. *mBio*. **5**(1).

Clegg, J.C. and Oram, J.D. 1985. Molecular cloning of Lassa virus RNA: nucleotide sequence and expression of the nucleocapsid protein gene. *Virology*. **144**(2), pp.363–72.

Clem, A., Izurieta, R. and Galwankar, S. 2008. Leptospirosis: The 'mysterious' mimic. *Journal of Emergencies, Trauma and Shock*. **1**(1), p.21.

Clement, J. 1997. The Hantaviruses of Europe: from the Bedside to the Bench. *Emerging Infectious Diseases*. **3**(2), pp.205–211.

Concannon, C.G., Orrenius, S. and Samali, A. 2001. Hsp27 inhibits cytochrome c-mediated caspase activation by sequestering both pro-caspase-3 and cytochrome c. *Gene expression*. **9**(4–5), pp.195–201.

Cooper, P.D. 1962. The Plaque Assay of Animal Viruses. *Advances in Virus Research*. **8**, pp.319–378.

Cortese, M., Goellner, S., Acosta, E.G., Neufeldt, C.J., Oleksiuk, O., Lampe, M., Haselmann, U., Funaya, C., Schieber, N., Ronchi, P., Schorb, M., Pruunsild, P., Schwab, Y., Chatel-Chaix, L., Ruggieri, A. and Bartenschlager, R. 2017. Ultrastructural Characterization of Zika Virus Replication Factories. *Cell reports*. **18**(9), pp.2113–2123.

Cosgriff, T.M. 1991. Mechanisms of Disease in Hantavirus Infection: Pathophysiology of Hemorrhagic Fever with Renal Syndrome. *Clinical Infectious Diseases*. **13**(1), pp.97–107.

Dalrymple, N.A. and Mackow, E.R. 2014. Virus interactions with endothelial cell receptors: implications for viral pathogenesis. *Current Opinion in Virology*. **7**, pp.134–140.

DeBorde, D.C., Donabedian, A.M., Herlocher, M.L., Naeve, C.W. and Maassab, H.F. 1988. Sequence comparison of wild-type and cold-adapted B/Ann Arbor/1/66 influenza virus genes. *Virology*. **163**(2), pp.429–43.

Deyde, V.M., Rizvanov, A.A., Chase, J., Otteson, E.W. and St. Jeor, S.C. 2005. Interactions and trafficking of Andes and Sin Nombre Hantavirus glycoproteins G1 and G2. *Virology*. **331**(2), pp.307–315.

Ding, B., Qin, Y. and Chen, M. 2016. Nucleocapsid proteins: Roles beyond viral RNA packaging. *Wiley Interdisciplinary Reviews: RNA*. **7**(2), pp.213–226.

Dubendorf, J.W. and Studier, F.W. 1991. Controlling basal expression in an inducible T7 expression system by blocking the target T7 promoter with lac repressor. *Journal of Molecular Biology*. **219**(1), pp.45–59.

Duggan, J., Close, R., Mccann, L., Mccarthy, N., Mannes, T., Walsh, A., Keys, M., Wright, D., Charlet, A. and Brooks, T. 2014. Hantavirus infection in people with contact with wild and pet rats in England – preliminary results of a sero-surveillance study.

Easterbrook, J.D. and Klein, S.L. 2008. Seoul virus enhances regulatory and reduces proinflammatory responses in male Norway rats. *Journal of medical virology*. **80**(7), pp.1308–18.

Elliott, R.M. 1990. Molecular biology of the Bunyaviridae. *Journal of General Virology*. **71**, pp.501–522.

Elliott, R.M. 1989. Nucleotide Sequence Analysis of the Small (S) RNA Segment of Bunyamwera Virus, the Prototype of the Family Bunyaviridae. *Journal of General Virology*. **70**(5), pp.1281–1285.

Emara, M.M. and Brinton, M.A. 2007. Interaction of TIA-1/TIAR with West Nile and dengue virus products in infected cells interferes with stress granule formation and processing body assembly. *Proceedings of the National Academy of Sciences of the United States of America*. **104**(21), pp.9041–6.

Ermonval, M., Baychelier, F. and Tordo, N. 2016. What do we know about how hantaviruses interact with their different hosts? *Viruses*. **8**(8).

Fay, N. and Panté, N. 2013. The intermediate filament network protein, vimentin, is required for parvoviral infection. *Virology*. **444**(1–2), pp.181–

190.

Feldmann, H., Sanchez, A., Morzunov, S., Spiropoulou, C.F., Rollin, P.E., Ksiazek, T.G., Peters, C.J. and Nichol, S.T. 1993. Utilization of autopsy RNA for the synthesis of the nucleocapsid antigen of a newly recognized virus associated with hantavirus pulmonary syndrome. *Virus Research*. **30**(3), pp.351–367.

Ferrando, M. and Spiess, W.E.L. 2000. Confocal scanning laser microscopy. A powerful tool in food science Revision: Microscopía láser confocal de barrido. Una potente herramienta en la ciencia de los alimentos. *Food Science and Technology International*. **6**(4), pp.267–284.

Fletcher, D.A. and Mullins, R.D. 2010. Cell mechanics and the cytoskeleton. *Nature*. **463**(7280), pp.485–492.

Földes-Papp, Z., Demel, U. and Tilz, G.P. 2003. Laser scanning confocal fluorescence microscopy: an overview. *International Immunopharmacology*. **3**(13–14), pp.1715–1729.

Fontana, J., López-Montero, N., Elliott, R.M., Fernández, J.J. and Risco, C. 2008. The unique architecture of Bunyamwera virus factories around the Golgi complex. *Cellular Microbiology*. **10**(10), pp.2012–2028.

French, G.R., Foulke, R.S., Brand, O.A., Eddy, G.A., Lee, H.W., Lee, P.W., Brummer-Korvenkontio, M., Vaheri, A., Tsai, T., Regnery, H. and et, al. 1981. Korean hemorrhagic fever: propagation of the etiologic agent in a cell line of human origin. *Science (New York, N.Y.)*. **211**(4486), pp.1046–8.

Frensing, T., Kupke, S.Y., Bachmann, M., Fritzsche, S., Gallo-Ramirez, L.E. and Reichl, U. 2016. Influenza virus intracellular replication dynamics, release kinetics, and particle morphology during propagation in MDCK cells. *Applied Microbiology and Biotechnology*. **100**(16), pp.7181–7192.

Fros, J.J., Domeradzka, N.E., Baggen, J., Geertsema, C., Flipse, J., Vlak, J.M. and Pijlman, G.P. 2012. Chikungunya Virus nsP3 Blocks Stress Granule Assembly by Recruitment of G3BP into Cytoplasmic Foci. *Journal of Virology*. **86**(19), pp.10873–10879.

Garcin, D., Lezzi, M., Dobbs, M., Elliott, R.M., Schmaljohn, C., Kang, C.Y. and Kolakofsky, D. 1995. The 5’ Ends of Hantaan virus (Bunyaviridae) RNAs Suggest a Prime-and-Realign Mechanism for the Initiation of RNA Synthesis. *Journal of Virology*. **69**(9), pp.5754–5762.

Garg, H., Mohl, J. and Joshi, A. 2012. HIV-1 induced bystander apoptosis. *Viruses*. **4**(11), pp.3020–43.

Gavrilovskaya, I., Gorbunova, E., Koster, F. and Mackow, E. 2012. Elevated VEGF Levels in Pulmonary Edema Fluid and PBMCs from Patients with Acute Hantavirus Pulmonary Syndrome. *Advances in virology*. **2012**, p.674360.

Gavrilovskaya, I.N., Apekina, N.S., Bernshtein, A.D., Demina, V.T., Okulova, N.M., Myasnikov, Y.A. and Chumakov, M.P. 1990. Pathogenesis of hemorrhagic fever with renal syndrome virus infection and mode of horizontal transmission of hantavirus in bank voles *In*: C. H. Calisher, ed. *Hemorrhagic Fever with Renal Syndrome, Tick- and Mosquito-Borne*

*Viruses*. Vienna: Springer Vienna, pp.57–62.

Gavrilovskaya, I.N., Brown, E.J., Ginsberg, M.H. and Mackow, E.R. 1999. Cellular Entry of Hantaviruses Which Cause Hemorrhagic Fever with Renal Syndrome Is Mediated by β3 Integrins.pdf. *Journal of virology*. **73**(5), pp.3951–3959.

Gavrilovskaya, I.N., Gorbunova, E.E. and Mackow, E.R. 2012. Andes Virus Infection of Lymphatic Endothelial Cells Causes Giant Cell and Enhanced Permeability Responses That Are Rapamycin and Vascular Endothelial Growth Factor C Sensitive. *Journal of Virology*. **86**(16), pp.8765–8772.

Gavrilovskaya, I.N., Gorbunova, E.E. and Mackow, E.R. 2010. Pathogenic Hantaviruses Direct the Adherence of Quiescent Platelets to Infected Endothelial Cells. *Journal of Virology*. **84**(9), pp.4832–4839.

Gavrilovskaya, I.N., Shepley, M., Shaw, R., Ginsberg, M.H. and Mackow, E.R. 1998. beta3 Integrins mediate the cellular entry of hantaviruses that cause respiratory failure. *Proceedings of the National Academy of Sciences of the United States of America*. **95**(12), pp.7074–9.

Ge, X.-Y., Yang, W.-H., Pan, H., Zhou, J.-H., Han, X., Zhu, G.-J., Desmond, J.S., Daszak, P., Shi, Z.-L. and Zhang, Y.-Z. 2016. Fugong virus, a novel hantavirus harbored by the small oriental vole (Eothenomys eleusis) in China. *Virology Journal*. **13**(1), p.27.

Geimonen, E., Neff, S., Raymond, T., Kocer, S.S., Gavrilovskaya, I.N. and Mackow, E.R. 2002. Pathogenic and nonpathogenic hantaviruses differentially regulate endothelial cell responses. *Proceedings of the National Academy of Sciences of the United States of America*. **99**(21), pp.13837–42.

Gerlach, P., Malet, H., Cusack, S. and Reguera, J. 2015. Structural insights into bunyavirus replication and its regulation by the vRNA promoter. *Cell*. **161**(6), pp.1267–1279.

Ghiringhelli, P.D., Rivera Pomar, R. V, Baro, N.I., Rosas, M.F., Grau, O. and Romanowski, V. 1989. Nucleocapsid protein gene of Junin arenavirus (cDNA sequence). *Nucleic acids research*. **17**(19), p.8001.

Gladue, D.P., O'Donnell, V., Baker-Branstetter, R., Holinka, L.G., Pacheco, J.M., Fernandez Sainz, I., Lu, Z., Ambroggio, X., Rodriguez, L. and Borca, M. V. 2013. Foot-and-Mouth Disease Virus Modulates Cellular Vimentin for Virus Survival. *Journal of Virology*. **87**(12), pp.6794–6803.

Goldsmith, C.S., Elliott, L.H., Peters, C.J. and Zaki, S.R. 1995. Ultrastructural characterisitics of Sin Nombre virus, causative agent of hantavirus pulmonary syndrome. *Arch Virol*. **140**(12).

Gorman, O.T., Bean, W.J., Kawaoka, Y., Donatelli, I., Guo, Y.J. and Webster, R.G. 1991. Evolution of influenza A virus nucleoprotein genes: implications for the origins of H1N1 human and classical swine viruses. *Journal of virology*. **65**(7), pp.3704–14.

Groen, J., Gerding, M., Koeman, J.P., Roholl, P.J.M., van Amerongen, G., Jordans, H.G.M., Niesters, H.G.M. and Osterhaus, A.D.M.E. 1995. A Macaque Model for Hantavirus Infection. *Journal of Infectious Diseases*. **172**(1), pp.38–44.

Gu, S.H., Hejduk, J., Markowski, J., Markowski, M., Liberski, P.P. and Yanagihara, R. 2015. Whole-Genome Sequence of a Novel Hantavirus Isolated from the European Mole ( *Talpa europaea* ). *Genome Announcements*. **3**(3).

Gu, S.H., Nicolas, V., Lalis, A., Sathirapongsasuti, N. and Yanagihara, R. 2013. Complete genome sequence and molecular phylogeny of a newfound hantavirus harbored by the Doucet's musk shrew (Crocidura douceti) in Guinea. *Infection, Genetics and Evolution*. **20**, pp.118–123.

Guo, W.-P.P., Lin, X.-D.D., Wang, W., Tian, J.-H.H., Cong, M.-L.L., Zhang, H.-L.L., Wang, M.-R.R., Zhou, R.-H.H., Wang, J.-B.B., Li, M.-H.H., Xu, J., Holmes, E.C. and Zhang, Y.-Z.Z. 2013. Phylogeny and Origins of Hantaviruses Harbored by Bats, Insectivores, and Rodents C. S. Schmaljohn, ed. *PLoS Pathogens*. **9**(2), p.e1003159.

Guo, Y., Wang, W., Sun, Y., Ma, C., Wang, X., Wang, X., Liu, P., Shen, S., Li, B., Lin, J., Deng, F., Wang, H. and Lou, Z. 2016. Crystal structure of the core region of Hantavirus nucleocapsid protein reveals the mechanism for ribonucleoprotein complex formation. *Journal of Virology*. **90**(2), pp.1048–1061.

Gupta, S., Braun, M., Tischler, N.D., Stoltz, M., Sundström, K.B., Björkström, N.K., Ljunggren, H.-G.G. and Klingström, J. 2013. Hantavirus-infection Confers Resistance to Cytotoxic Lymphocyte-Mediated Apoptosis M. T. Heise, ed. *PLoS Pathogens*. **9**(3), p.e1003272.

Guterres, A. and de Lemos, E.R.S. 2018. Hantaviruses and a neglected environmental determinant. *One Health*. **5**, pp.27–33.

Habjan, M., Andersson, I., Klingström, J., Schümann, M., Martin, A., Zimmermann, P., Wagner, V., Pichlmair, A., Schneider, U., Mühlberger, E., Mirazimi, A. and Weber, F. 2008. Processing of genome 5′ termini as a strategy of negative-strand RNA viruses to avoid RIG-I-dependent interferon induction. *PLoS ONE*. **3**(4).

Hagemeijer, M.C., Vonk, A.M., Monastyrska, I., Rottier, P.J.M. and de Haan, C.A.M. 2012. Visualizing coronavirus RNA synthesis in time by using click chemistry. *Journal of virology*. **86**(10), pp.5808–16.

Hallin, G.W., Simpson, S.Q., Crowell, R.E., James, D.S., Koster, F.T., Mertz, G.J. and Levy, H. 1996. Cardiopulmonary manifestations of hantavirus pulmonary syndrome. *Critical Care Medicine*. **24**(2), pp.252–258.

Haque, A. and Mir, M.A. 2010. Interaction of Hantavirus Nucleocapsid Protein with Ribosomal Protein S19. *Journal of Virology*. **84**(23), p.12450.

Hardestam, J., Karlsson, M., Falk, K.I., Olsson, G., Klingström, J., Lundkvist, Å. and Lundkvist, A. 2008. Puumala hantavirus excretion kinetics in bank voles (Myodes glareolus). *Emerging Infectious Diseases*. **14**(8), pp.1209–1215.

Hart, C.A. and Bennett, M. 1999. Hantavirus infections: epidemiology and pathogenesis. *Microbes and Infection*. **1**(14), pp.1229–1237.

Heinemann, P., Schmidt-Chanasit, J. and Günther, S. 2013. The N terminus of Andes virus L protein suppresses mRNA and protein expression in mammalian cells. *Journal of virology*. **87**(12), pp.6975–85.

Hengartner, M.O., Ellis, R. and Horvitz, R. 1992. Caenorhabditis elegans gene ced-9 protects cells from programmed cell death. *Nature*. **356**(6369), pp.494–499.

Hepojoki, J., Strandin, T., Lankinen, H. and Vaheri, A. 2012. Hantavirus structure - Molecular interactions behind the scene. *Journal of General Virology*. **93**(8), pp.1631–1644.

Herold, S., Ludwig, S., Pleschka, S. and Wolff, T. 2012. Apoptosis signaling in influenza virus propagation, innate host defense, and lung injury. *Journal of Leukocyte Biology*. **92**(1), pp.75–82.

Hirsch, F., Gonzalez, J.-P., Matheron, S., Dournon, E., Mccormick, J.B., Moriniere, B. and Girard, P.M. 2003. HFRS After a Wild Rodent Bite in the Haute-Savoie - And Risk of Exposure to Hantaan-like Virus in a Paris Laboratory. *The Lancet*. **323**(8378), pp.676–677.

Hjelle, B., Chavez-Giles, F., Torrez-Martinez, N., Yates, T., Sarisky, J., Webb, J. and Ascher, M. 1994. Genetic identification of a novel hantavirus of the harvest mouse Reithrodontomys megalotis. *Journal of virology*. **68**(10), pp.6751–4.

Hjelle, B. and Torres-Pérez, F. 2010. Hantaviruses in the Americas and their role as emerging pathogens. *Viruses*. **2**(12), pp.2559–2586.

Hjelle, B., Tórrez-Martínez, N., Koster, F.T., Jay, M., Ascher, M.S., Brown, T., Reynolds, P., Ettestad, P., Voorhees, R.E., Sarisky, J., Enscore, R.E., Sands, L., Mosley, D.G., Kioski, C., Bryan, R.T. and Sewell, C.M. 1996. Epidemiologic linkage of rodent and human hantavirus genomic sequences in case investigations of hantavirus pulmonary syndrome. *The Journal of infectious diseases*. **173**(4), pp.781–6.

Hoenen, T., Shabman, R.S., Groseth, A., Herwig, A., Weber, M., Schudt, G., Dolnik, O., Basler, C.F., Becker, S. and Feldmann, H. 2012. Inclusion bodies are a site of ebolavirus replication. *Journal of virology*. **86**(21), pp.11779–88.

Hooper, J.W., Larsen, T., Custer, D.M. and Schmaljohn, C.S. 2001. A Lethal Disease Model for Hantavirus Pulmonary Syndrome. *Virology*. **289**(1), pp.6–14.

Huggins, J.W., Hsiang, C.M., Cosgriff, T.M., Guang, M.Y., Smith, J.I., Wu, Z.O., LeDuc, J.W., Zheng, Z.M., Meegan, J.M., Wang, Q.N., Oland, D.D., Gui, X.E., Gibbs, P.H., Yuan, G.H. and Zhang, T.M. 1991. Prospective, Double-Blind, Concurrent, Placebo-Controlled Clinical Trial of Intravenous Ribavirin Therapy of Hemorrhagic Fever with Renal Syndrome. *Journal of Infectious Diseases*. **164**(6), pp.1119–1127.

Huiskonen, J.T., Hepojoki, J., Laurinmaki, P., Vaheri, A., Lankinen, H., Butcher, S.J. and Grunewald, K. 2010. Electron Cryotomography of Tula Hantavirus Suggests a Unique Assembly Paradigm for Enveloped Viruses. *Journal of Virology*. **84**(10), pp.4889–4897.

Hutchinson, K.L., Peters, C.J. and Nichol, S.T. 1996. Sin Nombre virus mRNA synthesis. *Virology*. **224**(1), pp.139–149.

Hutchinson, K.L., Rollin, P.E. and Peters, C.J. 1998. Pathogenesis of a North American hantavirus, Black Creek Canal virus, in experimentally infected

Sigmodon hispidus. *The American journal of tropical medicine and hygiene*. **59**(1), pp.58–65.

Hynes, R.O. 2002. Integrins: Bidirectional, allosteric signaling machines. *Cell*. **110**(6), pp.673–687.

Ikegami, T., Balogh, A., Nishiyama, S., Lokugamage, N., Saito, T.B., Morrill, J.C., Shivanna, V., Indran, S. V., Zhang, L., Smith, J.K., Perez, D., Juelich, T.L., Morozov, I., Wilson, W.C., Freiberg, A.N. and Richt, J.A. 2017. Distinct virulence of Rift Valley fever phlebovirus strains from different genetic lineages in a mouse model A. K. McElroy, ed. *PLOS ONE*. **12**(12), p.e0189250.

Jääskeläinen, K.M., Kaukinen, P., Minskaya, E.S., Plyusnina, A., Vapalahti, O., Elliott, R.M., Weber, F., Vaheri, A. and Plyusnin, A. 2007. Tula and Puumala hantavirus NSs ORFs are functional and the products inhibit activation of the interferon-beta promoter. *Journal of Medical Virology*. **79**(10), pp.1527–1536.

Jääskeläinen, K.M., Plyusnina, A., Lundkvist, Å., Vaheri, A., Plyusnin, A., Jaaskelainen, K.M., Plyusnina, A., Lundkvist, A., Vaheri, A. and Plyusnin, A. 2008. Tula hantavirus isolate with the full-length ORF for nonstructural protein NSs survives for more consequent passages in interferon-competent cells than the isolate having truncated NSs ORF. *Virology Journal*. **5**(1), p.3.

Jaiswal, J.K., Rivera, V.M. and Simon, S.M. 2009. Exocytosis of Post-Golgi Vesicles Is Regulated by Components of the Endocytic Machinery. *Cell*. **137**(7), pp.1308–1319.

Jameson, L.J., Logue, C.H., Atkinson, B., Baker, N., Galbraith, S.E., Carroll, M.W., Brooks, T. and Hewson, R. 2013. The continued emergence of hantaviruses: Isolation of a seoul virus implicated in human disease, United Kingdom, Cctober 2012. *Eurosurveillance*. **18**(1), pp.1–4.

Jang, M.-S., Ryu, S.-W. and Kim, E. 2002. Modification of Daxx by small ubiquitin-related modifier-1. *Biochemical and biophysical research communications*. **295**(2), pp.495–500.

Jangra, R.K., Herbert, A.S., Li, R., Jae, L.T., Kleinfelter, L.M., Slough, M.M., Barker, S.L., Guardado-Calvo, P., Román-Sosa, G., Dieterle, M.E., Kuehne, A.I., Muena, N.A., Wirchnianski, A.S., Nyakatura, E.K., Fels, J.M., Ng, M., Mittler, E., Pan, J., Bharrhan, S., Wec, A.Z., Lai, J.R., Sidhu, S.S., Tischler, N.D., Rey, F.A., Moffat, J., Brummelkamp, T.R., Wang, Z., Dye, J.M. and Chandran, K. 2018. Protocadherin-1 is essential for cell entry by New World hantaviruses. *Nature*. **563**(7732), pp.559–563.

Jao, C.Y. and Salic, A. 2008. Exploring RNA transcription and turnover in vivo by using click chemistry. *Proceedings of the National Academy of Sciences of the United States of America*. **105**(41), pp.15779–84.

Jiang, H., Du, H., Wang, L.M., Wang, P.Z. and Bai, X.F. 2016. Hemorrhagic Fever with Renal Syndrome: Pathogenesis and Clinical Picture. *Frontiers in Cellular and Infection Microbiology*. **6**(February), pp.1–11.

Jiang, W., Yu, H., Zhao, K., Zhang, Y., Du, H., Wang, P. and Bai, X. 2013. Quantification of Hantaan Virus with a SYBR Green Ⅰ-Based One-Step

qRT-PCR Assay X. Yu, ed. *PLoS ONE*. **8**(11), p.e81525.

Jin, H.K., Yoshimatsu, K., Takada, A., Ogino, M., Asano, A., Arikawa, J. and Watanabe, T. 2001. Mouse Mx2 protein inhibits hantavirus but not influenza virus replication. *Archives of Virology*. **146**(1), pp.41–49.

Jin, M., Park, J., Lee, S., Park, B., Shin, J., Song, K.J., Ahn, T.I., Hwang, S.Y., Ahn, B.Y. and Ahn, K. 2002. Hantaan virus enters cells by clathrin-dependent receptor-mediated endocytosis. *Virology*. **294**(1), pp.60–69.

Johnson, A.M., Bowen, M.D., Ksiazek, T.G., Williams, R.J., Bryan, R.T., Mills, J.N., Peters, C.. and Nichol, S.T. 1997. Laguna Negra Virus Associated with HPS in Western Paraguay and Bolivia. *Virology*. **238**(1), pp.115–127.

Johnson, K.M. 2000. Hantaviruses: History and overview. *Current Topics in Microbiology and Immunology*. **256**, pp.1–14.

Jonsson, C.B., Figueiredo, L.T.M. and Vapalahti, O. 2010. A global perspective on hantavirus ecology, epidemiology, and disease. *Clinical Microbiology Reviews*. **23**(2), pp.412–441.

Kallio, E.R., Klingström, J., Gustafsson, E., Manni, T., Vaheri, A., Henttonen, H., Vapalahti, O. and Lundkvist, Å. 2006. Prolonged survival of Puumala hantavirus outside the host: Evidence for indirect transmission via the environment. *Journal of General Virology*. **87**(8), pp.2127–2134.

Kallio, E.R., Voutilainen, L., Vapalahti, O., Vaheri, A., Henttonen, H., Koskela, E. and Mappes, T. 2007. Endemic hantavirus infection impairs the winter survival of its rodent host. *Ecology*. **88**(8), pp.1911–6.

Kanerva, M., Mustonen, J. and Vaheri, A. 1998. Pathogenesis of Puumala and other hantavirus infections. *Reviews in Medical Virology*. **8**(2), pp.67–86.

Kang, H.J., Bennett, S.N., Dizney, L., Sumibcay, L., Arai, S., Ruedas, L.A., Song, J.-W. and Yanagihara, R. 2009. Host switch during evolution of a genetically distinct hantavirus in the American shrew mole (Neurotrichus gibbsii). *Virology*. **388**(1), pp.8–14.

Kang, H.J., Bennett, S.N., Hope, A.G., Cook, J.A. and Yanagihara, R. 2011. Shared Ancestry between a Newfound Mole-Borne Hantavirus and Hantaviruses Harbored by Cricetid Rodents. *Journal of Virology*. **85**(15), pp.7496–7503.

Kariwa, H., Saasa, N., Sanchez-Hernandez, C., Romero-Almaraz, M., Yoshida, H., Almazan-Catalan, A., Miyashita, D., Ishizuka, M., Seto, T., Sanada, T., Ramos, C., Yoshimatsu, K., Arikawa, J., Yoshii, K. and Takashima, I. n.d. Genetic identification and characterization of distinct hantaviruses circulating in Mexico. *NCBI*.

Karjoo, Z., Chen, X. and Hatefi, A. 2016. Progress and problems with the use of suicide genes for targeted cancer therapy. *Advanced drug delivery reviews*. **99**(Pt A), pp.113–128.

Kaukinen, P., Kumar, V., Tulimäki, K., Engelhardt, P., Vaheri, A. and Plyusnin, A. 2004. Oligomerization of Hantavirus N protein: C-terminal alpha-helices interact to form a shared hydrophobic space. *Journal of virology*. **78**(24), pp.13669–77.

Kaukinen, P., Vaheri, A. and Plyusnin, A. 2003a. Mapping of the Regions

Involved in Homotypic Interactions of Tula Hantavirus N Protein. *Journal of Virology*. **77**(20), pp.10910–10916.

Kaukinen, P., Vaheri, A. and Plyusnin, A. 2003b. Non-covalent interaction between nucleocapsid protein of Tula hantavirus and small ubiquitin-related modifier-1, SUMO-1. *Virus Research*. **92**(1), pp.37–45.

Kerins, J.L., Koske, S.E., Kazmierczak, J., Austin, C., Gowdy, K., Dibernardo, A., Achenbach, J., Baber, J., Balsamo, G., Behravesh, C.B., Blythe, D., Boraks-Pielechaty, I., Brown, S.M., Brown, J., Brucker, R., Bruen, B.A., Campbell, C., Cannon, D., Carlson, B., Carter, K., Cary, C., Castillo, C., Chiang, C.-F., Choi, M., Christel, E., Clayton, A., Colton, L., Cronquist, L., Damsker, D., Davis, W.G., de St Maurice, A., Dieckman, J., Dunn, J., Dycus, D.D., Ervin, E., Feist, M., Feldpausch, A., Fill, M.M., Gabel, J., Garvey, A., Genzer, S., Gibbons-Burgener, S., Graziano, J., Hall, V., Heisey, R., Henderson, H., Hennebelle, J., Hiber, L., Holzbauer, S., House, J., Jackson, E., Jenks, M.H., CDC, D.J., Keller, S., Klena, J.D., Klos, R.F., Knust, B., Kocharian, A., Kohl, K., Langham, G., Lathrop, G., Layden, J., Lehatto, K., Lovejoy, J., Lowery, K., Lukovsky-Akhsanov, N., Luong, N., Maglio, M., Manning, C., Marriott, C., Marzec, N., Masters, M., McClanahan, S., McCloskey, L., McKnight, S., McQuiston, J., McReynolds, S., Megaro, G., Morales-Betoulle, M., Nakashima, A.K., Nichol, S., Paoline, J., Patel, N., Patel, K., Peterson, D., Posivak-Khouly, L., Powell, N., Pue, H., Purpura, L., Radcliffe, R., Reynolds, N., Roesch, L., Rollin, P., Sandberg, A.L., Scheftel, J., Schroeder, B., Shaikh, I.A., Shoemaker, T., Sidge, J., Sidwa, T., Signs, K., Singh, A., Smee, A., Stanek, D., Stobierski, M.G., Straily, A., Ströher, U., Tansey, C., Tengelsen, L., Thompson, B., Ward, S.L., Warren, K., Weinstein, S., Weiss, D., Weltman, A., Yirko, T., Zuzack, J., Buck, P.A., Grolla, A., Huynh, C., Lindsay, L.R., Loomer, C., Safronetz, D., Sloan, A., Strong, J.E., Tataryn, J.R. and Vrbova, L. 2018. Outbreak of Seoul Virus Among Rats and Rat Owners — United States and Canada, 2017. *MMWR. Morbidity and Mortality Weekly Report*. **67**(4), pp.131–134.

Khaiboullina, S.F., Morzunov, S.P., Boichuk, S. V., Palotás, A., Jeor, S. St., Lombardi, V.C. and Rizvanov, A.A. 2013. Death-domain associated protein-6 (DAXX) mediated apoptosis in hantavirus infection is counter-balanced by activation of interferon-stimulated nuclear transcription factors. *Virology*. **443**(2), pp.338–348.

King, B.R., Kellner, S., Eisenhauer, P.L., Bruce, E.A., Ziegler, C.M., Zenklusen, D. and Botten, J.W. 2017. Visualization of the lymphocytic choriomeningitis mammarenavirus (LCMV) genome reveals the early endosome as a possible site for genome replication and viral particle pre-assembly. *The Journal of general virology*. **98**(10), p.2454.

Kirsanovs, S., Klempa, B., Franke, R., Lee, M.-H., Schönrich, G., Rang, A. and Kruger, D.H. 2010. Genetic reassortment between high-virulent and low-virulent Dobrava-Belgrade virus strains. *Virus Genes*. **41**(3), pp.319–328.

Klempa, B., Fichet-Calvet, E., Lecompte, E., Auste, B., Aniskin, V., Meisel, H., Denys, C., Koivogui, L., Ter Meulen, J., Krüger, D.H., Jan Ter Meulen, # and Krüger, D.H. 2006. Hantavirus in African wood mouse, Guinea.

*Emerging Infectious Diseases*. **12**(5), pp.838–840.

Klempa, B., Witkowski, P.T., Popugaeva, E., Auste, B., Koivogui, L., Fichet-Calvet, E., Strecker, T., ter Meulen, J. and Kruger, D.H. 2012. Sangassou Virus, the First Hantavirus Isolate from Africa, Displays Genetic and Functional Properties Distinct from Those of Other Murinae-Associated Hantaviruses. *Journal of Virology*. **86**(7), pp.3819–3827.

Koma, T., Yoshimatsu, K., Taruishi, M., Miyashita, D., Endo, R., Shimizu, K., Yasuda, S.P., Amada, T., Seto, T., Murata, R., Yoshida, H., Kariwa, H., Takashima, I. and Arikawa, J. 2012. Development of a serotyping enzyme-linked immunosorbent assay system based on recombinant truncated hantavirus nucleocapsid proteins for New World hantavirus infection. *Journal of Virological Methods*. **185**(1), pp.74–81.

Koster, F., Levy, H., Mertz, G., Young, S., Foucar, K., McLaughlin, J., Bryt, B., Merlin, T., Zumwalt, R.E., McFeely, P., Nolte, K.B., Burkhart, M., Kalishman, N., Gallaher, M., Voorhees, R., Samuel, M., Tanuz, M., Simpson, G., Hughes, L., Umland, E., Oty, G., Nims, L., Sewell, C.M., Sands, L., Komatsu, K., Kioski, C., Fleming, K., Doll, J., Levy, C., Fink, T.M., Murphy, P., England, B., Smolinski, M., Erickson, B., Slanta, W., Gellert, G., Schillam, P., Hoffman, R.E., Lanser, S., Nichols, C.R., Hubbard-Pourier, L., Cheek, J., Craig, A., Haskins, R., Muneta, B. and Tempest, B. 1993. Emerging Infectious Diseases Outbreak of Acute Illness-Southwestern United States, 1993. *Morbidity and Mortality Weekly Report*. **42**(22), pp.421–422.

Kramski, M., Meisel, H., Klempa, B., Krüger, D.H., Pauli, G. and Nitsche, A. 2007. Detection and typing of human pathogenic hantaviruses by real-time reverse transcription-PCR and pyrosequencing. *Clinical Chemistry*. **53**(11), pp.1899–1905.

Krautkramer, E., Grouls, S., Stein, N., Reiser, J. and Zeier, M. 2011. Pathogenic Old World Hantaviruses Infect Renal Glomerular and Tubular Cells and Induce Disassembling of Cell-to-Cell Contacts. *Journal of Virology*. **85**(19), pp.9811–9823.

Krautkramer, E. and Zeier, M. 2008. Hantavirus Causing Hemorrhagic Fever with Renal Syndrome Enters from the Apical Surface and Requires Decay-Accelerating Factor (DAF/CD55). *Journal of Virology*. **82**(9), pp.4257–4264.

Krüger, D.H., Schönrich, G. and Klempa, B. 2011. Human pathogenic hantaviruses and prevention of infection. *Human Vaccines*. **7**(6), pp.685–693.

Kuismanen, E., Bång, B., Hurme, M. and Pettersson, R.F. 1984. Uukuniemi virus maturation: immunofluorescence microscopy with monoclonal glycoprotein-specific antibodies. *Journal of virology*. **51**(1), pp.137–46.

Kuismanen, E., Hedman, K., Saraste, J. and Pettersson, R.F. 1982. Uukuniemi virus maturation: accumulation of virus particles and viral antigens in the Golgi complex. *Molecular and cellular biology*. **2**(11), pp.1444–58.

Kukkonen, S.K.J., Vaheri, A. and Plyusnin, A. 2004. Tula hantavirus L protein is a 250 kDa perinuclear membrane-associated protein. *Journal of*

*General Virology*. **85**(5), pp.1181–1189.

Kumar, S., Stecher, G. and Tamura, K. 2016. MEGA7: Molecular Evolutionary Genetics Analysis Version 7.0 for Bigger Datasets. *Molecular Biology and Evolution*. **33**(7), pp.1870–1874.

Laenen, L., Vergote, V., Kafetzopoulou, L.E., Wawina, T.B., Vassou, D., Cook, J.A., Hugot, J.-P., Deboutte, W., Kang, H.J., Witkowski, P.T., Köppen-Rung, P., Krüger, D.H., Ličková, M., Stang, A., Striešková, L., Szemeš, T., Markowski, J., Hejduk, J., Kafetzopoulos, D., Van Ranst, M., Yanagihara, R., Klempa, B. and Maes, P. 2018. A Novel Hantavirus of the European Mole, Bruges Virus, Is Involved in Frequent Nova Virus Coinfections. *Genome Biology and Evolution*. **10**(1), pp.45–55.

Lahaye, X., Vidy, A., Pomier, C., Obiang, L., Harper, F., Gaudin, Y. and Blondel, D. 2009. Functional characterization of Negri bodies (NBs) in rabies virus-infected cells: Evidence that NBs are sites of viral transcription and replication. *Journal of virology*. **83**(16), pp.7948–58.

Lambert, A.J. n.d. NCBI Direct Submission, La Crosse virus segment S nucleocapsid gene, complete cds. *NCBI*.

Lee, B.-H.H., Yoshimatsu, K., Maeda, A., Ochiai, K., Morimatsu, M., Araki, K., Ogino, M., Morikawa, S. and Arikawa, J. 2003. Association of the nucleocapsid protein of the Seoul and Hantaan hantaviruses with small ubiquitin-like modifier-1-related molecules. *Virus Research*. **98**(1), pp.83–91.

Lee, H.W. 1989. Hemorrhagic fever with renal syndrome in korea. *Reviews of Infectious Diseases*. **11**, pp.S846–S876.

Lee, H.W., Baek, L.J. and Johnson, K.M. 1982. Isolation of Hantaan virus, the etiologic agent of Korean hemorrhagic fever, from wild urban rats. *The Journal of infectious diseases*. **146**(5), pp.638–644.

Lee, H.W., Lee, P.W. and Johnson, K.M. 1978. Isolation of the Etiologic Agent of Korean Hemorrhagic Fever. *Journal of Infectious Diseases*. **137**(3), pp.298–308.

Lee, H.W., Seong, I.W., Baek, L.J., Song, C.K. and Lee, P.W. 1981. Intraspecific Transmission of Hantaan Virus, Etiologic Agent of Korean Hemorrhagic Fever, in the Rodent Apodemus agrarius. *The American Journal of Tropical Medicine and Hygiene*. **30**(5), pp.1106–1112.

Lee, W.-C., Yu, J.-S., Yang, S.-D. and Lai, Y.-K. 1992. Reversible hyperphosphorylation and reorganization of vimentin intermediate filaments by okadaic acid in 9L rat brain tumor cells. *Journal of Cellular Biochemistry*. **49**(4), pp.378–393.

Lewandowski, K.S., Bell, A.J., Wooldridge, D., Chamberlain, J., Afrough, B., Dowall, S., Vipond, R., Gharbia, S. and Hewson, R. n.d. NCBI Genome Project. *NCBI*.

Li, J., Zhang, Q., Wang, T., Li, C., Liang, M. and Li, D. 2010. Tracking hantavirus nucleocapsid protein using intracellular antibodies. *Virology journal*. **7**, p.339.

Li, S., Rissanen, I., Zeltina, A., Hepojoki, J., Raghwani, J., Harlos, K., Pybus,

O.G., Huiskonen, J.T. and Bowden, T.A. 2016. A Molecular-Level Account of the Antigenic Hantaviral Surface. *Cell Reports*. **15**(5), pp.959–967.

Li, X.-D., Lankinen, H., Putkuri, N., Vapalahti, O. and Vaheri, A. 2005. Tula hantavirus triggers pro-apoptotic signals of ER stress in Vero E6 cells. *Virology*. **333**(1), pp.180–189.

Li, X.-D.D., Mäkelä, T.P., Guo, D., Soliymani, R., Koistinen, V., Vapalahti, O., Vaheri, A., Lankinen, H., Vaheri, A., Koistinen, V., Soliymani, R., Vapalahti, O., Guo, D., Mäkelä, T.P., Guo, D., Soliymani, R., Koistinen, V., Vapalahti, O., Vaheri, A. and Lankinen, H. 2002. Hantavirus nucleocapsid protein interacts with the Fas-mediated apoptosis enhancer Daxx. *Journal of General Virology*. **83**(4), pp.759–766.

Li, X.-D.X.-D., Kukkonen, S., Vapalahti, O., Plyusnin, A., Lankinen, H., Vaheri Correspondence Antti Vaheri AnttiVaheri, A. and Vaheri, A. 2004. Tula hantavirus infection of Vero E6 cells induces apoptosis involving caspase 8 activation. *Journal of General Virology*. **85**(11), pp.3261–3268.

Lin, X.-D., Guo, W.-P., Wang, W., Zou, Y., Hao, Z.-Y., Zhou, D.-J., Dong, X., Qu, Y.-G., Li, M.-H., Tian, H.-F., Wen, J.-F., Plyusnin, A., Xu, J. and Zhang, Y.-Z. 2012. Migration of Norway rats resulted in the worldwide distribution of Seoul hantavirus today. *Journal of virology*. **86**(2), pp.972–81.

Lin, X.-D., Zhou, R.-H., Fan, F.-N., Ying, X.-H., Sun, X.-Y., Wang, W., Holmes, E.C. and Zhang, Y.-Z. 2014. Biodiversity and evolution of Imjin virus and Thottapalayam virus in Crocidurinae shrews in Zhejiang Province, China. *Virus Research*. **189**, pp.114–120.

Linderholm, M., Ahlm, C., Settergren, B., Waage, A. and Tärnvik, A. 1996. Elevated Plasma Levels of Tumor Necrosis Factor (TNF)-α, Soluble TNF Receptors, Interleukin (IL)-6, and IL-IO in Patients with Hemorrhagic Fever with Renal Syndrome. *The Journal of Infectious Diseases*. **173**(1), pp.38–43.

Löber, C., Anheier, B., Lindow, S., Klenk, H.D. and Feldmann, H. 2001. The Hantaan virus glycoprotein precursor is cleaved at the conserved pentapeptide WAASA. *Virology*. **289**(2), pp.224–229.

Lofts, L.L., Wells, J.B., Bavari, S. and Warfield, K.L. 2011. Key Genomic Changes Necessary for an In Vivo Lethal Mouse Marburgvirus Variant Selection Process. *Journal of Virology*. **85**(8), pp.3905–3917.

Van Loock, F., Thomas, I., Clement, J., Ghoos, S. and Colson, P. 1999. A Case-Control Study after a Hantavirus Infection Outbreak in the South of Belgium: Who Is at Risk? *Clinical Infectious Diseases*. **28**(4), pp.834–839.

Mackay, I.M., Arden, K.E. and Nitsche, A. 2002. Real-time PCR in virology. *Nucleic Acids Research*. **30**(6), pp.1292–1305.

Mackow, E.R., Dalrymple, N.A., Cimica, V., Matthys, V., Gorbunova, E. and Gavrilovskaya, I. 2014. Hantavirus interferon regulation and virulence determinants. *Virus Research*. **187**, pp.65–71.

Maeda, A., Lee, B.-H., Yoshimatsu, K., Saijo, M., Kurane, I., Arikawa, J. and Morikawa, S. 2003. The Intracellular Association of the Nucleocapsid

Protein (NP) of Hantaan Virus (HTNV) with Small Ubiquitin-like Modifier-1 (SUMO-1) Conjugating Enzyme 9 (Ubc9). *Virology*. **305**(2), pp.288–297.

Maes, P., Adkins, S., Alkhovsky, S. V., Avšič-Županc, T., Ballinger, M.J., Bente, D.A., Beer, M., Bergeron, É., Blair, C.D., Briese, T., Buchmeier, M.J., Burt, F.J., Calisher, C.H., Charrel, R.N., Choi, I.R., Clegg, J.C.S., de la Torre, J.C., de Lamballerie, X., DeRisi, J.L., Digiaro, M., Drebot, M., Ebihara, H., Elbeaino, T., Ergünay, K., Fulhorst, C.F., Garrison, A.R., Gāo, G.F., Gonzalez, J.-P.J., Groschup, M.H., Günther, S., Haenni, A.-L., Hall, R.A., Hewson, R., Hughes, H.R., Jain, R.K., Jonson, M.G., Junglen, S., Klempa, B., Klingström, J., Kormelink, R., Lambert, A.J., Langevin, S.A., Lukashevich, I.S., Marklewitz, M., Martelli, G.P., Mielke-Ehret, N., Mirazimi, A., Mühlbach, H.-P., Naidu, R., Nunes, M.R.T., Palacios, G., Papa, A., Pawęska, J.T., Peters, C.J., Plyusnin, A., Radoshitzky, S.R., Resende, R.O., Romanowski, V., Sall, A.A., Salvato, M.S., Sasaya, T., Schmaljohn, C., Shí, X., Shirako, Y., Simmonds, P., Sironi, M., Song, J.-W., Spengler, J.R., Stenglein, M.D., Tesh, R.B., Turina, M., Wèi, T., Whitfield, A.E., Yeh, S.-D., Zerbini, F.M., Zhang, Y.-Z., Zhou, X. and Kuhn, J.H. 2019. Taxonomy of the order Bunyavirales: second update 2018. *Archives of Virology*. **164**(3), pp.927–941.

Malakhov, M.P., Mattern, M.R., Malakhova, O.A., Drinker, M., Weeks, S.D. and Butt, T.R. 2004. SUMO fusions and SUMO-specific protease for efficient expression and purification of proteins. *Journal of Structural and Functional Genomics*. **5**(1/2), pp.75–86.

Mallya, A.D., Deobagkar, D.D., Kumar, M., Reddy, N.M., Dhere, R.M. and Kapre, S. V n.d. Mumps virus NP gene L.Zagreb vaccine strain, Serum Institute of India Ltd, Pune, India. *NCBI*.

Mancini, R., Bignon, E.A., Tischler, N.D., Acuña, R. and Lozach, P.-Y. 2015. Acidification triggers Andes hantavirus membrane fusion and rearrangement of Gc into a stable post-fusion homotrimer. *Journal of General Virology*. **96**(11), pp.3192–3197.

Mandl, J.N., Ahmed, R., Barreiro, L.B., Daszak, P., Epstein, J.H., Virgin, H.W. and Feinberg, M.B. 2015. Reservoir host immune responses to emerging zoonotic viruses. *Cell*. **160**(1–2), pp.20–35.

Manzoni, T.B. and López, C.B. 2018. Defective (interfering) viral genomes re-explored: impact on antiviral immunity and virus persistence. *Future virology*. **13**(7), pp.493–503.

Mariën, J., Borremans, B., Gryseels, S., Soropogui, B., De Bruyn, L., Bongo, G.N., Becker-Ziaja, B., de Bellocq, J.G., Günther, S., Magassouba, N., Leirs, H. and Fichet-Calvet, E. 2017. No measurable adverse effects of Lassa, Morogoro and Gairo arenaviruses on their rodent reservoir host in natural conditions. *Parasites & Vectors*. **10**(1), p.210.

Markotic, A., Hensley, L., Geisbert, T., Spik, K. and Schmaljohn, C. 2003. Hantaviruses induce cytopathic effects and apoptosis in continuous human embryonic kidney cells. *Journal of General Virology*. **84**(8), pp.2197–2202.

Martinez, V.P., Bellomo, C., San Juan, J., Pinna, D., Forlenza, R., Elder, M.

and Padula, P.J. 2005. Person-to-Person Transmission of Andes Virus. *Emerging Infectious Diseases*. **11**(12), pp.1848–1853.

Matthys, V.S., Cimica, V., Dalrymple, N.A., Glennon, N.B., Bianco, C. and Mackow, E.R. 2014. Hantavirus GnT Elements Mediate TRAF3 Binding and Inhibit RIG-I/TBK1-Directed Beta Interferon Transcription by Blocking IRF3 Phosphorylation. *Journal of Virology*. **88**(4), pp.2246–2259.

McCaughey, C., Shi, X., Elliot, R.M., Wyatt, D.E., O'Neill, H.J. and Coyle, P. V 1999. Low pH-induced cytopathic effect--a survey of seven hantavirus strains. *Journal of virological methods*. **81**(1–2), pp.193–7.

McCormick, J.B., Sasso, D.R., Palmer, E.L. and Kiley, M.P. 1982. Morphological identification of the agent of Korean haemorrhagic fever (Hantaan virus)as a member of the Bunyaviridae. *Lancet (London, England)*. **1**(8275), pp.765–8.

McElhinney, L., Fooks, A.R., Featherstone, C., Smith, R. and Morgan, D. 2016. Hantavirus (Seoul virus) in pet rats: a zoonotic viral threat. *Veterinary Record*. **178**(7), pp.171–172.

McElroy, A.., Smith, J.., Hooper, J.. and Schmaljohn, C.. 2004. Andes virus M genome segment is not sufficient to confer the virulence associated with Andes virus in Syrian hamsters. *Virology*. **326**(1), pp.130–139.

Meissner, J.D., Rowe, J.E., Borucki, M.K. and St Jeor, S.C. 2002. Complete nucleotide sequence of a Chilean hantavirus. *Virus research*. **89**(1), pp.131–43.

Mertz, G.J., Miedzinski, L., Goade, D., Pavia, A.T., Hjelle, B., Hansbarger, C.O., Levy, H., Koster, F.T., Baum, K., Lindemulder, A., Wang, W., Riser, L., Fernandez, H. and Whitley, R.J. 2004. Placebo-Controlled, Double-Blind Trial of Intravenous Ribavirin for the Treatment of Hantavirus Cardiopulmonary Syndrome in North America. *Clinical Infectious Diseases*. **39**(9), pp.1307–1313.

Meyer, B. and Schmaljohn, C. 2000. Accumulation of terminally deleted RNAs may play a role in Seoul virus persistence. *Journal of virology*. **74**(3), pp.1321–31.

Milazzo, M.L., Cajimat, M.N.B., Hanson, J.D., Bradley, R.D., Quintana, M., Sherman, C., Velásquez, R.T. and Fulhorst, C.F. 2006. Catacamas virus, a hantaviral species naturally associated with Oryzomys couesi (Coues' oryzomys) in Honduras. *The American journal of tropical medicine and hygiene*. **75**(5), pp.1003–10.

Milholland, M.T., Castro-Arellano, I., Suzán, G., Garcia-Peña, G.E., Lee, T.E., Rohde, R.E., Alonso Aguirre, A. and Mills, J.N. 2018. Global Diversity and Distribution of Hantaviruses and Their Hosts. *EcoHealth*. **15**(1), pp.163–208.

Mir, M. a and Panganiban, a T. 2005. The Hantavirus Nucleocapsid Protein Recognizes Specific Features of the Viral RNA Panhandle and Is Altered in Conformation upon RNA Binding The Hantavirus Nucleocapsid Protein Recognizes Specific Features of the Viral RNA Panhandle and Is Altered in Confo. . **79**(3), pp.1824–1835.

Mir, M.A., Brown, B., Hjelle, B., Duran, W.A. and Panganiban, A.T. 2006.

Hantavirus N Protein Exhibits Genus-Specific Recognition of the Viral RNA Panhandle. *Journal of Virology*. **80**(22), pp.11283–11292.

Mir, M.A., Duran, W.A., Hjelle, B.L., Ye, C. and Panganiban, A.T. 2008. Storage of cellular 5' mRNA caps in P bodies for viral cap-snatching. *Proceedings of the National Academy of Sciences*. **105**(49), pp.19294–19299.

Mir, M.A. and Panganiban, A.T. 2008. A protein that replaces the entire cellular eIF4F complex. *The EMBO journal*. **27**(23), pp.3129–39.

Mir, M.A. and Panganiban, A.T. 2010. The Triplet Repeats of the Sin Nombre Hantavirus 5' Untranslated Region Are Sufficient in cis for Nucleocapsid-Mediated Translation Initiation. *Journal of Virology*. **84**(17), pp.8937–8944.

Mir, M.A., Sheema, S., Haseeb, A. and Haque, A. 2010. Hantavirus nucleocapsid protein has distinct m7G cap- and RNA-binding sites. *Journal of Biological Chemistry*. **285**(15), pp.11357–11368.

Möncke-Buchner, E., Szczepek, M., Bokelmann, M., Heinemann, P., Raftery, M.J., Krüger, D.H. and Reuter, M. 2016. Sin Nombre hantavirus nucleocapsid protein exhibits a metal-dependent DNA-specific endonucleolytic activity. *Virology*. **496**, pp.67–76.

Montoya-Ruiz, C., Cajimat, M.N.B., Milazzo, M.L., Diaz, F.J., Rodas, J.D., Valbuena, G. and Fulhorst, C.F. 2015. Phylogenetic Relationship of Necoclí Virus to Other South American Hantaviruses ( *Bunyaviridae: Hantavirus* ). *Vector-Borne and Zoonotic Diseases*. **15**(7), pp.438–445.

Mossessova, E. and Lima, C.D. 2000. Ulp1-SUMO crystal structure and genetic analysis reveal conserved interactions and a regulatory element essential for cell growth in yeast. *Molecular cell*. **5**(5), pp.865–76.

Mou, D.L., Wang, Y.P., Huang, C.X., Li, G.Y., Pan, L., Yang, W.S. and Bai, X.F. 2006. Cellular entry of Hantaan virus A9 strain: Specific interactions with β3 integrins and a novel 70 kDa protein. *Biochemical and Biophysical Research Communications*. **339**(2), pp.611–617.

Muranyi, W., Bahr, U., Zeier, M. and van der Woude, F.J. 2005. Hantavirus infection. *Journal of the American Society of Nephrology : JASN*. **16**(12), pp.3669–79.

Murphy, M.E., Kariwa, H., Mizutani, T., Tanabe, H., Yoshimatsu, K., Arikawa, J. and Takashima, I. 2001. Characterization of in vitro and in vivo Antiviral Activity of Lactoferrin and Ribavirin upon Hantavirus. *Journal of Veterinary Medical Science*. **63**(6), pp.637–645.

Mustonen, J., Mäkelä, S., Outinen, T., Laine, O., Jylhävä, J., Arstila, P.T., Hurme, M. and Vaheri, A. 2013. The pathogenesis of nephropathia epidemica: New knowledge and unanswered questions. *Antiviral Research*. **100**(3), pp.589–604.

Muyangwa, M., Martynova, E. V., Khaiboullina, S.F., Morzunov, S.P. and Rizvanov, A.A. 2015. Hantaviral proteins: Structure, functions, and role in hantavirus infection. *Frontiers in Microbiology*. **6**(NOV), p.1326.

Nadin-Davis, S.A., Casey, G.A. and Wandeler, A. 1993. Identification of

Regional Variants of the Rabies Virus within the Canadian Province of Ontario. *Journal of General Virology*. **74**(5), pp.829–837.

Nelson, R., Cañate, R., Pascale, J.M., Dragoo, J.W., Armien, B., Armien, A.G. and Koster, F. 2010. Confirmation of Choclo virus as the cause of hantavirus cardiopulmonary syndrome and high serum antibody prevalence in Panama. *Journal of medical virology*. **82**(9), pp.1586–93.

Nichol, S.T., Edelstein, A., Sanchez, A.J. and Padula, P.J. 2002. Complete nucleotide sequence of the M RNA segment of Andes virus and analysis of the variability of the termini of the virus S, M and L RNA segments. *Journal of General Virology*. **83**(9), pp.2117–2122.

Niemimaa, J., Laakkonen, J., Hänninen, T., Henttonen, H., Asikainen, K., Andersen, H.K., Plyusnin, A., Leirs, H., Vaheri, A. and Bille, N. 2000. Molecular evolution of Puumala hantavirus in Fennoscandia: phylogenetic analysis of strains from two recolonization routes, Karelia and Denmark. *Journal of General Virology*. **81**(12), pp.2833–2841.

Nwaneshiudu, A., Kuschal, C., Sakamoto, F.H., Rox Anderson, R., Schwarzenberger, K. and Young, R.C. 2012. Introduction to Confocal Microscopy. *Journal of Investigative Dermatology*. **132**(12), pp.1–5.

Ogino, M., Yoshimatsu, K., Ebihara, H., Araki, K., Lee, B.-H., Okumura, M. and Arikawa, J. 2004. Cell Fusion Activities of Hantaan Virus Envelope Glycoproteins. *Journal of Virology*. **78**(19), pp.10776–10782.

Olal, D., Daumke Correspondence, O. and Daumke, O. 2016. Structure of the Hantavirus Nucleoprotein Provides Insights into the Mechanism of RNA Encapsidation. *Cell Reports*. **14**.

Ontiveros, S.J., Li, Q. and Jonsson, C.B. 2010. Modulation of apoptosis and immune signaling pathways by the Hantaan virus nucleocapsid protein. *Virology*. **401**(2), pp.165–178.

Outinen, T.K., Mäkelä, S.M., Ala-Houhala, I.O., Huhtala, H.S., Hurme, M., Paakkala, A.S., Pörsti, I.H., Syrjänen, J.T. and Mustonen, J.T. 2010. The severity of Puumala hantavirus induced nephropathia epidemica can be better evaluated using plasma interleukin-6 than C-reactive protein determinations. *BMC Infectious Diseases*. **10**(1), p.132.

Padula, P J, Edelstein, A., Miguel, S.D., López, N.M., Rossi, C.M. and Rabinovich, R.D. 1998. Epidemic outbreak of Hantavirus pulmonary syndrome in Argentina. Molecular evidence of person to person transmission of Andes virus. *Medicina*. **58 Suppl 1**, pp.27–36.

Padula, P. J., Edelstein, A., Miguel, S.D.L., López, N.M., Rossi, C.M. and Rabinovich, R.D. 1998. Hantavirus pulmonary syndrome outbreak in Argentina: Molecular evidence for person-to-person transmission of Andes virus. *Virology*. **241**(2), pp.323–330.

Palacios, G., Hui, J., Savji, N., Bussetti, V. and Lipkin, W. n.d. Genetic diversity of Lymphocytic choriomeningitis viruses. *NCBI*.

Panina, Y., Germond, A., Masui, S. and Watanabe, T.M. 2018. Validation of Common Housekeeping Genes as Reference for qPCR Gene Expression Analysis during iPS Reprogramming Process. *Scientific Reports*. **8**(1).

Park, S.-W., Han, M.-G., Park, C., Ju, Y.R., Ahn, B.-Y. and Ryou, J. 2013. Hantaan virus nucleocapsid protein stimulates MDM2-dependent p53 degradation. *The Journal of general virology*. **94**(Pt 11), pp.2424–8.

Parrington, M.A. and Kang, C.Y. 1990. Nucleotide sequence analysis of the S genomic segment of Prospect Hill virus: comparison with the prototype Hantavirus. *Virology*. **175**(1), pp.167–75.

Pensiero, M.N., Sharefkin, J.B., Dieffenbach, C.W. and Hay, J. 1992. Hantaan virus infection of human endothelial cells. *Journal of virology*. **66**(10), pp.5929–36.

Perelygina, L., Adebayo, A., Metcalfe, M. and Icenogle, J. 2015. Differences in Establishment of Persistence of Vaccine and Wild Type Rubella Viruses in Fetal Endothelial Cells R. Tripp, ed. *PLOS ONE*. **10**(7), p.e0133267.

Perley, C.C., Brocato, R.L., Kwilas, S.A., Daye, S., Moreau, A., Nichols, D.K., Wetzel, K.S., Shamblin, J. and Hooper, J.W. 2019. Three asymptomatic animal infection models of hemorrhagic fever with renal syndrome caused by hantaviruses A. N. Freiberg, ed. *PLOS ONE*. **14**(5), p.e0216700.

Plyusnin, A., Cheng, Y., Vapalahti, O., Pejcoch, M., Unar, J., Jelinkova, Z., Lehväslaiho, H., Lundkvist, A. and Vaheri, A. 1995. Genetic variation in Tula hantaviruses: sequence analysis of the S and M segments of strains from Central Europe. *Virus research*. **39**(2–3), pp.237–50.

Plyusnin, A., Hörling, J., Kanerva, M., Mustonen, J., Cheng, Y., Partanen, J., Vapalahti, O., Kukkonen, S.K., Niemimaa, J., Henttonen, H., Niklasson, B., Lundkvist, A. and Vaheri, A. 1997. Puumala hantavirus genome in patients with nephropathia epidemica: correlation of PCR positivity with HLA haplotype and link to viral sequences in local rodents. *Journal of clinical microbiology*. **35**(5), pp.1090–6.

Plyusnin, A., Kukkonen, S.K.J., Plyusnina, A., Vapalahti, O. and Vaheri, A. 2002. Transfection-mediated generation of functionally competent Tula hantavirus with recombinant S RNA segment. *The EMBO journal*. **21**(6), pp.1497–503.

Plyusnin, A. and Sironen, T. 2014. Evolution of hantaviruses: Co-speciation with reservoir hosts for more than 100MYR. *Virus Research*. **187**, pp.22–26.

Plyusnin, A., Vapalahti, O. and Vaheri, A. 1996. Hantaviruses: genome structure, expression and evolution. *The Journal of general virology*. **77 ( Pt 11**(11), pp.2677–87.

Puertollano, R., van der Wel, N.N., Greene, L.E., Eisenberg, E., Peters, P.J. and Bonifacino, J.S. 2003. Morphology and Dynamics of Clathrin/GGA1-coated Carriers Budding from the *Trans* -Golgi Network S. R. Pfeffer, ed. *Molecular Biology of the Cell*. **14**(4), pp.1545–1557.

Puorger, M.E., Hilbe, M., Müller, J.-P., Kolodziejek, J., Nowotny, N., Zlinszky, K. and Ehrensperger, F. 2010. Distribution of Borna Disease Virus Antigen and RNA in Tissues of Naturally Infected Bicolored White-Toothed Shrews, *Crocidura leucodon* , Supporting Their Role as Reservoir Host Species. *Veterinary Pathology*. **47**(2), pp.236–244.

Radosa, L., Schlegel, M., Gebauer, P., Ansorge, H., Heroldová, M., Jánová, E., Stanko, M., Mošanský, L., Fričová, J., Pejčoch, M., Suchomel, J., Purchart, L., Groschup, M.H., Krüger, D.H., Ulrich, R.G. and Klempa, B. 2013. Detection of shrew-borne hantavirus in Eurasian pygmy shrew (Sorex minutus) in Central Europe. *Infection, Genetics and Evolution*. **19**, pp.403–410.

Raj, A., van den Bogaard, P., Rifkin, S.A., van Oudenaarden, A. and Tyagi, S. 2008. Imaging individual mRNA molecules using multiple singly labeled probes. *Nature Methods*. **5**(10), pp.877–879.

Ramanathan, H.N., Chung, D.-H., Plane, S.J., Sztul, E., Chu, Y., Guttieri, M.C., McDowell, M., Ali, G. and Jonsson, C.B. 2007. Dynein-Dependent Transport of the Hantaan Virus Nucleocapsid Protein to the Endoplasmic Reticulum-Golgi Intermediate Compartment. *Journal of Virology*. **81**(16), pp.8634–8647.

Ramanathan, H.N. and Jonsson, C.B. 2008. New and Old World hantaviruses differentially utilize host cytoskeletal components during their life cycles. *Virology*. **374**(1), pp.138–150.

Rasmuson, J., Pourazar, J., Linderholm, M., Sandström, T., Blomberg, A. and Ahlm, C. 2011. Presence of Activated Airway T Lymphocytes in Human Puumala Hantavirus Disease. *Chest*. **140**(3), pp.715–722.

Ravkov, E. V. and Compans, R.W. 2001. Hantavirus Nucleocapsid Protein Is Expressed as a Membrane-Associated Protein in the Perinuclear Region. *Journal of Virology*. **75**(4), p.1808.

Ravkov, E. V, Nichol, S.T. and Compans, R.W. 1997. Polarized Entry and Release in Epithelial Cells of Black Creek Canal Virus, a New World Hantavirus. *Journal of virology*. **71**(2), pp.1147–1154.

Ravkov, E. V, Nichol, S.T., Peters, C.J. and Compans, R.W. 1998. Role of actin microfilaments in Black Creek Canal virus morphogenesis. *Journal of virology*. **72**(4), pp.2865–70.

Reguera, J., Cusack, S. and Kolakofsky, D. 2014. Segmented negative strand RNA virus nucleoprotein structure. *Current Opinion in Virology*. **5**(1), pp.7–15.

Repetto, G., del Peso, A. and Zurita, J.L. 2008. Neutral red uptake assay for the estimation of cell viability/cytotoxicity. *Nature Protocols*. **3**(7), pp.1125–1131.

Reuter, M. and Krüger, D.H. 2018. The nucleocapsid protein of hantaviruses: much more than a genome-wrapping protein. *Virus Genes*. **54**(1), pp.5–16.

Reynes, J.-M., Razafindralambo, N.K., Lacoste, V., Olive, M.-M., Barivelo, T.A., Soarimalala, V., Heraud, J.-M. and Lavergne, A. 2014. Anjozorobe Hantavirus, a New Genetic Variant of Thailand Virus Detected in Rodents from Madagascar. *Vector-Borne and Zoonotic Diseases*. **14**(3), pp.212–219.

Richter, M.H., Milazzo, M.L. and Fulhorst, C.F. n.d. Sequence analyses of the large genomic segments of New World hantaviruses. *NCBI*.

Rima, B.K., Davidson, W.B. and Martin, S.J. 1977. The Role of Defective Interfering Particles in Persistent Infection of Vero Cells by Measles Virus. *Journal of General Virology*. **35**(1), pp.89–97.

Rincheval, V., Lelek, M., Gault, E., Bouillier, C., Sitterlin, D., Blouquit-Laye, S., Galloux, M., Zimmer, C., Eleouet, J.-F.F. and Rameix-Welti, M.-A.A. 2017. Functional organization of cytoplasmic inclusion bodies in cells infected by respiratory syncytial virus. *Nature Communications*. **8**(1), p.563.

Rissanen, I., Stass, R., Zeltina, A., Li, S., Hepojoki, J., Harlos, K., Gilbert, R.J.C., Huiskonen, J.T. and Bowden, T.A. 2017. Structural Transitions of the Conserved and Metastable Hantaviral Glycoprotein Envelope. *Journal of virology*. **91**(21), pp.e00378-17.

Rönnberg, T., Jääskeläinen, K., Blot, G., Parviainen, V., Vaheri, A., Renkonen, R., Bouloy, M. and Plyusnin, A. 2012. Searching for cellular partners of hantaviral nonstructural protein NSs: Y2H screening of mouse cDNA library and analysis of cellular interactome. *PLoS ONE*. **7**(4).

Rostovtsev, V. V., Green, L.G., Fokin, V. V. and Sharpless, K.B. 2002. A Stepwise Huisgen Cycloaddition Process: Copper(I)-Catalyzed Regioselective “Ligation” of Azides and Terminal Alkynes. *Angewandte Chemie International Edition*. **41**(14), pp.2596–2599.

Rothenberger, S., Torriani, G., Johansson, M.U., Kunz, S. and Engler, O. 2016. Conserved Endonuclease Function of Hantavirus L Polymerase. *Viruses*. **8**(5).

Rowe, R.K., Suszko, J.W. and Pekosz, A. 2008. Roles for the recycling endosome, Rab8, and Rab11 in hantavirus release from epithelial cells. *Virology*. **382**(2), pp.239–249.

Ruusala, A., Persson, R., Schmaljohn, C.S. and Pettersson, R.F. 1992. Coexpression of the membrane glycoproteins G1 and G2 of Hantaan virus is required for targeting to the Golgi complex. *Virology*. **186**(1), pp.53–64.

Sadeghi, M., Eckerle, I., Daniel, V., Burkhardt, U., Opelz, G. and Schnitzler, P. 2011. Cytokine expression during early and late phase of acute Puumala hantavirus infection. *BMC Immunology*. **12**(1), p.65.

Salanueva, I.J., Novoa, R.R., Cabezas, P., López-Iglesias, C., Carrascosa, J.L., Elliott, R.M. and Risco, C. 2003. Polymorphism and structural maturation of bunyamwera virus in Golgi and post-Golgi compartments. *Journal of virology*. **77**(2), pp.1368–81.

Sanada, T., Kariwa, H., Nagata, N., Tanikawa, Y., Seto, T., Yoshimatsu, K., Arikawa, J., Yoshii, K. and Takashima, I. 2011. Puumala virus infection in Syrian hamsters (Mesocricetus auratus) resembling hantavirus infection in natural rodent hosts. *Virus Research*. **160**(1–2), pp.108–119.

Sanchez, A., Kiley, M.P., Holloway, B.P., McCormick, J.B. and Auperin, D.D. 1989. The nucleoprotein gene of Ebola virus: cloning, sequencing, and in vitro expression. *Virology*. **170**(1), pp.81–91.

Sanderson, J. 2008. *Confocal versus Widefield-which microscope to use?* [Online]. [Accessed 27 March 2019]. Available from:

http://www.microscopist.co.uk/wp-content/uploads/2017/04/Confocal-versus-Widefield.pdf.

Schliwa, M. 1982. Action of cytochalasin D on cytoskeletal networks. *The Journal of cell biology*. **92**(1), pp.79–91.

Schmaljohn, C.S. and Dalrymple, J.M. 1983. Analysis of Hantaan virus RNA: evidence for a new genus of bunyaviridae. *Virology*. **131**(2), pp.482–91.

Schmaljohn, C.S., Hasty, S.E., Harrison, S.A. and Dalrymple, J.M. 1983. Characterization of hantaan virions, the prototype virus of hemorrhagic fever with renal syndrome. *Journal of Infectious Diseases*. **148**(6), pp.1005–1012.

Schmaljohn, C.S. and Nichol, S.T. 2012. Bunyaviridae *In*: D. M. (David M. Knipe and P. M. Howley, eds. *Virus Taxonomy* [Online]. Elsevier, pp.725–741. [Accessed 23 February 2019]. Available from: https://www.sciencedirect.com/science/article/pii/B978012384684600598.

Schountz, T., Prescott, J., Cogswell, A.C., Oko, L., Mirowsky-Garcia, K., Galvez, A.P. and Hjelle, B. 2007. Regulatory T cell-like responses in deer mice persistently infected with Sin Nombre virus. *Proceedings of the National Academy of Sciences*. **104**(39), pp.15496–15501.

Schultze, D., Lundkvist, Å., Blauenstein, U., Heyman, P., Lundkvist, A.̊, Blauenstein, U. and Heyman, P. 2002. Tula virus infection associated with fever and exanthema after a wild rodent bite. *European Journal of Clinical Microbiology and Infectious Diseases*. **21**(4), pp.304–306.

Schulze-Horsel, J., Schulze, M., Agalaridis, G., Genzel, Y. and Reichl, U. 2009. Infection dynamics and virus-induced apoptosis in cell culture-based influenza vaccine production—Flow cytometry and mathematical modeling. *Vaccine*. **27**(20), pp.2712–2722.

Sekellick, M.J. and Marcus, P.I. 1978. Persistent infection. I Interferon-inducing defective-interfering particles as mediators of cell sparing: possible role in persistent infection by vesicular stomatitis virus. *Virology*. **85**(1), pp.175–86.

Severson, W., Xu, X., Kuhn, M., Senutovitch, N., Thokala, M., Ferron, F., Longhi, S., Canard, B. and Jonsson, C.B. 2005. Essential amino acids of the hantaan virus N protein in its interaction with RNA. *Journal of virology*. **79**(15), pp.10032–9.

Shaw, P.J. 2006. Comparison of widefield/deconvolution and confocal microscopy for three-dimensional imaging *In*: *Handbook of Biological Confocal Microscopy: Third Edition* [Online]. Boston, MA: Springer US, pp.453–467. [Accessed 29 October 2018]. Available from: http://link.springer.com/10.1007/978-0-387-45524-2_23.

Shi, X. and Elliott, R.M. 2004. Analysis of N-Linked Glycosylation of Hantaan Virus Glycoproteins and the Role of Oligosaccharide Side Chains in Protein Folding and Intracellular Trafficking Analysis of N-Linked Glycosylation of Hantaan Virus Glycoproteins and the Role of Oligosaccharid. *Journal of Virology*. **78**(10), pp.5414–5422.

Shi, X. and Elliott, R.M. 2002. Golgi localization of Hantaan virus glycoproteins

requires coexpression of G1 and G2. *Virology*. **300**(1), pp.31–38.

Shi, X., van Mierlo, J.T., French, A. and Elliott, R.M. 2010. Visualizing the Replication Cycle of Bunyamwera Orthobunyavirus Expressing Fluorescent Protein-Tagged Gc Glycoprotein. *Journal of Virology*. **84**(17), pp.8460–8469.

Shim, S.H., Park, M.-S., Moon, S., Park, K.S., Song, J.-W., Song, K.-J. and Baek, L.J. 2011. Comparison of innate immune responses to pathogenic and putative non-pathogenic hantaviruses in vitro. *Virus Research*. **160**(1–2), pp.367–373.

Shimizu, K., Yoshimatsu, K., Koma, T., Yasuda, S.P. and Arikawa, J. 2013. Role of nucleocapsid protein of hantaviruses in intracellular traffic of viral glycoproteins. *Virus Research*. **178**(2), pp.349–356.

Shrivastava-Ranjan, P., Rollin, P.E. and Spiropoulou, C.F. 2010. Andes virus disrupts the endothelial cell barrier by induction of vascular endothelial growth factor and downregulation of VE-cadherin. *Journal of virology*. **84**(21), pp.11227–34.

Simons, J.F., Hellman, U. and Pettersson, R.F. 1990. Uukuniemi virus S RNA segment: ambisense coding strategy, packaging of complementary strands into virions, and homology to members of the genus Phlebovirus. *Journal of virology*. **64**(1), pp.247–55.

Sinisalo, M., Vapalahti, O., Ekblom-Kullberg, S., Laine, O., Mäkelä, S., Rintala, H. and Vaheri, A. 2010. Headache and low platelets in a patient with acute leukemia. *Journal of Clinical Virology*. **48**(3), pp.159–161.

Sironen, T., Vaheri, A. and Plyusnin, A. 2001. Molecular Evolution of Puumala Hantavirus. *Journal of virology*. **75**(23), pp.11803–11810.

Sobell, H.M. 1985. Actinomycin and DNA transcription. *Proceedings of the National Academy of Sciences of the United States of America*. **82**(16), pp.5328–31.

Solà-Riera, C., Gupta, S., Ljunggren, H.-G. and Klingström, J. 2019. Orthohantaviruses belonging to three phylogroups all inhibit apoptosis in infected target cells. *Scientific reports*. **9**(1), p.834.

Sola, I., Galan, C., Mateos-Gomez, P.A., Palacio, L., Zuniga, S., Cruz, J.L., Almazan, F. and Enjuanes, L. 2011. The Polypyrimidine Tract-Binding Protein Affects Coronavirus RNA Accumulation Levels and Relocalizes Viral RNAs to Novel Cytoplasmic Domains Different from Replication-Transcription Sites. *Journal of Virology*. **85**(10), pp.5136–5149.

Song, J.-W., Baek, L.J., Schmaljohn, C.S. and Yanagihara, R. n.d. Thottapalayam Virus: Partial Characterization of a Hantavirus Isolated from an Insectivore (Suncus murinus). *NCBI*.

Song, J.-W., Gu, S., Bennett, S.N., Arai, S., Puorger, M., Hilbe, M. and Yanagihara, R. 2007. Seewis virus, a genetically distinct hantavirus in the Eurasian common shrew (Sorex araneus). *Virology Journal*. **4**(1), p.114.

Song, J.W. and Kim, J.A. n.d. Genetic Diversity and Reassortment of Hantaan Virus Tripartite RNA Genomes in Nature, Republic of Korea. *NCBI*.

Song, J.Y., Woo, H.J., Cheong, H.J., Noh, J.Y., Baek, L.J. and Kim, W.J. 2016.

Long-term immunogenicity and safety of inactivated Hantaan virus vaccine (Hantavax™) in healthy adults. *Vaccine*. **34**(10), pp.1289–1295.

Spengler, J.R., Haddock, E., Gardner, D., Hjelle, B., Feldmann, H. and Prescott, J. 2013. Experimental Andes virus infection in deer mice: characteristics of infection and clearance in a heterologous rodent host. *PloS one*. **8**(1), p.e55310.

Spiropoulou, C.F. 2001. Hantavirus maturation. *Current topics in microbiology and immunology*. **256**, pp.33–46.

Spiropoulou, C.F., Goldsmith, C.S., Shoemaker, T.R., Peters, C.J. and Compans, R.W. 2003. Sin Nombre virus glycoprotein trafficking. *Virology*. **308**(1), pp.48–63.

Stauffer, W., Sheng, H. and Lim, H.N. 2018. EzColocalization: An ImageJ plugin for visualizing and measuring colocalization in cells and organisms. *Scientific Reports*. **8**(1).

Stefanovic, S., Windsor, M., Nagata, K.-I., Inagaki, M. and Wileman, T. 2005. Vimentin rearrangement during African swine fever virus infection involves retrograde transport along microtubules and phosphorylation of vimentin by calcium calmodulin kinase II. *Journal of virology*. **79**(18), pp.11766–75.

Strauss, J.H. and Strauss, E.G. 2008. Subviral Agents *In*: *Viruses and Human Disease*. Academic Press, pp.345–368.

Studier, F.W. and Moffatt, B.A. 1986. Use of bacteriophage T7 RNA polymerase to direct selective high-level expression of cloned genes. *Journal of Molecular Biology*. **189**(1), pp.113–130.

Sun, Y., Qian, Y., Zhu, R., Zhao, L., Deng, J. and Wang, F. n.d. Analysis of nucleotide and protein sequence of N gene of respiratory syncytial virus in Beijing. *NCBI*.

Szabó, R. 2017. Antiviral therapy and prevention against hantavirus infections. *Acta Virologica*. **61**(1), pp.3–12.

Tan, F.J., Fire, A.Z. and Hill, R.B. 2007. Regulation of apoptosis by C. elegans CED-9 in the absence of the C-terminal transmembrane domain. *Cell death and differentiation*. **14**(11), pp.1925–35.

Tan, X., Sun, L., Chen, J. and Chen, Z.J. 2018. Detection of Microbial Infections Through Innate Immune Sensing of Nucleic Acids. *Annual Review of Microbiology*. **72**(1), pp.447–478.

Tanishita, O., Takahashi, Y., Okuno, Y., Yamanishi, K. and Takahashi, M. 1984. Evaluation of focus reduction neutralization test with peroxidase-antiperoxidase staining technique for hemorrhagic fever with renal syndrome virus. *Journal of clinical microbiology*. **20**(6), pp.1213–5.

Taviner, M., Thwaites, G. and Gant, V. 1998. The English sweating sickness, 1485-1551: a viral pulmonary disease? *Medical history*. **42**(1), pp.96–8.

Taylor, S.L., Frias-Staheli, N., García-Sastre, A. and Schmaljohn, C.S. 2009. Hantaan virus nucleocapsid protein binds to importin alpha proteins and inhibits tumor necrosis factor alpha-induced activation of nuclear factor kappa B. *Journal of virology*. **83**(3), pp.1271–9.

Temonen, M., Vapalahti, O., Holthöfer, H., Brummer-Korvenkontio, M., Vaheri, A. and Lankinen, H. 1993. Susceptibility of human cells to Puumala virus infection. *The Journal of general virology*. **74 ( Pt 3)**, pp.515–8.

Teo, C.S.H. and Chu, J.J.H. 2014. Cellular vimentin regulates construction of dengue virus replication complexes through interaction with NS4A protein. *Journal of virology*. **88**(4), pp.1897–913.

Terajima, M. and Ennis, F.A. 2011. T cells and pathogenesis of hantavirus cardiopulmonary syndrome and hemorrhagic fever with renal syndrome. *Viruses*. **3**(7), pp.1059–1073.

Thompson, K.A.S. and Yin, J. 2010. Population dynamics of an RNA virus and its defective interfering particles in passage cultures. *Virology Journal*. **7**, p.257.

Tiede, C., Bedford, R., Heseltine, S.J., Smith, G., Wijetunga, I., Ross, R., Alqallaf, D., Roberts, A.P.E., Balls, A., Curd, A., Hughes, R.E., Martin, H., Needham, S.R., Zanetti-Domingues, L.C., Sadigh, Y., Peacock, T.P., Tang, A.A., Gibson, N., Kyle, H., Platt, G.W., Ingram, N., Taylor, T., Coletta, L.P., Manfield, I., Knowles, M., Bell, S., Esteves, F., Maqbool, A., Prasad, R.K., Drinkhill, M., Bon, R.S., Patel, V., Goodchild, S.A., Martin-Fernandez, M., Owens, R.J., Nettleship, J.E., Webb, M.E., Harrison, M., Lippiat, J.D., Ponnambalam, S., Peckham, M., Smith, A., Ferrigno, P.K., Johnson, M., McPherson, M.J. and Tomlinson, D.C. 2017. Affimer proteins are versatile and renewable affinity reagents. *eLife*. **6**(c), pp.1–35.

Tiede, C., Tang, A.A.S., Deacon, S.E., Mandal, U., Nettleship, J.E., Owen, R.L., George, S.E., Harrison, D.J., Owens, R.J., Tomlinson, D.C. and McPherson, M.J. 2014. Adhiron: a stable and versatile peptide display scaffold for molecular recognition applications. *Protein Engineering, Design and Selection*. **27**(5), pp.145–155.

Tiley, L.S., Hagen, M., Matthews, J.T. and Krystal, M. 1994. Sequence-specific binding of the influenza virus RNA polymerase to sequences located at the 5’ ends of the viral RNAs. *Journal of virology*. **68**(8), pp.5108–16.

Tischler, N.D., Galeno, H., Rosemblatt, M. and Valenzuela, P.D.T. 2005. Human and rodent humoral immune responses to Andes virus structural proteins. *Virology*. **334**(2), pp.319–326.

Truong, A.T., Mulders, M.N., Gautam, D.C., Ammerlaan, W., de Swart, R.L., King, C.C., Osterhaus, A.D. and Muller, C.P. 2001. Genetic analysis of Asian measles virus strains--new endemic genotype in Nepal. *Virus research*. **76**(1), pp.71–8.

Vaheri, A., Henttonen, H., Voutilainen, L., Mustonen, J., Sironen, T. and Vapalahti, O. 2013. Hantavirus infections in Europe and their impact on public health. *Reviews in Medical Virology*. **23**(1), pp.35–49.

Vaheri, A., Strandin, T., Hepojoki, J., Sironen, T., Henttonen, H., Mäkelä, S. and Mustonen, J. 2013. Uncovering the mysteries of hantavirus infections. *Nature Reviews Microbiology*. **11**(8), pp.539–550.

Vapalahti, O., Lundkvist, A., Kukkonen, S.K.J., Cheng, Y., Gilljam, M., Kanerva, M., Manni, T., Pejcoch, M., Niemimaa, J., Kaikusalo, A., Henttonen, H., Vaheri, A. and Plyusnin, A. 1996. Isolation and characterization of Tula virus, a distinct serotype in the genus Hantavirus, family Bunyaviridae. *Journal of General Virology*. **77**(12), pp.3063–3067.

Vasquez, R.J., Howell, B., Yvon, A.M.C., Wadsworth, P. and Cassimeris, L. 1997. Nanomolar concentrations of nocodazole alter microtubule dynamic instability in vivo and in vitro. *Molecular Biology of the Cell*. **8**(6), pp.973–985.

Vera-Otarola, J., Solis, L., Soto-Rifo, R., Ricci, E.P., Pino, K., Tischler, N.D., Ohlmann, T., Darlix, J.-L. and López-Lastra, M. 2012. The Andes hantavirus NSs protein is expressed from the viral small mRNA by a leaky scanning mechanism. *Journal of virology*. **86**(4), pp.2176–87.

Vergote, V., Laenen, L., Vanmechelen, B., Van Ranst, M., Verbeken, E., Hooper, J.W. and Maes, P. 2017. A lethal disease model for New World hantaviruses using immunosuppressed Syrian hamsters. *PLoS Neglected Tropical Diseases*. **11**(10).

Virtanen, J.O., Jääskeläinen, K.M., Djupsjöbacka, J., Vaheri, A., Plyusnin, A., Oskari, J., Kirsi, V.•, Jääskeläinen, M., Djupsjöbacka, J., Vaheri, A., Plyusnin, A., Virtanen, J.O., Jääskeläinen, Á.K.M., Djupsjöbacka, Á.J., Vaheri, Á.A., Plyusnin, Á.A., Plyusnin, A., Jääskeläinen, K.M., Djupsjöbacka, J., Vaheri, A. and Plyusnin, A. 2010. Tula hantavirus NSs protein accumulates in the perinuclear area in infected and transfected cells. *Archives of Virology*. **155**(1), pp.117–121.

Vitullo, A.D., Merani, M.S. and Hodara, V.L. 1987. Effect of Persistent Infection with Junin Virus on Growth and Reproduction of its Natural Reservoir, Calomys musculinus. *The American Journal of Tropical Medicine and Hygiene*. **37**(3), pp.663–669.

Voutilainen, L., Kallio, E.R., Niemimaa, J., Vapalahti, O. and Henttonen, H. 2016. Temporal dynamics of Puumala hantavirus infection in cyclic populations of bank voles. *Scientific Reports*. **6**(1), p.21323.

Wang, C.-Q., Gao, J.-H., Li, M.-H., Guo, W.-P., Lu, M.-Q., Wang, W., Hu, M.-X., Li, M.-H., Yang, J., Liang, H.-J., Tian, X.-F., Holmes, E.C. and Zhang, Y.-Z. 2014. Co-circulation of Hantaan, Kenkeme, and Khabarovsk Hantaviruses in Bolshoy Ussuriysky Island, China. *Virus Research*. **191**, pp.51–58.

Wang, L.F., Yu, M., Hansson, E., Pritchard, L.I., Shiell, B., Michalski, W.P. and Eaton, B.T. 2000. The exceptionally large genome of Hendra virus: support for creation of a new genus within the family Paramyxoviridae. *Journal of virology*. **74**(21), pp.9972–9.

Wang, W., Lin, X., Zhang, Y. and Guo, W. n.d. Genetic analysis of Dabieshan hantavirus in the white-bellied rat in Zhejiang Province, China. *NCBI*.

Wang, Y., Zhang, X., Zhang, J., Cao, X., Han, H., Huang, Y., Wang, H., Chen, M., Gao, B. and Yao, L. 2015. Complete Genome Sequence of a Novel Mutation of Seoul Virus Isolated from Suncus murinus in the Fujian Province of China. *Genome Announcements*. **3**(2).

Wang, Z. and Mir, M.A. 2015. Andes virus nucleocapsid protein interrupts protein kinase R dimerization to counteract host interference in viral protein synthesis. *Journal of virology*. **89**(3), pp.1628–39.

Wells, R.M., Estani, S.S., Yadon, Z.E., Enria, D., Padula, P., Pini, N., Mills, J.N., Peters, C.J. and Segura, E.L. 1997. An Unusual Hantavirus Outbreak in Southern Argentina: Person-to-Person Transmission? *Emerging Infectious Diseases*. **3**(2), pp.171–174.

Wells, R.M., Young, J., Williams, R.J., Armstrong, L.R., Busico, K., Khan, A.S., Ksiazek, T.G., Rollin, P.E., Zaki, S.R., Nichol, S.T. and Peters, C.J. 1997. Hantavirus Transmission in the United States. *Emerging Infectious Diseases*. **3**(3), pp.361–365.

Whelan, S. and Goldman, N. 2001. A General Empirical Model of Protein Evolution Derived from Multiple Protein Families Using a Maximum-Likelihood Approach. *Molecular Biology and Evolution*. **18**(5), pp.691–699.

WHO 2015. CDC - Technical/Clinical Information: HPS Treatment - Hantavirus. *HPS - Treatment*. [Online]. [Accessed 1 March 2019]. Available from: https://www.cdc.gov/hantavirus/technical/hps/treatment.html.

Wichgers Schreur, P.J. and Kortekaas, J. 2016. Single-Molecule FISH Reveals Non-selective Packaging of Rift Valley Fever Virus Genome Segments. *PLoS pathogens*. **12**(8), p.e1005800.

Wigren Byström, J., Näslund, J., Trulsson, F., Evander, M., Wesula Lwande, O., Ahlm, C., Bucht, G., Byström, J.W., Näslund, J., Trulsson, F., Evander, M., Lwande, O.W., Ahlm, C., Bucht, G., Wigren Byström, J., Näslund, J., Trulsson, F., Evander, M., Wesula Lwande, O., Ahlm, C. and Bucht, G. 2018. Quantification and kinetics of viral RNA transcripts produced in Orthohantavirus infected cells. *Virology Journal*. **15**(1), p.18.

Willensky, S., Bar-Rogovsky, H., Bignon, E.A., Tischler, N.D., Modis, Y. and Dessau, M. 2016. Crystal Structure of Glycoprotein C from a Hantavirus in the Post-fusion Conformation D. H. Fremont, ed. *PLOS Pathogens*. **12**(10), p.e1005948.

Wilson, M. 2017. Introduction to Widefield Microscopy. *Leica Microsystems*.

Witkowski, P.T., Perley, C.C., Brocato, R.L., Hooper, J.W., Jürgensen, C., Schulzke, J.-D., Krüger, D.H. and Bücker, R. 2017. Gastrointestinal Tract As Entry Route for Hantavirus Infection. *Frontiers in microbiology*. **8**, p.1721.

Wolff, S., Becker, S. and Groseth, A. 2013. Cleavage of the Junin Virus Nucleoprotein Serves a Decoy Function To Inhibit the Induction of Apoptosis during Infection. *Journal of Virology*. **87**(1), pp.224–233.

Worobey, M. and Holmes, E.C. 1999. Evolutionary aspects of recombination in RNA viruses. *Journal of General Virology*. **80**(10), pp.2535–2543.

Xu, L., Wu, J., He, B., Qin, S., Xia, L., Qin, M., Li, N. and Tu, C. 2015. Novel hantavirus identified in black-bearded tomb bats, China. *Infection, Genetics and Evolution*. **31**, pp.158–160.

Xu, Z., Wei, L., Wang, L., Wang, H. and Jiang, S. 2002. The in vitro and in vivo protective activity of monoclonal antibodies directed against Hantaan virus: potential application for immunotherapy and passive immunization. *Biochemical and Biophysical Research Communications*. **298**(4), pp.552–558.

Yan, N., Chai, J., Lee, E.S., Gu, L., Liu, Q., He, J., Wu, J.-W., Kokel, D., Li, H., Hao, Q., Xue, D. and Shi, Y. 2005. Structure of the CED-4–CED-9 complex provides insights into programmed cell death in Caenorhabditis elegans. *Nature*. **437**(7060), pp.831–837.

Yanagihara, R., Amyx, H.L. and Gajdusek, D.C. 1985. Experimental infection with Puumala virus, the etiologic agent of nephropathia epidemica, in bank voles (Clethrionomys glareolus). *Journal of virology*. **55**(1), pp.34–8.

Yanase, T., Kato, T., Hayama, Y., Akiyama, M., Itoh, N., Horiuchi, S., Hirashima, Y., Shirafuji, H., Yamakawa, M., Tanaka, S. and Tsutsui, T. 2018. Transition of Akabane virus genogroups and its association with changes in the nature of disease in Japan. *Transboundary and Emerging Diseases*. **65**(2), pp.e434–e443.

Yoshimatsu, K., Lee, B.-H.B.-H., Araki, K., Morimatsu, M., Ogino, M., Ebihara, H. and Arikawa, J. 2003. The Multimerization of Hantavirus Nucleocapsid Protein Depends on Type-Specific Epitopes. *Journal of Virology*. **77**(2), pp.943–952.

Yu, X. -j. X.J. and Tesh, R.B. 2014. The role of mites in the transmission and maintenance of Hantaan virus (Hantavirus: Bunyaviridae). *Journal of Infectious Diseases*. **210**(11), pp.1693–1699.

Zeitz, P.S., Butler, J.C., Cheek, J.E., Samuel, M.C., Childs, J.E., Shands, L.A., Turner, R.E., Voorhees, R.E., Sarisky, J. and Rollin, P.E. 1995. A case-control study of hantavirus pulmonary syndrome during an outbreak in the southwestern United States. *The Journal of infectious diseases*. **171**(4), pp.864–70.

Zhang, Y.-Z., Zou, Y., Yan, Y.-Z., Hu, G.-W., Yao, L.-S., Du, Z.-S., Jin, L.-Z., Liu, Y.-Y., Li, M.-H., Chen, H.-X. and Fu, Z.F. 2007. Detection of phylogenetically distinct Puumala-like viruses from red-grey voleClethrionomys rufocanus in China. *Journal of Medical Virology*. **79**(8), pp.1208–1218.

Zhang, Y., Yuan, J., Yang, X., Zhou, J., Yang, W., Peng, C., Zhang, H.-L. and Shi, Z. 2011. A novel hantavirus detected in Yunnan red-backed vole (Eothenomys miletus) in China. *Journal of General Virology*. **92**(6), pp.1454–1457.

Ziegler, C.M., Eisenhauer, P., Bruce, E.A., Weir, M.E., King, B.R., Klaus, J.P., Krementsov, D.N., Shirley, D.J., Ballif, B.A. and Botten, J. 2016. The Lymphocytic Choriomeningitis Virus Matrix Protein PPXY Late Domain Drives the Production of Defective Interfering Particles B. Lee, ed. *PLOS Pathogens*. **12**(3), p.e1005501.